Aus dem Physiologischen Institut, Lehrstuhl für Physiologische Genomik, der Ludwig-Maximilians-Universität München

Fakultät für Medizin

Vorstand: Prof. Dr. Magdalena Götz

# Neuartige Kontrollmechanismen der Glioblastom-Angiogenese und -Invasivität:

# Der neurovaskuläre Faktor Apelin und die neu-identifizierten myeloid-ähnlichen TAMEP Zellen

Habilitationsschrift

Zur Erlangung der *Venia legendi*

Für das Fach Physiologie

vorgelegt von Roland E. Kälin, Dr. sc.nat.

2022

# Inhaltsverzeichnis

# Danksagung

Die vorliegende Habilitationsschrift wäre ohne die wertvolle Unterstützung und Förderung vieler Personen nicht möglich gewesen. Sie haben meinen wissenschaftlichen Werdegang maßgeblich geprägt.

Prof. Magdalena Götz möchte ich herzlich dafür danken, dass sie meine Habilitation mit Nachdruck unterstützt hat und den Vorsitz des Fachmentorats übernommen hat. An ihrem Lehrstuhl konnte ich meine Unterrichtskompetenzen erfolgreich weiterentwickeln. Dabei hat mich die Professionalität des Lehrkörpers am Institut beeindruckt von deren Hilfsbereitschaft und zuverlässigen Zusammenarbeit ich stark profitieren konnte. Diesbezüglich möchte ich mich herzlich bei Corina Haupt, Dominik Schreiber, Ruth Klafke, Lana Sirko und Prof. Stephan Kröger bedanken.

Des Weiteren bedanke ich mich bei Prof. Jörg-Christian Tonn für die Unterstützung meiner Habilitation, die Bereitstellung der geeigneten Forschungsinfrastruktur am LMU Klinikum und die gute Zusammenarbeit mit der Neurochirurgischen Klinik sowie seine hilfreichen Ratschläge zur Therapie-Relevanz meiner Forschungsschwerpunkte aus Kliniker Sicht.

Die vorliegende Arbeit wäre ohne die Hilfe und Hingabe von Prof. Rainer Glass nicht möglich gewesen. Durch seine akribische und leidenschaftliche Herangehensweise an Forschungsfragen hat er mir vorgelebt wie man ohne Scheu, jedoch mit kalkuliertem Risiko, in unentdecktes Land vordringt. Er hat mich in meiner Entwicklung zum Forschungsleiter stets unterstützt und mit viel Ausdauer und Wissen zu neuen Fragestellungen angeregt. Sein Blick für die aktuellen Themen und Methoden waren bis heute von unschätzbarem Wert für meine eigenen Fortschritte.

Auch bei Prof. Frank Heppner bedanke ich mich für die Ermöglichung einer spannenden und herausfordernden «Sturm-und-Drang» -Phase während meiner Postdoc-Zeit an der Charité Berlin. Neben dem Aufbau des tierexperimentellen Labors konnte ich mich dort den Methoden der molekularen Medizin und unterschiedlichen Fragestellungen der Neuropathologie widmen. Diese stimulierende Zeit lehrte mich meine Projekte mit den besten Mitteln und mit Nachdruck zu betreiben.

Ebenso prägend war für mich meine Doktorandenzeit an der ETH Zürich unter Anleitung von Prof. André Brändli, der mich in die Welt der Entwicklungsbiologie einlud und mich zielgerichtetes Experimentieren lehrte. Hier durchlebte ich meine ersten «Hochs und Tiefs» des Forscheralltags. Er hat mich mit seinem unstillbaren Hunger nach neuem Wissen infiziert, der zu meinem eigenen Antrieb für meine Forschung wurde.

Prof. Hans-Peter Hauri möchte ich dafür danken, dass ich in seinem hilfsbereiten Team - vielen Dank an Kähty Bucher, Oliver Nufer, Franziska Kuhn und Freddy Schnüriger, meine ersten experimentellen Schritte (meistens im Kühlraum) in Zellbiologie und Biochemie machen durfte.

Bedanken möchte ich mich auch bei allen ehemaligen und aktuellen Kollegen unseres Teams der Neurochirurgischen Forschung, bei Stefanie Lange für ihre praktische Unterstützung und natürlich bei meinen exzellenten Doktoranden, darunter besonders bei Giorgia Mastrella, Mengzuo Hou, Min Li und Linzhi Cai, für ihre Ausdauer und ihren Durchhaltewillen, den jugendlichen Wissensdrang, die endlosen stimulierenden Fragen und den spannenden interkulturellen Austausch.

Schließlich möchte ich meiner Familie aus Uri und Usedom für den immerwährenden Beistand danken. Ich danke vor allem meiner Mutter für Ihre bedingungslose und liebevolle Unterstützung aber auch meiner Schwester und meinem Bruder, dass sie für mich da sind und waren. Außerdem gilt mein größter Dank meiner Frau Stefanie für Ihre Liebe und ausdauernde Rolle an meiner Seite und meinen beiden Söhnen Frederik und Raphael, die mir das Wunder des Lebens täglich neu vor Augen führen.

...für meinen Bruder Markus

*„Wenn jemand sucht," sagte Siddhartha, „dann geschieht es leicht, dass sein Auge nur noch das Ding sieht, das er sucht, dass er nichts zu finden, nichts in sich einzulassen vermag, weil er nur immer an das Gesuchte denkt, weil er ein Ziel hat, weil er vom Ziel besessen ist. Suchen heisst: ein Ziel haben. Finden aber heisst: frei sein, offen stehen, kein Ziel haben." (Hermann Hesse)*

# I. Einleitung

## A. Genetische Treiber des Glioblastoms

Maligne Gehirntumore wie das Glioblastom (GBM) gehören zu den häufigsten und aggressivsten primären Gehirntumoren (Louis *et al*., 2016). Die heutige Standardtherapie beim GBM besteht aus maximaler Resektion gefolgt von Strahlentherapie mit konkomitanter Chemotherapie mittels Temozolomid (Stupp *et al*., 2005; Weller *et al*., 2021). Leider kann damit das GBM aktuell, trotz multimodaler Therapiekonzepte im Wesentlichen nur palliativ behandelt werden.

Die große Mehrzahl der primären GBM wird durch Mutationen in bestimmten Tumorsuppressorgenen (vor allem *TP53* und *CDKN2A*) in Kooperation mit erhöhter Aktivität verschiedener proto-onkogener Signalwege (z.B. Epidermal growth factor receptor, *EGFR* oder platelet-derived growth factor-B, *PDGFB*) hervorgerufen (Brennan *et al*., 2013; Verhaak *et al*., 2010). Zusätzlich findet man oft eine Deletion des „Neurofibromatosis-1" (*NF1*) Gens in Koinzidenz mit einem Verlust des „phosphatase and tensin homolog deleted on chromosome-10" (*PTEN*) Gens. Unterschiedliche Kombinationen dieser genetischen Mutationen führen *unisono* zur Entstehung von Tumoren mit dem histopathologischen Erscheinungsbild eines GBMs. Aus diesem Grund wird das GBM, welches bislang wegen seines pathologischen Bildes als eine homogene Entität beschrieben wurde, nun in verschiedene (genetische) Subtypen unterteilt (Brennan *et al*., 2013; Verhaak *et al*., 2010). Neueste Forschungsergebnisse belegen, dass diese Subtypen sich in ihrer Prognose und Behandlungscharakteristik unterscheiden. Diese drei wesentlichen Subtypen werden als proneurales, klassisches oder mesenchymales GBM bezeichnet. Es scheint daher fast unmöglich, dass eine einzelne, standardisierte Therapie die spezifischen Schwachpunkte jedes einzelnen Tumorsubtyps angreifen kann (Aldape *et al*., 2015).

## B. Die Tumormikroumgebung beeinflusst das Gehirntumorwachstum

Aufgrund der beobachteten genetischen Heterogenität der GBM-Zellen ist in den letzten Jahren das Tumormikromilieu ins Zentrum des Forschungsinteresses gerückt. Die zelluläre Mikroumgebung des GBMs besteht aus einer komplexen Mischung von Gehirn-eigenen und Gehirn-fremden Zellen (Aldape *et al*., 2019; Glass *et al*., 2005; Hambardzumyan *et al*., 2016),

darunter auch Stammzellen und Vorläuferzellen (Audia *et al*., 2017; Stock *et al*., 2014). Pathologisch relevant sind dabei die mesenchymalen Stammzellen, neuronale und oligodendrogliale Vorläuferzellen (Audia *et al*., 2017; Huang *et al*., 2014; Stock *et al*., 2014). Mesenchymale Stammzellen zeigen sowohl eine Tumor-unterstützende Wirkung wie auch anti-neoplastisches Potential entsprechend ihrem Ursprung im Knochenmark oder in einer perivaskulären Position (Audia *et al*., 2017; Behnan *et al*., 2014; Ho *et al*., 2013). Neuronale Vorläuferzellen hemmen die GBM-Progression über die Freisetzung von bioaktiven Lipiden (Stock *et al*., 2014), aber die Anzahl an neuronalen Vorläuferzellen nimmt mit dem Alter ab, weshalb ihr Tumor-hemmender Effekt im Tierversuch auf junge Mäuse (auf die ersten 90 Tage nach Geburt) limitiert bleibt (Walzlein *et al*., 2008). Oligodendrogliale Vorläuferzellen können zur Bildung von perivaskulären Zellen im GBM beitragen und so die Gefäßneubildung unterstützen (Huang *et al*., 2014). Zusätzlich ist unklar ob noch andere Stamm- und Vorläuferzellen existieren, welche das GBM-Wachstum vorantreiben können.

Eine weitere Hauptkomponente in der Tumormikroumgebung machen die Immunzellen des Gehirns aus, die sogenannten Mikroglia. Ein Großteil der Zellen im GBM besteht nämlich aus diesen myeloischen Zellen (Audia *et al*., 2017). Die myeloische Population des GBM setzt sich jedoch nicht nur aus den hirneigenen Mikroglia, sondern auch aus Tumor-assoziierten Makrophagen (gemeinsam TAM genannt) zusammen. Unter physiologischen Bedingungen sind myeloische Zellen in der Lage durch zytotoxische und phagozytische Mechanismen Fremdmaterial zu eliminieren. Unter den pathologischen Bedingungen des GBMs scheint diese Wirkung unterdrückt und die Mikroglia können die lebensbedrohliche GBM-Zell-Streuung in das gesunde Gehirngewebe scheinbar sogar unterstützen (Aldape *et al*., 2019; Glass and Synowitz, 2014; Markovic *et al*., 2009). Zusätzlich häufen sich die Hinweise, dass die Tumor-assoziierten myeloischen Zellen eine aktive Rolle in der Bildung der Tumorgefäße (Angiogenese) und ihrer Reifung (Gefäßnormalisierung) spielen (Brandenburg *et al*., 2016; Mathivet *et al*., 2017). Dieses Krankheits-induzierte Gefäßwachstum des GBMs kann wiederum die Tumor-Progression befördern (Aldape *et al*., 2019; Glass and Synowitz, 2014). Insgesamt ist die Gesamtpopulation myeloischer Zellen sehr heterogen und eine Unterscheidung einzelner Subpopulationen aufgrund von überlappenden Markerprofilen äußerst komplex (Glass and Synowitz, 2014; Hambardzumyan *et al*., 2016; Prinz *et al*., 2019). Da jedoch unterschiedliche Subpopulationen von TAM sehr

unterschiedliche Funktionen für das Tumorwachstum aufweisen können ist die umfangreiche Charakterisierung des myeloischen Kompartiments im Tumormikromilieu entscheidend für die Identifikation neuer Therapiestrategien. Der einzige Weg unterschiedliche Subpopulationen eindeutig zuzuordnen und funktionell zu studieren, beruht im Moment auf der Nutzung neuartiger transgener Mausmodelle. Zum Beispiel können über das transgene Myeloid-Reportermodell Cx3cr1-CreER durch ein etabliertes „Pulse-Chase“ Verfahren die langlebigen Gehirn-eigenen Mikroglia von den kurzlebigen, aus der Peripherie-einwandernden, Makrophagen im GBM unterschieden werden (Wieghofer *et al*., 2015), während Tumor-invadierende periphere Makrophagen eine hohe Expression von Chemokin-Rezeptor CCR2 aufweisen und mittels CCR2-GFP Reporter-Modell verfolgt werden können (Chen *et al*., 2017).

Ein weiteres Hauptmerkmal des GBMs ist das zahlreiche Vorkommen von fehlgebildeten Gefäßkapillaren (Aldape *et al*., 2019; Louis *et al*., 2016; Weller *et al*., 2021). Diese entstehen aus proliferierenden Endothelzellen und werden während der Gefäßreifung von Gefäßstützzellen umhüllt (Armulik *et al*., 2011)**.** Diese sogenannten Perizyten teilen dieselbe extrazellulare Matrix („basement membrane“) mit den kapillaren Endothelzellen. Indem sie die Signale aus ihrer Nachbarschaft, bestehend aus Endothel, Astrozyten und Neuronen (die sogenannte Neurovaskuläre Einheit) integrieren, ermöglichen sie die physiologische Funktion des Zentralnervensystems (ZNS). Außerdem erhalten sie die Integrität der Bluthirnschranke und kontrollieren so deren Durchlässigkeit (Sweeney *et al*., 2016). Die molekularen Signalwege in der Kontrolle der Bluthirnschranken-Öffnung sind dabei noch wenig erforscht.

Aufgrund der starken Gefäßneubildung im GBM wurden in den letzten Jahren verschiedene anti-angiogene Behandlungsansätze gegen das GBM verfolgt (Jain *et al*., 2007), wobei jedoch in klinischen Studien bei Nutzung des Angiogenese-Faktors VEGFA als therapeutisches Ziel keine Verbesserung des allgemeinen Patientenüberlebens beobachtet werden konnte (Chinot *et al*., 2014; Gilbert *et al*., 2014). Aus diesem Grund wird dringend nach neuartigen anti-angiogene Therapien gesucht. Eine Möglichkeit bietet dabei die Erforschung alternativer angiogener Signalwege, wie wir sie in den letzten Jahren betrieben haben.

## C. Das neurovaskuläre Peptid Apelin und sein Rezeptor APLNR in der Gefäßentwicklung

Das humane APLNR-Gen (auch bekannt als APJ) wurde durch seine Sequenzhomologie zum „Angiotensin II Rezeptor type 1“ (AT1R) entdeckt (Kälin and Kälin, 2017; O'Dowd *et al*., 1993). Das orthologe Frosch-Gen für APLNR (auch bekannt als Msr) wurde danach kloniert und seine Expression in den venösen und arteriellen Gefäßen während der Embryonalentwicklung erstmalig beschrieben (Devic *et al*., 1996) In Folgestudien wurde APLNR als verlässlicher Gefäßmarker in *Xenopus* Kaulquappen (Cleaver *et al*., 1997; Devic *et al*., 1999; Kälin *et al*., 2009) und Nagetieren etabliert (De Mota *et al*., 2000; Devic *et al*., 1999; Hosoya *et al*., 2000; O'Carroll *et al*., 2000).
Über einen biochemischen Liganden-Screen für G-Protein-gekoppelte Rezeptoren wurde ein kleines bioaktives Peptid für APJ (APLNR) isoliert und nach seinem Rezeptor Apelin (für APJ endogener Ligand) benannt (Tatemoto *et al*., 1998). Dank der Peptidsequenz wurde danach die cDNA für das humane Apelin (APLN) kloniert welches für ein sezerniertes Präproprotein aus 77 Aminosäuren (Apelin-77) kodiert (Reaux *et al*., 2001; Tatemoto *et al*., 1998). Proteolytisch wird Apelin weiter in die Isoformen Apelin-36, Apelin-17, Apelin-13, und das pyroglutamylierte (Pyr1) Apelin-13 (Tatemoto *et al*., 1998) aufgespalten. Interessanterweise sind die letzten 14 Aminosäuren von APLN, welche das Peptid Apelin-13 enthalten, zu 100% in allen Wirbeltieren identisch, vom Frosch über die Maus bis hin zum Menschen (Kälin *et al*., 2007).

Während der Rezeptor APLNR embryonal in der gesamten Vaskulatur vorkommt (Devic *et al*., 1996; Devic *et al*., 1999), beschränkt sich die Expression des Liganden APLN auf die Gefäßregionen, die sich in der Aussprossung befinden (Cox *et al*., 2006; Kälin *et al*., 2007; Saint-Geniez *et al*., 2002). In Folgeexperimenten konnte von uns und von anderen Forschern gezeigt werden, dass APLN notwendig und hinreichend für die Angiogenese während der Embryonalentwicklung ist (Cox *et al*., 2006; Kälin *et al*., 2007). Die Hochregulation der APLN-Expression kann dabei durch den VEGFA-Signalweg (Kälin *et al*., 2007) oder durch Hypoxie ausgelöst werden; im APLN-Promoter befindet sich nämlich dafür ein „hypoxia-responsive element“ (Cox *et al*., 2006; Kasai *et al*., 2010). Während in APLN-KO Mäusen in erster Betrachtung nur milde Effekte auf die Vaskulatur gefunden wurden (z.B. ein reduzierter Gefäßdurchmesser) (Kidoya *et al*., 2008), wurde später auch eine Reduktion in der Gefäßentwicklung beobachtet (z.B.

in der Retina; Kasai *et al*., 2010). Apelin scheint dabei zuerst parakrin die angiogene Gefäßsprossung auszulösen und dann autokrin die Motilität der endothelialen „Tip“-Zellen, in denen APLN am höchsten exprimiert ist, zu steuern. (del Toro *et al*., 2010; Helker *et al*., 2020; Kälin *et al*., 2007; Kidoya *et al*., 2008; Strasser *et al*., 2010). In der Folge wurden APLN-Cre Reporter Mäuse entwickelt, mit welchen die Endothelien angezeigt werden, die sich während der Embryonalentwicklung oder sich unter pathologischen Umständen gerade in der Aussprossung befinden (Liu *et al*., 2015).

# II. Ziel der Arbeit

Ziel meines Habilitationsprojektes war es neuartige Kontrollmechanismen der Glioblastom-Angiogenese und Invasivität zu untersuchen. Dies geschah unter der Hypothese, dass über das Verständnis und die Manipulation der Zusammensetzung des Tumorparenchyms die genetische Heterogenität des GBMs (als erschwerender Faktor für eine erfolgreiche Tumor-Therapie) umgangen werden kann und somit einen neuartigen Weg zur Bekämpfung des GBMs zu erschliessen.

Wie im Kapitel I.B beschrieben, wurde in klinischen Studien über die anti-angiogene Therapie mittels Hemmung von VEGFA keine Verbesserung des allgemeinen Patientenüberlebens beim GBM erzielt. Daher wurde im ersten Teil meiner Arbeit untersucht, ob der APLN/APLNR Signalweg die Angiogenese auch in der Pathologie des GBMs steuert und ob er einen alternativen Angriffspunkt für die anti-angiogene Therapie darstellt.

Im zweiten Teil meines Habilitationsprojektes wurde erforscht, ob das antagonistische Peptid Apelin-F13A für die anti-angiogene Therapie beim GBM nutzbar gemacht werden kann. Insbesondere wurde die Frage adressiert, ob die zusätzliche Hemmung des APLNR-Signalweges die VEGFA/VEGFR2-gerichtete Therapie unterstützen kann und inwiefern sie sich auf die Invasivität des GBMs auswirkt.

Im dritten Teil meiner Arbeit sollte mittels eines transgenen Mausstammes, der als Reporter für die Aktivität des Stammzellgens Nestin dient, untersucht werden, inwiefern bekannte oder noch unbekannte Vorläuferzellen im Tumorparenchym die Pathologie des GBMs beeinflussen können. Die Modulation einer von uns dadurch neu-identifizierten Tumor-assoziierten Zelle mit myeloischem Expressionsmuster (TAMEP) sollte zeigen, inwiefern eine solche Zell-basierte-Therapie (im Gegensatz zur Blockade einzelner angiogener Signalwege) das Tumorwachstums beeinflussen kann.

# III. Ergebnisse

## A. Apelin kontrolliert die Tumor-Angiogenese im Glioblastom

Ziel dieses ersten Projektes war die Bestimmung der Rolle des APLN/APLNR Signalweges in der Tumormikroumgebung beim Glioblastom. Aus früheren Studien war bekannt, dass die Expression von APLN und seinem Rezeptor APLNR in den Gefäßproliferaten des Glioblastoms hochreguliert wird, während deren mRNA im gesunden Gehirn kaum detektierbar war (Kälin *et al*., 2007). Diese Ko-expression von Ligand und Rezeptor in den Tumorgefäßen wies auf eine autokrine Regulation des Signalweges hin, wie sie auch während der Embryonalentwicklung beobachtet wurde (Cox *et al*., 2006; Kälin *et al*., 2007). Zusätzlich zur Gefäßexpression war die APLN mRNA auch in hypoxischen Arealen prominent hochreguliert, in welchen VEGFA mRNA ebenfalls detektiert wurde (Kälin *et al*., 2007; Plate *et al*., 1992). Dies wies bereits auf eine kooperative Rolle beider Signalwege in der parakrinen Kommunikation von Tumorzelle zum Tumorgefäß hin.

Um nun die Funktion von APLN aus der Tumorzelle oder aus dem Tumorparenchym im Glioblastomwachstum getrennt zu untersuchen, haben wir im Folgenden einerseits die endogene APLN-Expression in einer GBM-Zelllinie mittels lentiviralem APLN Knockdown (KD) und andererseits im Mausmodell mittels Verwendung einer APLN Knockout (KO) Maus (Kuba *et al*., 2007) manipuliert.

In einem ersten Schritt wurden GBM-Zellen, humanen oder murinen Ursprungs, orthotop ins Hirnparenchym von Mäusen implantiert und die Validität des Mausmodells bezüglich APLN-Expression untersucht. Tatsächlich zeigte sich, dass auch im GBM-Mausmodell APLN einerseits in den Tumorzellen und andererseits in den neoplastischen Tumorgefäßen hochreguliert wurde (Anhang A.1, Abb.1B, (Fig. 1B)).

Als nächstes wurde die Rolle von APLN aus der Tumorumgebung untersucht, indem unterschiedliche GBM-Zellen in APLN-KO Mäuse implantiert wurden. Die Tumore, die nach GL261-Tumorzell-Implantation (Zellen ohne APLN-Expression, Anhang A.1, Abb1A, (Fig. 1A)) entstanden, zeigten eine signifikante Verminderung der Gefäßdichte und -komplexität im Vergleich zu den Tumoren in APLN Wildtyp (WT) Mäusen (Anhang A.1, Abb. 2, (Fig. 2)). Die

fehlgeformten Tumorgefäße wiesen dabei keine APLN Expression mehr auf (Anhang A.1, Abb. 2A, (Fig. 2A)).

Dann untersuchten wir den Beitrag des APLN-Signals aus der Tumorzelle zur Steuerung der Tumorangiogenese. Dazu benutzen wird die humane GBM-Zelllinie U87MG, welcher eine hohe APLN-Expression zu eigen ist (Anhang A.1, Abb. 1C, Fig. 1C), und generierten durch lentivirale Transduktion einer „small hairpin RNA“ (shRNA) gegen APLN einen stabilen APLN-knockdown (U87AKD) in diesen Zellen. Nach Implantation ins Mausgehirn wurden diese Zellen mit einer Kontroll-Zelllinie („U87 non-silencing control“; U87NSC) mit endogener APLN-Expression verglichen. Es zeigte sich, dass die sehr hohe Gefäßdichte dieses Tumormodells signifikant reduziert war, wenn APLN in der Tumorzelle fehlte (Abb. 1 und Anhang A.1, Abb. 3, Fig. 3). Zusätzlicher Verlust der APLN-Expression auch in den Tumorgefäßen unter Verwendung der genannten APLN-KO Maus drückte die Gefäßdichte sogar unter das Maß, welches in der Kontrollsituation beobachtet wurde.

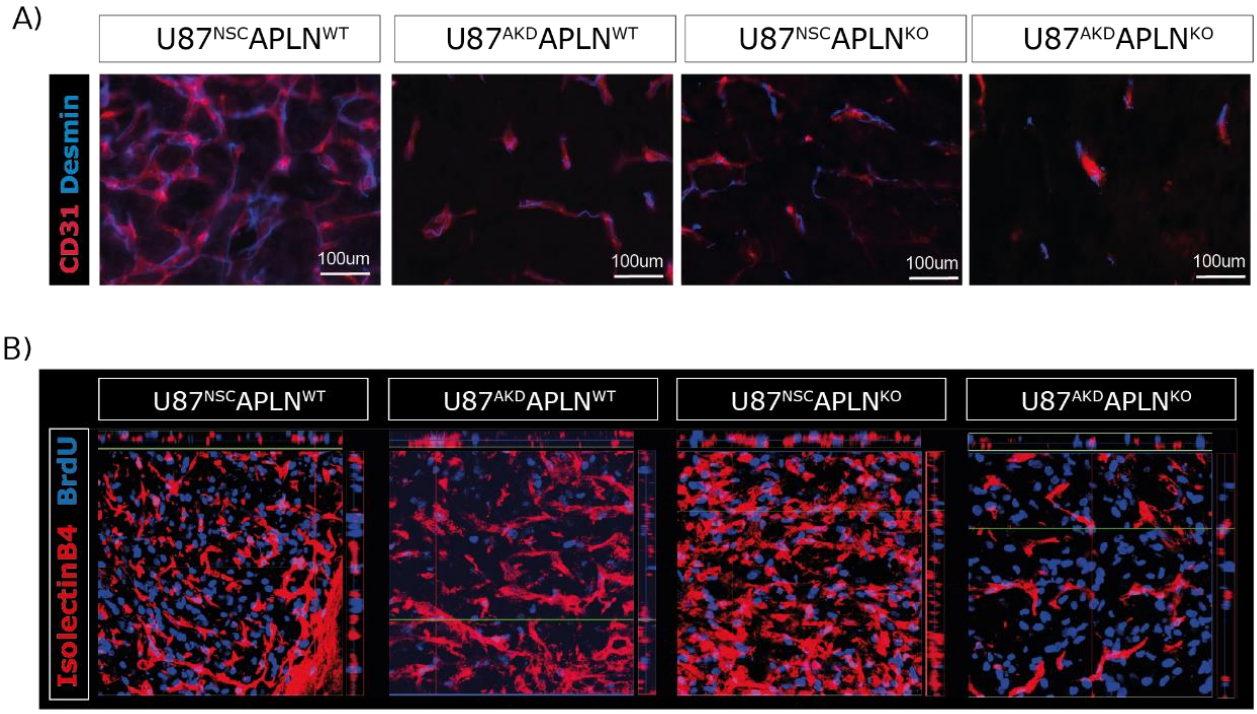


**Abb. 1: GBM- und Endothelzell-sezerniertes APLN sind beide wichtig für die Aussprossung der Tumorgefäße.**

A) U87MG Zellen wurden ins Mausgehirn implantiert und 28 Tage wachsen gelassen. Mittels doppelt-fluoreszenter Immunfärbung wurden die Tumorgefäße sichtbar gemacht („CD31“ für Endothelzellen in rot

und „Desmin“ für Perizyten in blau). Wenn APLN in den Tumorzellen ($U87^{AKD}APLN^{WT}$), der Mikroumgebung ($U87^{NSC}APLN^{KO}$) oder in beiden ($U87^{AKD}APLN^{KO}$) depletiert wird, ist die Gefäßdichte im Vergleich zur Kontrolle ($U87^{NSC}APLN^{WT}$) massiv reduziert. B) Drei Stunden vor Euthanasie der Mäuse wurde der Proliferationsmarker BrdU gespritzt. Mittels doppelt-fluoreszenter Immunfärbung wurden die Tumore gegen BrdU und Isolectin B4 (IB4) gefärbt und konfokale Bilder aufgenommen. In allen vier Versuchsgruppen gibt es sich noch teilende BrdU positive Endothelzellen (IB4+). (Supplementary Material aus Frisch *et al*., 2020).

Bisher konnten wir zeigen, dass die APLN-Expression notwendig für die Tumorangiogenese im GBM ist. Als nächstes untersuchten wir, ob die kleinste bioaktive Peptid-Isoform Apelin-13 auch hinreichend für die Sprossung der Tumorgefäße sein kann. Dazu infundierten wir Apelin-13 mittels osmotischer Mini-Pumpen intracerebral (ic) direkt in die U87AKD Gehirntumore der APLN-KO Mäuse, in denen kein APLN mehr vorhanden war. Im Vergleich zur Kontrolle, bei der nur künstliches Gehirnwasser (artifizielle cerebrospinale Flüssigkeit; aCSF) infundiert wurde, rettete Apelin-13 partiell die Tumorangiogenese indem es die Gefäßdichte signifikant erhöhte (Anhang A.1, Abb. 4 (Fig. 4)).

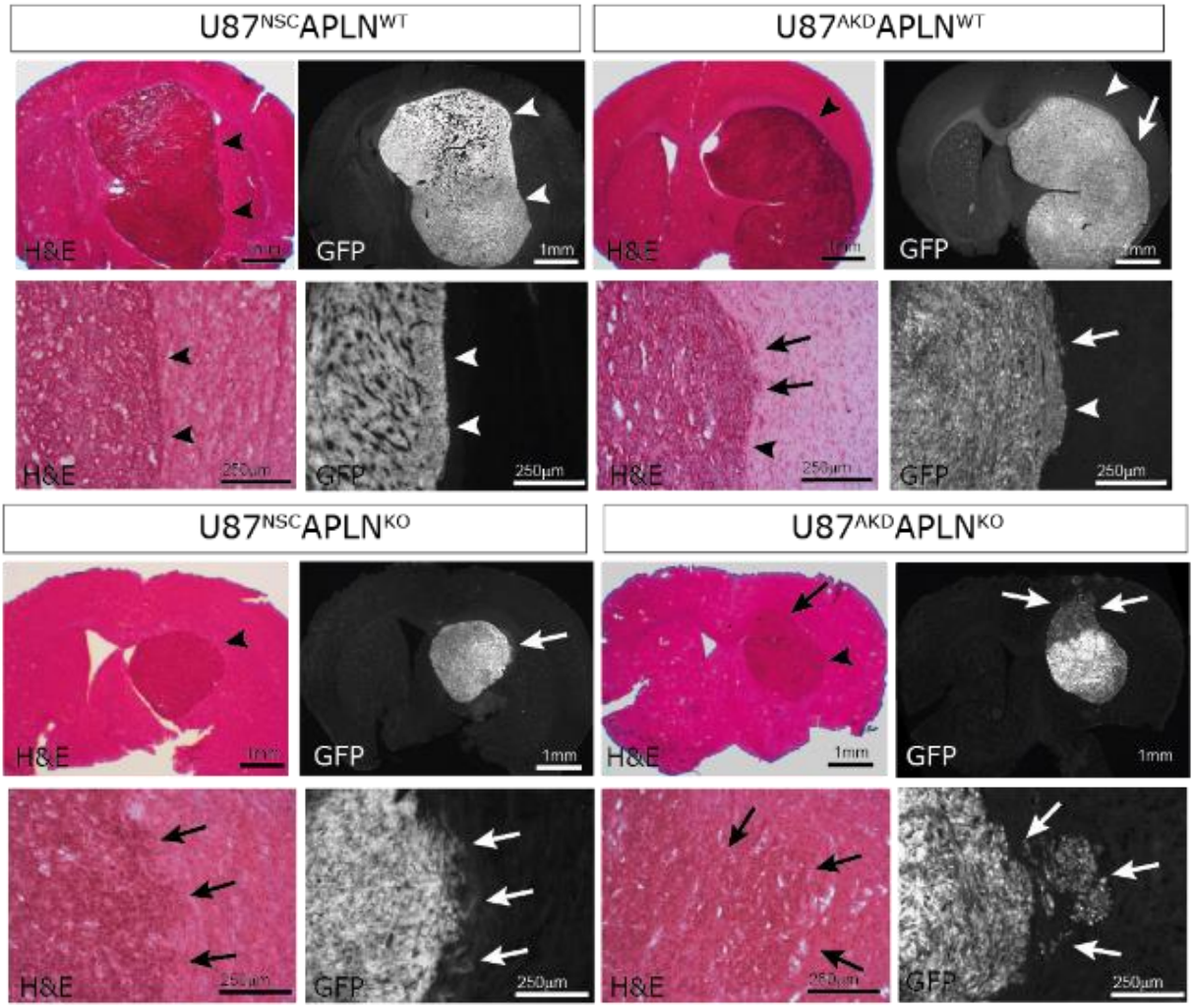


**Abb. 2: Der Verlust von APLN in der Tumorumgebung führt zu kleineren Tumorvolumen.**
U87MG-Zellen mit und ohne APLN-Expression wurden in WT oder APLN-KO Mäuse orthotop implantiert und bildeten 28 Tage später ein vorwiegend kompaktes GBM (Pfeilspitze) mit einzelnen Zellgruppen die ins Gehirnparenchym hineinragen (Pfeile). Tumorschnitte wurden mit H&E-Lösung gefärbt und GBM-Zellen wurden mittels GFP-Reporter sichtbar gemacht. (Supplementary Material aus Frisch *et al*., 2020).

Um den Einfluss der APLN-abhängigen Tumorangiogenese auf das Tumorwachstum zu bestimmen, führten wir ein Überlebens-Experiment durch und verfolgten das Wachstum der GBM Zellen im Mausgehirn mittels Magnetresonanz-Tomographie (MRT). Es zeigte sich in allen Versuchsgruppen ein exponentielles Tumorwachstum, allerdings zu einer signifikant niedrigeren Rate in APLN-KO Mäusen im Vergleich zu den WT Mäusen (Anhang A.1, Abb. 6 (Fig. 6)). Interessanterweise war der Größenunterschied am stärksten, wenn die APLN-Expression in den

Tumorzellen vorhanden war und in der Tumorumgebung fehlte (Abb. 2.). Diesen Befund untersuchten wir in einer Folgestudie ausführlicher (siehe Kapitel III.B).

Zusammenfassend konnte in dieser Studie gezeigt werden:

- dass der autokrine APLN-Signalweg im APLNR-exprimierenden Tumorendothel notwendig für die Aussprossung der Tumorgefäße ist.
- dass APLN sezerniert von der Tumorzelle sich parakrin stark auf die Komplexität der Tumorgefäße auswirkt.
- dass der endogene Ligand Apelin-13 hinreichend die Tumorangiogenese induziert.
- dass der Verlust von APLN in der Tumor-Mikroumgebung das GBM-Wachstum hemmt und das Überleben von GBM-tragenden Mäusen steigert.

Somit ließ sich zum ersten Mal nachweisen, dass Apelin spezifisch die Tumorangiogenese im GBM steuert und dass in einem kompakt wachsenden orthotopen GBM-Modell das Tumorwachstum vom Maße der APLN-induzierten Tumorangiogenese abhängt.

<u>Themenbezogene Publikation:</u>

Frisch, A.; Kälin, S.; Monk, R.; Radke, J.; Heppner, F. L.; **Kälin, R. E.**, Apelin Controls Angiogenesis-Dependent Glioblastoma Growth. *Int J Mol Sci* **2020,** 21, (11), 4179.

## B. APLN/APLNR als therapeutischer Angriffspunkt beim Glioblastom verbessert die Effizienz der VEGFA/VEGFR2 Blockade-vermittelten Antiangiogenese und vermindert dessen pro-invasive Nebenwirkung

Das Glioblastom ist charakterisiert durch schwach differenzierte Astrozyten, erhöhte Zellproliferation, Tumornekrosen, Gefäßproliferate und eine missgebildete Vaskulatur (Louis *et al*., 2016; Weller *et al*., 2021). Die Hemmung der Angiogenese scheint daher ein vielversprechender Therapieansatz zu sein (Jain *et al*., 2007). Klinische Studien zur Verwendung von Bevacizumab, einem humanisierten Antikörper zur Blockade des VEGFA Signalweges, zeitigten jedoch keine Verlängerung des allgemeinen Überlebens bei GBM-Patienten (Chinot *et al*., 2014; Gilbert *et al*., 2014). Unter der antiangiogenen Therapie entwickelte das GBM scheinbar eine Resistenz mittels Hochregulation von weiteren Angiogenese-Faktoren oder einer Verstärkung der Invasivität der Tumorzellen (Lu and Bergers, 2013).

Wie in der erstgenannten Studie unter Kapitel III.A gezeigt, spielt der APLN Signalweg eine entscheidende Rolle in der Tumorangiogenese des GBM (Frisch *et al*., 2020; Kälin *et al*., 2007). Im zweiten Teil dieser Arbeit fokussierten wir uns daher auf den Einfluss des APLN/APLNR Signalweges auf die antiangiogene Therapie des GBM.

Zunächst wurden Proben von GBM-Patienten, die vor und nach Gabe von Bevacizumab entnommen wurden, auf die Expression von APLN untersucht. Dabei konnten wir einerseits bestätigen, dass die APLN Expression im GBM im Vergleich zum umliegenden tumorfreien Gehirngewebe erhöht ist, andererseits fanden wir jedoch eine Herunterregulation der APLN Level nach Bevacizumab -Gabe sowohl per quantitativer PCR (Abb. 3A) wie auch per *in situ* Hybridisierung (Anhang A.2, Abb. 1D (Fig. 1D)).

Dann untersuchten wir die Verbindung zwischen dem VEGFA/VEGFR2- und dem APLN/APLNR-Signalweg im GBM Mausmodell. Dazu benutzten wir zwei neuartige Modelle für den proneuralen GBM-Subtyp, die durch den Wachstumsfaktor PDGFB in genetisch manipulierten neuronalen Vorläuferzellen angetrieben werden. Die Gehirntumore dieses ersten sogenannten Rcas/TVA-Modells (Hambardzumyan *et al*., 2009) wurden mit einer murinen Version von Bevacizumab behandelt (Pitter *et al*., 2016). Ein zweites von uns generiertes proneurales GBM-Modell mit Verlust des Onkogens Tp53 und mit ektoper PDGFB-Überexpression in neuronalen

Vorläuferzellen wurde nach orthotoper Tumorzellimplantation mit dem mausäquivalenten VEGFR2-inhibierenden Antikörper Ramucirumab behandelt. Beide Modelle imitierten das humane GBM ideal und zeigten Gefäßproliferate in der Nachbarschaft von pseudopalisaden-artigen Nekrosen. Während das Ausmaß der Nekrosen unverändert war (Abb. 3B, C), reduzierte sich die durch *in situ* Hybridisierung erhobene APLN-positive Fläche sowohl der Tumorzellen, wie auch der Gefäßproliferate, signifikant (Anhang A.2, Abb. 1A-C (Fig. 1A-C)).

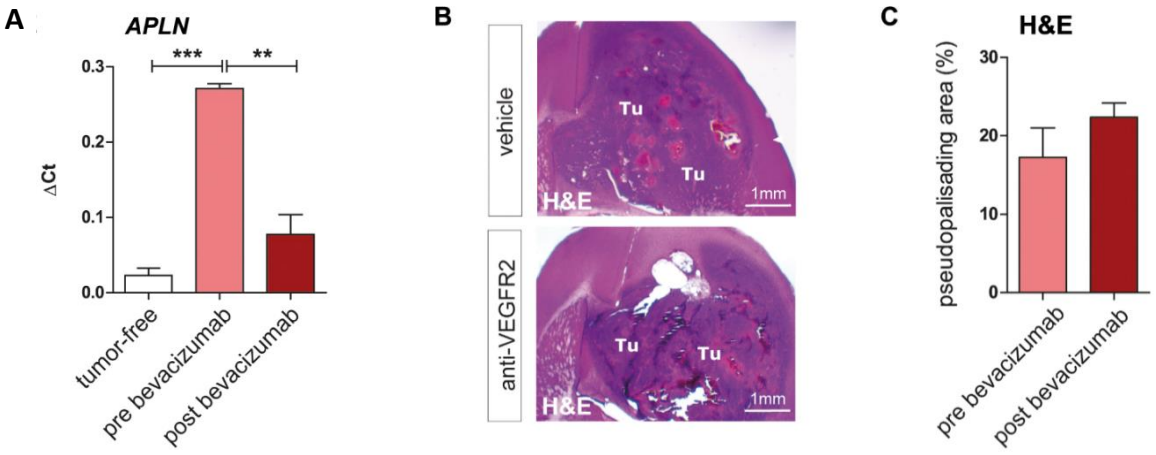


**Abb. 3: Anti-VEGFA/VEGFR2 Therapie im humanen und murinen GBM.**
A) Die APLN Expression ist in Biopsien von GBM-Patienten nach Bevacizumab-Therapie reduziert. Patientenbiopsien wurden vor und nach Bevacizumab-Therapie entnommen und per qPCR verglichen. Zwischen den Proben wurden die APLN- auf die GAPDH-Level normalisiert. B) Ein proneurales GBM-Implantationsmodell der Maus wurde mit Ramucirumab behandelt und die Fläche der Pseudopalisaden über H&E-Färbung quantifiziert (C). Signifikanzen wurden per einfachem T-Test erhoben und der mittlere Standardfehler ist angezeigt. p**<0,005, p***<0,0005. (Supplementary Material aus Mastrella *et al*., 2019).

Als nächstes untersuchen wir inwiefern sich die beiden Signalwege VEGF/VEGFR2 und APLN/APLNR ergänzen oder unterscheiden. Zuerst testeten wir den Effekt eines APLN-Verlustes auf die Angiogenese in primären GBM-Modellen, sowohl des proneuralen wie auch des klassischen Subtyps, welche ein verbessertes neuropathologisches Erscheinungsbild (hohe Tumorzellinvasivität und GBM-typischen Tumornekrosen) im Vergleich zu den etablierten Modellen (Frisch *et al*., 2020) zeigen. Dazu implantierten wir die von uns generierten GBM Zellen mit proneuralen (PDGFB-Überexpression und p53 Verlust) oder den klassischen Tumortreibern (EGFRvIII Überexpression und cdkn2a Verlust) in WT oder in APLN-KO Mäuse. In beiden Fällen fanden wir eine signifikante Reduktion der Tumorangiogenese in den Gehirntumoren der APLN-

KO Mäuse im Vergleich zu den APLN-exprimierenden WT Mäusen (Abb. 4 und Anhang A.2, Abb. 2 (Fig. 2)).

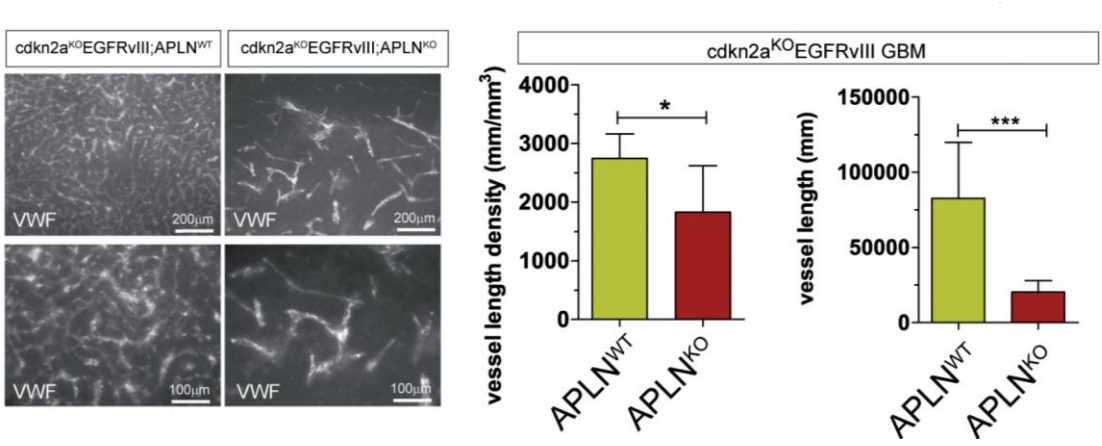


**Abb. 4: APLN aus Tumor- und aus Parenchym-Zellen steuert die Tumorangiogenese im primären Maus-GBM.**
Primäre Maus-GBM Zellen des klassischen Subtyps (cdkn2aKO; EGFRvIII), implantiert in APLN-WT oder APLN-KO Mäuse, wurden auf die Gefäßdichte mittels „von Willebrand-Faktor“ (VWF) -Immunfärbung analysiert, am Fluoreszenzmikroskop dokumentiert (linkes Panel) und die Gefäßdichte mittels Stereoinvestigator quantifiziert (rechtes Panel). Die Gefäßlängendichte („vessel length density“) und die totale Gefäßlänge („vessel length“) der Tumore in den APLN-KO Mäusen ist signifikant reduziert im Vergleich zu APLN-WT Mäusen. Signifikanzen wurden per einfachem T-Test erhoben und der mittlere Standardfehler ist angezeigt. p**<0,005, p***<0,0005. (Supplementary Material aus Mastrella *et al*., 2019).

Unter Nutzung einer öffentlichen Datenbank für regionale Genexpressionsanalysen beim GBM („IVY GBM Atlas Project RNAseq database“) fanden wir eine unterschiedliche Verteilung von APLN und APLNR im GBM (Anhang A.2, Abb. 3A (Fig. 3A)). Während die APLN-Expression vor allem in Regionen erhöhter Gefäßdichte vorlag, war der Rezeptor APLNR zusätzlich in den invasiven Tumorrandzonen hochreguliert. Dieses Expressionsmuster wurde von uns in stereotaktischen Proben von Patienten-GBM verifiziert (Anhang A.2, Abb. 3B (Fig. 3B)). Dies deutete auf eine zusätzliche Rolle des APLN/APLNR-Signalweges in der GBM-Zellinvasion hin. Tatsächlich konnten wir sowohl i) in einem Sphäroid-Invasions-Modell, ii) in einem Wundheilungs-Modell *in vitro* und iii) in einem *ex vivo* Schnittkultur-Modell nachweisen, dass APLN eine migratorische Wirkung auf die APLNR-exprimierenden primären humanen GBM-Zellen ausübt (Anhang A.2, Abb. 3 (Fig. 3C), zusätzliche Abb. 3G, H; 4F (Fig. S3H, G; S4F). In anschließenden *in vivo* Versuchen im murinen GBM-Modell fanden wir heraus, dass der schrittweise Verlust von APLN in den Tumorzellen und

in der Tumorzellumgebung nicht nur die Angiogenese reduzierte, sondern auch die Invasivität der GBM-Zellen vergrößerte (Anhang A.2, Abb. 4 (Fig. 4)). Während das mittels H&E-Färbung sichtbar gemachte kompakte Tumorvolumen signifikant abnahm, erhöhte sich das über GFP-Färbung angezeigte invasive Tumorvolumen im Vergleich zur APLN-exprimierenden Kontrolle (Abb. 5).

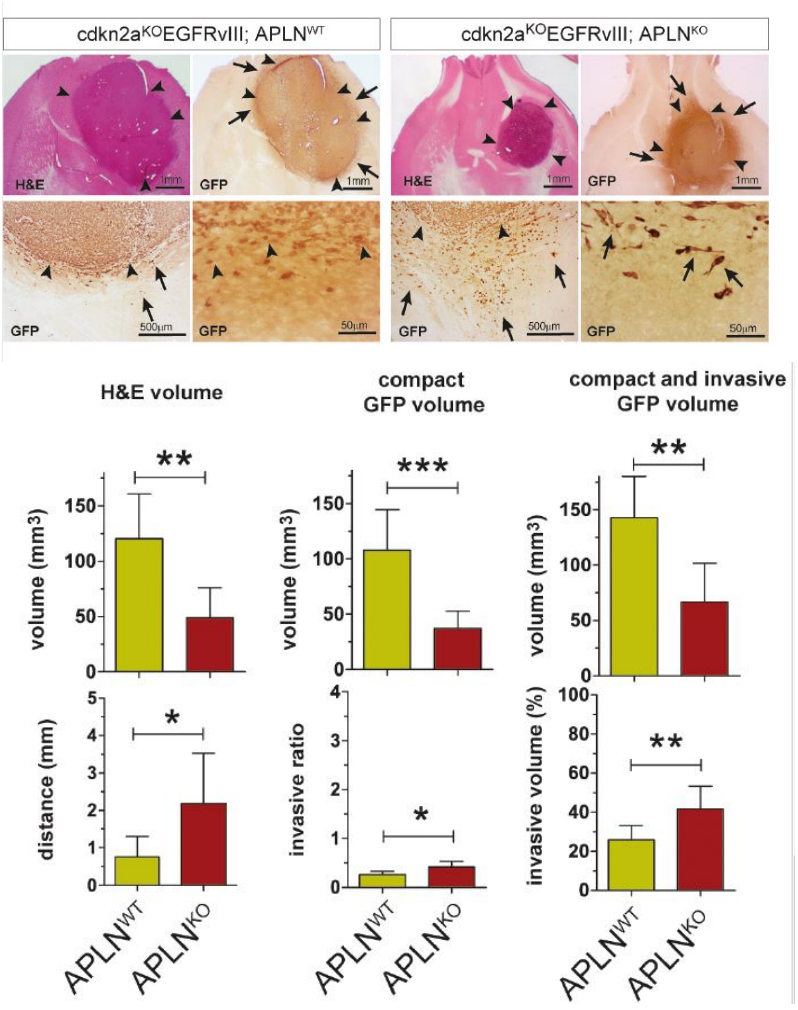


**Abb. 5: Die anti-invasive Rolle von APLN im orthotopen GBM-Modell.** Primäre Maus-GBM Zellen des klassischen Subtyps (cdkn2aKO; EGFRvIII) implantiert in APLN-WT oder APLN-KO Mäuse wurden auf das Tumorvolumen mittels H&E-Färbung oder GFP-Immunfärbung analysiert, und das Gesamtvolumen, bzw. das kompakte und das invasive Tumorvolumen quantifiziert. Die Invasivität wird mittels mittlerer invasiver Distanz („distance in mm“) der Tumorzellen in das umgebende Normalgewebe, und dem Verhältnis des invasiven zum kompakten Tumorvolumen („invasive ratio“ und „invasive Volume“ in %) dargestellt. Während das Kompakt- und das Gesamt-Volumen sich unter Verlust der APLN-Expression reduzierte, erhöhte sich der invasive Anteil signifikant. Signifikanzen wurden per einfachem T-Test erhoben und der mittlere Standardfehler ist angezeigt. p*<0,05 p**<0,005, p***<0,0005. (Supplementary Material aus Mastrella *et al*., 2019).

Zusammengefasst lässt sich festhalten, dass Apelin aus der Tumorumgebung oder der Tumorzelle selbst ein essentieller Mediator der Gefäßbildung im Tumor ist, jedoch auch die Tumorzellinvasivität unterdrücken kann. Dies wurde mittels inverser Korrelation zwischen APLN-Expression und GBM Invasivität in Patientenproben gefunden und sowohl *in vitro* als auch in unseren *in vivo* GBM Modellen beobachtet. Über einen direkten anti-invasiven Effekt auf die APLNR-Stimulation in *in vitro* Migrations-Versuchen konnte diese Beobachtung weiter bestätigt werden.

Sodann untersuchten wir das Potenzial von APLNR als therapeutischen Angriffspunkt für die GBM-Therapie. Dazu benutzten wir den bekannten APLNR-Antagonisten Apelin-F13A (Lee *et al*., 2006; Lee *et al*., 2005). Infusion von Apelin-F13A mittels osmotischer Minipumpen direkt in den Gehirntumor der Mäuse führte zu einer Verminderung sowohl der Tumorangiogenese, wie auch des Gesamt-Tumorvolumens unserer hoch-invasiven humanen oder murinen primären GBM-Modelle (Anhang A.2, Abb. 5 (Fig. 5)). Dass Apelin-F13A tatsächlich den Rezeptor APLNR auf den Tumorzellen aktivierte, konnten wir mittel Internalisierungs-Assay im Zellkultur-Experiment nachweisen (Anhang A.2, Abb. S5C (Fig. S5C).

Eine Hauptkomplikation in der Anwendung von Bevacizumab beim GBM ist die beobachtete Erhöhung der Tumorzellinvasivität (Lu and Bergers, 2013). Aus diesem Grund fragten wir uns ob die Blockade der pro-angiogenen und pro-invasiven Eigenschaften von APLNR diese pathologische Nebenwirkung der etablierten anti-VEGFR2-Therapie überwinden könnte. Orthotop implantierte immunkompetente p53$^{KO}$PDGFB-GBM Zellen konnten in Mäusen zu Tumoren anwachsen bevor wir diese direkt intracerebral mit Apelin-F13A und VEGFR2 Kombinations- bzw. Einzeltherapie behandelten. Es zeigte sich, dass die Ko-behandlung der Tumormäuse mit VEGFR2-Antikörpern und dem Apelin-F13A Peptid synergistische Effekte im Vergleich zur jeweiligen Einzelbehandlung entfaltete (Anhang A.2, Abb. 6C, D (Fig. 6C, D)). Immunhistologische Analysen der Tumore ergaben eine klare Reduktion der Tumorangiogenese in Kombination mit einer Verminderung des pro-invasiven Effekts der VEGFR2-Therapie mittel Apelin-F13A Gabe. Dies führte zu einer Erhöhung des Überlebens der mit beiden Substanzen behandelten Mäusen um bis zu 65% Prozent (Abb. 6).

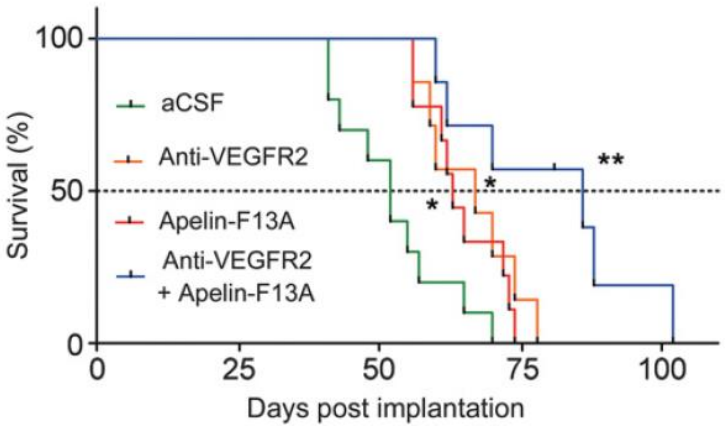


**Abb. 6: Die Kombinationstherapie gegen VEGFR2 und APLNR verbessert das Überleben von GBM-Mäusen.**

Apelin-F13A und anti-VEGFR2 erhöhen das Überleben der GBM-Mäuse signifikant im Vergleich zur Trägersubstanz (aCSF). Ko-behandlung mit Apelin-F13A und anti-VEGFR2 erhöht das Überleben zusätzlich um 28% im Vergleich zur anti-VEGFR2 Einzelbehandlung signifikant. («One-way ANOVA plus post-hoc Test»). p*<0,05 p**<0,005. (aus Mastrella *et al*., 2019).

Die Ergebnisse dieser Studie lassen sich wie folgt zusammenfassen:

- Apelin aus dem Tumorparenchym und den Endothelzellen ist notwendig für die Tumorangiogenese beim primären GBM des proneuralen und klassischen Subtyps.
- Zum ersten Mal wurde gezeigt, dass der APLN/APLNR Signalweg zusätzlich eine entscheidende Rolle in der Tumorzellinvasion spielt.
- Die Stimulation des APLN-Rezeptors APLNR durch Apelin-F13A stellt eine vielversprechende Strategie zur Behandlung spezifischer GBM-Subtypen dar.
- Die ergänzende Behandlung des GBMs mittels Apelin-F13A reduziert die durch VEGFA/VEGFR2-Blockade vermittelten invasiven Nebeneffekte der anti-angiogenen Therapie.

Aus dieser und der vorangehend erwähnten Studie (III.A) schlussfolgern wir, dass unsere Resultate eine neuartige Strategie zur Reduktion der Therapieresistenz durch die Antiangiogenese einführt und GBM Subtypen identifiziert, die eine bessere Antwort auf eine Kombinationstherapie mit APLN/APLNR und VEGFA/VEGFR2 als Angriffsziele zeigen.

<u>Themenbezogene Publikation:</u>

Mastrella, G.; Hou, M.; Li, M.; Stoecklein, V. M.; Zdouc, N.; Volmar, M. N. M.; Miletic, H.; Reinhard, S.; Herold-Mende, C. C.; Kleber, S.; Eisenhut, K.; Gargiulo, G.; Synowitz, M.; Vescovi, A. L.; Harter, P. N.; Penninger, J. M.; Wagner, E.; Mittelbronn, M.; Bjerkvig, R.; Hambardzumyan, D.; Schuller, U.; Tonn, J. C.; Radke, J.; Glass, R.; **Kälin, R. E**., Targeting APLN/APLNR Improves Antiangiogenic Efficiency and Blunts Proinvasive Side Effects of VEGFA/VEGFR2 Blockade in Glioblastoma. *Cancer Res* **2019,** 79, (9), 2298-2313.

## C. TAMEP sind neuartige Gehirn-eigene Vorläuferzellen, die die neoplastische Angiogenese und die Tumorprogression steuern

In dieser dritten Studie haben wir neuartige Gehirn-eigene Vorläuferzellen in der Tumor-Mikroumgebung entdeckt, die aufgrund ihres myeloischen Expressionsmusters Mikroglia-Zellen ähneln, aber nicht von Mikroglia oder peripheren Monozyten abstammen. Diese Zellen haben wir TAMEP genannt, für „Tumor-assoziierte Zellen mit einem myeloid-ähnlichen Expressions-Profil".

Im Mausmodell lässt sich eine ZNS-eigene Vorläuferzelle und dessen Nachkommen mittels künstlich induzierter Expression unter der Kontrolle des Nestin-Genpromotors verfolgen. Berichte zur Nestin-Expression in Vorläuferzellen gab es bereits bezüglich neuronaler und oligodendroglialer Vorläufer-Zellen und Perizyten (Sun *et al*., 2014), die ihrerseits alle gewisse Eigenschaften mit mesenchymalen Vorläuferzellen teilen. All diese Zellen sind Teil des Tumorparenchyms im GBM (Audia *et al*., 2017; Huang *et al*., 2014; Stock *et al*., 2014).

Für unsere Studie nutzten wir ein Mausmodell (Nes-RFP) in welchem der Promotor für das Intermediär-Filament Nestin eine Cre-Rekombinase exprimiert (Giachino and Taylor, 2009). Die Rekombinase (CRE) ist mit einem mutierten Östrogen-Rezeptor (ER) fusioniert. Dies erlaubt, dass Tamoxifen-induziert (getimed) ein Transgen (hier z.B. das rot-fluoreszierende Reporterprotein tdTomato (Madisen *et al*., 2010)) exprimiert wird, und die so markierte Zelle und ihre Nachfahren verfolgt (getraced) werden können.

Zur Beobachtung von eventuellen Tumor-assoziierten Vorläuferzellen während des Tumorwachstums implantierten wir nun GL261-Gliomzellen ins Maus-Gehirn, behandelten die Tiere in den folgenden drei Tagen mit Tamoxifen und untersuchten die Maus-GBMs histologisch an Tag 7, 14 und 21. Dieses erste Experiment zeigte avaskuläre rote Zellen, die in ihrer Anzahl am siebten Tag am höchsten waren und dann stetig abnahmen, wohingegen rot-markierte vaskuläre Zellen beobachtet wurden, die in ihrer Anzahl über 21 Tage stetig zunahmen (Abb. 7 A, B). Mittels Immunfluoreszenz-Färbung für PDGFRB, Desmin, NG2 und CD146 (Armulik *et al*., 2011) konnten diese vaskulären Zellen als Perizyten identifiziert werden (Abb. 7C). Intravitale Bildgebung mittels 2-Photonen Mikroskopie zeigte, dass die vaskuläre und die avaskuläre RFP-positive Zellpopulation sich während der Gliomexpansion örtlich nicht vermischte, sondern an deren jeweiligen Position verweilte (Anhang A.3, Abb. S2 (Fig. S2)).

Dies schloss die Möglichkeit aus, dass die vaskuläre aus der avaskulären Population hervorging und ließ damit die Frage offen um welche Zellen es sich bei der avaskulären Fraktion handelte.

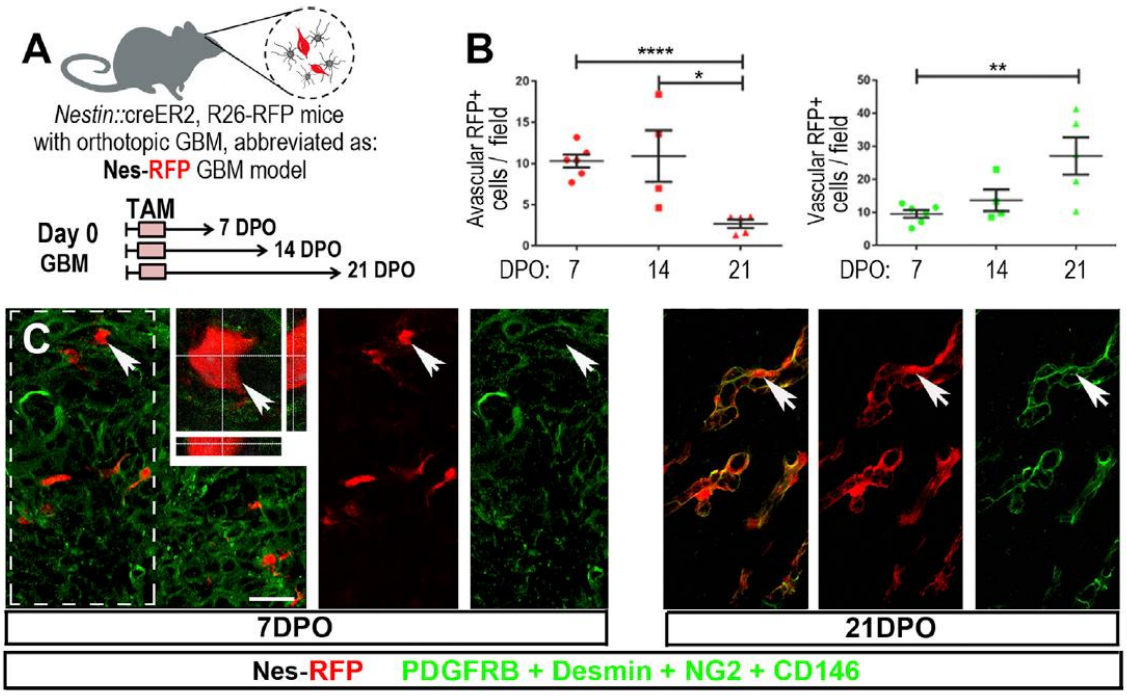


**Abb. 7: Ein Model zur Verfolgung von Tumor-assoziierten Zellen mit einem myeloid-ähnlichen Expressionsprofil (TAMEP).**
A) Nes-RFP Mäuse orthotop implantiert mit Gliomzellen wurden 7, 14 und 21 Tage post Operation (DPO) inspiziert. B) Anzahl der RFP-positiven Zellen in avaskulärer (links) und Gefäß-assoziierter (rechts) Position (jeder Punkt repräsentiert die Daten von einer Maus). C) Immunfluoreszenz von Perizytenmarker (alle in grün); bei 7 DPO dominieren die Perizytenmarker-negativen RFP-positiven Zellen; die Pfeilspitze markiert dieselbe Zelle in Einzelkanal- und Orthogonal- Ansicht; bei 21 DPO sind die meisten RFP-positiven Zellen auch Perizytenmarker-positiv. Der Maßstab entspricht 50 µm. Statistische Signifikanzen («One-way ANOVA plus post-hoc Test») sind angezeigt. p*<0,05 p**<0,01, p****<0,0001. (aus Kälin *et al.*, 2021).

Um die Identität der avaskulären RFP-positiven Zellen zu entschlüsseln reinigten wir diese aus Mausgliomen per Fluoreszenz-Durchflusszytometrie (FACS) auf und untersuchten sie per Einzelzell-Transkriptomanalyse (scRNAseq). Die Einzelzell-Expressionsprofile (60-50´000 Transkripte/Zelle) der avaskulären Zellen (155 aus 180 prozessierter Zellen) wurden dann mit Expressionsprofilen von über 3´000 neuronalen und nicht-neuronalen Zellen des Mausgehirns (Zeisel *et al.*, 2015) verglichen. Dabei wurden unsere avaskulären Zellen als eine eigenständige

homogene Zellfraktion mit höchster Ähnlichkeit zu Mikroglia-Zellen klassifiziert (Abb. 8 und Anhang A.3, Abb. 1D-F (Fig. 1D-F)).

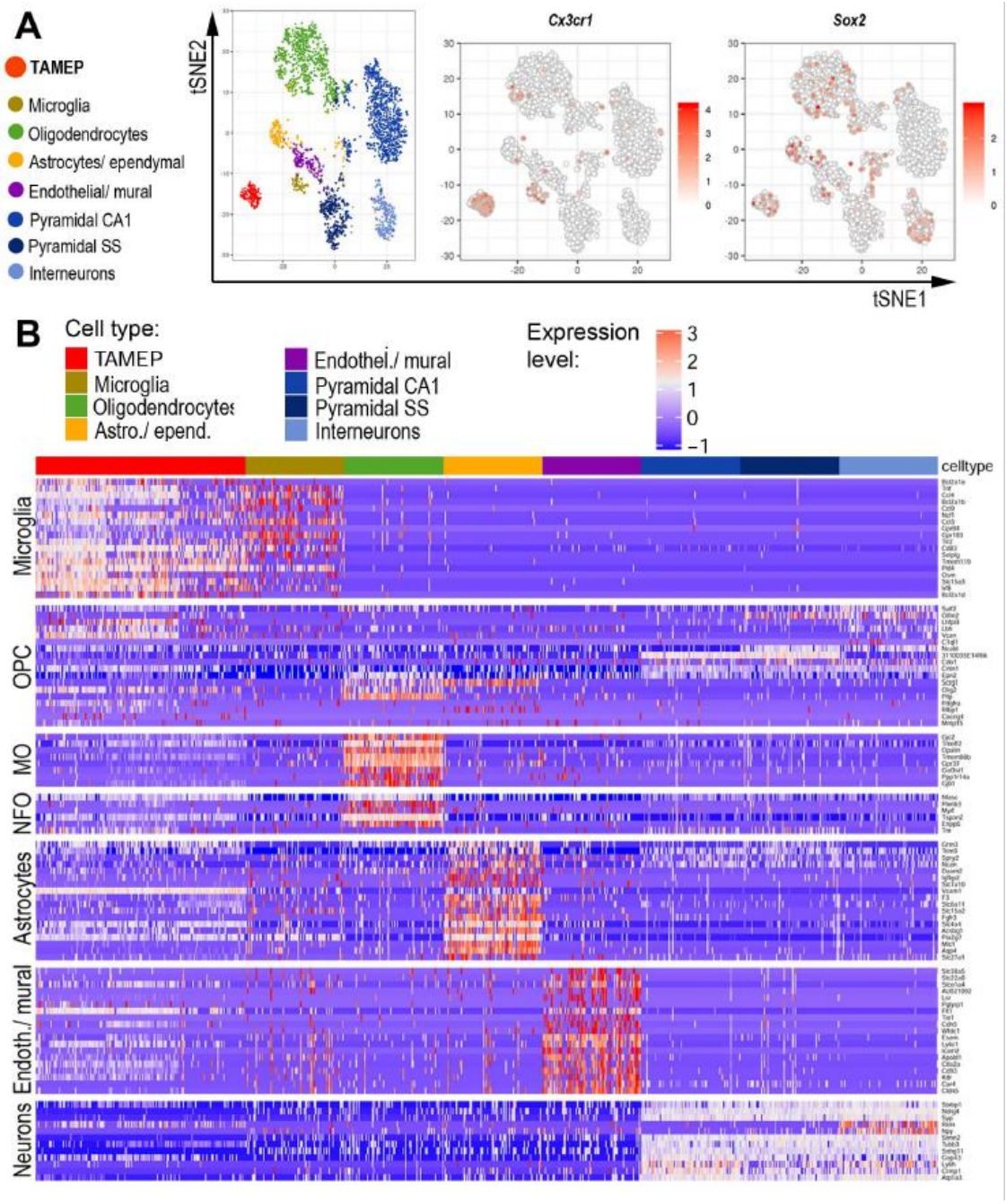


**Abb. 8: TAMEP sind eine eigenständige Zellpopulation charakterisiert durch ihre Positivität auf myeloische Marker.**

A) Einzelzell-Sequenzierungs-Daten von RFP-positiven avaskulären Zellen aus Gliomen von Nes-RFP Mäusen wurden mit publizierten Expressionsmustern aus Mikroglia, Oligodendrozyten, Astrozyten und ependymalen Zellen (Astrocytes/ependymal), Endothel/vaskulär-muralen Zellen (Endothel/mural) und drei neuronalen Subtypen (pyramidal CA1, pyramidal SS und Interneuronen) verglichen und werden als

tSNE-Plot angezeigt. TAMEP sind rot markiert. Das Expressions-Level für den myeloischen Marker CX3CR1 wurde in allen Zellpopulationen quantifiziert und ist erhöht in Mikroglia und TAMEP, jedoch niedrig bis abwesend in allen anderen Zellpopulationen. Auch das Expressions-Level für den Stammzell-Marker Sox2 wurde quantifiziert und ist erhöht in Neuronen, Astrozyten und TAMEP. B) TAMEP wurden mit etablierten Gehirnzellen mittels „Unsupervized Clustering" verglichen und teilen die größte Überlappung im Expressionsprofil mit Mikroglia, nur limitierte Ähnlichkeit mit oligodendroglialen Vorläuferzellen (OPC) und keine Übereinstimmung mit anderen reifen Gehirnzellen. (Supplementary Material aus Kälin *et al.*, 2021).

Eine ausführliche vergleichende Immunhistologie- und Genexpressions-Analyse (Anhang A.3, Abb. 2A, B (Fig. 2A, B)) unserer RFP-getracten Zellen auf typische Marker für Mikroglia, oligodendrogliale Vorläuferzellen (OPC), Astrozyten oder Neuronen bestätigte die Ähnlichkeit unserer neu-identifizierten Zellen mit Mikroglia (plus kleinerer Überlappungen mit oligodendroglialen Vorläuferzellen). Zusätzlich zeigte die immunhistologische Auswertung, dass die avaskulären Zellen unterschiedlich zu Perizyten, mesenchymalen Vorläuferzellen, reifen/unreifen Neuronen, Oligodendrozyten und Astrozyten sind. Während einige Mikroglia-Marker wie CD11b, F4/80 und CX3CR1 häufig vorkamen, waren andere wie Iba1 oder CD45 auf Proteinebene nicht auffindbar. Die Kombination unseres Nes-RFP Mausmodells mit dem myeloischen CX3CR1-GFP Tracer-Modell und begleitende FACS-Analysen bestätigte den myeloischen Charakter dieser Zellen (Anhang A.3, Abb. 2C-F (Fig. 2C-F).

Die Verbindung aller dieser Resultate aus Einzelzellsequenzierung, Immunfluoreszenz, Mausreporterstämmen und FACS-Analysen offenbarte eine atypische myeloische Zellkomponente im GBM-Parenchym, die wir als TAMEP für „Tumor-Assoziierte Zellen mit einem Myeloid-artigen Expressions-Profil", einführen.

Modifikationen unseres Tamoxifen-Zeitplans zeigten, dass TAMEP auch zu verschiedenen Zeitpunkten des Gliomwachstums (1 oder 7 Tage nach Operation) beobachtet werden konnten, aber nicht, wenn Tamoxifen an tumorfreie Mäuse ohne Tumorwachstum (Anhang A.3, Abb. 3A (Fig. 3A)) verabreicht wurde. Dieses Resultat ließ uns vermuten, dass die avaskulären Zellen aus wenigen Vorläuferzellen hervorgegangen sein könnten. Aus diesem Grund haben wir in unseren Daten nach einer Expression von Vorläuferzellgenen gesucht. Fündig wurden wir mit der Expression des Stammzell-Transkriptionsfaktors *SOX2* in der TAMEP-Zellpopulation (Abb. 8A und Anhang A.3, Abb. 3C (Fig. 3C)).

Um zu untersuchen, ob *SOX2* eine biologische Funktion in den avaskulären Zellen ausübt, verkreuzten wir die *Nes*-RFP Reporter-Maus mit *SOX2*-flox Mäusen um einen konditionellen KO in den TAMEP zu erhalten. Es zeigte sich, dass der Verlust von *SOX2* in den avaskulären RFP-positiven Zellen zu einer starken Reduktion der TAMEP-Zellzahl führte (Anhang A.3, Abb. 3C (Fig. 3C-E)). Interessanterweise war eine viel größere Population an getracten Zellen betroffen, als die Anzahl der *SOX2*-positiven RFP-positiven Zellen vermuten ließ. Daraus schlossen wir, dass die *SOX2*-positiven TAMEP die Quelle für alle TAMEP darstellen und nennen sie daher TAMEP-Vorläuferzellen.

Ob TAMEP und ihre Vorläufer aus dem hematopoietischen System hervorgehen untersuchten wir im Anschluss. Zu diesem Zweck führten wir Experimente mit Knochenmarkschimären durch. Als Knochenmark-Spender dienten Spi1-GFP Mäuse (Back *et al*., 2005), als Empfänger die Nes-RFP Reporter Mäuse. Das *SPI1* Gen kodiert für den Transkriptionsfaktor PU.1, der essentiell für die Entstehung der myeloischen Zelllinie ist (Back *et al*., 2005). Wie erwartet fanden wir eine massive Ansammlung von Spi1-GFP-positiven Zellen im Gehirntumor von Nes-RFP Knochenmarkschimären (Abb. 9A, B), die TAMEP Zellzahl blieb jedoch unverändert. Im umgekehrten Chimären-Experiment fanden wir keine Nes-RFP-positiven Zellen im Gehirntumor, welche aus dem Knochenmark hätten stammen können. Intratumoral getracte Zellen der Nes-RFP Maus exprimierten auch nie den pan-Leukozyten-Marker CD45 (Abb. 9C) oder den Monozyten-Marker CCR2 (Abb. 9D), wie wir mittels Nes-RFP; Ccr2-GFP-transgener Maus (Bowman *et al*., 2016; Chen *et al*., 2017) zeigen konnten. Die *Flt3*cre Mauslinie, mit welcher Zellen aus dem Knochenmark spezifisch verfolgt werden können (Benz *et al*., 2008), zeigte nie SOX2-positive, GFP-positive Zellen aus dem Knochenmark. Auch Zellen aus der Mikroglia-Zelllinie exprimierten nie SOX2 (Abb. 9F) bei der Verwendung des etablierten Cx3cr1cre-RFP Verfolgungs-Protokolls (Huang *et al*., 2018; Wieghofer *et al*., 2015). Zusammengefasst lassen uns diese Experimente ausschließen, dass TAMEP von Makrophagen, Mikroglia oder anderen ZNS-residenten Phagozyten abstammen. TAMEP scheinen daher nicht mit den bisher bekannten myeloischen Zellen verwandt (Abb. 9G).

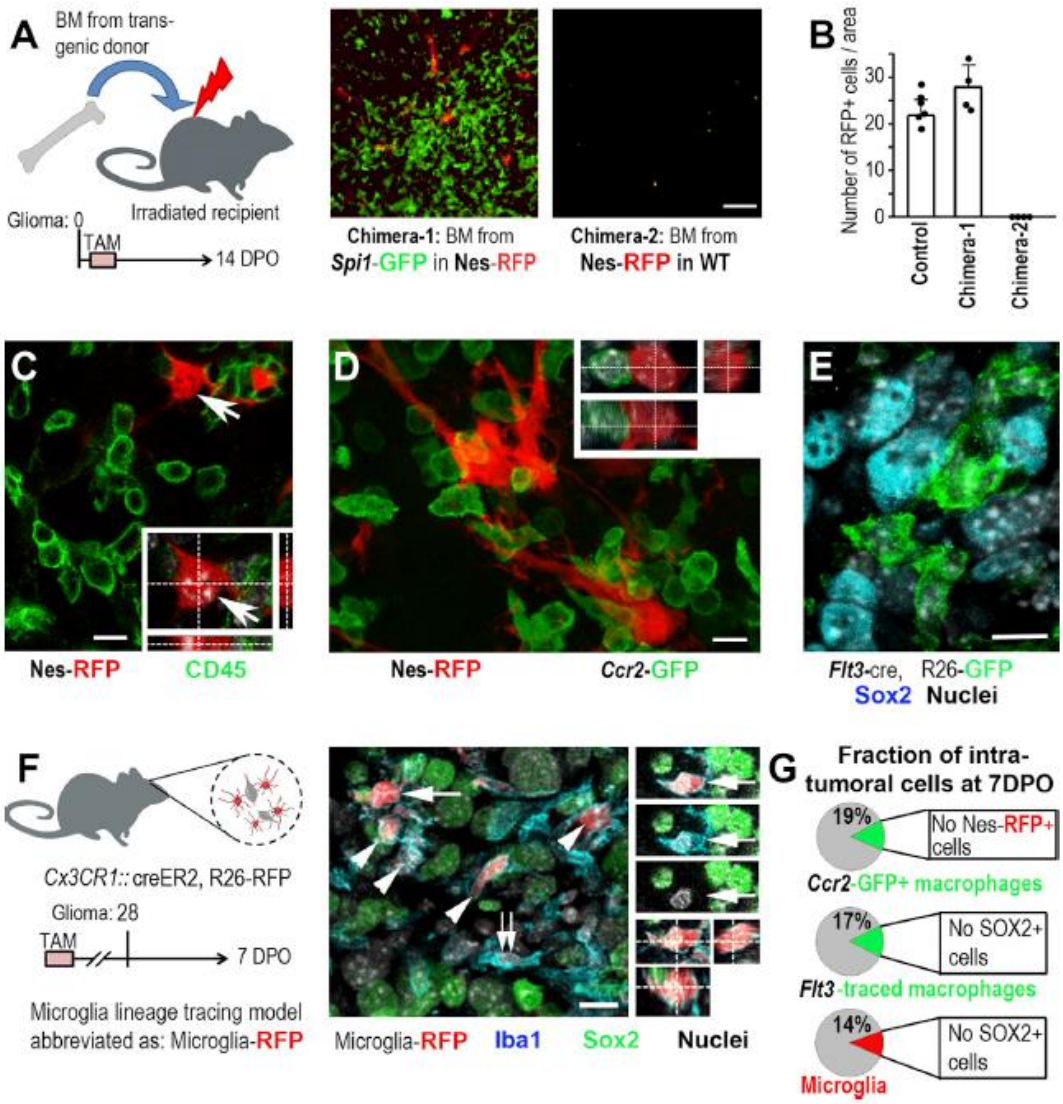


**Abb. 9: TAMEP und ihre Vorläufer gehören nicht zur myeloischen Zelllinie.**

A) Verfolgung der Zellabstammung in Knochenmarks (KM) -Chimären 14 Tage nach Tumorimplantation (14 DPO). Chimera-1: KM-Transplantation von der Spi1-GFP Maus in die Nes-RFP-Maus. Chimera-2: KM-Transplantation aus der Nes-RFP-Maus in eine WT-Maus. B) Der erfolgreiche KM-Transfer dokumentiert durch GFP-positive Zellen im Gliom von Chimera-1 (n = 4); Chimera-2 zeigt keine RFP-positiven Zellen die aus dem KM stammen (n = 4), im Gegensatz zur Kontrolle aus Nes-RFP-Maus ohne KM-Transfer (n = 6). C) RFP-positive avaskuläre Zellen exprimieren kein CD45. D) Nes-RFP; *Ccr2*-GFP-Gliommäuse enthalten keine GFP/RFP-doppelpositive Zellen. E) *Flt3*cre getracte Zellen (GFP-positiv) sind nicht SOX2-positiv. F) Ein Puls-Verfolgungs-Protokoll in *Cx3c1*::creERT2,R26-RFP positiven Mäusen lässt ausschließen, dass echte getracte Mikroglia Sox2 exprimieren. G) Nes-RFP- oder Sox2-positive Zellen überlappen nicht mit Makrophagen (CCR2-GFP+), Sox2-positive Zellen stammen nicht von KM-Stammzellen (*Flt3*-getract) oder echten Mikroglia ab. Der Maßstab entspricht 50 μm in A; 10 μm in C, D und E. Statistische Signifikanzen («One-way ANOVA plus post-hoc Test») sind angezeigt. p*<0,05 p***<0,0001. (aus Kälin *et al.*, 2021).

Bisher konnten wir zeigen, dass TAMEP den Myeloid-Marker CX3CR1 exprimieren und von SOX2-positiven Zellen abstammen. Die immunhistologische Detektion mittels Kombination von zwei (nukleär-lokalisierten) Transkriptionsfaktoren stellt eine verlässliche Methode zur Identifizierung bestimmter Zellen dar. Deshalb verifizierten wir zuerst, dass SOX2-positive TAMEP auch den myeloischen Transkriptionsfaktor PU.1 enthalten (Anhang A.3, Abb. 5B (Fig. 5B)). Ebenso fanden wir SOX2-positive Zellen in Myeloid-Reporter Mäusen (CX3CR1-GFP, SPi1-GFP; Anhang A.3, Abb. 5D (Fig. 5D)). Dies bedeutet, dass die kombinierte Immundetektion von SOX2 und PU.1 oder CX3CR1 eine nützliche Methode zur Identifikation von TAMEP in humanen Patientenproben darstellt.

Im Folgenden untersuchten wir verschiedene genetische und patienten-derivierte Maus-GBM-Modelle per Immunfluoreszenzfärbung auf SOX2/PU.1-Koexpression und fanden damit tatsächlich TAMEP-Vorläuferzellen in unterschiedlicher loco-regionaler Anhäufung (Abb. 10A, B). Im Gegensatz dazu, waren in Mausmodellen für andere Krankheiten wie der Hirnschlag oder die Neuroinflammation keine SOX2/PU.1 doppel-positiven Zellen detektierbar (Anhang A.3, Abb. S5D-K (Fig. S5D-K)). Interessanterweise waren in GBM-Proben von verschiedenen Patienten SOX2/PU.1 doppel-positive TAMEP-Vorläuferzellen, wie im Mausmodell beobachtet, in regional unterschiedlicher Häufigkeit auffindbar (Abb. 10C). Per Transkriptomanalyse verglichen wir das Expressionsprofil der TAMEP aus den Maus-GBMs mit dem von humanen Patientenproben und fanden Zellen mit dem TAMEP-spezifischen Expressionsmuster, unter anderem angereichert an SOX2/SPI1-exprimierenden Zellen (Anhang A.3, Abb. 5E und Abb. S4C (Fig.5E und Fig. S4C)). Aus diesen Daten lässt sich ableiten, dass TAMEP auch im humanen GBM prominent vertreten sind.

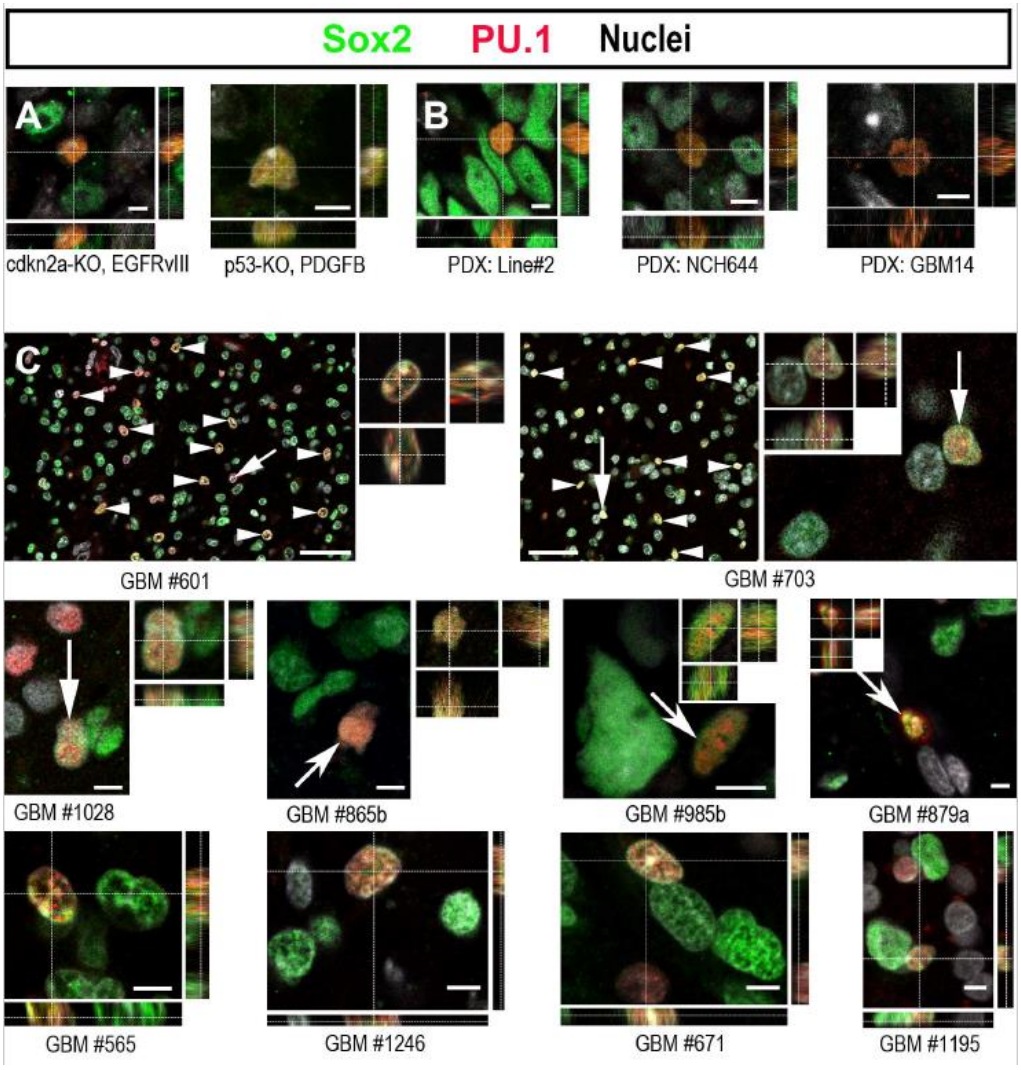


**Abb. 10: Bestätigung der Anwesenheit von TAMEP in murin-transgenen und in humanen GBM.**

SOX2/PU.2-Kofärbungen indizieren die Anwesenheit von TAMEP A) in unterschiedlichen orthotop implantierten Maus-GBM Zellen, B) in Xenografts von patienten-derivierten GBM-Zellen (PDX) und C) in Proben aus verschiedenen GBM-Patienten. Ko-markierte TAMEP-Vorläufer Zellen sind durch Pfeilspitzen hervorgehoben und einzelne dieser Zellen (Pfeile) werden zusätzlich vergrößert in der Orthogonal-Ansicht dargestellt. Der Maßstab entspricht 30 µm in den Übersichten und 5 µm in den Vergrößerungen. (Supplementary Material aus Kälin *et al.*, 2021).

Nachdem nun die pathologische Relevanz von TAMEP im humanen und murinen GBM nachgewiesen war, untersuchten wir deren Rolle im Tumorwachstum. In den konditionellen SOX2-KO Mäusen schalteten wir Sox2 spezifisch in TAMEP-Vorläuferzellen aus und fanden eindrückliche morphologische Veränderungen in den Tumorgefäßen der *Nestin*::creERT2,R26-RFP,Sox2$^{fl/wt}$ -Mäuse (Abb. 11A-G und Anhang A.3, Abb. 7A-C (Fig.7A-C)) im Vergleich zu den

Kontrollmäusen (Nes-RFP). Mittels quantitativer Auswertung an 7, 14 und 21 Tagen post Operation (DPO) entdeckten wir eine starke Reduktion der Gefäßdichte im konditionellen SOX2-KO im Vergleich zum WT (Abb. 11A, H und Anhang A.3, Abb. 7B (Fig.7B)) ermittelt per Stereoinvestigation über die Anzahl Verzweigungen („average branch points“), die Gefäßlängendichte („vessel length density“) und die totale Gefäßlänge („vessel length“). In einem zusätzlichen Kontrollexperiment ablatierten wir die komplette TAMEP-Zelllinie mittels Cre-induzierter Expression des Suizidgens Diphteria Toxin (iDTA) zu Beginn des Tumorwachstums (Anhang A.3, Abb. 7B (Fig.7B)). Dies reduzierte ebenso die Gefäßdichte im Tumor, bewirkte aber keinen zusätzlichen Effekt auf die Tumorangiogenese im Vergleich zum konditionellen Sox2-KO. Der Verlust von Sox2 in TAMEP führte zu Tumorgefäßen mit vergrößertem Lumen und kleinerer Komplexität. Diese Gefäßstrukturen trugen zusätzlich weniger Perizyten (Anhang A.3, Abb. 7C (Fig.7C)). Die Antiangiogenese mittels VEGFR2-Antikörperbehandlung hatte hingegen keine Auswirkung auf die Anzahl der TAMEP-Zellen im Tumor (Abb. 11I). Zusammengefasst zeigten diese Versuche, dass TAMEP einen starken Einfluss auf die Bildung der Tumorgefäße ausüben.

Das GBM-Wachstum wird bekanntermaßen durch die Vaskularisierung des Tumors unterstützt (Jain *et al*., 2007) und die reduzierte Gefäßdichte sollte daher einen Effekt auf das Tumorwachstum zeigen, wie wir es bereits in den vorhergehenden Studien in den Kapiteln III.A und III.B über die *APLN*-abhängige Tumorangiogenese beobachten konnten (Frisch *et al*., 2020; Mastrella *et al*., 2019). Um dies zu untersuchen benutzten wir unsere etablierten Mausmodelle zur Reduktion der TAMEP-Zellen (*Nestin*::creERT2,R26-RFP,Sox2$^{fl/fl}$) oder der TAMEP und den zusätzlich „getracten“ Perizyten (*Nestin*::creERT2,R26-RFP,iDTA), sowie anderer Modelle, in denen wir Sox2 konditionell in Endothelzellen (*VE-cadherin*::creERT2,R26-RFP,Sox2$^{fl/fl}$), Perizyten (*Pdgfb*::creERT2,R26-RFP,Sox2$^{fl/fl}$) oder Mikroglia (*Cx3c1*::creERT2,R26-RFP,Sox2$^{fl/fl}$) ablatierten. Nach erfolgtem Tumorwachstum untersuchten wir die GBM-Volumen in allen Modellen und fanden, dass die Reduktion der TAMEP oder der TAMEP mitsamt den Perizyten, im gleichen Maße, zu einem signifikant kleineren Tumorvolumen führte (Abb. 11J und Anhang A.3, Abb. 7D-F (Fig.7D-F)). Der Verlust der Sox2-Expression in Perizyten alleine, in den Endothelzellen oder in Mikroglia, führte dagegen zu keiner Veränderung im Tumorvolumen im Vergleich zur Kontrolle (Abb. 11J;

Nes-RFP). Dies beweist, dass TAMEP und ihre Vorläuferzellen eine entscheidende Rolle in der GBM-Pathologie, der Gefäßbildung und Tumorausdehnung, spielen.

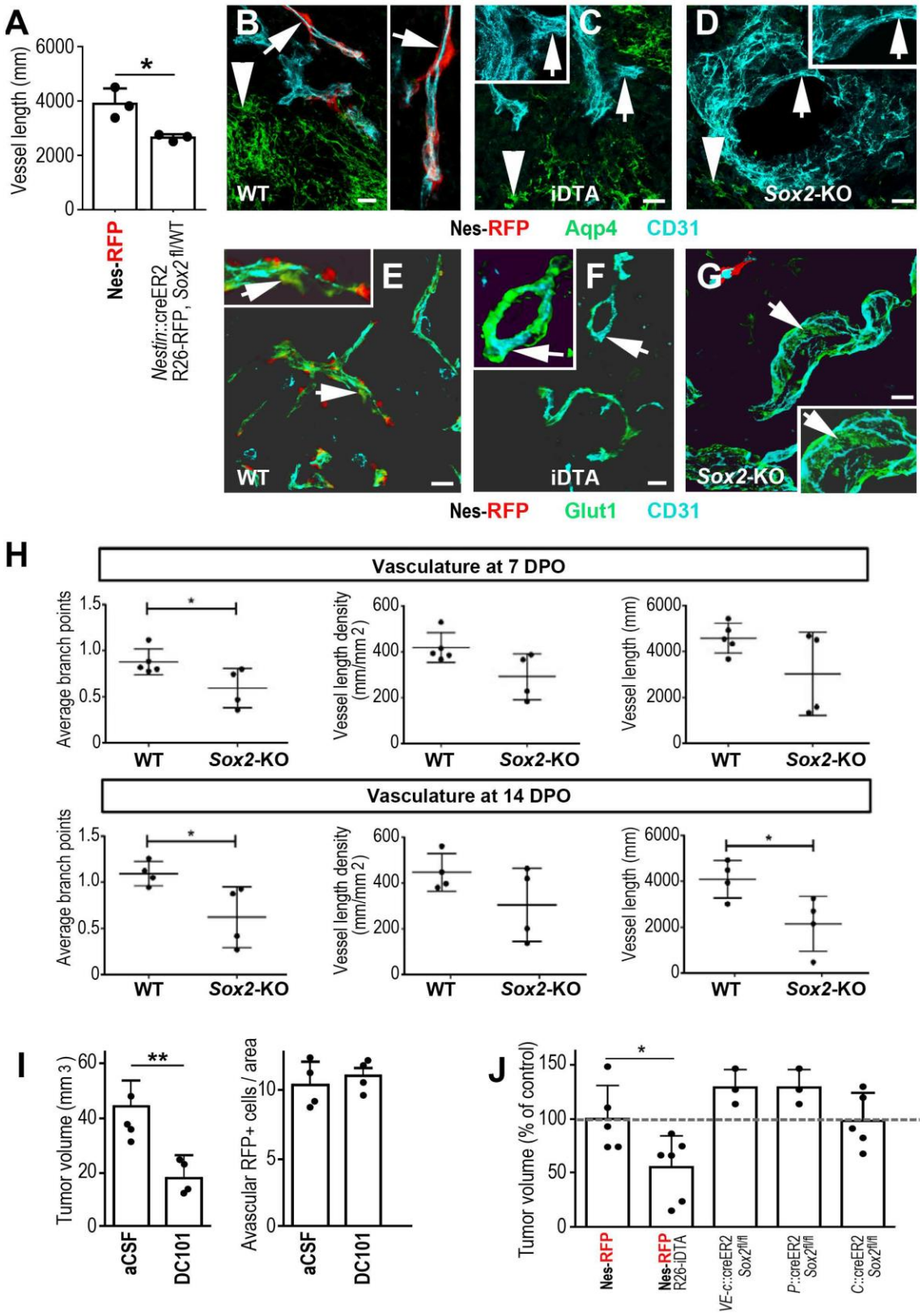

**Abb. 11: TAMEP und deren Vorläufer steuern das Gefäßwachstum und die Tumorexpansion beim GBM.**

A) Orthotope GBM Mäusen von Nes-RFP oder Nes-RFP mit heterozygotem Sox2-Verlust ($Sox2^{fl/wt}$) wurden 21 Tage nach Implantation bzgl. der Gefäße analysiert (n = 3 pro Gruppe). Die Gefäßlänge war in den Sox2 heterozygoten Tumoren signifikant reduziert im Vergleich zur WT-Kontrolle (Nes-RFP). B-G) Mittels Immunfluoreszenzanalyse auf verschiedene vaskuläre Marker (Aqp4, CD31, Glut1) wurden konditionelle Sox2-KO in TAMEP oder TAMEP-Depletions-Mäuse (iDTA) mit Nes-RFP (Kontrolle) -Mäusen verglichen und so die abnormalen Tumorgefäße (Pfeile), und normale Gefäße aus der Tumorumgebung (Pfeilspitze), in den manipulierten Mäusen dokumentiert. Der Glukose-Transporter Glut1 ist auf allen Gefäßen (CD31+) aller Gruppen unverändert vorhanden und das Aquaporin Protein Aqp4 ist in den Tumorgefäßen aller Gruppen abwesend. H) Die Gefäßdichte am Mikroskop quantifiziert per Stereoinvestigation für die Anzahl Verzweigungen („average branch points“), die Gefäßlängendichte („vessel length density“) und die totale Gefäßlänge („vessel length“) in den Tumoren zeigte eine signifikante Reduktion in der konditionellen Sox2-KO Maus im Vergleich zur WT-Kontrolle (n = 4 pro Gruppe). I) GBM-Mäuse wurden mit VEGFR2-Antikörper (DC101) oder aCSF Trägersubstanz intracerebral während des Tumorwachstums behandelt (n = 4 pro Gruppe). Das Tumorvolumen war aufgrund der Antiangiogenese signifikant reduziert, die Zahl der TAMEP („avascular RFP“) -Zellen blieb jedoch unverändert. J) Tiermodelle für die Verfolgung von TAMEP (Nes-RFP; n = 5), die Ablation von TAMEP und Perizyten (*Nestin*::creERT2,R26-RFP,iDTA; n = 6), den Verlust von Sox2 in Endothelzellen (*VE-cadherin*::creERT2,R26-RFP,$Sox2^{fl/fl}$; n = 3), Perizyten (*Pdgfb*::creERT2,R26-RFP,$Sox2^{fl/fl}$ n = 3) oder Mikroglia (*Cx3c1*::creERT2,R26-RFP,$Sox2^{fl/fl}$; n = 5) wurden auf die Tumorgröße 14 Tage nach Tumorwachstum analysiert und auf die Kontrollgruppe (Nes-RFP) normalisiert (100%). Nur in der TAMEP- und Perizyten- Ablation (und der TAMEP-Vorläuferablations-Gruppe; siehe zusätzlich Anhang Abb. 7C (Fig. 7C)) war die Tumorgröße signifikant verkleinert. Der Maßstab entspricht 30 μm. Statistische Signifikanzen erhoben per einfachem T-Test oder One-way ANOVA plus post-hoc Test sind angezeigt. p*<0,05, p***<0,01 p***<0,001. (Supplementary Material aus Kälin *et al.*, 2021).

In dieser Studie konnten wir folgende neue Erkenntnisse gewinnen:

- Wir entdeckten im Glioblastom eine bisher unbeschriebene „Tumor-Assoziierte Zelle mit einem Myeloid-ähnlichen Expressions-Profil“, genannt TAMEP.
- TAMEP weisen weitestgehend das Erscheinungsbild von myeloischen Zellen auf, stammen aber weder von Mikroglia noch von Knochenmarkszellen ab.
- TAMEP gehen aus lokalen Vorläuferzellen nach Aktivierung durch Gehirntumorzellen hervor.
- TAMEP fördern die Tumorexpansion durch die Anregung der Gefäßbildung.

In dieser Arbeit verfolgten wir eine neuartige CD11b-positive (myeloische) Zelle, genannt TAMEP, die eine erstaunliche angiogene Kapazität aufweist. Durch die beschriebenen Eigenschaften, stellen TAMEP ein vielversprechendes und neuartiges therapeutisches Ziel in der Neuroonkologie dar.

Themenbezogene Publikation:

**Kälin, R. E.**; Cai, L.; Li, Y.; Zhao, D.; Zhang, H.; Cheng, J.; Zhang, W.; Wu, Y.; Eisenhut, K.; Janssen, P.; Schmitt, L.; Enard, W.; Michels, F.; Fluh, C.; Hou, M.; Kirchleitner, S. V.; Siller, S.; Schiemann, M.; Andra, I.; Montanez, E.; Giachino, C.; Taylor, V.; Synowitz, M.; Tonn, J. C.; von Baumgarten, L.; Schulz, C.; Hellmann, I.; Glass, R., TAMEP are brain tumor parenchymal cells controlling neoplastic angiogenesis and progression. *Cell Syst* **2021,** Mar 17;12(3):248-262.e7.

# IV. Zusammenfassung und Ausblick

Das Tumormikromilieu spielt eine entscheidende Rolle in der Pathologie des Glioblastoms, indem es das Tumorwachstum antreibt und dessen angiogene und invasiven Eigenschaften und somit seine Aggressivität mitbestimmt. Die zelluläre Mikroumgebung des GBMs besteht aus einer Vielzahl von Gehirn-eigenen und Gehirn-fremden Zellen, darunter Stamm- und Vorläuferzellen wie mesenchymale Stammzellen, neuronale oder oligodendrogliale Vorläuferzellen, deren Einfluss auf die GBM-Progression bereits in früheren Studien gezeigt wurde. Eine Hauptkomponente des Tumorparenchyms bilden vaskuläre und Tumor-assoziierte myeloische Zellen, bestehend aus Mikroglia und peripheren Makrophagen. Durch ihre wichtige tumortrophe Funktion und die Sekretion angiogener und immunsuppressiver Faktoren treiben diese das GBM-Wachstum weiter voran.

In dieser Arbeit fanden wir eine bisher unbekannte Population an GBM-assoziierten Zellen mit einem myeloischen Expressionsmuster (Kälin *et al.*, 2021). Diese myeloid-artigen Zellen stammen von Gehirn-eigenen Vorläuferzellen ab, ohne Beitrag aus dem Knochenmark. Sie unterscheiden sich damit komplett von den bekannten Mikroglia oder Monozyten-derivierten Makrophagen (Abb. 12).

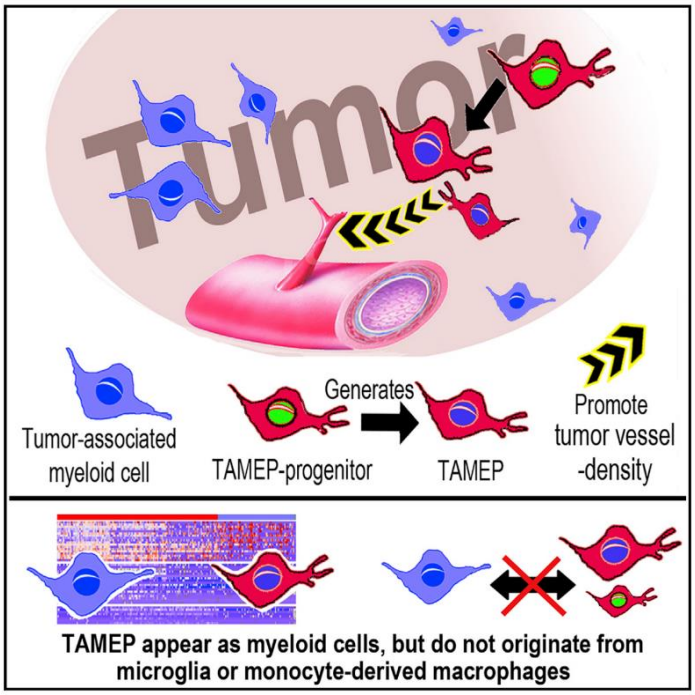


**Abb. 12: Graphische Zusammenfassung der Rolle von TAMEP.**
TAMEP sind Tumor-assoziierte Zellen mit einem myeloischen Expressionsmuster. TAMEP und deren Vorläufer sind Gehirn-eigene Zellen, charakterisiert durch die Expression von SOX2 und Nestin, und stammen nicht von Mikroglia oder Monozyten-derivierten Makrophagen aus dem Knochenmark ab. Im Glioblastom steuern sie das Gefäßwachstum und die Tumorexpansion. (aus Kälin *et al.*, 2021).

Diese Vorläuferzellen definieren sich ursprünglich durch die Expression des Stammzellmarkers SOX2 und durch die Aktivität des Nestin Gen-Promoters, der als Marker für unreife Zellen dient. Durch konditionelle Ablation von SOX2 wird die Ansammlung von TAMEP im GBM spezifisch verhindert. TAMEP exprimieren viele bekannte myeloische Marker auf RNA-Niveau und auf Protein-Ebene (z.B. Pu.1, CD11b, F4/80 und CX3CR1). Wir konnten jedoch zeigen, dass TAMEP nicht von der hematopoietischen Zelllinie abstammen, indem wir CCR2-, Flt3- oder CX3CR1-Reporter Mäuse benutzten. Dies unterstützt die momentane Sicht, dass Tumor-assoziierte myeloische Zellen äußerst heterogen sind und sich sogar als solche „verkleiden“, aber keine sind (Audia *et al*., 2017; Glass and Synowitz, 2014; Hambardzumyan *et al*., 2016). Durch weitere Immunfluoreszenz-Analysen konnten wir ausschließen, dass es sich bei TAMEP um mesenchymale Stammzellen oder um neuronale oder oligodendrogliale Vorläuferzellen handelt. Wir zeigten außerdem, dass die Ablation der kleinen TAMEP Zellpopulation einen großen Einfluss auf die gesamte GBM-Angiogenese ausübt und somit die Tumorprogression hemmt.

Daraus schließen wir, dass diese GBM-assoziierte CD11b-positive kleine Zellpopulation notwendig für das angiogene Wachstum des Tumors ist und sich daher für eine neuartige Strategie der Zell-basierten Tumor-Therapie eignet. Indem eine spezifisch Tumor-assoziierte hirnständige Zelle therapeutisch adressiert wird, könnte eine eventuelle Behandlungsresistenz aufgrund der Tumorheterogenität umgangen werden (Weller *et al*., 2017). Tumor-assoziierte myeloische Zellen bieten sich also als mögliches zelluläres Ziel zur GBM-Therapie an, da gezeigt wurde, dass sie die GBM-Progression und –Invasion unterstützen können (Markovic *et al*., 2009). Die ZNS-spezifische Ablation von myeloischen Zellen (in einem transgenen CD11b-Mausmodell) führte bereits zu einer Reduktion von Tumorgefäßen und Tumorgröße (Brandenburg *et al*., 2016). Eine pharmakologische Intervention gegen Tumor-assoziierte myeloische Zellen erreichte jedoch hauptsächlich periphere myeloische Zellen und führte zu einer Normalisierung der Tumorgefäße ohne Tumor-hemmenden Effekt (Mathivet *et al*., 2017). Dies zeigt, dass eine spezifische hirnständige myeloische Subpopulation sich prinzipiell als Zielzelle für eine anti-angiogene Wirkung anbietet. Unser Mausmodell für TAMEP-Zellen erlaubt es uns, diese neuartige Zell-Population als alternativen Therapieansatz weiterzuverfolgen. Indem wir TAMEP- und ihre Vorläufer-Zellen mittels Einzelzell-Sequenzierung mit etablierten Zell-Reporter Linien für reife

Tumorparenchymzellen (Perizyten, Endothel, Oligodendrozyten, Neuronen und Astrozyten) auf deren Genexpression untersuchen und vergleichend analysieren, erwarten wir die Entschlüsselung von neuen Signalwegen, die für die TAMEP-Zellpopulation einzigartig sind und sich als molekulares Therapieziel gegen das GBM eignen.

Ein Signalweg, der sich bereits für die GBM-Therapie eignen könnte, ist der APLN/APLNR Signalweg. In unseren früheren Studien beschrieben wir eine dramatische Hochregulation der APLN- und APLNR-mRNA Expression in den GBM-assoziierten mikrovaskulären Proliferaten (Kälin *et al*., 2007). Zusammen mit einer Studie über das Genexpresssionsmuster des Tumorendothels (Seaman *et al*., 2007), stellte dies den ersten Hinweis dar, dass der APLN/APLNR Signalweg auch in der Tumorigenese eine entscheidende Rolle spielen könnte. Unter Verwendung eines seriellen Transplantationsmodells in Ratten, in welchem der Wechsel von einem hoch-invasiven zu einem hoch-angiogenen GBM nachvollzogen wird (der sogenannte angiogene Switch), konnten wir die Hochregulation von APLN experimentell beobachten (Mastrella *et al*., 2019). Um den Einfluss von APLN aus dem Tumorparenchym zu untersuchen, wendeten wir verschiedene orthotope GBM-Modelle (syngene und xenobiotische) in APLN-KO Mäusen an (Frisch *et al*., 2020; Mastrella *et al*., 2019). Der Verlust der APLN-Hochregulation in der Tumorvaskulatur führte zu einer signifikant verminderten Gefäßbildung im GBM (Frisch *et al*., 2020; Mastrella *et al*., 2019), was die Bedeutung des autokrinen APLN/APLNR Signalweges in Endothelzellen aufzeigte. Zusätzlich zur vaskulären APLN-Expression untersuchten wir auch die Wirkung des APLN-Signals aus den GBM Pseudopalisaden (Kälin *et al*., 2007; Mastrella *et al*., 2019). Durch einen shRNA-vermittelten APLN Knockdown in den GBM-Zellen fanden wir, dass die Gefäßdichte im Tumor weiter erniedrigt wurde. Aus der Kombination beider Ansätze resultierte eine komplette Blockade der Tumorangiogenese. Die Infusion des Peptids Apelin-13 ermöglichte die teilweise Erholung der Tumorgefäße im APLN-defizienten GBM-Modell (Frisch *et al*., 2020), wodurch bewiesen war, dass APLN beim GBM die Gefäßbildung direkt steuert.

Im zweiten Teil unserer Analysen der APLN-Funktion untersuchten wir das invasive Wachstum unserer GBM-Mausmodelle. Es zeigte sich, dass GBM-Zellen in hohem Maße APLNR exprimieren können und dass diese Expression mit einer erhöhten Tumorzellinvasivität einhergeht. Gleichzeitige hohe APLN-Expression korrelierte dagegen mit hoher Tumorzelldichte, wenig

Invasivität aber einem hohen Gefäßreichtum (Abb.13). Durch die oben beschriebene experimentelle APLN-Reduktion zeigte sich auch eine erhöhte GBM-Invasivität *in vivo* (Mastrella *et al*., 2019).

Außerdem fanden wir, dass VEGFA und APLN im humanen GBM in hypoxischen Arealen ko-exprimiert sind und dass die Blockade des VEGFA/VEGFR2 Signalweges (über Bevacizumab oder Ramucirumab) diese APLN Expression beim Patienten reduzierte. Im Mausmodell wurde ersichtlich, dass die Blockade von VEGFA/VEGFR2 und die gleichzeitige Verminderung der APLN-levels zwar die Tumorangiogenese weiter hemmte, die Tumorzellinvasivität jedoch erhöhte (Lu-Emerson *et al*., 2015; Mastrella *et al*., 2019). Im Gegensatz dazu führte die gleichzeitige Gabe des partiellen APLNR-Antagonisten Apelin-F13A mit VEGF/VEGFR blockierenden Antikörpern zu einer reduzierten Angiogenese und einer verminderten GBM-Invasivität, sowie einem erhöhten Überleben der GBM-tragenden Mäuse (Abb.13 und Anhang A.2 Abb. 6 (Fig.6A)).

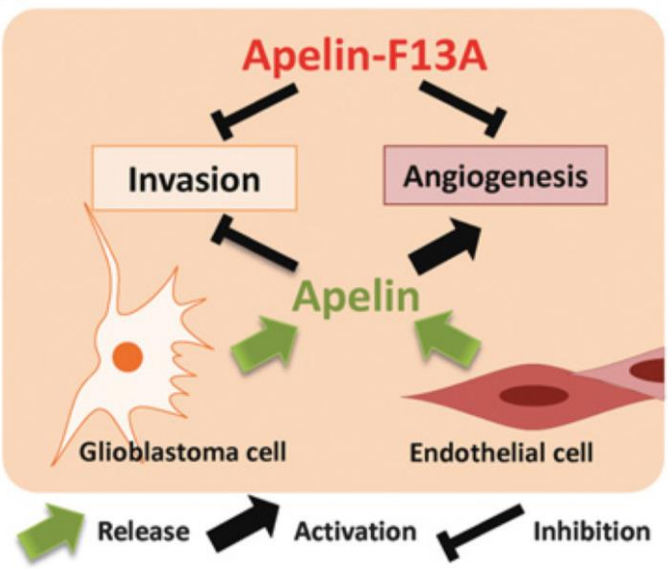


**Abb. 13: Modell für die Rolle von Apelin im GBM.**
Das Apelin-Peptid wird von GBM- und/oder Endothelzellen ausgeschüttet und aktiviert seinen Rezeptor APLNR auf den Tumorzellen (was die Invasion verhindert) und auf Endothelzellen (was die Angiogenese aktiviert/erhält). Die Zugabe von Apelin-F13A vermindert sowohl die Tumor-Angiogenese als auch die GBM-Zellinvasivität (aus Mastrella *et al.*, 2019).

Vor kurzem konnte in anderen Studien gezeigt werden, dass das bizyklisch-stabilisierte MM54 Peptid von erhöhter *in vivo* Stabilität (Macaluso *et al*., 2011) ebenfalls eine Reduktion der Tumor-Angiogenese in einem Maus-GBM-Modell bewirkt und das Überleben der Versuchstiere erhöht (Harford-Wright *et al*., 2017). Dieses MM54 Peptid war auch in Mausmodellen für Brust- und Lungen-Krebs erfolgreich darin die Tumorgefäßdichte zu erniedrigen (Uribesalgo *et al*., 2019). Ebenso konnte es die Nebenwirkung einer anti-angiogenen Therapie mittels Sunitinib (ein

VEGFR2 Kinase-Hemmer) vermindern, indem es die Metastasierung dieser Tumorzellen in die Lunge signifikant reduzierte.

Zusammen mit unseren Untersuchungen bestärken uns diese Resultate in der Annahme, dass die APLNR-Blockade in Synergie zur VEGF-Blockade eine verbesserte anti-angiogene Wirkung entfalten und durch die zusätzliche Reduktion der GBM-Zellinfiltration die Resistenz gegen gängige anti-angiogene Therapien auflösen kann.

Einer verbesserten Therapie gegen das GBM stehen allerdings noch weitere Hindernisse im Weg. Eine gemeinsame Komplikation bei primären ZNS-Tumoren stellt das Tumor-assoziierte Hirnödem dar, welches zu neurologischen Ausfällen führt (Schnell and Tonn, 2017). Kortikosteroide sind hier die am häufigsten verwendeten Mittel zur Kontrolle dieser Tumor-vermittelten Ödeme. (Galicich *et al*., 1961; Vecht *et al*., 1994). Obwohl die Anwendung des Kortisols Dexamethason (DEX) zur Auflösung des Hirnödems führen kann, sollte den klinischen Nebenwirkungen wie abnormaler Glukose-Metabolismus, Leukopenie und Pneumonie mehr Beachtung geschenkt werden (Cenciarini *et al*., 2019). Häufig wird DEX auch bei Tumorrezidiven erfolgreich angewendet, um die neurologischen Symptome zu kontrollieren. Trotz dieses günstigen Effektes bezüglich des zerebralen vasogenen Ödems scheint die Kortisol-Anwendung ein eigener unabhängiger Risikofaktor zu sein, mit der erwähnten Gefahr einer Lymphopenie und der damit assoziierten Verminderung des Überlebens (Hui *et al*., 2019). Dieser Zusammenhang wurde kürzlich im GBM Mausmodell bestätigt (Pitter *et al*., 2016). Zu einer Zeit in der Immuntherapien (z.B. durch CAR-T Zell-Therapie) immer neue Erfolge erzielen, verstellt eine DEX-Behandlung des vasogenen Ödems möglichicherweise einem therapeutischen Fortschritt den Weg (Cloughesy *et al*., 2019; Keskin *et al*., 2019; O'Rourke *et al*., 2017; Schalper *et al*., 2019; Zhao *et al*., 2019). Aus diesem Grund ist es wichtig Alternativen für die gängige Ödem-Therapie bei GBM-Patienten zu finden (Cloughesy *et al*., 2019). Eine anti-VEGF Therapie hat beim GBM in der Klinik einen gewissen Nutzen gezeigt und wird unterdessen zur temporären Symptomkontrolle unter Auslassung von Kortikosteroiden verwendet (Weller *et al*., 2021).

Leider vermindert die VEGF/VEGFR2-zentrierte Therapie, wie oben beschrieben, nicht nur die entartete Tumorvaskulatur, sondern führt auch zu einer erhöhten Tumorzellinvasivität. Hier könnte der APLN/APLNR als neues multimodales Therapieziel in die Lücke springen (Abb. 14), da

In früheren Studien gezeigt wurde, dass APLN die Gefäßreifung fördert und die Durchlässigkeit neuer Gefäße vermindert (Kidoya *et al*., 2011). Eine Reduktion des vasogenen Ödems wäre als Effekt beim GBM denkbar. Zusätzlich könnte eine Normalisierung der Tumorvaskulatur helfen das GBM-Standardtherapeutikum Temozolomid (Temodal) effizienter an den Ort des Geschehens zu befördern. Darüber hinaus wurde erst kürzlich gezeigt, dass APLNR essenziell für die adaptive Immunantwort gegen Krebs ist (Patel *et al*., 2017). Die Autoren konnten zeigen, dass die APLNR-Expression die Anzahl der T-Effektorzellen erhöht und somit eine T-Zell-vermittelte Immuntherapie beim GBM zusätzlich in Aussicht stellt.

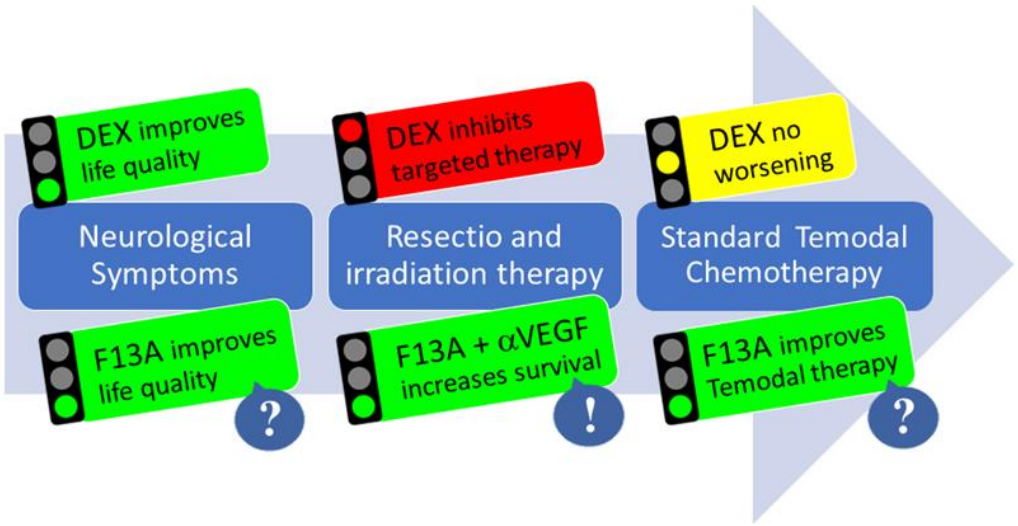


**Abb. 14: Die multimodale Wirkung einer zielgerichteten APLN/APLNR-Therapie beim GBM.**
Während der ersten Phase der Krankheit verbessert eine DEX Behandlung die neurologischen Symptome, in der zweiten Phase nach der Resektion kann DEX eine mögliche zielgerichtete Therapie behindern (z.B. die Immuntherapie). In Phase 3 während der Chemotherapie und einem Tumorrezidiv entfaltet DEX keine Wirkung mehr. Für eine mögliche Apelin-F13A Therapie gibt es Evidenzen, dass sie durch eine Ödemreduktion die Lebensqualität erhöhen könnte, dass die Antiangiogene Kombinations-Therapie das Überleben steigert und dass eine Gefäßnormalisierung die Temodal-Chemotherapie zusätzlich verbessern könnte (aus Kälin and Glass, 2021).

Zusammengefasst lässt sich sagen, dass eine pharmakologische Modulation des APLN/APLNR Signalweges möglich ist und dass diese eine anti-angiogene und anti-invasive Wirkung entfaltet. Zusätzlich scheint die Inhibierung des APLN/APLNR Signalweges die Proliferation von Gliomstammzellen zu verhindern und eine neuroprotektive Wirkung zu besitzen. Außerdem bietet APLN/APLNR als neues Angriffsziel die einmalige Chance neurologische Symptome zu

mindern und die Überlebensspanne des Patienten zu erhöhen, indem es die Tumorgefäße normalisiert und so die Ödembildung reduziert, aber auch die Chemotherapie verbessert und eine zukünftige Immuntherapie unterstützt. Eine kleines Bluthirnschranken-gängiges Pharmazeutikum, das auf den APLN/APLNR-Signalweg zielt, trägt daher ein vielversprechendes Potential für ein GBM-Medikament mit multimodaler Wirkung in sich.

# V. Referenzen


Aldape, K., Brindle, K.M., Chesler, L., Chopra, R., Gajjar, A., Gilbert, M.R., Gottardo, N., Gutmann, D.H., Hargrave, D., Holland, E.C*., et al.* (2019). Challenges to curing primary brain tumours. Nat Rev Clin Oncol *16*, 509-520.

Aldape, K., Zadeh, G., Mansouri, S., Reifenberger, G., and von Deimling, A. (2015). Glioblastoma: pathology, molecular mechanisms and markers. Acta neuropathologica *129*, 829-848.

Armulik, A., Genove, G., and Betsholtz, C. (2011). Pericytes: developmental, physiological, and pathological perspectives, problems, and promises. Developmental cell *21*, 193-215.

Audia, A., Conroy, S., Glass, R., and Bhat, K.P.L. (2017). The Impact of the Tumor Microenvironment on the Properties of Glioma Stem-Like Cells. Front Oncol *7*, 143.

Back, J., Allman, D., Chan, S., and Kastner, P. (2005). Visualizing PU.1 activity during hematopoiesis. Exp Hematol *33*, 395-402.

Behnan, J., Isakson, P., Joel, M., Cilio, C., Langmoen, I.A., Vik-Mo, E.O., and Badn, W. (2014). Recruited brain tumor-derived mesenchymal stem cells contribute to brain tumor progression. Stem cells *32*, 1110-1123.

Benz, C., Martins, V.C., Radtke, F., and Bleul, C.C. (2008). The stream of precursors that colonizes the thymus proceeds selectively through the early T lineage precursor stage of T cell development. J Exp Med *205*, 1187-1199.

Bowman, R.L., Klemm, F., Akkari, L., Pyonteck, S.M., Sevenich, L., Quail, D.F., Dhara, S., Simpson, K., Gardner, E.E., Iacobuzio-Donahue, C.A*., et al.* (2016). Macrophage Ontogeny Underlies Differences in Tumor-Specific Education in Brain Malignancies. Cell Rep *17*, 2445-2459.

Brandenburg, S., Muller, A., Turkowski, K., Radev, Y.T., Rot, S., Schmidt, C., Bungert, A.D., Acker, G., Schorr, A., Hippe, A*., et al.* (2016). Resident microglia rather than peripheral macrophages promote vascularization in brain tumors and are source of alternative pro-angiogenic factors. Acta neuropathologica *131*, 365-378.

Brennan, C.W., Verhaak, R.G., McKenna, A., Campos, B., Noushmehr, H., Salama, S.R., Zheng, S., Chakravarty, D., Sanborn, J.Z., Berman, S.H*., et al.* (2013). The somatic genomic landscape of glioblastoma. Cell *155*, 462-477.

Cenciarini, M., Valentino, M., Belia, S., Sforna, L., Rosa, P., Ronchetti, S., D'Adamo, M.C., and Pessia, M. (2019). Dexamethasone in Glioblastoma Multiforme Therapy: Mechanisms and Controversies. Front Mol Neurosci *12*, 65.

Chen, Z., Feng, X., Herting, C.J., Garcia, V.A., Nie, K., Pong, W.W., Rasmussen, R., Dwivedi, B., Seby, S., Wolf, S.A*., et al.* (2017). Cellular and Molecular Identity of Tumor-Associated Macrophages in Glioblastoma. Cancer Res *77*, 2266-2278.

Chinot, O.L., Wick, W., Mason, W., Henriksson, R., Saran, F., Nishikawa, R., Carpentier, A.F., Hoang-Xuan, K., Kavan, P., Cernea, D*., et al.* (2014). Bevacizumab plus radiotherapy-temozolomide for newly diagnosed glioblastoma. The New England journal of medicine *370*, 709-722.

Cleaver, O., Tonissen, K.F., Saha, M.S., and Krieg, P.A. (1997). Neovascularization of the Xenopus embryo. Dev Dyn *210*, 66-77.

Cloughesy, T.F., Mochizuki, A.Y., Orpilla, J.R., Hugo, W., Lee, A.H., Davidson, T.B., Wang, A.C., Ellingson, B.M., Rytlewski, J.A., Sanders, C.M*., et al.* (2019). Neoadjuvant anti-PD-1

immunotherapy promotes a survival benefit with intratumoral and systemic immune responses in recurrent glioblastoma. Nature medicine *25*, 477-486.

Cox, C.M., D'Agostino, S.L., Miller, M.K., Heimark, R.L., and Krieg, P.A. (2006). Apelin, the ligand for the endothelial G-protein-coupled receptor, APJ, is a potent angiogenic factor required for normal vascular development of the frog embryo. Developmental biology *296*, 177-189.

De Mota, N., Lenkei, Z., and Llorens-Cortes, C. (2000). Cloning, pharmacological characterization and brain distribution of the rat apelin receptor. Neuroendocrinology *72*, 400-407.

del Toro, R., Prahst, C., Mathivet, T., Siegfried, G., Kaminker, J.S., Larrivee, B., Breant, C., Duarte, A., Takakura, N., Fukamizu, A.*, et al.* (2010). Identification and functional analysis of endothelial tip cell-enriched genes. Blood *116*, 4025-4033.

Devic, E., Paquereau, L., Vernier, P., Knibiehler, B., and Audigier, Y. (1996). Expression of a new G protein-coupled receptor X-msr is associated with an endothelial lineage in Xenopus laevis. Mech Dev *59*, 129-140.

Devic, E., Rizzoti, K., Bodin, S., Knibiehler, B., and Audigier, Y. (1999). Amino acid sequence and embryonic expression of msr/apj, the mouse homolog of Xenopus X-msr and human APJ. Mech Dev *84*, 199-203.

Frisch, A., Kälin, S., Monk, R., Radke, J., Heppner, F.L., and Kälin, R.E. (2020). Apelin Controls Angiogenesis-Dependent Glioblastoma Growth. Int J Mol Sci *21*.

Galicich, J.H., French, L.A., and Melby, J.C. (1961). Use of dexamethasone in treatment of cerebral edema associated with brain tumors. J Lancet *81*, 46-53.

Giachino, C., and Taylor, V. (2009). Lineage analysis of quiescent regenerative stem cells in the adult brain by genetic labelling reveals spatially restricted neurogenic niches in the olfactory bulb. Eur J Neurosci *30*, 9-24.

Gilbert, M.R., Dignam, J.J., Armstrong, T.S., Wefel, J.S., Blumenthal, D.T., Vogelbaum, M.A., Colman, H., Chakravarti, A., Pugh, S., Won, M.*, et al.* (2014). A randomized trial of bevacizumab for newly diagnosed glioblastoma. The New England journal of medicine *370*, 699-708.

Glass, R., and Synowitz, M. (2014). CNS macrophages and peripheral myeloid cells in brain tumours. Acta neuropathologica *128*, 347-362.

Glass, R., Synowitz, M., Kronenberg, G., Walzlein, J.H., Markovic, D.S., Wang, L.P., Gast, D., Kiwit, J., Kempermann, G., and Kettenmann, H. (2005). Glioblastoma-induced attraction of endogenous neural precursor cells is associated with improved survival. J Neurosci *25*, 2637-2646.

Hambardzumyan, D., Amankulor, N.M., Helmy, K.Y., Becher, O.J., and Holland, E.C. (2009). Modeling Adult Gliomas Using RCAS/t-va Technology. Transl Oncol *2*, 89-95.

Hambardzumyan, D., Gutmann, D.H., and Kettenmann, H. (2016). The role of microglia and macrophages in glioma maintenance and progression. Nature neuroscience *19*, 20-27.

Harford-Wright, E., Andre-Gregoire, G., Jacobs, K.A., Treps, L., Le Gonidec, S., Leclair, H.M., Gonzalez-Diest, S., Roux, Q., Guillonneau, F., Loussouarn, D.*, et al.* (2017). Pharmacological targeting of apelin impairs glioblastoma growth. Brain *140*, 2939-2954.

Helker, C.S., Eberlein, J., Wilhelm, K., Sugino, T., Malchow, J., Schuermann, A., Baumeister, S., Kwon, H.B., Maischein, H.M., Potente, M.*, et al.* (2020). Apelin signaling drives vascular endothelial cells toward a pro-angiogenic state. Elife *9*.

Ho, I.A., Toh, H.C., Ng, W.H., Teo, Y.L., Guo, C.M., Hui, K.M., and Lam, P.Y. (2013). Human bone marrow-derived mesenchymal stem cells suppress human glioma growth through inhibition of angiogenesis. Stem cells *31*, 146-155.

Hosoya, M., Kawamata, Y., Fukusumi, S., Fujii, R., Habata, Y., Hinuma, S., Kitada, C., Honda, S., Kurokawa, T., Onda, H.*, et al.* (2000). Molecular and functional characteristics of APJ. Tissue distribution of mRNA and interaction with the endogenous ligand apelin. The Journal of biological chemistry *275*, 21061-21067.

Huang, Y., Hoffman, C., Rajappa, P., Kim, J.H., Hu, W., Huse, J., Tang, Z., Li, X., Weksler, B., Bromberg, J.*, et al.* (2014). Oligodendrocyte progenitor cells promote neovascularization in glioma by disrupting the blood-brain barrier. Cancer Res *74*, 1011-1021.

Huang, Y., Xu, Z., Xiong, S., Sun, F., Qin, G., Hu, G., Wang, J., Zhao, L., Liang, Y.X., Wu, T.*, et al.* (2018). Repopulated microglia are solely derived from the proliferation of residual microglia after acute depletion. Nature neuroscience *21*, 530-540.

Hui, C.Y., Rudra, S., Ma, S., Campian, J.L., and Huang, J. (2019). Impact of overall corticosteroid exposure during chemoradiotherapy on lymphopenia and survival of glioblastoma patients. Journal of neuro-oncology *143*, 129-136.

Jain, R.K., di Tomaso, E., Duda, D.G., Loeffler, J.S., Sorensen, A.G., and Batchelor, T.T. (2007). Angiogenesis in brain tumours. Nat Rev Neurosci *8*, 610-622.

Kälin, R.E., Banziger-Tobler, N.E., Detmar, M., and Brändli, A.W. (2009). An in vivo chemical library screen in Xenopus tadpoles reveals novel pathways involved in angiogenesis and lymphangiogenesis. Blood *114*, 1110-1122.

Kälin, R.E., Cai, L., Li, Y., Zhao, D., Zhang, H., Cheng, J., Zhang, W., Wu, Y., Eisenhut, K., Janssen, P.*, et al.* (2021). TAMEP are brain tumor parenchymal cells controlling neoplastic angiogenesis and progression. Cell Syst.

Kälin, R.E., and Glass, R. (2021). APLN/APLNR Signaling Controls Key Pathological Parameters of Glioblastoma. *13*, 3899.

Kälin, R.E., Kretz, M.P., Meyer, A.M., Kispert, A., Heppner, F.L., and Brändli, A.W. (2007). Paracrine and autocrine mechanisms of apelin signaling govern embryonic and tumor angiogenesis. Developmental biology *305*, 599-614.

Kälin, S., and Kälin, R.E. (2017). Apelin and Cancer. In Adipocitokines, Energy Balance and Cancer, R. O., and B. N.A., eds. (Springer International Publishing Switzerland ), pp. 137-166.

Kasai, A., Ishimaru, Y., Kinjo, T., Satooka, T., Matsumoto, N., Yoshioka, Y., Yamamuro, A., Gomi, F., Shintani, N., Baba, A.*, et al.* (2010). Apelin is a crucial factor for hypoxia-induced retinal angiogenesis. Arteriosclerosis, thrombosis, and vascular biology *30*, 2182-2187.

Keskin, D.B., Anandappa, A.J., Sun, J., Tirosh, I., Mathewson, N.D., Li, S., Oliveira, G., Giobbie-Hurder, A., Felt, K., Gjini, E.*, et al.* (2019). Neoantigen vaccine generates intratumoral T cell responses in phase Ib glioblastoma trial. Nature *565*, 234-239.

Kidoya, H., Kunii, N., Naito, H., Muramatsu, F., Okamoto, Y., Nakayama, T., and Takakura, N. (2011). The apelin/APJ system induces maturation of the tumor vasculature and improves the efficiency of immune therapy. Oncogene *31*, 3254-3264.

Kidoya, H., Ueno, M., Yamada, Y., Mochizuki, N., Nakata, M., Yano, T., Fujii, R., and Takakura, N. (2008). Spatial and temporal role of the apelin/APJ system in the caliber size regulation of blood vessels during angiogenesis. EMBO J *27*, 522-534.

Kuba, K., Zhang, L., Imai, Y., Arab, S., Chen, M., Maekawa, Y., Leschnik, M., Leibbrandt, A., Markovic, M., Schwaighofer, J.*, et al.* (2007). Impaired heart contractility in Apelin gene-deficient mice associated with aging and pressure overload. Circulation research *101*, e32-42.

Lee, D.K., George, S.R., and O'Dowd, B.F. (2006). Unravelling the roles of the apelin system: prospective therapeutic applications in heart failure and obesity. Trends in pharmacological sciences *27*, 190-194.

Lee, D.K., Saldivia, V.R., Nguyen, T., Cheng, R., George, S.R., and O'Dowd, B.F. (2005). Modification of the terminal residue of apelin-13 antagonizes its hypotensive action. Endocrinology *146*, 231-236.

Liu, Q., Hu, T., He, L., Huang, X., Tian, X., Zhang, H., He, L., Pu, W., Zhang, L., Sun, H.*, et al.* (2015). Genetic targeting of sprouting angiogenesis using Apln-CreER. Nature communications *6*, 6020.

Louis, D.N., Perry, A., Reifenberger, G., von Deimling, A., Figarella-Branger, D., Cavenee, W.K., Ohgaki, H., Wiestler, O.D., Kleihues, P., and Ellison, D.W. (2016). The 2016 World Health Organization Classification of Tumors of the Central Nervous System: a summary. Acta neuropathologica *131*, 803-820.

Lu-Emerson, C., Duda, D.G., Emblem, K.E., Taylor, J.W., Gerstner, E.R., Loeffler, J.S., Batchelor, T.T., and Jain, R.K. (2015). Lessons from anti-vascular endothelial growth factor and anti-vascular endothelial growth factor receptor trials in patients with glioblastoma. Journal of clinical oncology : official journal of the American Society of Clinical Oncology *33*, 1197-1213.

Lu, K.V., and Bergers, G. (2013). Mechanisms of evasive resistance to anti-VEGF therapy in glioblastoma. CNS oncology *2*, 49-65.

Macaluso, N.J., Pitkin, S.L., Maguire, J.J., Davenport, A.P., and Glen, R.C. (2011). Discovery of a competitive apelin receptor (APJ) antagonist. ChemMedChem *6*, 1017-1023.

Madisen, L., Zwingman, T.A., Sunkin, S.M., Oh, S.W., Zariwala, H.A., Gu, H., Ng, L.L., Palmiter, R.D., Hawrylycz, M.J., Jones, A.R.*, et al.* (2010). A robust and high-throughput Cre reporting and characterization system for the whole mouse brain. Nature neuroscience *13*, 133-140.

Markovic, D.S., Vinnakota, K., Chirasani, S., Synowitz, M., Raguet, H., Stock, K., Sliwa, M., Lehmann, S., Kälin, R., van Rooijen, N.*, et al.* (2009). Gliomas induce and exploit microglial MT1-MMP expression for tumor expansion. Proceedings of the National Academy of Sciences of the United States of America *106*, 12530-12535.

Mastrella, G., Hou, M., Li, M., Stoecklein, V.M., Zdouc, N., Volmar, M.N.M., Miletic, H., Reinhard, S., Herold-Mende, C.C., Kleber, S.*, et al.* (2019). Targeting APLN/APLNR Improves Antiangiogenic Efficiency and Blunts Proinvasive Side Effects of VEGFA/VEGFR2 Blockade in Glioblastoma. Cancer Res *79*, 2298-2313.

Mathivet, T., Bouleti, C., Van Woensel, M., Stanchi, F., Verschuere, T., Phng, L.K., Dejaegher, J., Balcer, M., Matsumoto, K., Georgieva, P.B.*, et al.* (2017). Dynamic stroma reorganization drives blood vessel dysmorphia during glioma growth. EMBO Mol Med *9*, 1629-1645.

O'Carroll, A.M., Selby, T.L., Palkovits, M., and Lolait, S.J. (2000). Distribution of mRNA encoding B78/apj, the rat homologue of the human APJ receptor, and its endogenous ligand apelin in brain and peripheral tissues. Biochimica et biophysica acta *1492*, 72-80.

O'Dowd, B.F., Heiber, M., Chan, A., Heng, H.H., Tsui, L.C., Kennedy, J.L., Shi, X., Petronis, A., George, S.R., and Nguyen, T. (1993). A human gene that shows identity with the gene encoding the angiotensin receptor is located on chromosome 11. Gene *136*, 355-360.

O'Rourke, D.M., Nasrallah, M.P., Desai, A., Melenhorst, J.J., Mansfield, K., Morrissette, J.J.D., Martinez-Lage, M., Brem, S., Maloney, E., Shen, A.*, et al.* (2017). A single dose of peripherally infused EGFRvIII-directed CAR T cells mediates antigen loss and induces adaptive resistance in patients with recurrent glioblastoma. Sci Transl Med *9*.

Patel, S.J., Sanjana, N.E., Kishton, R.J., Eidizadeh, A., Vodnala, S.K., Cam, M., Gartner, J.J., Jia, L., Steinberg, S.M., Yamamoto, T.N.*, et al.* (2017). Identification of essential genes for cancer immunotherapy. Nature *548*, 537-542.

Pitter, K.L., Tamagno, I., Alikhanyan, K., Hosni-Ahmed, A., Pattwell, S.S., Donnola, S., Dai, C., Ozawa, T., Chang, M., Chan, T.A.*, et al.* (2016). Corticosteroids compromise survival in glioblastoma. Brain *139*, 1458-1471.

Plate, K.H., Breier, G., Weich, H.A., and Risau, W. (1992). Vascular endothelial growth factor is a potential tumour angiogenesis factor in human gliomas in vivo. Nature *359*, 845-848.

Prinz, M., Jung, S., and Priller, J. (2019). Microglia Biology: One Century of Evolving Concepts. Cell *179*, 292-311.

Reaux, A., De Mota, N., Skultetyova, I., Lenkei, Z., El Messari, S., Gallatz, K., Corvol, P., Palkovits, M., and Llorens-Cortes, C. (2001). Physiological role of a novel neuropeptide, apelin, and its receptor in the rat brain. Journal of neurochemistry *77*, 1085-1096.

Saint-Geniez, M., Masri, B., Malecaze, F., Knibiehler, B., and Audigier, Y. (2002). Expression of the murine msr/apj receptor and its ligand apelin is upregulated during formation of the retinal vessels. Mech Dev *110*, 183-186.

Schalper, K.A., Rodriguez-Ruiz, M.E., Diez-Valle, R., Lopez-Janeiro, A., Porciuncula, A., Idoate, M.A., Inoges, S., de Andrea, C., Lopez-Diaz de Cerio, A., Tejada, S.*, et al.* (2019). Neoadjuvant nivolumab modifies the tumor immune microenvironment in resectable glioblastoma. Nature medicine *25*, 470-476.

Schnell, O., and Tonn, J.C. (2017). Treatment of Edema Formation in Oncology In Brain Edema; From Molecular Mechanisms to Clinical Practice

J. Badaut, and N. Plesnila, eds. (Academic Press), pp. 477- 495.

Seaman, S., Stevens, J., Yang, M.Y., Logsdon, D., Graff-Cherry, C., and St Croix, B. (2007). Genes that distinguish physiological and pathological angiogenesis. Cancer cell *11*, 539-554.

Stock, K., Garthe, A., de Almeida Sassi, F., Glass, R., Wolf, S.A., and Kettenmann, H. (2014). The capsaicin receptor TRPV1 as a novel modulator of neural precursor cell proliferation. Stem cells *32*, 3183-3195.

Strasser, G.A., Kaminker, J.S., and Tessier-Lavigne, M. (2010). Microarray analysis of retinal endothelial tip cells identifies CXCR4 as a mediator of tip cell morphology and branching. Blood *115*, 5102-5110.

Stupp, R., Mason, W.P., van den Bent, M.J., Weller, M., Fisher, B., Taphoorn, M.J., Belanger, K., Brandes, A.A., Marosi, C., Bogdahn, U.*, et al.* (2005). Radiotherapy plus concomitant and adjuvant temozolomide for glioblastoma. The New England journal of medicine *352*, 987-996.

Sun, M.Y., Yetman, M.J., Lee, T.C., Chen, Y., and Jankowsky, J.L. (2014). Specificity and efficiency of reporter expression in adult neural progenitors vary substantially among nestin-CreER(T2) lines. J Comp Neurol *522*, 1191-1208.

Sweeney, M.D., Ayyadurai, S., and Zlokovic, B.V. (2016). Pericytes of the neurovascular unit: key functions and signaling pathways. Nature neuroscience *19*, 771-783.

Tatemoto, K., Hosoya, M., Habata, Y., Fujii, R., Kakegawa, T., Zou, M.X., Kawamata, Y., Fukusumi, S., Hinuma, S., Kitada, C*., et al.* (1998). Isolation and characterization of a novel endogenous peptide ligand for the human APJ receptor. Biochemical and biophysical research communications *251*, 471-476.

Uribesalgo, I., Hoffmann, D., Zhang, Y., Kavirayani, A., Lazovic, J., Berta, J., Novatchkova, M., Pai, T.P., Wimmer, R.A., Laszlo, V*., et al.* (2019). Apelin inhibition prevents resistance and metastasis associated with anti-angiogenic therapy. EMBO Mol Med *11*, e9266.

Vecht, C.J., Hovestadt, A., Verbiest, H.B., van Vliet, J.J., and van Putten, W.L. (1994). Dose-effect relationship of dexamethasone on Karnofsky performance in metastatic brain tumors: a randomized study of doses of 4, 8, and 16 mg per day. Neurology *44*, 675-680.

Verhaak, R.G., Hoadley, K.A., Purdom, E., Wang, V., Qi, Y., Wilkerson, M.D., Miller, C.R., Ding, L., Golub, T., Mesirov, J.P*., et al.* (2010). Integrated genomic analysis identifies clinically relevant subtypes of glioblastoma characterized by abnormalities in PDGFRA, IDH1, EGFR, and NF1. Cancer cell *17*, 98-110.

Walzlein, J.H., Synowitz, M., Engels, B., Markovic, D.S., Gabrusiewicz, K., Nikolaev, E., Yoshikawa, K., Kaminska, B., Kempermann, G., Uckert, W*., et al.* (2008). The antitumorigenic response of neural precursors depends on subventricular proliferation and age. Stem cells *26*, 2945-2954.

Weller, M., van den Bent, M., Preusser, M., Le Rhun, E., Tonn, J.C., Minniti, G., Bendszus, M., Balana, C., Chinot, O., Dirven, L*., et al.* (2021). EANO guidelines on the diagnosis and treatment of diffuse gliomas of adulthood. Nat Rev Clin Oncol *18*, 170-186.

Weller, M., van den Bent, M., Tonn, J.C., Stupp, R., Preusser, M., Cohen-Jonathan-Moyal, E., Henriksson, R., Le Rhun, E., Balana, C., Chinot, O*., et al.* (2017). European Association for Neuro-Oncology (EANO) guideline on the diagnosis and treatment of adult astrocytic and oligodendroglial gliomas. The Lancet Oncology *18*, e315-e329.

Wieghofer, P., Knobeloch, K.P., and Prinz, M. (2015). Genetic targeting of microglia. Glia *63*, 1-22.

Zeisel, A., Munoz-Manchado, A.B., Codeluppi, S., Lonnerberg, P., La Manno, G., Jureus, A., Marques, S., Munguba, H., He, L., Betsholtz, C*., et al.* (2015). Brain structure. Cell types in the mouse cortex and hippocampus revealed by single-cell RNA-seq. Science *347*, 1138-1142.

Zhao, J., Chen, A.X., Gartrell, R.D., Silverman, A.M., Aparicio, L., Chu, T., Bordbar, D., Shan, D., Samanamud, J., Mahajan, A*., et al.* (2019). Immune and genomic correlates of response to anti-PD-1 immunotherapy in glioblastoma. Nature medicine *25*, 462-469.

# VI. Abbildungsverzeichnis

# VII. Verzeichnis eigener Publikationen

## A. Originalarbeiten als Erstautor

| Nr | Autoren/Jahr/Titel/Zeitschrift/Band/Seitenzahlen | Einflussfaktor |
|---|---|---|
| 1 | **Kälin RE***, Cai L*, Li Y, Zhao D, Zhang H, Cheng J, Zhang W, Wu Y, Eisenhut K, Janssen P, Schmitt L, Enard W, Michels F, Flüh C, Hou M, Kirchleitner SV, Siller S, Schiemann M, Andrä I, Montanez E, Giachino C, Taylor V, Synowitz M, Tonn JC, von Baumgarten L, Schulz C, Hellmann I, Glass R. TAMEP are brain tumor parenchymal cells controlling neoplastic angiogenesis and progression. Cell Syst. 2021 Mar 17;12(3):248-262.e7. | 8.673 |
| 2 | Grathwohl SA*, **Kälin RE***, Bolmont T, Prokop S, Winkelmann G, Kaeser SA, Odenthal J, Radde R, Eldh T, Gandy S, Aguzzi A, Staufenbiel M, Mathews PM, Wolburg H, Heppner FL, Jucker M: Formation and maintenance of Alzheimer's disease beta-amyloid plaques in the absence of microglia. Nat Neurosci. 2009 Nov;12(11):1361-3. | 20.071 |
| 3 | **Kälin RE***, Banziger-Tobler* NE, Detmar M, Brändli AW: An *in vivo* chemical library screen in Xenopus tadpoles reveals novel pathways involved in angiogenesis and lymphangiogenesis. Blood. 2009 Jul 30;114(5):1110-22. | 17.794 |
| 4 | **Kälin RE**, Kretz MP, Meyer AM, Kispert A, Heppner FL, Brändli AW: Paracrine and autocrine mechanisms of apelin signaling govern embryonic and tumor angiogenesis. Dev Biol. 2007 May 15;305(2):599-614. | 2.936 |

## B. Originalarbeiten als Letztautor

| Nr | Autoren/Jahr/Titel/Zeitschrift/Band/Seitenzahlen | Einflussfaktor |
|---|---|---|
| 1 | Zhao D*, Zhang H*, Uyar R, Hossain JA, Miletic H, Tonn JC, Glass R* and **Kälin RE***. Comparing tumor cell invasion and myeloid cell composition in compatible primary and relapsing glioblastoma. Cancers (Basel). 2021 Jul 20;13(14):3636. | 6.639 |
| 2 | Volmar MNM, Cheng J, Alenezi H, Richter S, Haug A, Hassan Z, Goldberg M, Li Y, Hou M, Herold-Mende C, Maire CL, Lamszus K, Flüh C, Held-Feindt J, Gargiulo G, Topping G, Schilling F, Saur D, Schneider G, Synowitz M, Schick JA, **Kälin RE*** and Glass R*. Neuro Oncol. 2021 Apr 17:noab095. | 10.247 |
| 3 | Frisch A, Kälin S, Monk R, Radke J, Heppner FL and **Kälin RE**. Apelin Controls Angiogenesis-Dependent Glioblastoma Growth. Int J Mol Sci 2020 Jun 11;21(11):4179. | 5.923 |
| 4 | Cai L*, Kirchleitner SV*, Zhao D, Li M, Tonn JC, Glass R* and **Kälin RE***. Glioblastoma exhibits inter-individual heterogeneity of TSPO and LAT1 expression in neoplastic and parenchymal cells. Int J Mol Sci. 2020 Jan 17;21(2):612. | 5.923 |

| | | |
|---|---|---|
| 5 | Mastrella G *, Hou M*, Li M*, Stöcklein V, Zdouc N, Volmar MNM, Miletic M, Reinhard S, Herold-Mende C, Kleber S, Eisenhut K, Gargiulo G, Synowitz M, Vescovi AL, Harter PN, Penninger JM, Wagner E, Mittelbronn M, Bjerkvig R, Hambardzumyan D, Schüller U, Tonn JC, Radke J, Glass R and **Kälin RE**. APLN/APLNR-targeting improves anti-angiogenic efficiency and blunts pro-invasive side effects of VEGFA/VEGFR2-blockade in glioblastoma. Can Res. 2019 May 1;79(9):2298-2313. | 12.701 |

## C. Koautorenschaften

| Nr | Autoren/Jahr/Titel/Zeitschrift/Band/Seitenzahlen | Einflussfaktor |
|---|---|---|
| 1 | Kälin S*, Miller KR*, **Kälin RE**, Jendrach M., Witzel, C., Heppner FL: CNS myeloid cells critically regulate heat hyperalgesia J Clin Invest. 2018 Jul 2;128(7):2774-2786. | 14.808 |
| 2 | Langenfurth A, Gu S, Bautze V, Zhang C, Neumann JE, Schüller U, Stock K, Wolf SA, Maier AM, Mastrella G, Pak A, Cheng H, **Kälin RE**, Holmbeck K, Strotmann J, Kettenmann H, Glass R. Decreased demand for olfactory periglomerular cells impacts on neural precursor cell viability in the rostral migratory stream. Sci Rep. 2016 Aug 30;6:32203. | 3.998 |
| 3 | Holzgreve A, Brendel M, Gu S, Carlsen J, Mille E, Böning G, Mastrella G, Unterrainer M, Gildehaus FJ, Rominger A, Bartenstein P, **Kälin RE**, Glass R, Albert NL. Monitoring of Tumor Growth with [(18)F]-FET PET in a Mouse Model of Glioblastoma: SUV Measurements and Volumetric Approaches. Front Neurosci. 2016 Jun 14;10:260. | 3.566 |
| 4 | Dasari R, De Carvalho A, Medellin DC, Middleton KN, Hague F, Volmar MNM, Frolova LV, Rossato MV,De La Chapa JJ, Dybdal-Hargreaves NF; Pillai A, **Kälin RE**, Mathieu V, Rogelj S, Gonzales CB, Calixto JB, Evidente A, Gautier M, Munirathinam G, Glass R,Burth P, Pelly SC, van Otterlo WAL, Kiss R and Kornienko A. Wittig derivatization of sesquiterpenoid polygodial leads to cytostatic agents with activity against drug resistant cancer cells and capable of pyrrolylation of primary amines. Eur J Med Chem. 2015 Oct 20;103:226-37. | 5.572 |
| 5 | vom Berg J , Prokop S , Miller KR, Obst J, **Kälin RE** , Lopategui-Cabezas I, Wegner A, Mair F, Schipke CG, Peters O, Winter Y, Becher B, Heppner FL: Inhibition of IL-12/IL-23 signaling reduces Alzheimer's disease-like pathology and cognitive decline. Nat Med. 2012 Dec;18(12):1812-9. | 53.440 |
| 6 | Lehmann SM, Krüger C, Park B, Derkow K, Rosenberger K, Baumgart J, Trimbuch T, Eom G, Hinz, M, Kaul D, Habbel P, **Kälin R**, Franzoni E, Rybak A, Nguyen D, Veh R, Ninnemann O, Peters O, ,Nitsch R, Heppner FL, Golenbock D, Schott E, Wulczyn GF, Ploegh HL, Wulczyn G, Lehnardt S: Let7 microRNA mediates neurodegeneration via Tolllike receptor 7. Nat Neurosci. 2012 Jun;15(6):827-35. | 20.071 |

| | | |
|---|---|---|
| 7 | Gertz K, Kronenberg, G, **Kälin RE**, Baldinger T, Werner C, Balkaya, M, Eom GD, Hellmann J, Kröber J, Miller KR, Lindauer U, Laufs U, Dirnagl U, Heppner FL Endres M: Essential Role of Interleukin-6 for Post-Stroke Angiogenesis Brain 135, 1964-1980, 2012. | 13.501 |
| 8 | Vinet J, van Weering HRJ, Heinrich A, **Kälin RE**, Wegner A, Brouwer N, Heppner FL, van Rooijen N, Boddeke HWGM, Biber K: Neuroprotective function for ramified microglia in hippocampal excitotoxicity. J Neuroinflammation. 2012 Jan 31;9:27. | 5.193 |
| 9 | Herdeis L, Bernet B, Augustine A, **Kälin RE**, Brändli AW, Vasella A: Oligonucleotide analogues with integrated bases and backbone Part 27 Synthesis and association of thiomethylene-linked cytidine-derived dinucleosides and tetranucleosides Hel Chim Acta. 2011 94, 545-577, | 2.309 |
| 10 | Leslie Pedrioli DM, Karpanen T, Dabouras V, Jurisic G, van de Hoek G, Shin JW, Marino D, **Kälin RE**, Leidel S, Cinelli P, Schulte-Merker S, Brändli AW, Detmar M: miR-31 functions as a negative regulator of lymphatic vascular lineage-specific differentiation *in vitro* and vascular development *in vivo*. Mol Cell Biol. 2010 Jul;30(14):3620-34. | 4.279 |
| 11 | Steinberg F, Zhuang L, Beyeler M, **Kälin RE**, Mullis PE, Brändli AW, Trueb B: The FGFRL1 receptor is shed from cell membranes, binds fibroblast growth factors (FGFs), and antagonizes FGF signaling in Xenopus embryos J Biol Chem. 2010 Jan 15;285(3):2193-202. | 5.157 |
| 12 | Markovic DS, Vinnakota K, Chirasani S, Synowitz M, Raguet H, Stock K, Sliwa M, Lehmann S, **Kälin R**, van Rooijen N, Holmbeck K, Heppner FL, Kiwit J, Matyash V, Lehnardt S, Kaminska B, Glass R, Kettenmann H: Gliomas induce and exploit microglial MT1-MMP expression for tumor expansion. Proc Natl Acad Sci U S A. 2009 Jul 28;106(30):12530-5. | 11.205 |
| 13 | Kuehnle K, Crameri A, **Kälin RE**, Luciani P, Benvenuti S, Peri A, Ratti F, Rodolfo M, Kulic L, Heppner FL, Nitsch RM Mohajeri MH: Prosurvival effect of DHCR24/Seladin-1 in acute and chronic responses to oxidative stress. Mol Cell Biol. 2008 Jan;28(2):539-50. | 4.279 |
| 14 | Ny A, Koch M, Schneider M, Neven E, Tong RT, Maity S, Fischer C, Plaisance S, Lambrechts D, Heligon C, Terclavers S, Ciesiolka M, **Kälin R**, Man WY, Senn I, Wyns S, Lupu F, Brändli A, Vleminckx K, Collen D, Dewerchin M, Conway EM, Moons L, Jain RK, Carmeliet P: A genetic Xenopus laevis tadpole model to study lymphangiogenesis. Nat Med. 2005 Sep;11(9):998-1004. | 53.440 |

## D. Übersichtsartikel/Buchkapitel

| Nr | Autoren/Jahr/Titel/Zeitschrift/Band/Seitenzahlen | Einflussfaktor |
|---|---|---|
| 1 | **Kälin RE** and Glass R. APLN/APLNR -signaling controls key pathological parameters of glioblastoma. Cancers (Basel). 2021 Aug 2;13(15):3899. | 6.639 |
| 2 | Kälin S and **Kälin RE**. Apelin and Cancer (book chapter). In Reizes O and Berger NA (Eds.), Adipocitokines, Energy Balance and Cancer. Energy Balance and Cancer 12 137-160, Springer Int Publishing AG, Switzerland 2017. | |

# VIII. Curriculum Vitae

***Der Lebenslauf wurde aus datenschutzrechtlichen Gründen entfernt.***

# IX. Anhang

A.1 Apelin controls angiogenesis-dependent glioblastoma growth

A.2 APLN/APLNR-targeting improves anti-angiogenic efficiency and blunts pro-invasive side effects of VEGFA/VEGFR2-blockade in glioblastoma

A.3 TAMEP are brain tumor parenchymal cells controlling neoplastic angiogenesis and progression

International Journal of
*Molecular Sciences*

MDPI

*Article*

# Apelin Controls Angiogenesis-Dependent Glioblastoma Growth

**Anne Frisch [1,†], Stefanie Kälin [1,‡], Raymond Monk [1,§], Josefine Radke [1,2], Frank L. Heppner [1] and Roland E. Kälin [1,*,‖]**

1 Department of Neuropathology, Charité–Universitätsmedizin, 10117 Berlin, Germany; anne.frisch@charite.de (A.F.); kaelin.stefanie@gmail.com (S.K.); bashfull30@gmail.com (R.M.); Josefine.Radke@charite.de (J.R.); frank.heppner@charite.de (F.L.H.)
2 German Cancer Consortium (DKTK), Partner Site Charité Berlin AND Berlin Institute of Health (BIH), 10178 Berlin, Germany
* Correspondence: Roland.Kaelin@med.uni-muenchen.de
† Present Address: Department of Radiology, Charité–Universitätsmedizin, 10117 Berlin, Germany.
‡ Present Address: BSL BIOSERVICE Scientific Laboratories Munich GmbH, 82152 Planegg, Germany.
§ Present Address: Institute of Experimental Endocrinology, Charité–Universitätsmedizin, 13353 Berlin, Germany.
‖ Present Address: Neurosurgical Research, Department of Neurosurgery, University Hospital and Walter-Brendel-Centre of Experimental Medicine, Faculty of Medicine, LMU Munich, 81377 Munich, Germany.

Received: 28 May 2020; Accepted: 9 June 2020; Published: 11 June 2020


**Abstract:** Glioblastoma (GBM) present with an abundant and aberrant tumor neo-vasculature. While rapid growth of solid tumors depends on the initiation of tumor angiogenesis, GBM also progress by infiltrative growth and vascular co-option. The angiogenic factor apelin (*APLN*) and its receptor (*APLNR*) are upregulated in GBM patient samples as compared to normal brain tissue. Here, we studied the role of apelin/APLNR signaling in GBM angiogenesis and growth. By functional analysis of apelin in orthotopic GBM mouse models, we found that apelin/APLNR signaling is required for in vivo tumor angiogenesis. Knockdown of tumor cell-derived *APLN* massively reduced the tumor vasculature. Additional loss of the apelin signal in endothelial tip cells using the *APLN*-knockout (KO) mouse led to a further reduction of GBM angiogenesis. Direct infusion of the bioactive peptide apelin-13 rescued the vascular loss-of-function phenotype specifically. In addition, *APLN* depletion massively reduced angiogenesis-dependent tumor growth. Consequently, survival of GBM-bearing mice was significantly increased when *APLN* expression was missing in the brain tumor microenvironment. Thus, we suggest that targeting vascular apelin may serve as an alternative strategy for anti-angiogenesis in GBM.

**Keywords:** Apelin-13; APLN; APLNR; glioblastoma; GBM angiogenesis

## 1. Introduction

Glioblastoma (GBM) is the most frequent and most aggressive primary brain tumor [1], and, -despite intensive efforts including recent advances of anti-GBM treatment modalities, there are still only limited therapeutic options, offering patients only an average survival time of one year after diagnosis, at best [2,3]. Hallmarks of GBM biology include strong invasiveness of tumor cells and the abundance of an aberrant vasculature [4]. GBM cells infiltrate normal brain tissue and, as a result, surgical resection is always incomplete [3,5,6]. Regardless of aggressive surgery and radio and chemotherapy, GBM remain uniformly fatal in patients. Hence, alternative therapeutic approaches for treatment against GBM are urgently needed.

The finding that highly vascularized tumors are rapidly growing while tumors with low vessel density are rather dormant led to the idea that tumor angiogenesis was required for tumor progression [7]. Vascular endothelial growth factor—A (VEGFA), which was first identified as a vascular permeability factor—turned out to be a potent endothelial mitogen [8]. The treatment of xenografted mice with a specific monoclonal VEGFA antibody demonstrated that VEGFA was a strong in vivo pro-angiogenic factor and that its blockade suppressed tumor growth [9]. This led to the first successful anti-angiogenic therapy with a humanized monoclonal antibody that blocks VEGFA (bevacizumab) in colorectal cancer and resulted in FDA approval [10]. However, recent clinical studies performed in patients with GBM using bevacizumab (AVAglio, RTOG-0825) did not show an improved overall survival [11,12]. Possible explanations for treatment resistance to bevacizumab are the ability of GBM cells for vascular co-option to obtain access to blood supply [13] or the upregulation of alternative angiogenic factors [14]. In the search for such additional factors involved in tumor angiogenesis, Masiero and colleagues [15] analyzed the expression profile of more than 1000 well-vascularized primary human cancers (head and neck squamous cell carcinomas, breast cancers, and clear cell renal cell carcinomas) for genes correlating with that of several well-recognized angiogenesis signature genes. The angiogenesis core signature they identified contained a set of 40 genes, including the apelin receptor (*APLNR*; also known as APJ). The human *APLNR* gene was coincidently cloned with primers designed to obtain vasopressin receptors in 1993 and found to encode a 7 transmembrane receptor related to the angiotensin II receptor type (*AGTRL1*) [16]. By screening various tissue extracts for ligands of orphan G-protein coupled receptors (GPCR) in an extracellular acidification assay, Tatemoto et al. (1998) [17] identified the apelin isoforms apelin-36, apelin-17, apelin-13, and the pyro-glutamylated (Pyr)apelin-13 as bioactive peptides encoded by the apelin gene (*APLN*). It is now established that the different apelin isoforms are the cognate ligands for APLNR with different binding properties [18].

In our previous work, we described a proangiogenic role of apelin acting as chemoattractant during vertebrate development [19]. That apelin signaling is instrumental for cell attraction was first shown for *APLNR*-transfected cell lines [20,21] and then verified for immortalized and primary vascular endothelial cells [19,22,23], vascular smooth muscle cells [24,25], lymphatic endothelial cells [26], and one tumor cell line (lung adenocarcinoma cell line A549) [27]. The functional importance of apelin in angiogenesis and its epistatic relationship with VEGFA signaling was established in a series of loss- and gain-of-function experiments in *Xenopus* tadpoles [19,22] and further confirmed in other organisms, like zebrafish and mouse [28]. In early vessel development, apelin appears to act in a paracrine fashion to first induce intersomitic blood vessel outgrowth shaping the primitive vascular plexus [19,29,30]. Next, during vessel sprouting, *APLN*-expression gets confined to endothelial tip cells, while the receptor is also found in the stalk cells controlling vessel-guidance and -maturation [19,28,31]. *APLN* can thus be used as a tip cell marker for ongoing angiogenesis and has a role in sprouting angiogenesis in pathology [32]. While *APLNR* mutant mice are born at sub-mendelian ratios, *APLN* knockout (KO) mice are viable and fertile [33–35]. The lethality observed in *APLNR*-KO mice is due to growth retardations and cardiac malformations during embryogenesis [36].

By in situ hybridization on GBM patient specimens, we found the first indication of a role for apelin signaling in tumor development. While *APLN* RNA was undetectable and only low level of *APLNR* RNA was found in normal brain vessels, we detected a dramatic upregulation of both within GBM-associated microvascular proliferations, particularly in areas of vessel sprouting and branching as assessed by in situ hybridization [19]. Co-expression of ligand and receptor in the tumor vasculature suggested an autocrine mode of signaling, similar to the one observed during embryonic development [19]. In addition, we also found abundant *APLN* expression in the pseudo-palisading areas of GBM. In these hypoxic regions, *APLN* is co-expressed with VEGFA [19,37], suggesting a cooperative function of apelin and VEGFA in paracrine signaling from tumor to endothelial cells during GBM angiogenesis.

All these data hint towards a vascular function for apelin/APLNR signaling during GBM growth. To study the role of apelin in establishing the structure and function of the GBM vascular beds

and its implications to tumor growth, we here used established GBM mouse models. Intracerebral implantation of GBM cell lines with different *APLN* expression levels showed that tumor-derived apelin is required for the formation of the GBM neo-vasculature. Moreover, loss-of-*APLN* in the tumor microenvironment of *APLN*-KO mice showed that *APLN* expression controls patterning of the glioma vasculature. We also show, for the first time, that this sprouting angiogenesis effect is specific to *APLN* gene function as the vascular patterning phenotype was rescued by adding back the bioactive apelin-13 peptide. Furthermore, we found that the loss-of-*APLN* expression in the tumor microenvironment reduced angiogenesis-dependent tumor growth and increased the survival of GBM-bearing mice. Together, our data demonstrates that the endothelial *APLN* signal can serve as an alternative target to reduce GBM growth by specifically blocking sprouting angiogenesis.

## 2. Results

### 2.1. APLN Is Expressed at Variable Levels in GBM Cells and Upregulated in the Pathologic Neo-Vasculature

To study if tumor cell-derived *APLN* controls angiogenesis-dependent GBM growth, we first tested widely used GBM cell lines for *APLN* expression, revealing differing levels of expression. Using *APLN* expression levels in mouse wildtype (WT) brains as a comparison, we characterized the human cell-line U87MG as having high levels of *APLN* expression and the human U251 (formerly known as U373MG) cell line expression as being lower, whilst in the murine GL261 glioma cell-line *APLN* expression was not detectable (n.d.; Figure 1A).

In the next step, we orthotopically implanted human, as well as murine, GBM cells into immunodeficient or immunocompetent mice, respectively, to assess *APLN* expression in in situ pathology. In a previous study, we had found that *APLN* was not only expressed in GBM cells but was also upregulated in the vascular proliferates of the disease [19]. Thus, we also tested our experimental GBM models for vascular *APLN* expression and found that *APLN* expression was upregulated in newly forming tumor vessels (Figure 1B; arrowheads) of the xenografts. Interestingly, the vascular *APLN* RNA signal was highest in the tumor regions where human *VEGFA* RNA was also detected. *VEGFA* expression is a marker for hypoxic tumor areas in pseudopalisading necrosis in GBM. In addition, in murine GL261 glioma, *APLN* expression became localized to newly forming tumor vessels but remained absent from GL261 tumor cells (Figure 1B). To also address the role of GBM cell-derived *APLN*-levels, we selected the high *APLN*-expressing U87MG cell line, in addition, and lentivirally transduced it with shRNA against *APLN* RNA to create tumor cells with stable reduction of *APLN* RNA expression by 90% ($U87^{AKD}$) compared to the non-silencing control (NSC) shRNA-transduced cells ($U87^{NSC}$) or to untransduced parental U87MG cells (Figure 1C). Viability, as well as in vitro proliferation, of the manipulated cells was tested and turned out to be unchanged compared to their parental controls (Figure 1D,E). In contrast, cells transduced with the shRNA against EG5 kinesin (encoded by the Kinesin Family Member 11 gene *KIF11* involved in nuclear division and cell growth [38]) caused reduced viability and proliferation rates (Figure 1D,E).

### 2.2. APLN Expression Is Required for the Formation of the GBM Neo-Vasculature

In agreement with a range of previous reports [39,40], we observed that orthotopic implantation of GL261 cells generated compact glioma mass 21 days post-implantation (dpi) with an abundant but aberrant tumor vasculature (Figure 2A, upper panel). To investigate the impact of *APLN* expression derived from the tumor microenvironment, namely *APLN* expressed on endothelial tip cells [19,28,31,32] during sprouting angiogenesis (Figure 1B), we implanted GL261 cells into $APLN^{KO}$ mice. We found that the tumor vasculature was significantly attenuated compared to $APLN^{WT}$ control mice (Figure 2A,B). Specifically, we found by stereological assessment of the tumor tissues that the vessel length density (VLD), as a read-out for the extent of tumor vascularization independent of tumor-size [41–43], was 856 mm/mm$^3$ in controls, while this number significantly decreased to 653 mm/mm$^3$ in $APLN^{KO}$ glioma (Figure 2B). Note that in situ hybridization for mouse *APLN* RNA shows that *APLN* is absent

in tumor cells, as well as in the GBM microenvironment, of $APLN^{KO}$ mice, while *APLN* expression in $APLN^{WT}$ mice is specifically upregulated in endothelia of the tumor neo-vasculature (Figure 2A; arrows). Interestingly, the VLD determined in GL261 implants is smaller than the values observed for a healthy tumor-free brain. In the caudate putamen, which is the brain region targeted by the tumor cell implantation, we measured a VLD of 1269 mm/mm$^3$ for $APLN^{WT}$ mice and 1359 mm/mm$^3$ for $APLN^{KO}$ mice, without the difference being significant (Figure 2C). Similar values for VLD were also previously reported for the tumor-free hippocampus (1100 mm/mm$^3$) of adult mice [44]. This finding of reduced vessel density in GBM as compared to healthy brain can be explained by the neoplastic growth and the higher cell density inside tumors. While the VLD of tumor-free brain is unchanged in $APLN^{KO}$ mice, the VLD of the glioma is reduced in $APLN^{KO}$ mice compared to $APLN^{WT}$ controls. In addition, loss-of host-derived *APLN* also resulted in reduced vascular complexity, serving as an indicator of the extent of angiogenic sprouting [45]. We found that the average number of vessel branch-points (ABP), which measured 1.25 in $APLN^{WT}$ glioma, was reduced to 1 in tumor vessels of $APLN^{KO}$ mice. In addition, the ABP values in the tumor were thus lower than the values observed in tumor-free striatum (Figure 2C; ABP = 2.5 in $APLN^{WT}$ and 2.6 in $APLN^{KO}$). This means that the vascular complexity in $APLN^{KO}$ GBM is low to nearly linear, and this indicates that no more angiogenic sprouting took place during tumor growth.

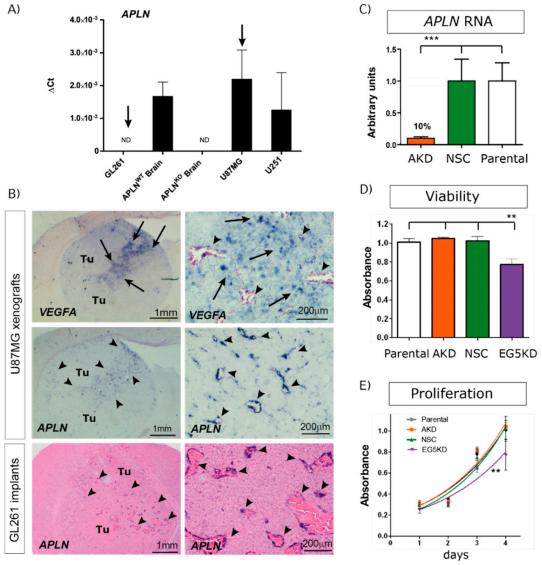


**Figure 1.** Angiogenic factor apelin (*APLN*) expression in glioblastoma (GBM) cells and the tumor neo-vasculature. (**A**) Expression analysis of *APLN* RNA was performed by qPCR on the human cells U87MG and U251, the murine GL261 cells and on $APLN^{WT}$ or $APLN^{KO}$ mouse brain tissue. *APLN* RNA expression was not detectable (n.d.) in GL261 cells but high in U87MG cells. (**B**) In situ hybridization against mouse *APLN* showed no expression in implanted mouse GL261 tumor cells but an upregulation of *APLN* in the tumor vessels of GL261 or U87MG gliomas (arrowheads). The right panel is the magnifications within the tumor that is depicted in the overview panel on the left. Note that vascular *APLN* RNA expression is highest in hypoxic regions marked by human vascular endothelial growth factor (*VEGFA*) RNA expression (arrows) in the U87MG xenografts. (**C**) Lentiviral transduction of U87MG parental cells caused shRNAmir-mediated stable *APLN* knock-down (AKD) by 90% (as analyzed by qPCR) compared to the non-silencing shRNA control (NSC) transduced cells. (**D**) Cell viability, as well as in vitro proliferation (**E**), was unchanged in $U87^{AKD}$ cells compared to $U87^{NSC}$ control or untransduced U87MG cells. In contrast, U87 cells transduced with the shRNA against the kinesin EG5 significantly reduced viability and proliferation of $U87^{E5KD}$ cells compared to $U87^{NSC}$ control. Data are obtained from more than 3 independent experiments each and reported as mean +/-SEM; statistical significance (one-way ANOVA plus Bonferroni's post hoc test) is indicated ** $p < 0.005$, *** $p < 0.0005$. WT = wildtype; KO = knockout.

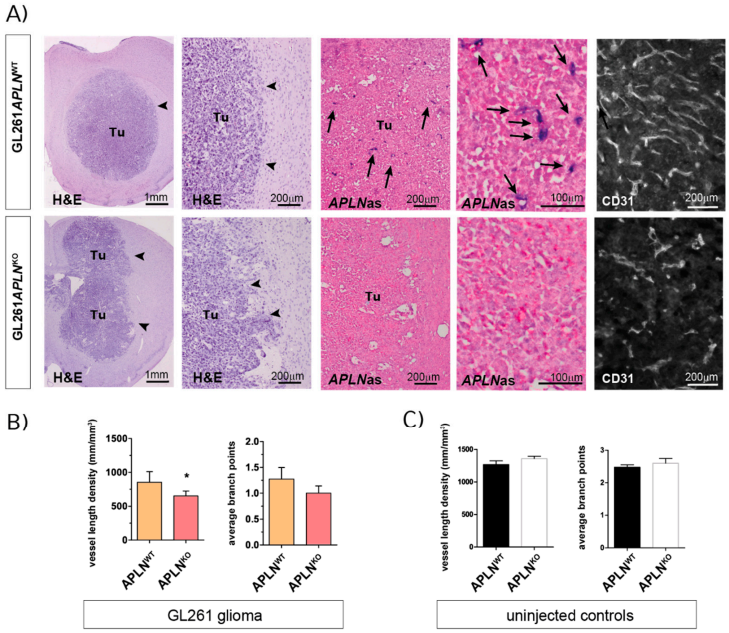


**Figure 2.** Endothelial *APLN* expression controls formation of a complex GBM vasculature. Orthotopic GL261 implants in *APLN*$^{WT}$ or *APLN*$^{KO}$ mice 21 days post-implantation (dpi). (**A**) The panels on the left indicate the tumor (tumor boarder highlighted by arrowheads) in the right brain hemisphere in overview and close up view on Hematoxylin & Eosin (H&E) sections. The in situ hybridization panels in the middle show the loss-of vascular *APLN* expression (arrows) in the tumor in overview and close up view when comparing *APLN*$^{WT}$ to *APLN*$^{KO}$ mice. The CD31-immunostaining shown in the panel on the right illustrates the reduced vessel density in *APLN*$^{KO}$ mice. (**B**) Vessel length density (VLD) was assessed on CD31 immunofluorescent brain slides and demonstrated a significant decrease in *APLN*$^{KO}$ mice. In addition, vascular complexity measured by the average branch points (ABP) was reduced in *APLN*$^{KO}$ as compared to *APLN*$^{WT}$. (**C**) In the healthy brain, VLD and ABP do not differ in *APLN*$^{KO}$ compared to *APLN*$^{WT}$ mice. Data of $n = 9$ *APLN*$^{WT}$ vs. 6 *APLN*$^{KO}$ mice are reported as mean +/-SEM; statistical significance (students test) is indicated * $p < 0.05$.

Together, these results show that autocrine signaling of endothelial apelin to *APLNR*-expressing vessels is required for sprouting angiogenesis to take place and shape the complex tumor neo-vasculature.

### 2.3. Paracrine and Autocrine APLN Signaling Controls GBM Angiogenesis

Next, we wanted to study the contribution of GBM cell-derived *APLN* to tumor angiogenesis and thus we compared vascular patterns generated by U87MG cells with a stable knock-down for *APLN* (U87$^{AKD}$) to non-silencing control cells (U87$^{NSC}$; Figure 1C–E). The modulation of human GBM-derived *APLN* is pathologically meaningful in mouse models as the amino acid sequence of the bioactive peptide apelin-13 of human or mouse origin is 100% identical [19]. Four weeks after tumor-induction with U87$^{NSC}$ cells in immune-deficient WT mice (U87$^{NSC}$*APLN*$^{WT}$), we observed an extremely dense tumor vasculature (Figure 3A) with a VLD of 3937 mm/mm$^3$ (Figure 3B), while the VLD of U87$^{AKD}$-induced GBM in WT mice (U87$^{AKD}$*APLN*$^{WT}$) was 1519 mm/mm$^3$ (62% reduced as compared to U87$^{NSC}$*APLN*$^{WT}$). Injection of U87$^{NSC}$ into *APLN*$^{KO}$ mice (U87$^{NSC}$*APLN*$^{KO}$) resulted in a VLD of 2601 mm/mm$^3$, whereas combined ablation of *APLN* expression in U87MG cells and in the host (implantation of U87$^{AKD}$ cells into immune-deficient *APLN*$^{KO}$ mice; U87$^{AKD}$*APLN*$^{KO}$) largely blocked tumor angiogenesis and resulted in a VLD of 766 mm/mm$^3$, which is lower than in tumor-free brain-tissue (Figures 2C and 3B). While vessel branching reflects the picture observed by VLD assessment, the total vessel length (that is the VLD multiplied by the individual tumor volume) was highly reduced in all three xenografts with reduction of *APLN* expression (Figure 3B).

At the same time, the change in *APLN*-levels did not affect the extent of pericyte cell coverage as assessed by CD31/Desmin double-immunofluorescence (Figure S1A). BrdU in vivo labeling of the tumor vasculature further demonstrated that endothelial cells are still able to proliferate upon *APLN* level reduction (Figure S1B).

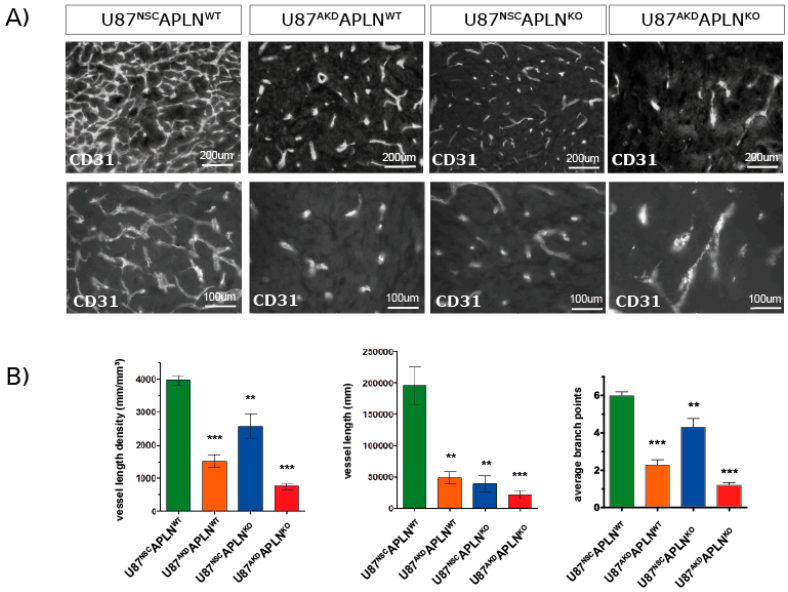


**Figure 3.** GBM-and endothelial cell-derived *APLN* are both controlling sprouting angiogenesis. (**A**) U87MG was implanted into immunodeficient mice and grown to big xenografts within 28 dpi. Fluorescent immunostaining for CD31 was performed and is depicted in an overview and a close up view for every xenograft. (**B**) The microvasculature in the green fluorescent protein (GFP)-positive tumor area was analyzed by stereomorphology. In comparison to U87$^{NSC}$*APLN*$^{WT}$ controls ($n$ = 8), VLD in U87$^{AKD}$*APLN*$^{WT}$ xenografts ($n$ = 13) was reduced by 62% and vessel length by 75%. Additional loss-of-*APLN* expression in the tumor neo-vasculature of the *APLN*$^{KO}$ mouse (U87$^{AKD}$*APLN*$^{KO}$, $n$ = 10) lead to further reduction of the tumor vasculature. VLD was also reduced when only the tumor cells express *APLN* (U87$^{NSC}$*APLN*$^{KO}$, $n$ = 9) but was the highest of all manipulated xenografts. While vascular complexity measured by vascular branch points (ABP values are 6, 2.3; 4.3; and 1.2, respectively) reflects the results seen by VLD, the total vessel length was highly reduced in all three xenografts with reduction of *APLN* expression. Data are reported as mean +/−SEM; statistical significance (one-way ANOVA plus Bonferroni´s post hoc test) is indicated ** $p < 0.005$, *** $p < 0.0005$.

These data showed, on one hand, that the high expression of *APLN* in the U87MG (and U87$^{NSC}$ control) cells induces a very dense and complex tumor vasculature as compared to U87$^{AKD}$ cells depleted in *APLN*-expression, as well as the APLN-non expressing GL261 cells. On the other hand, the loss-of-*APLN* in both GBM cell models in the tumor microenvironment decreased vascular sprouting to a level even lower than the vessel density observed throughout the healthy brain.

Together, these experiments indicate that paracrine (from the tumor) and autocrine (from the host microenvironment) *APLN* release has profound effects on the extent of GBM angiogenesis and thus the vascular pattern generated.

### *2.4. Apelin-13 Specifically Controls Vessel Density in the GBM Neo-Vasculature*

In the following experiment, we addressed the question if *APLN*-deficiency in our mouse model (i.e., in the *APLN*$^{KO}$ mice) would lead to, e.g., developmentally regulated alterations in the signal transduction pathways controlling angiogenesis or if *APLN*-responsiveness by *APLN*R is maintained in the absence of the ligand. Therefore, we infused the bioactive apelin-13 peptide into the U87$^{AKD}$*APLN*$^{KO}$ xenograft model and were indeed able to obtain a partial rescue of the tumor

neo-vasculature increasing VLD from 766 mm/mm$^3$ (infusion of artificial cerebrospinal fluid; aCSF control) to 2573 mm/mm$^3$ (Figure 4). In contrast, the C-terminally mutated peptide apelin-F13A (which had been used as an antagonist for physiological functions on *APLNR* before [46]) was not able to rescue tumor angiogenesis. Instead, when apelin-F13A was infused into U87$^{NSC}$APLN$^{WT}$ GBMs expressing endogenous APLN levels, it significantly reduced VLD working as a competitive antagonist on APLNR (Figure S1C). Together, this part of our study supports the notion that *APLN*$^{KO}$ mice are devoid of endogenous *APLN* but can respond to exogenous or tumor-derived *APLN*. This is a prerequisite to explain the gradual anti-angiogenic responses to *APLN*-ablation in our GBM models. Here, we observed that *APLN* -deficiency in the GBM-cells or in the host generates a tumor mass with a reduced vascularization, as compared to tumor with unmodulated *APLN* levels. Ablation of *APLN* in both the GBM cells and in the tumor-bearing animals resulted in a striking cooperative anti-angiogenic effect. The partial rescue of the vascular GBM phenotype by addition of apelin-13 peptide to *APLN*-depleted xenografts shows that these effects are specifically mediated by apelin-signaling.

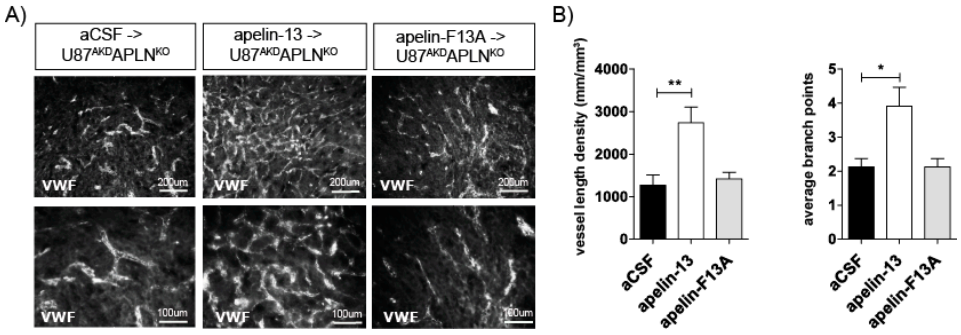


**Figure 4.** Apelin peptide rescues the vascular loss-of-function phenotype. (**A**) Intracerebral infusion of 30 µg of apelin-13 peptide ($n$ = 9) increased glioma angiogenesis in U87$^{AKD}$*APLN*$^{KO}$ xenografts compared to infusion of artificial cerebrospinal fluid (aCSF, $n$ = 8) or apelin-F13A ($n$ = 6) antagonist as shown by von Willebrand factor (VWF) staining. (**B**) Quantification on a Stereoinvestigator resulted in a VLD of 1269 mm/mm$^3$ in U87$^{AKD}$*APLN*$^{KO}$ xenografts infused with aCSF only; 2573 mm/mm$^3$ with the *APLN* receptor (*APLNR*) agonist apelin-13 peptide or 1419 mm/mm$^3$ with the *APLNR* antagonist apelin-F13A. ABP obtained were 2.2; 3.9 and 2.2, respectively. Data are reported as mean +/−SEM; statistical significance (one-way ANOVA plus Bonferroni´s post hoc test) is indicated. * $p < 0.05$, ** $p < 0.005$.

### 2.5. Loss of APLN Reduces Angiogenesis-Dependent Tumor Growth

To compare the effect of *APLN* on tumor growth, we performed a classical test for in vivo anti-angiogenic pharmacological function [9,47]. By generating subcutaneous xenografts, we found that *APLN* knockdown in tumor cells, as well as the loss-of-*APLN*, in the tumor microenvironment significantly reduced VLD by 36% (U87$^{AKD}$*APLN*$^{WT}$) and 48% (in U87$^{NSC}$*APLN*$^{KO}$), respectively, as compared to U87$^{NSC}$*APLN*$^{WT}$ controls (Figure 5). The depletion of both, tumor and host *APLN* in U87$^{AKD}$*APLN*$^{KO}$ xenografts further reduced VLD by 61% as compared to U87$^{NSC}$*APLN*$^{WT}$ control. Interestingly, the tumor volume was reduced by 50% when tumor-cell derived *APLN* was depleted compared to *APLN*-expressing control cells. Strikingly, if *APLN* was missing in the tumor microenvironment, the tumor volume decreased to less than 15% compared to WT controls. We also assessed if the tumor cells were growing equally well in all mice. We found that tumor take was similar for *APLN*-knockdown (87% for U87$^{AKD}$*APLN*$^{WT}$) compared to U87$^{NSC}$ control cells (90% for U87$^{NSC}$*APLN*$^{WT}$) when implanted in WT mice and only slightly reduced when *APLN* was missing in the tumor microenvironment in *APLN*$^{KO}$ but still present in the tumor cells (72% for U87$^{NSC}$*APLN*$^{KO}$ xenografts). However, when *APLN* expression was fully depleted as in U87$^{AKD}$*APLN*$^{KO}$ xenografts, only 50% of tumor cell implantation led to successful tumor growth.

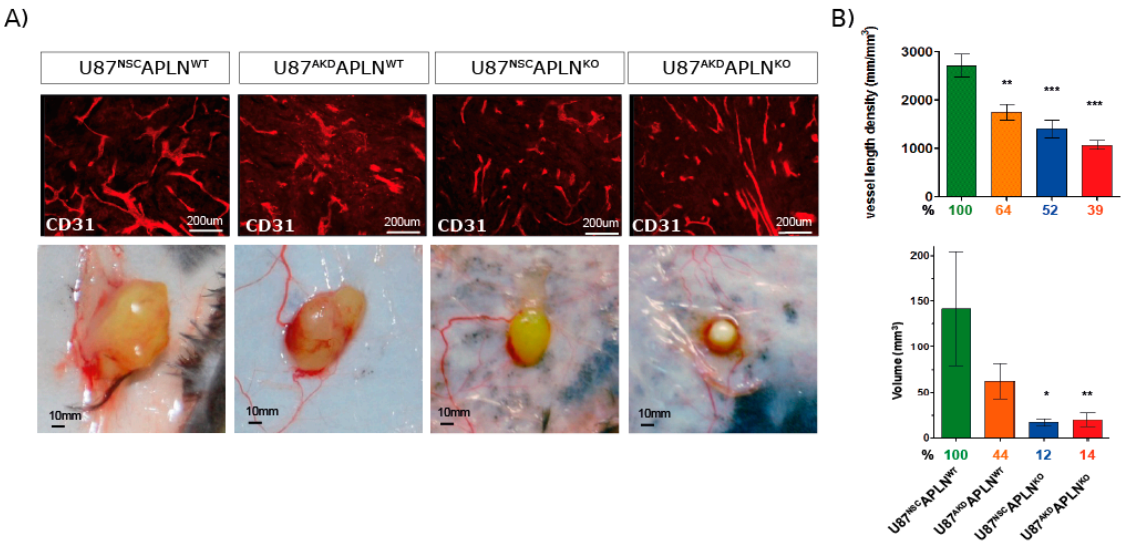


**Figure 5.** Apelin is required for compact tumor growth. Mice were inoculated subcutaneously with U87 cells and grown for 28 dpi. (**A**) Tumor volumes were measured, and vessel density was quantified on CD31-immunostained sections. Representative pictures of subcutaneous tumors are shown. (**B**) VLD and tumor volume was significantly attenuated upon reduction of *APLN* expression as compared to U87$^{NSC}$*APLN*$^{WT}$ controls (percentages compared to the control group are indicated). Tumor volumes were reduced to 50% in *APLN* knockdown U87$^{AKD}$*APLN*$^{WT}$ xenografts. Further reduction to less than 15% was observed in *APLN*$^{KO}$ mice. Number of cell implantations for U87$^{NSC}$*APLN*$^{WT}$, U87$^{AKD}$*APLN*$^{WT}$, U87$^{NSC}$*APLN*$^{KO}$, U87$^{AKD}$*APLN*$^{KO}$ were $n$ = 38, 31, 18, 24, while tumor take was 87%, 90% 72%, 50%, respectively. For VLD analysis $n$ = 7, 6, 7, 6 of the respective xenografts were analyzed. Data are reported as mean +/−SEM; statistical significance (one-way ANOVA plus Bonferroni's post hoc test) is indicated * $p < 0.05$, ** $p < 0.005$, *** $p < 0.0005$.

This experiment demonstrated that apelin is important for tumor angiogenesis and that compact subcutaneous tumors depend on the apelin-induced neo-vasculature for their growth.

### *2.6. Loss-of-APLN Expression in the Tumor Microenvironment Increases Survival of Glioma-Bearing Mice*

Finally, to assess the impact of apelin-controlled tumor angiogenesis on survival, we implanted the human GBM cells into *APLN*$^{WT}$ or *APLN*$^{KO}$ mice orthotopically. To follow in vivo tumor growth over time, we performed longitudinal magnetic resonance imaging (MRI) and found that all four groups of xenografts expanded exponentially however at a lower rate in *APLN*$^{KO}$ mice (Figure 6A). At 28 dpi, the U87$^{NSC}$*APLN*$^{KO}$ glioma showed a significantly smaller tumor volume of 31% compared to U87$^{NSC}$*APLN*$^{WT}$ tumors (defined as 100%). These results are pathologically relevant as we could confirm them in the survival experiment in which the *APLN*$^{KO}$ mice bearing U87$^{NSC}$*APLN*$^{KO}$ xenografts survived longest (Figure 6B). Survival of this group increased by 42.3% compared to the U87$^{NSC}$*APLN*$^{WT}$ control group. Surprisingly, *APLN*$^{WT}$ mice receiving the apelin-deficient xenografts (U87$^{AKD}$*APLN*$^{WT}$) survived by 14.7%, significantly shorter than controls (U87$^{NSC}$*APLN*$^{WT}$). Interestingly, when *APLN* levels were decreased stepwise in the tumor microenvironment and the tumor cells, the cell behavior of the GBM cells changed towards increased invasiveness (Figure S2).

In summary, we found that the absence of *APLN* expression from the tumor microenvironment showed a beneficial effect on the survival of GBM-bearing mice.

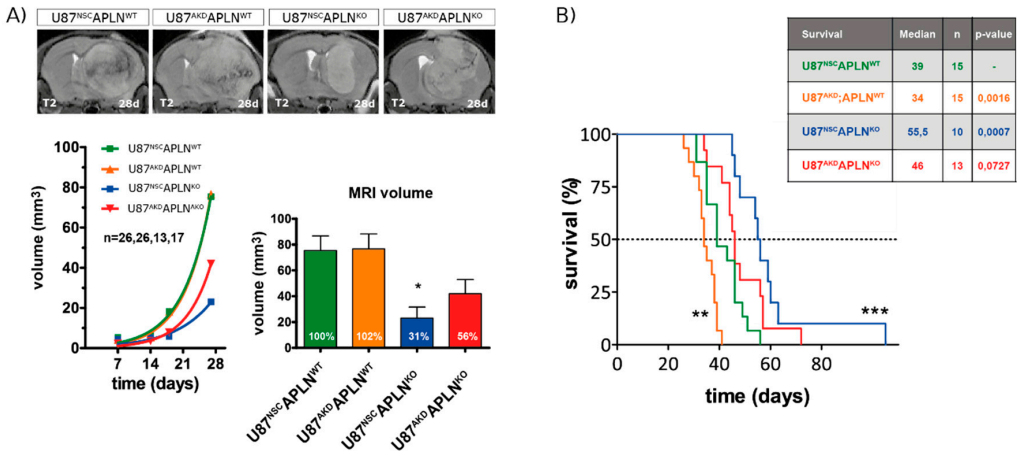


**Figure 6.** Loss-of-*APLN* in the tumor microenvironment increases survival of GBM mice. Human U87 cells modulated for *APLN* levels were orthotopically implanted into $APLN^{WT}$ or $APLN^{KO}$ mice. (**A**) T2-weighted magnetic resonance imaging (MRI) was performed weekly and MRI volumes were measured producing an in vivo growth curve for every xenograft. After 28 days, $U87^{NSC}$ or $U87^{AKD}$ cells in $APLN^{KO}$ mice showed reduced tumor volume by 69% and 44%, respectively, compared to $U87^{NSC}APLN^{WT}$ controls. Number of mice per group are indicated. Data are reported as mean +/−SEM; statistical significance (one-way ANOVA plus Bonferroni's post hoc test) is indicated * $p < 0.05$. (**B**) A mouse survival experiment with orthotopically implanted tumor cells was performed and mice sacrificed at humane endpoints. Median survival differed significantly in $U87^{AKD}APLN^{WT}$ (shorter survival) and $U87^{NSC}APLN^{KO}$ (longer survival) mice compared to $U87^{NSC}APLN^{WT}$ control mice. $U87^{AKD}$ xenografts in $APLN^{KO}$ mice showed a trend to longer survival. Number of mice per group are indicated. Survival data are shown as Kaplan-Meier Curves and significant differences between the experimental groups and the $U87^{NSC}APLN^{WT}$ control group assessed by long-rank (Mantel-Cox) test is given in the table and is indicated in the graph by * $p < 0.05$, ** $p < 0.01$, *** $p < 0.001$.

## 3. Discussion

In this study, we show, for the first time, that apelin peptide specifically and directly controls in vivo GBM angiogenesis. Moreover, we demonstrate that compact GBM growth depends on apelin-directed angiogenesis. Interestingly, the absence of apelin upregulation in the tumor vasculature of $APLN^{KO}$ mice led to smaller tumor volume and a significant extension of the survival time for GBM-bearing mice. The results of our study fit with previous in vivo observations made, where ectopic apelin overexpression enhanced angiogenesis and tumor cell proliferation in subcutaneous tumor models [26,48,49]. Moreover, recent results obtained in a mouse model of breast cancer showed that loss-of-*APLN* markedly reduced tumor angiogenesis leading to impaired tumor growth and, consequently, improved survival of these animals [50,51].

In line with these findings, we found in our GBM mouse model that the absence of *APLN* expression from the tumor vasculature showed a beneficial effect on the survival of GBM-bearing mice; however, the reduction of *APLN* expression from the tumor cell had an ambiguous effect on in vivo GBM volume. Specifically, we found that tumor-derived, as well as ectopically infused, apelin-13 could rescue partially the vascular phenotype. However, the tumor volume did not increase in these models (Figure S2D). Thus, vascular *APLN* expression seems to be essential for the formation of a mature tumor neo-vasculature that supports GBM growth. One explanation for this finding might be that the apelin-peptide is present in many different isoforms that could confer additional biological effects [17,52].

Another possibility could be that certain effects might be mediated by the second APLNR ligand APELA that was recently identified to be expressed in GBM [53]. *APELA* expression was associated with poor patient survival and correlated with glioma grade. APELA had been identified as an early APLNR ligand during embryogenesis being essential for early cardiovascular development and

controlling cellular movements through APLNR [54,55]. In GBM, *APELA* expression was detected in stem cell niches and may thus drive tumorigenesis by supporting GSC growth [53]. A role in GBM angiogenesis has not been described yet.

Previously, ectopic expression of *APLN* in subcutaneous tumors was described to stabilize tumor vessels and support vascular maturation [56]. Moreover, overexpression of *APLN* reduced the leakiness of vessels in models of ischemia [35]. Our finding that the in vivo volume assessed by MRI was smallest when *APLN* was expressed by the tumor cells, but not by the vessels, might be explained by improved tightness of the neo-vasculature and, consequently, improved function and reduced formation of brain edema. In contrast, the loss-of-*APLN* expression in the tumor cells and the tumor vessels may lead to less functional vessels that finally induce the tumor cells to change their growth behavior. Indications for such a change in tumor cell behavior we recently found in a study of highly invasive glioblastoma stem-like cells [57]. Using these infiltrative GBM mouse models, we found increased in vivo, as well as in vitro, invasion, when the tumor cells lost autocrine apelin signaling [57]. Interestingly, U87$^{AKD}$ cells with low apelin expression also showed increased invasion in vitro as compared to U87$^{NSC}$ cells [57]. Thus, we re-inspected the U87MG xenografts (Figure S2A–C) and found that single invasive cells were detectable detaching from the compact GBM mass when *APLN* expression was knocked down in tumor cells (U87$^{AKD}$). Hence, the notoriously low invasiveness that is generally observed with the U87MG cell line (Figure 1B) seemed to be increased upon loss-of tumor-derived apelin/APLNR signaling. We also observed in our second immunocompetent GBM model, the *APLN*-non-expressing GL261 cells, that GBMs growing in *APLN*$^{KO}$ mice exhibited a drastic increase in glioma cell-invasion (Figure 2A; see arrowheads in Gl261 *APLN*$^{KO}$ samples) as compared to controls. While tumor volume slightly decreased, the invasive score significantly increased from 1.2 to 2.8 (Figure S2E). Moreover, by confocal microscopy, we observed that the GBM cells in the invasive U87$^{AKD}$*APLN*$^{KO}$ GBMs adhere to remaining tumor vessels instead of being equally distributed amongst the highly dense vascular network in the U87$^{AKD}$*APLN*$^{KO}$ control GBMs. And, finally, we found in a qPCR screen for angiogenesis and invasion-related genes that loss-of-apelin directed angiogenesis led to a change in their expression Figure S2F). Marker gene expression levels for angiogenesis like *KDR*, *VEGFA*, *FGF2*, *HIF1a*, and *APLN* itself were decreased. Instead *Timp1*, the inhibitor of the matrix metalloproteinase 2 *MMP2*, was downregulated in U87$^{AKD}$*APLN*$^{KO}$ GBMs compared to the wildtype situation, and *MMP2* itself, a proteinase degrading the extracellular matrix to support tumor cell invasion, was upregulated. Taken together, it seems that *APLN*-deficient GBM cells can change their cellular behavior to adhere to the remaining tumor vessels supporting tumor growth by increased invasiveness into the tumor-free brain. Such a shift towards a more invasive behavior of the tumor might be a reason for GBM recurrence after VEGFA-centered anti-angiogenic therapy, in addition to utilizing alternative pro-angiogenic factors [14], as previously observed in glioma models after blockage of angiogenesis by inhibition of VEGFA signaling [58–60]. We also showed that anti-VEGF therapy resulted in decreased *APLN* expression in the glioblastoma-stem-like model, resulting in increased tumor cell invasiveness [57]. To avoid this pro-invasive side effect, we used an alternative approach to target apelin/APLNR signaling by infusion of APLNR antagonists [57]. We, and others, found that the use of such competitive antagonistic peptides, like apelin-F13A or MM54, indeed led to reduced vascularization (Figure S1C), attenuated tumor progression, and increased survival in GBM mouse models, as well as models of breast cancer [51,57,61]. In the breast cancer model, tumor cell invasion was also changed and led to reduced metastatic growth [51]. What hampers the clinical application of such a peptidic agent is their usually low penetration into the target tissue.

Moreover, clinical trials of GBM therapies have highlighted the need to identify predictive markers for clinical outcomes of new therapeutic strategies [2,62]. *APLN* expression levels inversely correlate with overall survival in breast, colorectal, and lung cancer by directly correlating with increased angiogenesis in these tumors [48,51,63,64]. Furthermore, *APLNR* is a marker of increased angiogenesis in many cancer types [15]. However, in GBM, we found that the ratio between *APLN* and *APLNR* expression is an important indicator of therapy success, as low *APLN* and high *APLNR*

expression correlated with increased GBM cell invasiveness [57]. Interestingly, targeting vascular APLNR by conditional ablation of APLNR-positive tumor vessels led to a significant reduction of tumor growth [65].

Thus, an overall depletion of apelin in GBM might not be the therapy of choice. Instead, together with our here-presented results, we propose that a more targeted-strategy to specifically deplete vascular apelin (e.g., using an apelin-specific antibody delivered intravenously) can open a new treatment avenue. This strategy would specifically block sprouting angiogenesis by not targeting the established brain vasculature and may lead to additional normalization of the tumor vasculature [50] also in GBM. In addition to the anti-angiogenic effect such an approach would circumvent the increased GBM cell invasion and carry the potential to reduce tumor hypoxia and edema formation, as well [66].

In summary, we found that apelin expression correlated with enhanced vascularization in GBM. Reduction of apelin expression in tumor cells attenuated tumor angiogenesis and ectopic infusion of apelin-13 peptide specifically reversed this vascular GBM phenotype. Moreover, loss-of-*APLN* in the mouse brain further reduced GBM vessel density below normal levels that are observed in the striatum of a healthy mouse brain, underlining the switch to an avascular tumor growth. By this blockade of *APLN*-dependent tumor angiogenesis, tumor growth was reduced and survival of GBM-bearing mice was, in turn, increased. Thus, we believe that targeting vascular apelin/APLNR signaling in the GBM microenvironment specifically offers a promising new opportunity to overcome resistance to anti-angiogenic therapy, as observed by VEGFA blockade, in GBM.

## 4. Materials and Methods

### 4.1. Cell Culture

U87MG and U373 cells were obtained from the American Type Culture Collection (ATCC), GL261 cells were obtained from the National Cancer Institute, NCI-Frederick (Tumor Cell Repository) and all cells were cultured under adherent conditions in DMEM containing 1× MEM non-essential amino acids, 5% penicillin-streptomycin and 10% FBS (all Thermo Fisher Scientific, Waltham, MA, USA). All cell lines were maintained at 37 °C in a humidified atmosphere of 95% $O_2$ and 5% $CO_2$.

### 4.2. Cell Transduction

For gene silencing of U87MG cells, lentiviral shRNAmir constructs for *APLN* (AKD; cat. RHS4430: V3LHS_401190), *EG5* positive control (EG5KD; cat. RHS4480), or non-silencing control (NSC; cat. RHS4346) were produced in HEK293T cells using the TransLenti Viral GIPZ Packaging System (cat. TPLP4614, all, Dharmacon GE Life Sciences, Lafayette, CO, USA) according to the manufacturer´s instructions. Virus particle-containing supernatant was harvested two days after transfection, filtered with a 0.22 µm filter to avoid cellular contamination and stored at −80 °C. U87MG cells were detached with Trypsin/EDTA (Merck Millipore, Burlington, MA, USA). Eight by ten [4] cells were incubated with 500 µL of virus particles with an multiplicity of infection of 0.6–0.7 for six hours in a 24-well plate; then, 1 mL of medium was added, and cells were left overnight at 37 °C. The day after, cells were centrifuged and resuspended in fresh medium. After cell recovery, selection with puromycin (Sigma Aldrich, St.Louis, MO, USA) was performed for up to three weeks. Concentration of antibiotics had been previously determined by a kill curve. More than 99% efficiency of transduction/selection was confirmed by FACS and immunofluorescence.

### 4.3. Animals

All experiments were performed in compliance with the National Guidelines for Animal Protection, Germany, with approval of the local animal care committee of the "Landesamt für Gesundheit und Soziales" (LaGeSO) in Berlin, and every experiment was conducted after the guidelines of the UK Co-ordinating Committee on Cancer Research [67]. $APLN^{KO}$ mice were obtained from J.P. (Vienna, Austria) [34] and crossed to $Rag2^{KO}$ mice (B6.129S6-$Rag2^{tm1Fwa}$) [68] kindly provided by Prof. G.

Willimsky/Charité–Univeritätsmedizin Berlin previously purchased from Taconic (Rensselaer, NY, USA) (all on C57Bl/6J background). All mice were kept in a 12 h light/dark cycle with ad libitum access to food and water. Mice were sacrificed at defined presymptomatic time points or at humane end-point for the survival experiment.

### 4.4. Tumor Implantation

Mice were anesthetized with 7 µL/g of body weight of a mixture of Xylazine (Rompun 2%; Bayer Health Care, Leverkusen, Germany) and Ketamin (Ketavet; Zoetis, Berlin, Germany) in 0.9% NaCl, immobilized on a stereotactic frame (David Kopf Instruments, Tujunga, CA, USA) in flat-skull position and kept warm. A midline incision was made with a scalpel. One by ten [5] cells/µL in medium without supplements were implanted by stereotactic injection 1 mm anterior and 1.5 mm right to the bregma with a 22-gauge Hamilton syringe (Hamilton, Bonaduz, Switzerland) after drilling a whole into the skull with a 23G needle. At a depth of 4 mm, cells were slowly injected within 2 min and, after a settling period of another minute, the needle was removed in 1 mm step/minute. The incision was sutured and patched with Opsite spray dressing (Smith&Nephew, London, UK).

### 4.5. Intracerebral Drug Application

One day before implantation, micro-osmotic pumps were filled with 30 µg pyr-apelin-13 or apelin-F13A for 14 days (micro-osmotic pumps cat. 1002; Alzet; Charles River) in artificial cerebrospinal fluid (aCSF; as described by Alzet) or aCSF alone to be primed overnight in aCSF at 37 °C. Pump implantation was performed under anesthesia using the brain infusion kit 3 (Alzet) inserting the needle into the previously drilled hole after initial orthotopic tumor establishment as observed by magnetic resonance imaging. At the end of pump performance, animals were sacrificed.

### 4.6. Magnetic Resonance Imaging

MRI was performed using a 7 Tesla rodent scanner (Pharmascan 70/16AS, Bruker BioSpin Bruker, Billerica, MA, USA) with a 16 cm horizontal bore magnet and a 9 cm (inner diameter) shielded gradient with a H-resonance-frequency of 300 MHz and a maximum gradient strength of 300 mT/m. For imaging, a $^{1}$H-RF quadrature-volume resonator with an inner diameter of 20 mm was used. Data acquisition and image processing were carried out with the Bruker software Paravision 5.1. During the examinations, mice were placed on a heated circulating water blanket to ensure constant body temperature of 37 °C. Anesthesia was induced with 3% and maintained with 1.5–2.0% isoflurane (Forene, Abbot) delivered in 0.5 L/min of 100% $O_2$ via a facemask under constant ventilation monitoring (Small Animal Monitoring & Gating System, SA Instruments, Stony Brook, NY, USA). For imaging the mouse brain, T2-weighted 2D turbo spin-echo sequence was used (imaging parameters for T2 TR/TE = 4200/36 ms, RARE factor 8.4 averages). Twenty axial slices with a slice thickness of 0.5 mm, a field of view of 2.60 × 2.60 cm and a matrix of 256 × 256 were positioned over the brain. Calculation of lesion volume was carried out with the program Analyze 5.0 (AnalyzeDirect, Inc., Mayo Clinic, MI, USA). The hyperintense tumor areas were assigned with a region of interest tool. This enables a threshold-based segmentation by connecting all pixels within a specified threshold range about the selected seed pixel and results in a 3D object map of the whole tumor region. Further, the total volume of the whole object map was automatically calculated.

### 4.7. HE Tumor Volume Analysis

Tumor volumes were obtained from Hematoxylin & Eosin (H&E)-stained tumor sections measuring the area of every 9th section and calculated by the Cavalieri Method [69].

### 4.8. Quantitative PCR

RNA extraction was performed using Trizol (Thermo Fisher Scientific) according to the manufacturer´s instructions. One microgram total RNA was reverse-transcribed into cDNA using QuantiTect Reverse Transcription Kit (Qiagen) and the cDNA was analyzed by quantitative PCR using TaqMan Gene Expression Assays for *APLN* (Hs00936329_m1; Mm00443562_m1; Rn00581093_m1), *EG5* (Hs00189698_m1), and *GAPDH* (Hs99999905_m1; Mm99999915_g1; Rn01775763_g1) with TaqMan Gene Expression Master Mix (Cat. 4369016) in a StepOnePlus Instrument (all Thermo Fisher Scientific). Samples were amplified with the standard running method provided by StepOne Software v2.2.2, increasing the cycle numbers to 45. In every run, gene-of-interest expression levels were normalized to the house-keeping gene GAPDH.

### 4.9. Viability and Proliferation Assays

Six thousand cells/well were plated in 96-well plates in DMEM-F12 medium on day 0. Cell viability was measured after 24, 48, 72, and 96 h using a MTT assay (CellTiter 96 Non-Radioactive Cell Proliferation Assay, Promega, Fitchburg, WI, USA) for cell metabolic activity according to manufacturer´s instruction, incubating the cells one hour with the "Stop Mix" solution. Absorbance was measured with Versa Max microplate reader and SoftMax Pro software (Molecular Devices) with a reference wavelength of 630 nm. Background absorbance from wells containing no cells was subtracted from all measurements, and six replicate samples were used in each experiment. Three experiments per cell type were performed.

### 4.10. In Situ Hybridization

Solutions were prepared with RNAse free water and sterilized. Sections on slides were deparaffinized by serial passages into Roti-Histol and graded alcohol (100–25%). Tissue was permeabilized with 10 min incubation in 10 µg/mL of Proteinase K (PeqLab, VWR). Slides were fixed for 10 min in 4% paraformaldehyde (PFA) and blocked for 10 min with Acetic Anhydride (0.25%; Sigma Aldrich) in Triethanolamine (1.5%; Sigma Aldrich). Sections were dried for 2 h at room temperature, then incubated overnight at 65 °C in a humidified chamber with DIG-labeled (DIG RNA labeling; Roche Diagnostics) antisense or sense probes at a final concentration of 7 µg/mL, and diluted in a hybridization solution containing ssDNA (100 µg/mL, Salmon sperm DNA; Ambion, Thermo Fisher Scientific) to mask unspecific binding and co-precipitant RNA (100 µg/mL, Yeast RNA; Ambion). RNA probes were generated from human VEGFA and mouse *APLN* cDNA as previously described [19]. Probe-containing hybridization solution was boiled at 95 °C for 10 min before application. On day two, unspecific signal was removed with graded stringency washes with saline sodium citrate from 20× to 0.1× and incubated with alkaline phosphatase conjugated anti-DIG antibody (Roche Diagnostics) overnight at 4 °C. On day three, slides were washed in PBT (0.1% Tween in 1×PBS) and incubated with BCIP/NBT substrate (Vector Laboratories, Burlingham, CA, USA) at 37 °C for up to four days. For counterstaining with Eosin, slides underwent serial passages in graded alcohol (70–100%) till Roti-Histol and were then mounted with Entellan (Merck Millipore). Pictures were taken under an Axioskop2 microscope with Axiocam 105 Color and Axiovision SE64 Rel. 4.9 software (Carl Zeiss, Jena, Germany).

### 4.11. Immunofluorescence and Vessel Density Quantification

Mice were transcardially perfused under Narcoren (Merial) anesthesia with 1x PBS followed by 4% phosphate buffered PFA. Brains were post-fixed for two days in 4% PFA and then left in 30% sucrose for at least 24 h at 4 °C. Freezing was performed embedding the tissue in Cryomatrix (Thermo Fisher Scientific) and brains were preserved at −20 °C. Tissue was sectioned horizontally in 40 µm-thick slices on a microtome. Floating sections were blocked for 1 h at room temperature in 1x PBS containing 5% normal donkey serum (NDS; cat. 017-000-121; Jackson Immuno-Research,) and 0.3% Triton-X

(cat. 93418; Fluka) and incubated overnight at 4 °C with primary antibodies rat anti-CD31 (1:50, cat. 550274; BD Biosciences) or rabbit anti-VWF (1:400, cat. A0082; Dako, Agilent Technologies, Santa Clara, CA, USA). The next day, sections were incubated for 3 h at room temperature with the secondary antibodies biotin donkey anti-rabbit, anti-rat (1:250, cat. 711-065-152; 712-065-150), and/or 2 h at room temperature with Streptavidin-AF488 or -AF594 (1:500, cat. 016-540-084; 016-580-084, Jackson Immuno-Research). Alternatively, sections were directly incubated for 2 h at room temperature with the secondary antibodies donkey anti-rabbit AF488 or AF594 (1:500, cat. A-21206, A-21207 Thermo Fisher Scientific). All antibodies were diluted in blocking solution. After staining, tissue was mounted in Fluorescent Mounting Medium (Dako) and pictures taken at Axiovert25 microscope with Axiocam MRm and Axiovision Rel 4.8 software (Zeiss) or with confocal laser scanning microscopy at the Leica TCS SP5 Confocal with LAS AF software (Leica Microsystems). Stereological analysis of vessel density was performed in green fluorescent protein (GFP)-positive tumor area of the CD31- or VWF-positive red fluorescent vessels on every 9th section using the space ball method of the StereoInvestigator Software 10.21.1 (MicroBrightField Bioscience, Williston, VT, USA) connected to an Olympus-BX53-microscope (Olympus Europe, Hamburg, Germany, USA) and a motorized object table MicroBrightField Bioscience.

**Supplementary Materials:** Supplementary materials can be found at http://www.mdpi.com/1422-0067/21/11/4179/s1. Figure S1. Modulation of APLN-signaling changes vessel density but not pericyte coverage and endothelial proliferation. (A) U87MG was implanted into immunodeficient mice and grown to big xenografts within 28 dpi. Double-fluorescent immunostaining for CD31+ endothelial cells and Desmin+ pericytes was performed. Double-fluorescent staining confirms decreased vessel density upon reduction of APLN expression in tumour cells ($U87^{AKD}APLN^{WT}$), the microenvironment ($U87^{NSC}APLN^{KO}$) or both ($U87^{AKD}APLN^{KO}$) compared to control ($U87^{NSC}APLN^{WT}$). The number of pericyte-covered vessel objects was assessed by the "Count and measure" function in the Cellsense software (Olympus Life Science) on 20× micrographs of different tumour areas of three different tumour sections per animal (six animals per group) and no significant difference of the experimental group compared to the control group was observed (graph not shown). (B) U87MG were grown for 28 dpi and mice intravenously injected with the proliferation marker BrdU three hours before sacrifice. Tumours were stained by double-immuofluorescence for BrdU and Isolectin B4 (IB4) and confocal images were taken. In all four groups BrdU+ endothelial cells (IB4+) could be observed. (C) $U87^{NSC}APLN^{WT}$ GBM cells were treated with aCSF or the antagonistic peptide apelin-F13A by intracerebral infusion for 14 days and tumours assessed 28 dpi for vessel density by stereomorphometry ($n = 6.5$). Vessel length density significantly decreased compared to controls when apelin-F13A was used. Data are reported as mean +/-SEM; statistical significance (students t-test) is indicated ** $p < 0.01$. Figure S2. Decrease in *APLN*-expression correlates with increased GBM cell invasion. (A) U87MG cells generally form a very compact tumour 28 dpi (see $U87^{NSC}APLN^{WT}$ control in the left panel) but single invading cells (arrows) are especially detectable in $U87^{AKD}APLN^{KO}$ xenografts (right panel) by the GFP reporter. By H&E staining a gradual loosening of the tumor border (arrowhead) from left to right panel can be observed (arrows). (B) To assess the extent of GBM cell-invasion, we analysed every 8th tumour section per mouse assigning it an invasive score from 0 to 3 (where 0 is no histological sign of cell invasion from the tumour mass, 1 describes a larger, connected group of invading GBM cells, 2 indicates smaller scattered groups of invading GBM cells and 3 highlights single scattered highly invasive GBM cells). While the $U87^{NSC}APLN^{WT}$ control tumours grow fully compact, the invasive score gradually increases when *APLN* expression is knocked down in the tumor cells ($U87^{AKD}APLN^{WT}$), the microenvironment ($U87^{NSC}APLN^{KO}$) or both ($U87^{AKD}APLN^{KO}$). In particular the $U87^{NSC}APLN^{KO}$ GBMs exhibit a strong and inter-individually heavily heterogeneous invasive behavior. Here, one set of tumours had moderate levels of invasion (invasive scores below 1, which are comparable to the invasive pattern in the $U87^{AKD}APLN^{WT}$ or $U87^{NSC}APLN^{KO}$ group), while other gliomas generated by the $U87^{NSC}APLN^{KO}$ cells were strongly invasive (invasive scores above 2). (C) Double immunofluorescent staining for GFP-positive tumor (green) and CD31-positive endothelial cells (red) of U87 tumours 28 dpi were performed for $U87^{NSC}APLN^{WT}$ or $U87^{AKD}APLN^{KO}$ xenografts and merged confocal micrographs (left panels) or a Volocity representation of the confocal z-stacks (right panels) are shown. Note that In the *APLN*-deficient $U87^{AKD}APLN^{KO}$ xenografts the GBM cells largely associate with the vasculature which may support directed invasion towards the tumour-free brain. (D) Infusion of Apelin-13 peptide intracerebrally decreased T2-weighted MRI tumour volume of $U87^{AKD}APLN^{KO}$ xenografts ($n = 5$) compared to control aCSF treated mice ($n = 6$). (E) Orthotopic GL261 tumor cell implants in $APLN^{WT}$ or $APLN^{KO}$ mice 21 days post implantation show a reduced tumour volume assessed by the Cavalieri Estimator method (StereoInvestigator) and increased tumor cell invasiveness (arrowheads) as quantified on H&E sections ($n = 9.6$ mice). Data are reported as mean +/-SEM; statistical significance (students t-test) is indicated *** $p < 0.001$. (F) Gene expression screen for change in 84 angiogenesis and invasion related genes. RNA was isolated from microdissected orthotpic xenografts of all four U87 GBM groups ($n = 4$ per group) 28 dpi with different APLN expression levels and a qPCR screen using an "$RT^2$ Profile PCR Array Mouse Angiogenesis" (Qiagen PAMM 024Z) was performed. Marker genes involved in angiogenesis were downregulated when APLN expression was decreaed in the tumour cells or the microenvironment. Instead the marker for cell invasion MMP2

was found to be upregulated, while its inhibitor TIMP1 was downregulated. Data are reported as mean +/-SEM; statistical significance (one-way ANOVA plus Bonferroni's post hoc test) is indicated * $p < 0.05$, ** $p < 0.01$.

**Author Contributions:** Conceptualization, F.L.H. and R.E.K.; methodology, A.F., S.K., R.M., and R.E.K.; formal analysis, A.F., S.K., R.M., J.R. and R.E.K.; resources, R.E.K. and F.L.H.; data curation, R.E.K. and S.K.; writing R.E.K.; review and editing, all authors; visualization, R.E.K; supervision, F.L.H. and R.E.K.; funding acquisition, F.L.H. and R.E.K. All authors have read and agreed to the published version of the manuscript.

**Funding:** This research was supported by funding of the "Berliner Krebsgesellschaft", the "Wilhelm Sander-Stiftung", the "Anni-Hofmann Stiftung" and the "Familie Mehdorn Stiftung".

**Acknowledgments:** We are thankful to Li Fohs-Li, Giorgia Mastrella and Mengzhuo Hou for technical assistance with in situ hybridizations, immunohistochemisty, and genotyping. We would especially like to thank Susanne Müller for great support with MRI imaging and analysis and Josef Penninger for providing the APLN-KO strain.

**Conflicts of Interest:** The authors declare no conflict of interest.

## Abbreviations

| | |
|---|---|
| ABP | Average branch points |
| aCSF | Artificial cerebrospinal fluid |
| AKD | Apelin knock-down |
| $APLN^{KO}$ | Apelin knock-out |
| $APLN^{WT}$ | Apelin wildtype |
| APLN | Apelin |
| APLNR | Apelin Receptor |
| dpi | days post implantation |
| GBM | Glioblastoma |
| GFP | Green fluorescent protein |
| NSC | Non-silencing control |
| VEGFA | Vascular endothelial growth factor-A |
| VLD | Vessel length density |
| VWF | von Willebrand factor |
| WT | Wild-type |

## References

1. Kleihues, P.; Cavenee, W.K. *Pathology and Genetics of Tumours of the Nervous System*; IARC Press: Lyon, France, 2000.
2. Stupp, R.; Mason, W.P.; van den Bent, M.J.; Weller, M.; Fisher, B.; Taphoorn, M.J.; Belanger, K.; Brandes, A.A.; Marosi, C.; Bogdahn, U.; et al. Radiotherapy plus concomitant and adjuvant temozolomide for glioblastoma. *N. Engl. J. Med.* **2005**, *352*, 987–996. [CrossRef] [PubMed]
3. Weller, M.; van den Bent, M.; Tonn, J.C.; Stupp, R.; Preusser, M.; Cohen-Jonathan-Moyal, E.; Henriksson, R.; Le Rhun, E.; Balana, C.; Chinot, O.; et al. European Association for Neuro-Oncology (EANO) guideline on the diagnosis and treatment of adult astrocytic and oligodendroglial gliomas. *Lancet Oncol.* **2017**, *18*, e315–e329. [CrossRef]
4. Louis, D.N.; Perry, A.; Reifenberger, G.; von Deimling, A.; Figarella-Branger, D.; Cavenee, W.K.; Ohgaki, H.; Wiestler, O.D.; Kleihues, P.; Ellison, D.W.; et al. The 2016 World Health Organization Classification of Tumors of the Central Nervous System: A summary. *Acta Neuropathol.* **2016**, *131*, 803–820. [CrossRef]
5. Hegi, M.E.; Diserens, A.C.; Gorlia, T.; Hamou, M.F.; de Tribolet, N.; Weller, M.; Kros, J.M.; Hainfellner, J.A.; Mason, W.; Mariani, L.; et al. MGMT gene silencing and benefit from temozolomide in glioblastoma. *N. Engl. J. Med.* **2005**, *352*, 997–1003. [CrossRef] [PubMed]
6. Stupp, R.; van den Bent, M.J.; Hegi, M.E. Optimal role of temozolomide in the treatment of malignant gliomas. *Curr. Neurol. Neurosci. Rep.* **2005**, *5*, 198–206. [CrossRef]
7. Folkman, J. Tumor angiogenesis: Therapeutic implications. *N. Engl. J. Med.* **1971**, *285*, 1182–1186.
8. Ferrara, N.; Henzel, W.J. Pituitary follicular cells secrete a novel heparin-binding growth factor specific for vascular endothelial cells. *Biochem. Biophys. Res. Commun.* **1989**, *161*, 851–858. [CrossRef]
9. Kim, K.J.; Li, B.; Winer, J.; Armanini, M.; Gillett, N.; Phillips, H.S.; Ferrara, N. Inhibition of vascular endothelial growth factor-induced angiogenesis suppresses tumour growth in vivo. *Nature* **1993**, *362*, 841–844. [CrossRef]

10. Hurwitz, H.; Fehrenbacher, L.; Novotny, W.; Cartwright, T.; Hainsworth, J.; Heim, W.; Berlin, J.; Baron, A.; Griffing, S.; Holmgren, E.; et al. Bevacizumab plus irinotecan, fluorouracil, and leucovorin for metastatic colorectal cancer. *N. Engl. J. Med.* **2004**, *350*, 2335–2342. [CrossRef] [PubMed]
11. Chinot, O.L.; Wick, W.; Mason, W.; Henriksson, R.; Saran, F.; Nishikawa, R.; Carpentier, A.F.; Hoang-Xuan, K.; Kavan, P.; Cernea, D.; et al. Bevacizumab plus radiotherapy-temozolomide for newly diagnosed glioblastoma. *N. Engl. J. Med.* **2014**, *370*, 709–722. [CrossRef]
12. Gilbert, M.R.; Dignam, J.J.; Armstrong, T.S.; Wefel, J.S.; Blumenthal, D.T.; Vogelbaum, M.A.; Colman, H.; Chakravarti, A.; Pugh, S.; Won, M.; et al. A randomized trial of bevacizumab for newly diagnosed glioblastoma. *N. Engl. J. Med.* **2014**, *370*, 699–708. [CrossRef] [PubMed]
13. Holash, J.; Maisonpierre, P.C.; Compton, D.; Boland, P.; Alexander, C.R.; Zagzag, D.; Yancopoulos, G.D.; Wiegand, S.J. Vessel cooption, regression, and growth in tumors mediated by angiopoietins and VEGF. *Science* **1999**, *284*, 1994–1998. [CrossRef] [PubMed]
14. Lu, K.V.; Bergers, G. Mechanisms of evasive resistance to anti-VEGF therapy in glioblastoma. *CNS Oncol.* **2013**, *2*, 49–65. [CrossRef] [PubMed]
15. Masiero, M.; Simoes, F.C.; Han, H.D.; Snell, C.; Peterkin, T.; Bridges, E.; Mangala, L.S.; Wu, S.Y.; Pradeep, S.; Li, D.; et al. A core human primary tumor angiogenesis signature identifies the endothelial orphan receptor ELTD1 as a key regulator of angiogenesis. *Cancer Cell* **2013**, *24*, 229–241. [CrossRef] [PubMed]
16. O'Dowd, B.F.; Heiber, M.; Chan, A.; Heng, H.H.; Tsui, L.C.; Kennedy, J.L.; Shi, X.; Petronis, A.; George, S.R.; Nguyen, T. A human gene that shows identity with the gene encoding the angiotensin receptor is located on chromosome 11. *Gene* **1993**, *136*, 355–360. [CrossRef]
17. Tatemoto, K.; Hosoya, M.; Habata, Y.; Fujii, R.; Kakegawa, T.; Zou, M.X.; Kawamata, Y.; Fukusumi, S.; Hinuma, S.; Kitada, C.; et al. Isolation and characterization of a novel endogenous peptide ligand for the human APJ receptor. *Biochem. Biophys. Res. Commun.* **1998**, *251*, 471–476. [CrossRef] [PubMed]
18. Kawamata, Y.; Habata, Y.; Fukusumi, S.; Hosoya, M.; Fujii, R.; Hinuma, S.; Nishizawa, N.; Kitada, C.; Onda, H.; Nishimura, O.; et al. Molecular properties of apelin: Tissue distribution and receptor binding. *Biochim. Biophys. Acta* **2001**, *1538*, 162–171. [CrossRef]
19. Kälin, R.E.; Kretz, M.P.; Meyer, A.M.; Kispert, A.; Heppner, F.L.; Brändli, A.W. Paracrine and autocrine mechanisms of apelin signaling govern embryonic and tumor angiogenesis. *Dev. Biol.* **2007**, *305*, 599–614. [CrossRef] [PubMed]
20. Hashimoto, Y.; Ishida, J.; Yamamoto, R.; Fujiwara, K.; Asada, S.; Kasuya, Y.; Mochizuki, N.; Fukamizu, A. G protein-coupled APJ receptor signaling induces focal adhesion formation and cell motility. *Int. J. Mol. Med.* **2005**, *16*, 787–792.
21. Hosoya, M.; Kawamata, Y.; Fukusumi, S.; Fujii, R.; Habata, Y.; Hinuma, S.; Kitada, C.; Honda, S.; Kurokawa, T.; Onda, H.; et al. Molecular and functional characteristics of APJ. Tissue distribution of mRNA and interaction with the endogenous ligand apelin. *J. Biol. Chem.* **2000**, *275*, 21061–21067. [CrossRef]
22. Cox, C.M.; D'Agostino, S.L.; Miller, M.K.; Heimark, R.L.; Krieg, P.A. Apelin, the ligand for the endothelial G-protein-coupled receptor, APJ, is a potent angiogenic factor required for normal vascular development of the frog embryo. *Dev. Biol.* **2006**, *296*, 177–189. [CrossRef]
23. Kasai, A.; Shintani, N.; Oda, M.; Kakuda, M.; Hashimoto, H.; Matsuda, T.; Hinuma, S.; Baba, A. Apelin is a novel angiogenic factor in retinal endothelial cells. *Biochem. Biophys. Res. Commun.* **2004**, *325*, 395–400. [CrossRef] [PubMed]
24. Samura, M.; Morikage, N.; Suehiro, K.; Tanaka, Y.; Nakamura, T.; Nishimoto, A.; Ueno, K.; Hosoyama, T.; Hamano, K. Combinatorial Treatment with Apelin-13 Enhances the Therapeutic Efficacy of a Preconditioned Cell-Based Therapy for Peripheral Ischemia. *Sci. Rep.* **2016**, *6*, 19379. [CrossRef]
25. Wang, Z.; Wen, J.; Zhou, Y.; Li, L.; Cui, X.; Wang, J.; Pan, L.; Ye, Z.; Liu, P.; Wu, L. Elabela-apelin receptor signaling pathway is functional in mammalian systems. *Sci. Rep.* **2015**, *5*, 8170. [CrossRef] [PubMed]
26. Berta, J.; Hoda, M.A.; Laszlo, V.; Rozsas, A.; Garay, T.; Torok, S.; Grusch, M.; Berger, W.; Paku, S.; Renyi-Vamos, F.; et al. Apelin promotes lymphangiogenesis and lymph node metastasis. *Oncotarget* **2014**, *5*, 4426–4437. [CrossRef]
27. Lv, D.; Li, L.; Lu, Q.; Li, Y.; Xie, F.; Li, H.; Cao, J.; Liu, M.; Wu, D.; He, L.; et al. PAK1-cofilin phosphorylation mediates human lung adenocarcinoma cells migration induced by apelin-13. *Clin. Exp. Pharmacol. Physiol.* **2016**, *43*, 569–579. [CrossRef] [PubMed]

28. Del Toro, R.; Prahst, C.; Mathivet, T.; Siegfried, G.; Kaminker, J.S.; Larrivee, B.; Breant, C.; Duarte, A.; Takakura, N.; Fukamizu, A.; et al. Identification and functional analysis of endothelial tip cell-enriched genes. *Blood* **2010**, *116*, 4025–4033. [CrossRef]
29. Kasai, A.; Shintani, N.; Kato, H.; Matsuda, S.; Gomi, F.; Haba, R.; Hashimoto, H.; Kakuda, M.; Tano, Y.; Baba, A. Retardation of retinal vascular development in apelin-deficient mice. *Arterioscler. Thromb. Vasc. Biol.* **2008**, *28*, 1717–1722. [CrossRef]
30. Kidoya, H.; Ueno, M.; Yamada, Y.; Mochizuki, N.; Nakata, M.; Yano, T.; Fujii, R.; Takakura, N. Spatial and temporal role of the apelin/APJ system in the caliber size regulation of blood vessels during angiogenesis. *EMBO J.* **2008**, *27*, 522–534. [CrossRef]
31. Strasser, G.A.; Kaminker, J.S.; Tessier-Lavigne, M. Microarray analysis of retinal endothelial tip cells identifies CXCR4 as a mediator of tip cell morphology and branching. *Blood* **2010**, *115*, 5102–5110. [CrossRef]
32. Liu, Q.; Hu, T.; He, L.; Huang, X.; Tian, X.; Zhang, H.; He, L.; Pu, W.; Zhang, L.; Sun, H.; et al. Genetic targeting of sprouting angiogenesis using Apln-CreER. *Nat. Commun.* **2015**, *6*, 6020. [CrossRef] [PubMed]
33. Sheikh, A.Y.; Chun, H.J.; Glassford, A.J.; Kundu, R.K.; Kutschka, I.; Ardigo, D.; Hendry, S.L.; Wagner, R.A.; Chen, M.M.; Ali, Z.A.; et al. F genetic profiling and cellular localization of apelin reveals a hypoxia-sensitive, endothelial-centered pathway activated in ischemic heart failure. *Am. J. Physiol. Heart Circ. Physiol.* **2008**, *294*, H88–H98. [CrossRef]
34. Kuba, K.; Zhang, L.; Imai, Y.; Arab, S.; Chen, M.; Maekawa, Y.; Leschnik, M.; Leibbrandt, A.; Markovic, M.; Schwaighofer, J.; et al. Impaired heart contractility in Apelin gene-deficient mice associated with aging and pressure overload. *Circ. Res.* **2007**, *101*, e32–e42. [CrossRef]
35. Kidoya, H.; Naito, H.; Takakura, N. Apelin induces enlarged and nonleaky blood vessels for functional recovery from ischemia. *Blood* **2010**, *115*, 3166–3174. [CrossRef] [PubMed]
36. Charo, D.N.; Ho, M.; Fajardo, G.; Kawana, M.; Kundu, R.K.; Sheikh, A.Y.; Finsterbach, T.P.; Leeper, N.J.; Ernst, K.V.; Chen, M.M.; et al. Endogenous regulation of cardiovascular function by apelin-APJ. *Am. J. Physiol. Heart Circ. Physiol.* **2009**, *297*, H1904–H1913. [CrossRef] [PubMed]
37. Plate, K.H.; Breier, G.; Weich, H.A.; Risau, W. Vascular endothelial growth factor is a potential tumour angiogenesis factor in human gliomas in vivo. *Nature* **1992**, *359*, 845–848. [CrossRef]
38. Weil, D.; Garcon, L.; Harper, M.; Dumenil, D.; Dautry, F.; Kress, M. Targeting the kinesin Eg5 to monitor siRNA transfection in mammalian cells. *Biotechniques* **2002**, *33*, 1244–1248. [CrossRef] [PubMed]
39. Machein, M.R.; Renninger, S.; de Lima-Hahn, E.; Plate, K.H. Minor contribution of bone marrow-derived endothelial progenitors to the vascularization of murine gliomas. *Brain Pathol.* **2003**, *13*, 582–597. [CrossRef] [PubMed]
40. Markovic, D.S.; Vinnakota, K.; Chirasani, S.; Synowitz, M.; Raguet, H.; Stock, K.; Sliwa, M.; Lehmann, S.; Kälin, R.; van Rooijen, N.; et al. Gliomas induce and exploit microglial MT1-MMP expression for tumor expansion. *Proc. Natl. Acad. Sci. USA* **2009**, *106*, 12530–12535. [CrossRef]
41. Dockery, P.; Fraher, J. The quantification of vascular beds: A stereological approach. *Exp. Mol. Pathol.* **2007**, *82*, 110–120. [CrossRef]
42. Lokkegaard, A.; Nyengaard, J.R.; West, M.J. Stereological estimates of number and length of capillaries in subdivisions of the human hippocampal region. *Hippocampus* **2001**, *11*, 726–740. [CrossRef]
43. Mouton, P.R.; Gokhale, A.M.; Ward, N.L.; West, M.J. Stereological length estimation using spherical probes. *J. Microsc.* **2002**, *206*, 54–64. [CrossRef]
44. Franciosi, S.; Gama Sosa, M.A.; English, D.F.; Oler, E.; Oung, T.; Janssen, W.G.; De Gasperi, R.; Schmeidler, J.; Dickstein, D.L.; Schmitz, C.; et al. Novel cerebrovascular pathology in mice fed a high cholesterol diet. *Mol. Neurodegener.* **2009**, *4*, 42. [CrossRef]
45. Walchli, T.; Mateos, J.M.; Weinman, O.; Babic, D.; Regli, L.; Hoerstrup, S.P.; Gerhardt, H.; Schwab, M.E.; Vogel, J. Quantitative assessment of angiogenesis, perfused blood vessels and endothelial tip cells in the postnatal mouse brain. *Nat. Protoc.* **2015**, *10*, 53–74. [CrossRef]
46. Lee, D.K.; Saldivia, V.R.; Nguyen, T.; Cheng, R.; George, S.R.; O'Dowd, B.F. Modification of the terminal residue of apelin-13 antagonizes its hypotensive action. *Endocrinology* **2005**, *146*, 231–236. [CrossRef] [PubMed]
47. Ferrara, N.; Hillan, K.J.; Gerber, H.P.; Novotny, W. Discovery and development of bevacizumab, an anti-VEGF antibody for treating cancer. *Nat. Rev. Drug Discov.* **2004**, *3*, 391–400. [CrossRef] [PubMed]

48. Berta, J.; Kenessey, I.; Dobos, J.; Tovari, J.; Klepetko, W.; Jan Ankersmit, H.; Hegedus, B.; Renyi-Vamos, F.; Varga, J.; Lorincz, Z.; et al. Apelin expression in human non-small cell lung cancer: Role in angiogenesis and prognosis. *J. Thorac. Oncol. Off. Publ. Int. Assoc. Study Lung Cancer* **2010**, *5*, 1120–1129. [CrossRef]
49. Sorli, S.C.; Le Gonidec, S.; Knibiehler, B.; Audigier, Y. Apelin is a potent activator of tumour neoangiogenesis. *Oncogene* **2007**, *26*, 7692–7699. [CrossRef]
50. Claesson-Welsh, L. What is normal? Apelin and VEGFA, drivers of tumor vessel abnormality. *EMBO Mol. Med.* **2019**, *11*, e10892. [CrossRef]
51. Uribesalgo, I.; Hoffmann, D.; Zhang, Y.; Kavirayani, A.; Lazovic, J.; Berta, J.; Novatchkova, M.; Pai, T.P.; Wimmer, R.A.; Laszlo, V.; et al. Apelin inhibition prevents resistance and metastasis associated with anti-angiogenic therapy. *EMBO Mol. Med.* **2019**, *11*, e9266. [CrossRef] [PubMed]
52. Kälin, S.; Kälin, R.E. *Adipocitokines, Energy Balance and Cancer—Energy Balance and Cancer*; Reizes, O., Berger, N.A., Eds.; Springer International Publishing Switzerland: Cham, Switzerland, 2017; pp. 137–166.
53. Ganguly, D.; Cai, C.; Sims, M.M.; He Yang, C.; Thomas, M.; Cheng, J.; Saad, A.G.; Pfeffer, L.M. APELA Expression in Glioma, and Its Association with Patient Survival and Tumor Grade. *Pharmaceuticals* **2019**, *12*, 45. [CrossRef] [PubMed]
54. Chng, S.C.; Ho, L.; Tian, J.; Reversade, B. Elabela: A hormone essential for heart development signals via the apelin receptor. *Dev. Cell* **2013**, *27*, 672–680. [CrossRef] [PubMed]
55. Pauli, A.; Norris, M.L.; Valen, E.; Chew, G.L.; Gagnon, J.A.; Zimmerman, S.; Mitchell, A.; Ma, J.; Dubrulle, J.; Reyon, D.; et al. Toddler: An embryonic signal that promotes cell movement via apelin receptors. *Science* **2014**, *343*, 1248636. [CrossRef] [PubMed]
56. Kidoya, H.; Kunii, N.; Naito, H.; Muramatsu, F.; Okamoto, Y.; Nakayama, T.; Takakura, N. The apelin/APJ system induces maturation of the tumor vasculature and improves the efficiency of immune therapy. *Oncogene* **2011**, *31*, 3254–3264. [CrossRef] [PubMed]
57. Mastrella, G.; Hou, M.; Li, M.; Stoecklein, V.M.; Zdouc, N.; Volmar, M.N.M.; Miletic, H.; Reinhard, S.; Herold-Mende, C.C.; Kleber, S.; et al. Targeting APLN/APLNR Improves Antiangiogenic Efficiency and Blunts Proinvasive Side Effects of VEGFA/VEGFR2 Blockade in Glioblastoma. *Cancer Res.* **2019**, *79*, 2298–2313. [CrossRef] [PubMed]
58. Kunkel, P.; Ulbricht, U.; Bohlen, P.; Brockmann, M.A.; Fillbrandt, R.; Stavrou, D.; Westphal, M.; Lamszus, K. Inhibition of glioma angiogenesis and growth in vivo by systemic treatment with a monoclonal antibody against vascular endothelial growth factor receptor-2. *Cancer Res.* **2001**, *61*, 6624–6628.
59. Lamszus, K.; Kunkel, P.; Westphal, M. Invasion as limitation to anti-angiogenic glioma therapy. *Acta Neurochir. Suppl.* **2003**, *88*, 169–177.
60. Keunen, O.; Johansson, M.; Oudin, A.; Sanzey, M.; Rahim, S.A.; Fack, F.; Thorsen, F.; Taxt, T.; Bartos, M.; Jirik, R.; et al. Anti-VEGF treatment reduces blood supply and increases tumor cell invasion in glioblastoma. *Proc. Natl. Acad. Sci. USA* **2011**, *108*, 3749–3754. [CrossRef]
61. Harford-Wright, E.; Andre-Gregoire, G.; Jacobs, K.A.; Treps, L.; Le Gonidec, S.; Leclair, H.M.; Gonzalez-Diest, S.; Roux, Q.; Guillonneau, F.; Loussouarn, D.; et al. Pharmacological targeting of apelin impairs glioblastoma growth. *Brain* **2017**, *140*, 2939–2954. [CrossRef]
62. Haynes, H.R.; Camelo-Piragua, S.; Kurian, K.M. Prognostic and predictive biomarkers in adult and pediatric gliomas: Toward personalized treatment. *Front. Oncol.* **2014**, *4*, 47. [CrossRef]
63. Heo, K.; Kim, Y.H.; Sung, H.J.; Li, H.Y.; Yoo, C.W.; Kim, J.Y.; Park, J.Y.; Lee, U.L.; Nam, B.H.; Kim, E.O.; et al. Hypoxia-induced up-regulation of apelin is associated with a poor prognosis in oral squamous cell carcinoma patients. *Oral Oncol.* **2012**, *48*, 500–506. [CrossRef]
64. Zuurbier, L.; Rahman, A.; Cordes, M.; Scheick, J.; Wong, T.J.; Rustenburg, F.; Joseph, J.C.; Dynoodt, P.; Casey, R.; Drillenburg, P.; et al. Apelin: A putative novel predictive biomarker for bevacizumab response in colorectal cancer. *Oncotarget* **2017**, *8*, 42949–42961. [CrossRef]
65. Zhao, H.; Tian, X.; He, L.; Li, Y.; Pu, W.; Liu, Q.; Tang, J.; Wu, J.; Cheng, X.; Liu, Y.; et al. Apj (+) Vessels Drive Tumor Growth and Represent a Tractable Therapeutic Target. *Cell Rep.* **2018**, *25*, 1241–1254. [CrossRef]
66. Amoozgar, Z.; Jain, R.K.; Duda, D.G. Role of Apelin in Glioblastoma Vascularization and Invasion after Anti-VEGF Therapy: What Is the Impact on the Immune System? *Cancer Res.* **2019**, *79*, 2104–2106. [CrossRef] [PubMed]
67. United Kingdom Co-Ordinating Committee on Cancer. Guidelines for the welfare of animals in experimental neoplasia. *Cancer Metastasis Rev.* **1989**, *8*, 82–88. [CrossRef] [PubMed]

68. Shinkai, Y.; Rathbun, G.; Lam, K.P.; Oltz, E.M.; Stewart, V.; Mendelsohn, M.; Charron, J.; Datta, M.; Young, F.; Stall, A.M.; et al. RAG-2-deficient mice lack mature lymphocytes owing to inability to initiate V(D)J rearrangement. *Cell* **1992**, *68*, 855–867. [CrossRef]
69. Mayhew, T.M.; Mwamengele, G.L.; Dantzer, V. Stereological and allometric studies on mammalian cerebral cortex with implications for medical brain imaging. *J. Anat.* **1996**, *189*, 177–184. [PubMed]

© 2020 by the authors. Licensee MDPI, Basel, Switzerland. This article is an open access article distributed under the terms and conditions of the Creative Commons Attribution (CC BY) license (http://creativecommons.org/licenses/by/4.0/).

Cancer Research

# Targeting APLN/APLNR Improves Antiangiogenic Efficiency and Blunts Proinvasive Side Effects of VEGFA/VEGFR2 Blockade in Glioblastoma

Giorgia Mastrella[1], Mengzhuo Hou[1], Min Li[1], Veit M. Stoecklein[2], Nina Zdouc[1], Marie N.M. Volmar[1], Hrvoje Miletic[3,4], Sören Reinhard[5], Christel C. Herold-Mende[6], Susanne Kleber[7], Katharina Eisenhut[1], Gaetano Gargiulo[8], Michael Synowitz[9], Angelo L. Vescovi[10], Patrick N. Harter[11], Josef M. Penninger[12], Ernst Wagner[5], Michel Mittelbronn[11,13], Rolf Bjerkvig[3], Dolores Hambardzumyan[14], Ulrich Schüller[15], Jörg-Christian Tonn[2], Josefine Radke[16], Rainer Glass[1,17,18], and Roland E. Kälin[1,18]

## Abstract

Antiangiogenic therapy of glioblastoma (GBM) with bevacizumab, a VEGFA-blocking antibody, may accelerate tumor cell invasion and induce alternative angiogenic pathways. Here we investigate the roles of the proangiogenic apelin receptor APLNR and its cognate ligand apelin in VEGFA/VEGFR2 antiangiogenic therapy against distinct subtypes of GBM. In proneural GBM, apelin levels were downregulated by VEGFA or VEGFR2 blockade. A central role for apelin/APLNR in controlling GBM vascularization was corroborated in a serial implantation model of the angiogenic switch that occurs in human GBM. Apelin and APLNR are broadly expressed in human GBM, and knockdown or knockout of *APLN* in orthotopic models of proneural or classical GBM subtypes significantly reduced GBM vascularization compared with controls. However, reduction in apelin expression led to accelerated GBM cell invasion. Analysis of stereotactic GBM biopsies from patients as well as from *in vitro* and *in vivo* experiments revealed increased dissemination of APLNR-positive tumor cells when apelin levels were reduced. Application of apelin-F13A, a mutant APLNR ligand, blocked tumor angiogenesis and GBM cell invasion. Furthermore, cotargeting VEGFR2 and APLNR synergistically improved survival of mice bearing proneural GBM. In summary, we show that apelin/APLNR signaling controls GBM angiogenesis and invasion and that both pathologic features are blunted by apelin-F13A. We suggest that apelin-F13A can improve the efficiency and reduce the side effects of established antiangiogenic treatments for distinct GBM subtypes.

**Significance:** Pharmacologic targeting of the APLNR acts synergistically with established antiangiogenic treatments in glioblastoma and blunts therapy resistance to current strategies for antiangiogenesis.

*See related commentary by Amoozgar et al., p. 2104*

## Introduction

Glioblastoma (GBM) is the most common and most malignant primary brain tumor (1). Current standard treatment consists of maximal resection followed by radiotherapy with concomitant temozolomide chemotherapy, if safe (2, 3). A subgroup of GBM is generated by epigenetic dysregulation (CpG-island methylator phenotype in isocitrate dehydrogenase mutant gliomas; $IDH^{MUT}$), but the majority of GBM represents

[1]Neurosurgical Research, Department of Neurosurgery, University Hospital, LMU Munich, Munich, Germany. [2]Department of Neurosurgery, University Hospital, LMU Munich, Munich, Germany. [3]Department of Biomedicine, University of Bergen, Bergen, Norway. [4]Department of Pathology, Haukeland University Hospital, Bergen, Norway. [5]Department of Pharmacy, LMU Munich, Munich, Germany. [6]Division of Neurosurgical Research, Department of Neurosurgery, University of Heidelberg, Germany. [7]Department of Molecular Neurobiology, German Cancer Research Center (DKFZ), Heidelberg, Germany. [8]Max Delbrück Center for Molecular Medicine, Berlin, Germany. [9]Department of Neurosurgery, University Hospital Center Schleswig Holstein, Kiel, Germany. [10]IRCCS Casa Sollievo della Sofferenza, San Giovanni Rotondo, Italy. [11]Edinger-Institute (Neurological Institute), Goethe-University Medical School, Frankfurt am Main, Germany and German Cancer Consortium (DKTK), partner site Frankfurt/Mainz; German Cancer Research Center (DKFZ), Heidelberg, Germany. [12]Institute of Molecular Biotechnology, Austrian Academy of Sciences, Vienna, Austria. [13]Luxembourg Centre of Neuropathology (LCNP), Luxembourg and NORLUX Neuro-Oncology Laboratory, Luxembourg Institute of Health (LIH), and Luxembourg Centre for Systems Biomedicine (LCSB), University of Luxembourg, Esch-sur-Alzette, Luxembourg. [14]Department of Pediatrics and Aflac Cancer Center of Children's Health Care of Atlanta, Emory University School of Medicine, Atlanta, Georgia. [15]Institute of Neuropathology and Department of Pediatric Haematology and Oncology, University Medical Center, Hamburg-Eppendorf and Research Institute Children's Cancer Center, Hamburg, Germany. [16]Department of Neuropathology, Charité-Universitätsmedizin Berlin, corporate member of Freie Universität Berlin, Humboldt-Universität zu Berlin, and Berlin Institute of Health, Berlin, German; Berlin Institute of Health (BIH), Berlin, Germany; German Cancer Consortium (DKTK), Heidelberg, Germany, Partner Site Berlin, Berlin, Germany. [17]German Cancer Consortium (DKTK), partner site Munich and German Cancer Research Center (DKFZ), Heidelberg, Germany. [18]Walter Brendel Center of Experimental Medicine, Faculty of Medicine, LMU Munich, Munich, Germany.

**Note:** Supplementary data for this article are available at Cancer Research Online (http://cancerres.aacrjournals.org/).

G. Mastrella, M. Hou, and M. Li contributed equally to this article.

**Corresponding Author:** Roland E. Kälin, University Hospital, LMU Munich, Marchioninistr. 15, Munich 81377, Germany. Phone: 4989-4400-73148; Fax: 4989-4400-77789; E-mail: roland.kaelin@med.lmu.de

**doi:** 10.1158/0008-5472.CAN-18-0881

©2019 American Association for Cancer Research.

IDH wild-type (WT) GBM (4), which can originate from neoplastic neural precursor cells (NPC; refs. 5, 6) after ablation or somatic mutation of the tumor suppressor p53, deletion of neurofibromatosis-1 (*NF1*), or loss of *CDKN2A*. Such genetic aberrations can coincide with loss of the *PTEN*. The vast majority of primary GBM is driven by genetic mutation in key tumor suppressor genes concomitant with accelerated activity of different proto-oncogenic signaling pathways (e.g., *EGFR* or platelet-derived growth factor receptor-A, *PDGFRA*) or through a mutant (ligand independent) form of *EGFR* (EGFR-variant-3, EGFRvIII; ref. 5).

Hallmarks of GBM include poorly-differentiated neoplastic astrocytes, increased cell proliferation, tumor necrosis, microvascular proliferation, and formation of an aberrant vasculature (1). Thus, antiangiogenic treatments appear to be a promising strategy for GBM (7). However, clinical studies using bevacizumab (AVAglio, RTOG-0825), a humanized mAb that blocks VEGFA signaling, did not improve overall survival in patients with GBM (8, 9). GBM often develops resistance to bevacizumab owing to upregulation of alternative proangiogenic pathways and the induction of tumor cell invasion (10). Moreover, differences in angiogenic responses could originate from interindividual GBM heterogeneity, as evidenced by the genetic stratification of GBM (11). The Cancer Genome Atlas (TCGA) revealed three subtypes of GBM, namely proneural, classical, and mesenchymal, which show differences in prognosis and response to treatment (4, 12). The neural GBM subtype was recently considered as a potential artefact (13). A retrospective analysis of the AVAglio trial indicated that patients with ($IDH^{WT}$) proneural GBM can benefit from bevacizumab by increased overall survival (14).

We previously hypothesized that the G-protein coupled receptor (GPCR) APJ (APLNR) and its cognate peptide-ligand apelin play some roles in tumor development (15). Here, apelin was undetectable in the healthy brain and APLNR mRNA expression was very low in normal brain vessels and we observed a dramatic upregulation of both apelin and APLNR in GBM -associated microvascular proliferations, as well as in radially oriented neoplastic cells surrounding band-like foci ("pseudopalisading necroses"). In hypoxic regions, apelin was highly coexpressed with VEGFA (15–17). In this context, it was suggested that apelin levels indicate improved tumor hypoxia due to vascular normalization upon bevacizumab treatment (18).

In this study using *in vitro* and *in vivo* models, we confirm that apelin/APLNR signaling has a strong proangiogenic role in proneural GBM. We show for the first time that blocking VEGFA/VEGFR2 signaling in GBM reduces apelin levels and accelerates the invasion of APLNR-expressing GBM cells. Importantly, administration of apelin-F13A, a mutant form of the natural apelin-13 peptide with avidity for APLNR (19), reduced tumor angiogenesis and cell invasion in GBM models, and had synergistic effects with VEGFR2 blockade.

## Materials and Methods

### Cell culture

GBM stem-like cell (GSC) were derived from human glioblastoma biopsies [as previously reported for NCH644 and NCH588J (20); GBM10, GBM13 and GBM14 (21); and GBM5av to 10av (22)] and were maintained under stem cell cultivation conditions in DMEM-F12 (catalog no. 11320-074) supplemented with 1 × B27 (catalog no. 17504-044), 5% penicillin–streptomycin (catalog no. 151140-122; all Thermo Fisher Scientific), 10 ng/mL epidermal growth factor (EGF; catalog no. 236-EG; Biotechne), and 10 ng/mL fibroblast growth factor (FGF; catalog no. 100-18B PeproTech). For all cultures, gene copy number analysis was performed and the *TP53*, *EGFR*, *PDGFRA*, *PIK3CA*, *PIK3R1*, *PIK3CG*, *PTEN*, *NF1*, *RB1*, *IDH1*, and *ATRX* loci were sequenced. We confirmed that all cultures were tumorigenic upon orthotopic implantation in immunodeficient mice. All of the GSCs, except for GBM10 cells, corresponded to the GBM subtype of the parental tumor.

NPCs were isolated from the subventricular zone of 5-day-old Bl6/J or FVB mice with homozygous deletion of *TP53* or *CDKN2A*. Isolated cells were cultured in spheroid conditions with DMEM-F12 medium supplemented with 1 × B27, 1% penicillin-streptomycin, 10 ng/mL EGF (catalogno. 236-EG; Biotechne) and 10 ng/mL FGF (catalog no. 100-18B; PeproTech). U87MG (HTB14) cells were obtained from the ATCC and cultured under adherent conditions in DMEM containing 1× MEM nonessential amino acids (catalog no. 11140-035), 5% penicillin–streptomycin, and 10% FBS (catalog no. 102270-106; all Thermo Fisher Scientific). GL261 cells were obtained from the National Cancer Institute, NCI-Frederick (Frederick, MD; Tumor Cell Repository) and maintained under neurosphere cell culture conditions as described above. All cells were maintained at 37°C in a humidified atmosphere of 95% $O_2$ and 5% $CO_2$. GSCs were validated repeatedly (2015 and 2017) by short tandem repeat (STR) fingerprinting (Eurofins Medignomix Forensik) and were regularly tested for *Mycoplasma* contamination by PCR.

### Cell transduction

Mouse transgenic glioma cells as a model of the proneural GBM subtype ($p53^{KO}$*PDGFB* GSCs) were generated by transduction of a single-cell suspension of $p53^{KO}$ NPCs for 1 hour with a multiplicity of infection (MOI) of 80 of VSV-G pseudotyped GFP-PDGFB retroviral particles (kindly provided by F.Calzolari/M. Götz, Department of Physiological Genomics, LMU Munich, Munich, Germany). Human *PDGFB* cDNA was derived from the RCAS-pBIG plasmid (kindly provided by E. Holland, Fred Hutchinson Cancer Research Center Seattle). Transduction efficiency was verified by GFP immunofluorescence and was >99%. To study the influence of p53 status in the generated $p53^{KO}$*PDGFB* mouse GSCs, cells were transfected with lipofectamine (catalog no. 18324020; Thermo Fisher Scientific) and 3 μg of empty vector containing ampicillin-neomycin resistance, hotspot *p53* mutant (R172H, R175H, R248W, R249S, R270H, R273H, V143A) or wild-type *p53* plasmid DNA. Transfected GSCs were first selected for 4 weeks with 3 mg/mL of G418 antibiotics and selection was maintained using 1 mg/mL of G418.

As a model of the classical GBM subtype, $cdkn2a^{KO}$ NPCs were transfected with EGFRvIII-blasticidin/GFP plasmids to obtain $cdkn2a^{KO}$EGFRvIII GSCs. To obtain EGFRvIII-EGFR–overexpressing cells, cells were then transfected with 3 μg of neomycin-EGFR plasmid, and the cells were selected for 2 weeks with 1 mg/mL of Geneticin (catalog no. 10131027; Thermo Fisher Scientific). For proneural-like $p53^{KO}$EGFR GSCs, $p53^{KO}$NPCs were transfected with 3 μg of neomycin-EGFR plasmid and selected for 2 weeks with 1 mg/mL of Geneticin.

For gene silencing in GBM14 and NCH644, we used three different lentiviral shRNAmir constructs for apelin (AKD; catalog no. RHS4430: V3LHS_401190) or nonsilencing control (NSC;

catalog no. RHS4346) to produce viral particles in HEK293T cells with the TransLenti Viral GIPZ Packaging System (catalog no. TPLP4614, all Dharmacon GE Life Sciences) according to the manufacturer's instructions. Virus particle-containing supernatant was harvested 2 days after transfection, filtered with a 0.22-μm filter to avoid cellular contamination, and stored at −80°C. Primary GSC spheroids were dissociated with Accutase (catalog no. A6964; Sigma Aldrich), while U87MG cells were detached with trypsin/EDTA (catalog no. L2153; Merck Millipore). Then, $8 \times 10^4$ cells were incubated with 500 μL of virus particles at an MOI of 0.6–0.7 for 6 hours in a 24-well plate. Next, 1 mL of medium was added and the cells were left overnight at 37°C. The next day, the cells were centrifuged and resuspended in fresh medium. After cell recovery, cells were selected using puromycin (catalog no. P8833; Sigma Aldrich) for up to 3 weeks. The concentration of antibiotics was determined beforehand using a lethal dose curve. The efficiency of transduction/selection was >99%, as confirmed by FACS and immunofluorescence.

### Animals

All experiments were performed in compliance with the National Guidelines for Animal Protection, Germany, with approval of the local animal care committee of the Government of Oberbayern (Regierung von Oberbayern). All experiments were conducted in accordance with the UK Coordinating Committee on Cancer Research guidelines (23). APLN-Knockout ($APLN^{KO}$) mice were obtained from J.M. Penninger (Institute of Molecular Biotechnology, Austrian Academy of Sciences, Vienna, Austria; ref. 24) and crossed with $Rag2^{KO}$ mice (B6.129S6-$Rag2^{tm1Fwa}$; ref. 25) kindly provided by G. Willimsky (Charité – Universitätsmedizin Berlin, Berlin, Germany) and previously purchased from Taconic. All mice had a C57Bl/6J background and genotyping was performed as previously described (24, 25). $Foxn1^{nu/nu}$ mice were ordered from Envigo. All mice were kept in a 12-hour light/dark cycle with *ad libitum* access to food and water. Mice were sacrificed at defined presymptomatic time points or at a humane endpoint in survival studies.

### Tumor implantation

Mice were anesthetized with 7 μL/g of body weight of a mixture of xylazine (Rompun 2%; Bayer) and ketamine (Ketavet; Zoetis) in 0.9% NaCl. They were immobilized on a stereotactic frame (David Kopf Instruments) in flat-skull position and kept warm. A midline incision was made on the skull with a scalpel. To prevent the cornea from drying out, the eyes of the mice were covered with a moisturizing cream (Bepanthen; Bayer). Then, $1 \times 10^5$ (human) or $1 \times 10^4$ (mouse) cells/μL in supplement-free medium were implanted by stereotactic injection 1 mm anterior and 1.5 mm right to the bregma using a 22G Hamilton syringe (Hamilton) after drilling a hole into the skull with a 23G needle. At a depth of 4 mm, the cells were slowly injected within 2 minutes. After a settling period of another minute, the needle was removed at 1-mm steps/minute. The incision was sutured and patched with Opsite spray dressing (Smith & Nephew). Analgesia was achieved by administering a dose of 4 mg/kg before surgery and $2 \times 2$ mg/kg doses of intraperitoneal carprofen (Rymadil, Zoetis) for 3 days after surgery.

### Intracerebral drug application

One day before implantation, mini-osmotic pumps were filled with 30 μg of apelin-F13A (Bachem) or 0.8 mg of DC101 (Eli Lilly) for sustained delivery over 14 days (Model 1002; Alzet) or 60 μg of apelin-F13A for sustained delivery over 28 days (Model 2004, Alzet) in artificial cerebrospinal fluid (aCSF; as described by Alzet) or with aCSF alone following priming overnight in aCSF at 37°C. The mini-osmotic pumps were implanted under anesthesia as described previously (26). For $p53^{KO}$PDGFB GBM treatment, 14-day pumps were implanted one week postimplantation, for GBM14 GBM 28-day pumps were implanted 2 weeks postimplantation. The needle of the brain infusion kit 3 (Alzet) was inserted into the hole originally prepared for orthotopic tumor implantation. The mice were sacrificed at the end of the pump's life (14 or 28 days) or at humane endpoints in survival studies.

### Quantitative PCR

RNA was extracted using TRIzol (catalog no. 15596-026; Thermo Fisher Scientific) according to the manufacturer's instructions. Total RNA (1 μg) was reverse-transcribed into cDNA using a QuantiTect Reverse Transcription Kit (catalog no. 205313; Qiagen) and the cDNA was analyzed by quantitative PCR using TaqMan Gene Expression Assays for apelin (Hs00936329_m1; Mm00443562_m1; Rn00581093_m1), APLNR (Hs00945496_s1; Mm00442191_s1; Rn00580252_s1), KDR (Hs009117_m1; Rn00564986_m1), VEGFA (Hs00900054_m1), EG5 (Hs00189698_m1), and GAPDH (Hs99999905_m1; Mm99999915_g1; Rn01775763_g1) with TaqMan Gene Expression Master Mix (catalog no. 4369016) in a StepOnePlus Instrument (all Thermo Fisher Scientific). Samples were amplified using the standard running method within StepOne Software v2.2.2 by increasing the cycle number to 45. In each run, the expression levels of the target gene were normalized to those of *GAPDH* as a housekeeping gene.

### Copy number analysis

Copy number analysis of all primary GBM was performed using Affymetrix Cytoscan HD Microarray at IMGM Laboratories. The array data are deposited at http://www.ebi.ac.uk/arrayexpress/ (Acc. E-MTAB-7649).

### Viability and proliferation assays

For viability and proliferation assays, 6,000 cells/well were plated in 96-well plates in DMEM-F12 medium on day 0. Cell viability was measured after 24, 48, 72, and 96 hours using a MTT assay (CellTiter 96 Non-Radioactive Cell Proliferation Assay, catalog no. G4000; Promega) to assess cell metabolic activity. Cells were incubated for 1 hour with the Stop Mix solution. Absorbance was measured on a Versa Max microplate reader with SoftMax Pro software (Molecular Devices) at a reference wavelength of 630 nm. The background absorbance of wells containing cell-free supernatant was subtracted from all measurements. Six replicate samples were used in each experiment. Three experiments were performed for each cell type.

### Invasion assays

For this assay, we used U87MG cells that had been maintained in spheroid conditions in DMEM-F12 medium. Spheroids were picked under an Axiovert25 microscope (Carl Zeiss). Spheroids were plated onto 24-well plates in 50 μL containing 1 mg/mL Rat Tail Collagen I (catalog no. A10483-01; Thermo Fisher Scientific), 10× PBS, 1 N NaOH, and diluted in bi-distilled water according to the manufacturer's instructions. As a chemoattractant source, the U87MG spheroids were added to the collagen

mix. Apelin-F13A was added at to the collagen mix at a concentration of 1 μmol/L. The collagen matrix was left to gel for 50 minutes at 37°C and then covered with 600 μL DMEM-F12 medium. Cell invasion was monitored for 7 days by taking photographs every day under an Axiovert25 microscope with Axiocam MRm and Axiovision Rel. 4.8 software (Carl Zeiss). The images were analyzed with ImageJ distribution Fiji and the invasive area ($mm^2$) was calculated as: $\Delta A$ = (area covered on day n) − (sphere area on day 0).

**Human GBM specimens**

The study was approved by the local Institutional Review Board of the LMU Munich (number 599-16, 18-304) and the UCT Frankfurt, Frankfurt am Main (GS4/09 SNO-6-2018) and agrees with all standards regarding the use of informed consent according to the guidelines of the local Institutional Review Board and the etical standards of the Helsinki Declaration. Informed written consent was obtained from all individual participants included in the study. GBM samples obtained from the Neurosurgery Department of the University Hospital, LMU Munich (Munich, Germany) were classified according to whether they were taken from the center or border of the original tumor mass at the time of surgical resection. Necrotic tumor tissue, as evaluated by H&E staining, was excluded from the analysis. Paraffin-embedded GBM samples were obtained from the Center for Neuropathology and Prion Research (ZNP), LMU Munich (Munich, Germany). For stereotactic biopsy, the surgical depth (the distance in mm from the target point 0 defined by the neurosurgeon) and the histopathologic description was recorded for each section obtained per specimen. Displayed in Fig. 3B are successive biopsies of the same patient taken along the stereotactic trajectory (*z*-axis), that were described by a neuropathologist to show a cell-dense pleomorphic glial tumor expressing glial fibrillary acidic protein (GFAP) and microtubule-associated protein 2 (MAP2), $IDH1^{WT}$, 15% Ki67-positive tumor cell nuclei, and numerous vascular proliferates from coordinate $z = 0$ until 3 mm toward the tumor border. From 5 mm to 8 mm along the *z*-axis, the biopsies contained central nervous system tissue with a progressively decreasing number of infiltrating glial tumor cells. Sections of patients pre- and post-bevacizumab treatment were obtained from the Edinger Institute, Frankfurt am Main. Quantification of pseudopalisading areas was performed in ImageJ using the threshold function on H&E overview images of the tumor area.

***In situ* hybridization**

The work bench and instruments were carefully cleaned with RNAse-Zap (catalog no. R2020; Sigma Aldrich). Solutions were prepared using RNAse-free water and sterilized. Sections on slides were deparaffinized by serial passages into Roti-Histol and graded alcohol (100%–25%). Tissue was permeabilized by incubation for 10 minutes in 10 μg/mL proteinase K (catalog no. 04-1070; PeqLab, VWR). Slides were fixed for 10 minutes in 4% paraformaldehyde (PFA) and blocked for 10 minutes with acetic anhydride (0.25%; catalog no. 320102; Sigma Aldrich) in triethanolamine (1.5%; catalog no. 09278; Sigma Aldrich). Sections were dried for 2 hours at room temperature, incubated overnight at 65°C in a humidified chamber with digoxigenin (DIG)-labelled (DIG RNA labeling, cat. 11277073910; Roche Diagnostics) antisense or sense probes at a final concentration of 7 μg/mL, and diluted in a hybridization solution containing 100 μg/mL salmon sperm DNA (catalog no. AM9680; Ambion, Thermo Fisher Scientific) to mask unspecific binding, and 100 μg/mL of coprecipitant RNA (yeast RNA; catalog no. AM7118; Ambion). RNA probes were generated from human and mouse *APLN* and *APLNR* cDNA as described previously (15). The probe-containing hybridization solution was boiled at 95°C for 10 minutes before application. On day 2, nonspecific signals were removed by stringency washing in graded saline sodium citrate (from 20 × to 0.1 ×) and incubated with alkaline phosphatase–conjugated anti-DIG antibody (catalog no. 11093274910; Roche Diagnostics) overnight at 4°C. On day 3, the slides were washed in PBS-T (0.1% Tween in 1 × PBS) and incubated with 5-bromo-4-chloro-3-indolyl phosphate (BCIP)/nitro blue tetrazolium (NBT) substrate (catalog no. SK-5400; Vector Laboratories) in 0.1 mol/L Tris-HCl (pH 9.5) at 37°C for up to 4 days. For counterstaining with eosin, the slides underwent serial passages in graded alcohol (70%–100%) followed by application of Roti-Histol, and were then mounted with Entellan (catalog no. 107960, Merck Millipore). Pictures were taken under an Axioskop2 microscope with Axiocam 105 Color and Axiovision SE64 Rel. 4.9 software (Carl Zeiss). Quantification of pseudopalisading or apelin-positive areas was performed in ImageJ using the threshold function on six representative pictures (×5 magnification) per animal on hematoxylin and eosin (H&E) or on consecutive sections stained for apelin mRNA.

**Immunofluorescence and vessel density quantification**

Under pentobarbital (Narcoren; Merial) anesthesia, mice were transcardially perfused with 1× PBS followed by 4% phosphate-buffered PFA. The brain was postfixed for 2 days in 4% PFA and then left in 30% sucrose for ≥24 hours at 4°C. The brain was then embedded in Cryomatrix (catalog no. 6769006; Thermo Fisher Scientific) and frozen at −20°C. Tissue samples were prepared as horizontal sections (40-μm–thick) using a microtome. Floating sections were blocked for 1 hour at room temperature in 1× PBS containing 5% normal donkey serum (NDS; catalog no. 017-000-121; Jackson Immuno-Research), and 0.3% Triton-X (catalog no. 93418; Fluka). The sections were then incubated overnight at 4°C with the following primary antibodies: rabbit anti-MKi67 (1:200, catalog no. ab16667), rabbit anti-APLNR (1:100, catalog no. ab66218), rabbit anti-APLN 1:100, catalog no. ab59469 (all Abcam), rat anti-CD31 (1:50, catalog no. 550274; BD Biosciences), rabbit anti-von Willebrand factor (vWF; 1:400, catalog no. A0082; Dako, Agilent Technologies), or rabbit anti-GFP (1:500, catalog no. A11122; Thermo Fisher Scientific). The next day, the sections were incubated for 3 hours at room temperature with the following secondary antibodies: biotin-labeled donkey anti-rabbit or anti-rat antibody (1:250, catalog no. 711-065-152; 712-065-150) and/or 2 hours at room temperature with streptavidin-AF488 or -AF594 (1:500, catalog no. 016-540-084; 016-580-084, all Jackson Immuno-Research). Alternatively, sections were directly incubated for 2 hours at room temperature with the secondary antibodies donkey anti-rabbit AF488 or AF594 (1:500, catalog no. A-21206; A-21207, Thermo Fisher Scientific). All antibodies were diluted in blocking solution. For nuclear DAPI, 1:1,000 was used. After staining, tissue was mounted in fluorescent mounting medium (catalog no. S3023; Dako) and photographs were taken using an Axiovert25 microscope with Axiocam MRm and Axiovision Rel 4.8 software (Carl Zeiss).

Stereological analysis of vessel length density was performed for the GFP-positive tumor area of CD31- or vWF-positive red fluorescent vessels on every 12th section using the space ball method of StereoInvestigator Software 10.21.1 (MicroBrightField Bioscience) connected to an Olympus-BX53-microscope (Olympus Europe) and a motorized object table (MicroBrightField Bioscience).

### IHC and tumor volume

Free-floating sections were immersed in 0.3% peroxide for 10 minutes to block endogenous peroxidase, washed in PBS, and incubated for 1 hour at room temperature in PBS containing 0.3% Triton X-100 and 5% NDS. Sections were then incubated with the primary antibodies rabbit anti-MKi67, rabbit anti-GFP (1:1,000, catalog no. A-11122, Thermo Fisher Scientific), or mouse anti-VIM (1:200, catalog no. sc-6260, Santa Cruz Biotechnology) overnight at 4°C in PBS containing 5% NDS. The next day, after three washes in PBS to remove unbound antibodies, the sections were incubated with secondary biotin donkey anti-rabbit, anti-rat, or anti-mouse antibodies (1:250, catalog no. 711-065-152; 712-065-150; 115-065-166, Jackson Immuno-Research) for 3 hours and then for 1 hour at room temperature with streptavidin-conjugated horseradish peroxidase (1:200, catalog no. SA-5004, Vector Laboratories). After washing in PBS, the sections were stained with DAB substrate according to the manufacturer's instructions (catalog no. DC137C100DCS, Innovative Diagnostik-Systeme). Finally, sections were mounted on glass slides (Superfrost Plus, R.Langenbrinck GmbH) and air dried for 10 minutes, followed by counterstaining with hematoxylin for 1 minutes. The slides were then rinsed with tap water, dehydrated with a graded series of ethanol (70%, 80%, 96%, 100%), cleared two times with xylene, and coverslipped with RotiHistokit II mounting medium (catalog no. 6640.1, Carl Roth GmbH). Tumor volumes were obtained from H&E or GFP-stained tumor sections by measuring the area of every 12th section and calculated using the Cavalieri method. The overall tumor volume was determined by measuring the total area including regions with single invasive tumor cells visible on GFP-stained sections. In addition, the compact tumor volume was determined by measuring the area of GFP-positive tumor cells that were in direct contact with neighboring tumor cells. The invasive tumor volume was determined as the difference between overall GFP and compact GFP tumor volume, and tumor invasiveness was determined as the percentage of invasive tumor volume over overall GFP tumor volume.

### Statistical analysis

The distribution of each variable was summarized by its mean, SD, or SEM. Number of individuals, replicates, and or repetition of independent experiments are indicated in the figure text. In treatment groups comparing two groups, values are reported as the mean ± SD and unpaired Student *t* test was used to determine statistical significance. In treatment groups comparing more than two groups, values are reported as the mean ± SD and one-way ANOVA with Newman–Keuls *post hoc* test was used to determine statistical significance. For spheroid invasion assay, data are reported as the mean ± SEM and two-way ANOVA was used to determine the statistical significance. For survival experiments, Kaplan–Meier curves were used and log-rank (Mantel–Cox) test was applied to determine statistical significance. *P* values are indicated as $^{*}$, $P < 0.05$; $^{**}$, $P < 0.005$; and $^{***}$, $P < 0.0005$ in all results. All statistical analyses were conducted using GraphPad Prism 5.

## Results

### Apelin is downregulated by VEGFA/VEGFR2 blockade

We explored the pathophysiologic context of apelin signaling in a GBM subtype-specific manner by searching the TCGA dataset for genes coexpressed with *APLN* (the gene encoding for apelin; ref. 27). Interestingly, gene ontology analysis revealed that high apelin expression was associated with angiogenesis and blood vessel morphogenesis (Supplementary Fig. S1A) in the proneural or classical subtypes, but not in the mesenchymal subtype of GBM (Supplementary Table S1), which relates to previous observations that particularly the proneural and classical GBM subtypes may respond to antiangiogenic treatments (14, 28). To investigate a functional link between the VEGFA/VEGFR2 and apelin/APLNR signaling pathways, we examined the effects of bevacizumab in a mouse model of proneural GBM. First, we analyzed tumor samples from a murine platelet-derived growth factor B (PDGFB)-driven proneural-like GBM model based on the RCAS/Tva system (29). In this model, genetically manipulated NPCs are the point of origin for GBM. Tumor-bearing mice were then treated with a murine bevacizumab surrogate anti-VEGFA antibody (B20-4.1.1, Roche), which increased survival and decreased total vessel area, but also let to an increased tumor volume compared with mice treated with vehicle (30). *In situ* hybridization of control tumors revealed strong apelin mRNA expression in areas corresponding to GBM pseudopalisades (Fig. 1A asterisks) and tumor vessels (Fig. 1A arrows). In the anti-VEGFA antibody–treated samples, pseudopalisades were less prominently stained by apelin *in situ* hybridization (Fig. 1A asterisks) and smaller and less numerous vascular proliferates were detectable (Fig. 1A arrows). qPCR confirmed that apelin expression was downregulated in the treated samples as compared with control samples (Fig. 1A).

In a second set of experiments, we orthotopically implanted mice with murine transgenic GBM stem-like cells (GSCs; *p53* knockout GSCs overexpressing PDGFB, $p53^{KO}$PDGFB GSCs) as a model of human proneural GBM (31, 32). After tumor establishment, the murine VEGFR2-blocking antibody DC101 (corresponding to ramucirumab, Eli Lilly) was intracerebrally infused into the mice (Supplementary Fig. S1B). As in the RCAS/Tva model, the vehicle-treated control tumors showed strong apelin expression in tumor cells (Fig. 1B, asterisks) and in tumor vessels (Fig. 1B, arrows). Apelin mRNA expression was greatly reduced in the anti-VEGFR2–treated tumors. In particular, we found that apelin-labeling was strongly and significantly reduced in pseudopalisades within anti-VEGFR2–treated (5.1%) compared with control tumors (34.3%) while the extent of pseudopalisades (quantification of the total pseudopalisading area) was unchanged (Fig. 1C). Also *APLN*-positive vessel area was significantly reduced by 35% in anti-VEGFR2–treated tumors. Comparable observations were made in biopsies of GBM from patients before and after bevacizumab treatment. While the total area of pseudopalisading necrosis did not change (Fig. 1D; Supplementary Fig. S1C), we found that apelin expression was lower in the tumor samples obtained after antiangiogenic treatment (Fig. 1D; Supplementary

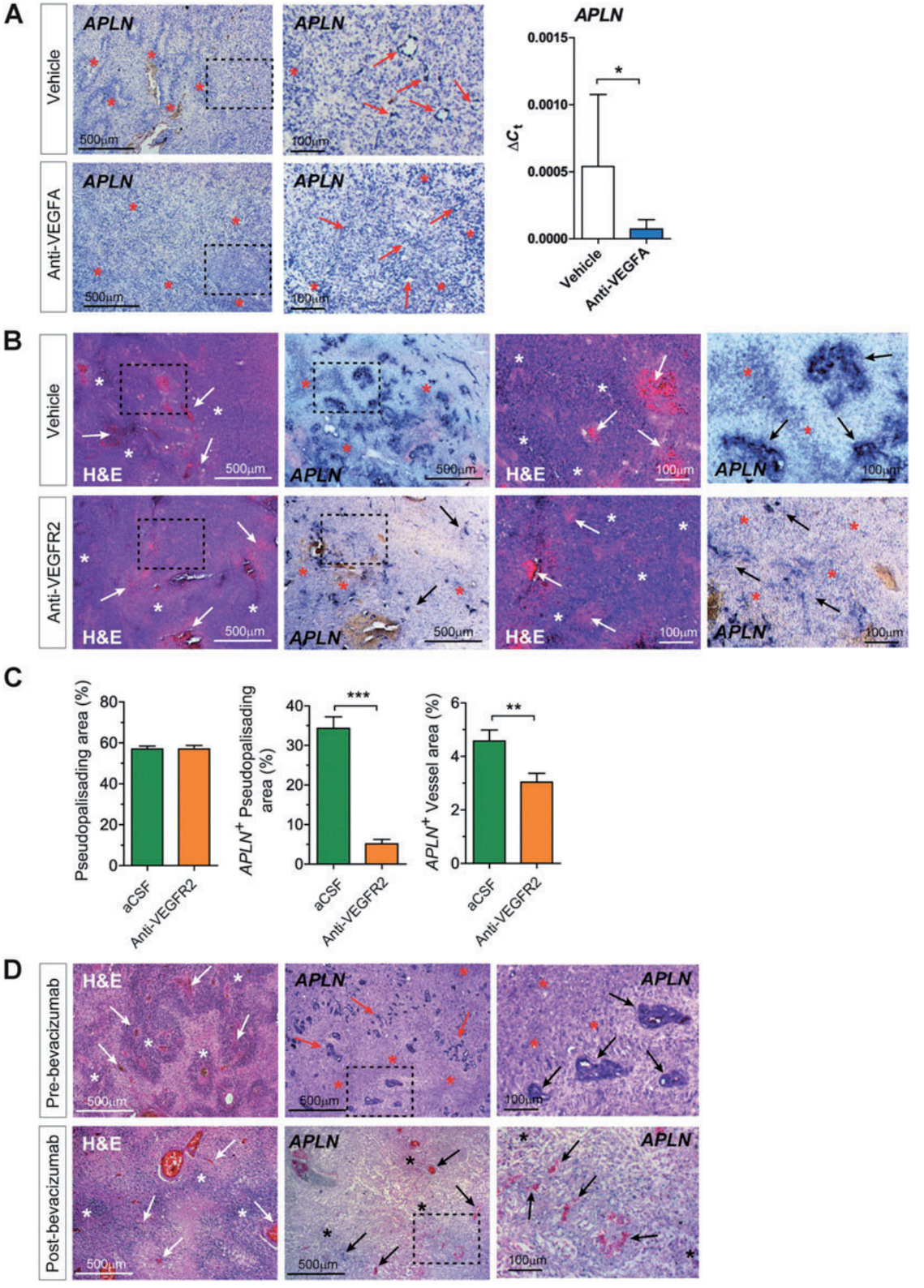


**Figure 1.**

Apelin is downregulated by anti-VEGFA or anti-VEGFR2 treatment. Mouse or human GBM samples were stained by H&E and consecutive sections were analyzed by *APLN in situ* hybridization; cell-dense pseudopalisading structures (asterisks) and vascular proliferates (arrows) are indicated. **A,** In a murine PDGFB-driven GBM model (RCAS/Tva system; ref. 29), apelin is strongly expressed in pseudopalisades and tumor vessels of controls (vehicle) but is weak in anti-VEGFA antibody-treated samples, with few apelin-positive vessels; this is corroborated by qPCR ($n = 4$ vs. 4). **B**, Mice orthotopically implanted with $p53^{KO}$PDGFB GSCs were intracerebrally infused with anti-VEGFR2 antibody or vehicle ($n = 7$ vs. 10). The overall extent of pseudopalisading structures was unchanged, but apelin levels were reduced in pseudopalisades and tumor vessels in anti-VEGFR2–treated tumors compared with controls. This was quantified in **C**. **D,** Biopsies from 7 patients pre- and post-bevacizumab were stained histologically and consecutive sections were inspected by *in situ* hybridization for apelin; note that apelin labeling is strong in vascular proliferates and pseudopalisades pre-bevacizumab but greatly reduced post-treatment. Scale size is indicated in individual micrographs; statistical significance (*t* test) is indicated. **, $P < 0.005$; ***, $P < 0.0005$.

Fig. S1D) than in the initial resected samples; note that control genes (e.g., *HPRT*, *ACTB*) were unchanged or upregulated (e.g., *NEK7*, *VAMP4*) confirming good RNA quality of patient samples (Supplementary Fig. S1D). In agreement with previous studies (15), we observed that apelin expression was also much higher in GBM (initial biopsy before antiangiogenesis) than in tumor-free human brain tissue (Supplementary Fig. S1E).

These results indicate that the *APLN* and *VEGFA* genes are coexpressed in GBM and that blocking VEGFA/VEGFR2 signaling with antibodies reduced apelin expression. Hence, we sought to

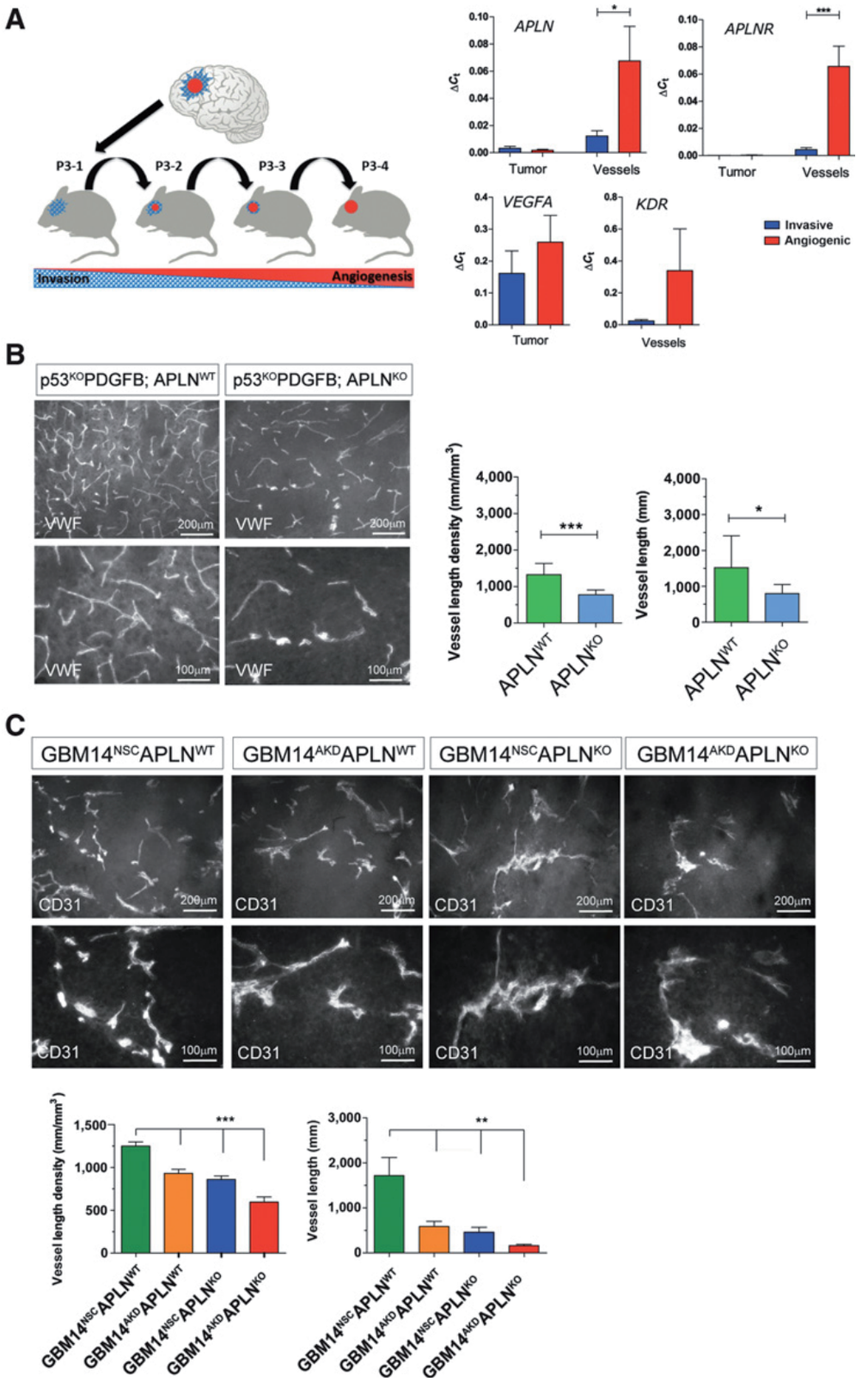


**Figure 2.**

Glioma cell- and host-derived apelin control GBM angiogenesis. **A,** A xenograft serial implantation model was used to investigate the angiogenic switch; *APLN, APLNR*, and *KDR* were upregulated in the rat tumor microenvironment after the angiogenic switch (while *VEGFA* was unchanged). *APLN* and *APLNR* expression remained constantly low in human tumor cells (quantified by species-specific qPCR in 8 invasive vs. 5 angiogenic tumors originating from 7 different patients; ref. 33). **B** and **C,** GBM were immunostained for vWF or CD31 and analyzed for vascular patterns. **B,** Vascular density (VLD and VL) in *p53*$^{KO}$PDGFB GBM was higher in *APLN*$^{WT}$ mice ($n = 7$) and was significantly reduced in *APLN*$^{KO}$ mice ($n = 8$). **C,** In GBM14 orthotopic xenografts, VLD and VL were greatly diminished in tumors with reduced apelin levels relative to controls (group-size was between $n = 4$ and $n = 7$). Scale size is indicated in individual micrographs; statistical significance (*t* test or one-way ANOVA plus *post hoc* test) is indicated. *, $P < 0.05$; **, $P < 0.005$; ***, $P < 0.0005$.

elucidate whether APLNR targeting has synergistic effects with VEGFA/VEGFR2 blockade. We also investigated the potential adverse effects of reduced apelin expression in GBM.

### Apelin and APLNR upregulation is correlated with the angiogenic switch in GBM

We previously established a rodent model of the angiogenic switch in GBM that involved serial transplantation of a patient-derived xenograft (33–35). This model is initially characterized by highly infiltrative brain tumors without apparent neoangiogenesis (Fig. 2A; ref. 33), but after several generations of *in vivo* passaging acquires an angiogenic, noninvasive phenotype (angiogenic switch; ref. 34). This model (and an alternative model; ref. 35) allowed us to determine the relative expression levels of individual genes derived from the GBM cells or the host.

In both models, we compared the gene expression patterns in the initial generation of tumors against later-generation tumors (Fig. 2A). We found that the vascular expression levels of apelin and APLNR mRNA were dramatically increased in the tumor microenvironment of angiogenic versus invasive GBM (Fig. 2A; Supplementary Fig. S2A) highlighting a central role of the APLNR signaling pathway in promoting angiogenesis in GBM.

### Host-derived apelin controls GBM angiogenesis

To study the role of APLNR signaling within the tumor microenvironment, we orthotopically implanted murine GSCs into *APLN*-wild-type ($APLN^{WT}$) or *APLN*-knockout ($APLN^{KO}$) mice. In the first set of *in vivo* experiments, we used proneural-like $p53^{KO}$PDGFB GSCs expressing low levels of apelin (Supplementary Fig. S2B). The GBM originating from these cells produced an invasive and well-vascularized tumor. The vessel length density (VLD) was quantified in the tumor area (1,327 mm/mm$^3$; Fig. 2B). When $p53^{KO}$PDGFB GSCs were implanted into $APLN^{KO}$ mice, the VLD was significantly reduced by 41% to 776 mm/mm$^3$. The intratumoral vessel length (VL) was reduced by 47% from 1,520 mm in $APLN^{WT}$ mice to 799 mm in $APLN^{KO}$ mice (Fig. 2B).

In human GBM, the apelin expression levels were related to angiogenic signaling pathways in proneural and classical, but not mesenchymal GBM. Therefore, we also established a mouse GSC culture model of the classical GBM subtype ($cdkn2a^{KO}$EGFRvIII GSCs; *CDKN2A*-knockout cells overexpressing EGFRvIII; refs. 28,

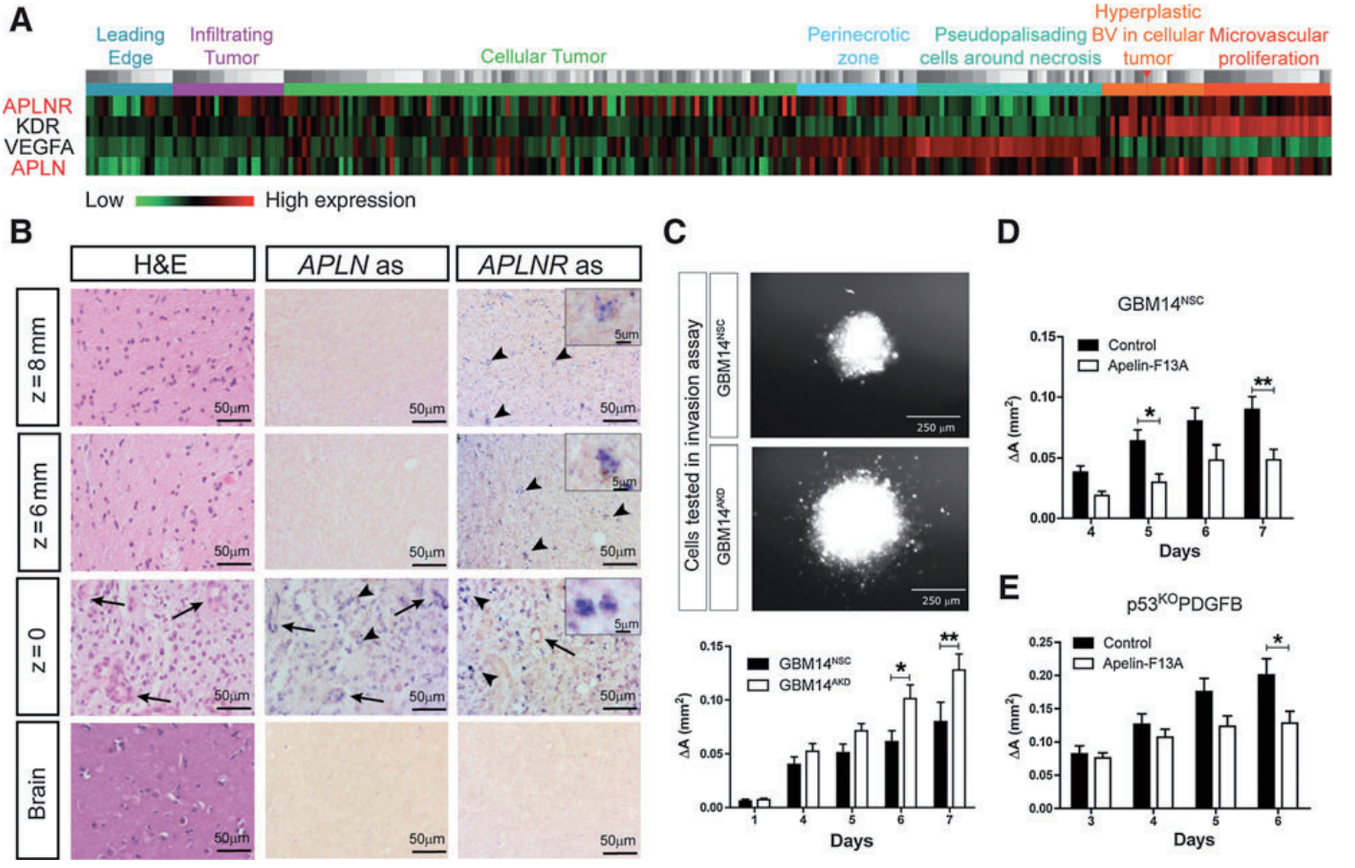


**Figure 3.**

APLNR is expressed in the tumor margin and attenuation of apelin/APLNR signaling *in vitro* uncovers a role of APLNR in GBM cell invasion. **A,** IVY GBM Atlas Project dataset depicting regional gene expression levels; note that *APLN* expression is high in pseudopalisades and *APLN* or *APLNR* are abundant in microvascular proliferations; *APLNR* alone is high in the infiltrating tumor area. **B,** Stereotactic GBM biopsies taken along a trajectory from the cell dense tumor (z = 0 mm) to the infiltrative tumor in the tumor periphery (z = 6 and 8 mm). *APLN* is expressed in tumor vessels (arrows) and individual cells (arrowheads) in the cell-dense tumor (z = 0), but is undetectable in the periphery (z = 6 and 8 mm). *APLNR* is expressed in tumor vessels (arrows) and in individual cells at z = 0, and in peripheral cells at z = 6 and 8 mm. The magnified insets show the cellular staining. *APLN* and *APLNR* are undetectable in tumor-free brain. **C**, *In vitro* spheroid invasion assay with $GBM14^{AKD}$ cells demonstrated significantly greater invasion compared with the control $GBM14^{NSC}$ cells. **D** and **E,** Application of 1 μmol/L of apelin-F13A attenuated invasion of $GBM14^{NSC}$ (**D**) and $p53^{KO}$PDGFB (**E**) GSCs. Data were obtained from at least five different spheres per condition. Scale size is indicated in individual micrographs; statistical significance (one-way ANOVA plus *post hoc* test) is indicated. *, $P < 0.05$; **, $P < 0.005$.

32). The GBM originating from *cdkn2a*$^{KO}$EGFRvIII GSCs produced a high vascular density (Supplementary Fig. S2C). The VLD was 2,746 mm/mm$^3$ in *APLN*$^{WT}$ mice (Supplementary Fig. S2C) and was significantly reduced by 33% to 1,830 mm/mm$^3$ in *APLN*$^{KO}$ mice. Overall vessel length (VL) was reduced by 75.4% from 82,726 mm in *APLN*$^{WT}$ mice to 20,349 mm in *APLN*$^{KO}$ mice. This set of experiments corroborated our working hypothesis that host-derived apelin plays a prominent role in controlling the extent of tumor vascularization.

### Combined effects of GBM cell- and host-derived apelin on tumor angiogenesis

Next, we investigated the contribution of GBM cell–derived apelin on tumor angiogenesis *in vivo*. We selected two patient-derived GBM cultures of the proneural subtype that expressed relatively high levels of apelin (arrows in Supplementary Fig. S2D). First, we manipulated primary GBM14 cells (21) to express a shRNA construct to knockdown endogenous *APLN* (GBM14$^{AKD}$; Supplementary Fig. S2E) or a nonsilencing control shRNA (GBM14$^{NSC}$). *APLN*-knockdown (APLN$^{KD}$ or AKD) did not affect GBM viability or expansion *in vitro* (Supplementary Fig. S2E). Six weeks after orthotopic injection of GBM14$^{NSC}$ cells into immunocompromised wild-type mice, we detected the formation of a vascularized brain tumor mass with a VLD of 1,249 mm/mm$^3$ (Fig. 2C). The VLD of GBM14$^{AKD}$ orthotopic xenografts in wild-type mice was 930 mm/mm$^3$, a reduction of 25.5% versus GBM14$^{NSC}$, which suggests that GBM-derived apelin is proangiogenic. The modulation of human GBM-derived apelin is pathologically meaningful in mouse models because the amino acid sequences of the bioactive peptide apelin-13 of human or mouse origin are identical (15).

Implantation of GBM14$^{NSC}$ into *APLN*$^{KO}$ mice reduced the tumor vasculature by approximately 25% as compared with GBM14$^{NSC}$ gliomas grown in *APLN*$^{WT}$ mice (Fig. 2C). When GBM14$^{AKD}$ cells were implanted into immunodeficient *APLN*$^{KO}$ mice, we detected scant tumor angiogenesis with a VLD of 569 mm/mm$^3$, a 54% reduction relative to that in control mice (Fig. 2C). Furthermore, the overall VL was reduced from 1,720 mm to 588 mm (by 66%), 460 mm (by 73%), and 161 mm (by 91%), respectively.

We also orthotopically implanted mice with a second well-established human primary GSC model (NCH644 cells (20)) corresponding to the proneural subtype (36). These cells produced a GBM with a VLD of 1,168 mm/mm$^3$ in wild-type mice (Supplementary Fig. S2F and S2G). Stable knockdown of *APLN* in the tumor cells (NCH644$^{AKD}$; Supplementary Fig. S2F) reduced the VLD by 50% to 648 mm/mm$^3$ (Supplementary Fig. S2G).

This series of experiments consistently indicated that tumor cell–derived and/or host-derived *APLN* levels are directly correlated with the level of tumor angiogenesis. GBM vascularization was reduced by *APLN* knockdown in tumor cells or *APLN* knockout. Injection of *APLN*$^{KD}$ GBM cells into *APLN*$^{KO}$ mice achieved an even greater reduction in GBM angiogenesis.

### Reduced apelin in APLNR-expressing GBM is related to invasion

In the IVY Glioblastoma Atlas Project RNA-seq database, we found regionally distinct expression levels of apelin and APLNR (Fig. 3A; Supplementary Fig. S3A). In particular, apelin was more abundantly expressed in tumor areas enriched with microvascular proliferation and hyperplastic blood vessels (BV; with high levels of *KDR* expression). However, apelin expression was very low in microdissected GBM samples containing an infiltrating tumor or a leading edge (Fig. 3A), whereas APLNR mRNA expression remained high, especially in the infiltrating tumor zone (Fig. 3A). The elevated expression of APLNR was also associated with increased expression of genes involved in tumor cell invasion like *MMP2* (matrix metallopeptidase 2) and *BAI1/3* (brain-specific angiogenesis inhibitor 1/2), but the expression of tissue inhibitor of metalloproteinase-1 (TIMP1), an MMP2 inhibitor, was low (Supplementary Fig. S3A).

To further investigate a potential role of *APLNR* in invasive GBM areas, we used GBM biopsies obtained by neurosurgical resection using a neuronavigation system (Supplementary Fig. S3B). *In situ* hybridization revealed that the tumor center expressed apelin in cellular (arrowheads) and vascular regions (arrows; also visible on consecutive H&E), whereas apelin was not detected at the tumor border. APLNR was also expressed in the cellular (arrowheads) and vascular (arrows) regions in the tumor center, but APLNR expression was more pronounced in some dispersed cells along the tumor border (Supplementary Fig. S3B, arrowheads). To provide a greater resolution of local *APLN*/*APLNR* expression, we examined stereotactic GBM biopsies with defined three-dimensional coordinates (Fig. 3B). In successive biopsies taken along the stereotactic trajectory (*z*-axis), from the tumor core to the invasive zone, we observed a progressive reduction in apelin expression (Fig. 3B), but APLNR expression was maintained in individual cells (arrowheads) of the invasive margin. Also, immunostaining for APLNR in orthotopic GBM mouse models (see below) confirmed its expression in invasive tumor cells (Supplementary Fig. S3C and S3D). Taken together, these findings indicate that APLNR expression is maintained in scattered GBM cells within the apelin-free invasive tumor margin.

To investigate a potential role for apelin/APLNR signaling in GBM invasion *in vitro*, we embedded GBM14 cells (GBM14$^{AKD}$ or GBM14$^{NSC}$) in a collagen matrix (28). We found that the GBM14$^{AKD}$ cells were much more invasive than the control GBM14$^{NSC}$ cells (Fig. 3C). To exclude that the increase in invasive area observed with GBM14$^{AKD}$ cells compared with GBM14$^{NSC}$ control cells was a result of enhanced proliferation we analyzed *in vitro* proliferation assays and compared their Ki67 status, but did not detect any differences (Supplementary Fig. S2E, S3E, and S3F).

Next by performing a wound healing and a Boyden chamber chemotaxis assay (Supplementary Fig. S3G and S3H), we confirmed that the depletion of apelin in GBM cells (GBM14 and U87MG) accelerates invasion *in vitro*. However, application of apelin-F13A, another APLNR ligand (37), to GBM14 spheres reduced invasiveness (Fig. 3D). A similar inhibitory effect of apelin-F13A on glioma cell invasion was also observed in murine *p53*$^{KO}$PDGFB GSCs (Fig. 3E). In line with that, addition of apelin-F13A in the two migration assays also attenuated the invasiveness of *APLN*$^{KD}$ cells (Supplementary Fig. S3G–S3I).

Overall, we found that APLNR is expressed in the apelin-free invasive zone of patient-derived GBM samples, that the absence of endogenous apelin can increase GBM cell invasion *in vitro*, and that application of the APLNR ligand apelin-F13A has an anti-invasive effect.

### Anti-invasive role of apelin in GBM *in vivo*

Next, we investigated whether apelin modulates tumor invasion in murine GBM models *in vivo*. Immunostaining for a GFP reporter in GBM14 cells and histologic staining revealed the

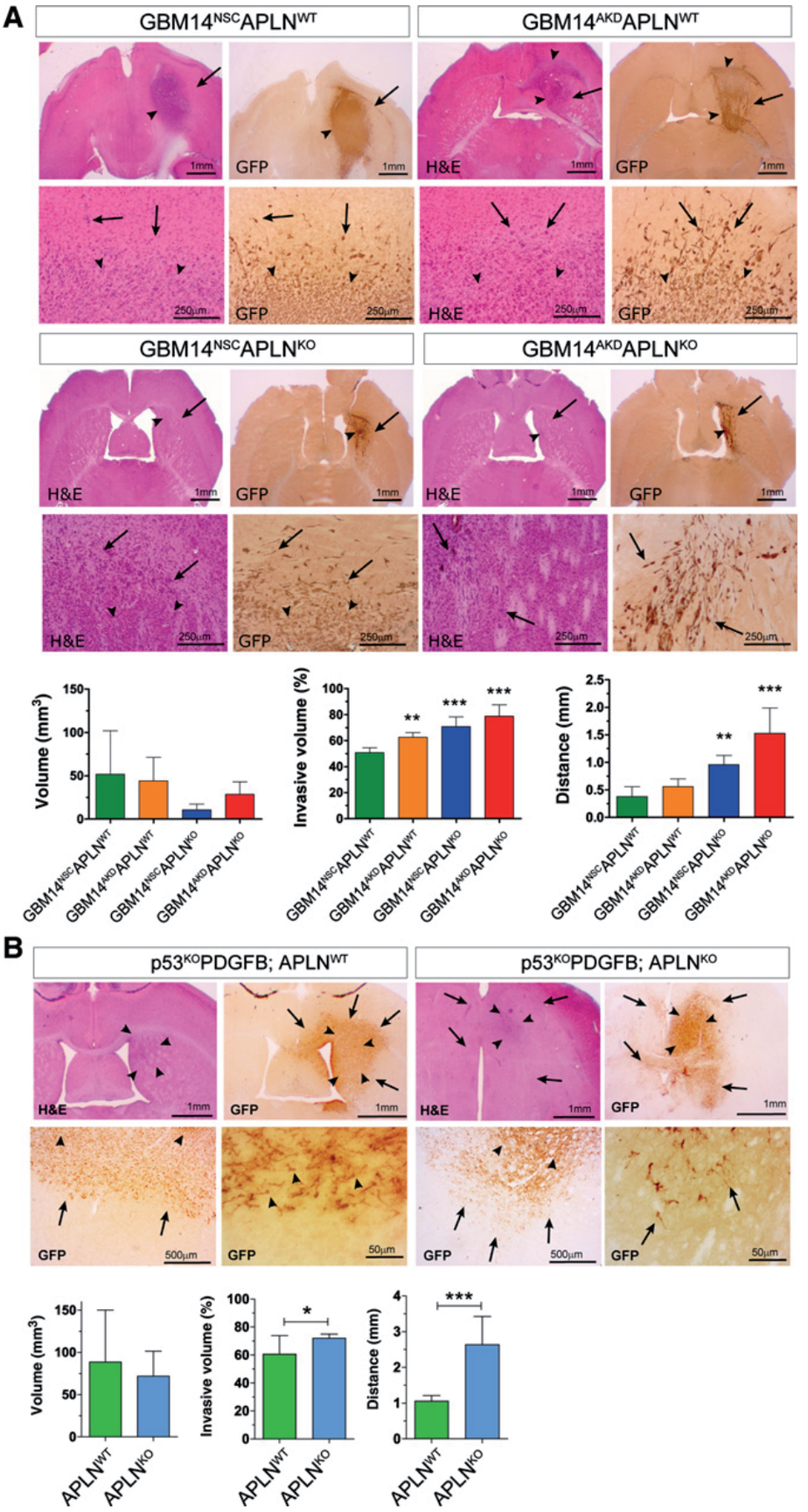


**Figure 4.**

Anti-invasive role of apelin in orthotopic models of proneural GBM. **A** and **B,** GBM were analyzed by H&E and GFP immunostaining to assess overall, compact, and invasive tumor volumes, as well as the migration distance of single cells from the tumor mass Arrowheads, compact tumor border; arrows, single invading cells. **A,** GBM14$^{NSC}$ or GBM14$^{AKD}$ GSCs were grown in immunodeficient *APLN*$^{WT}$ or *APLN*$^{KO}$ mice. Although there is no difference in overall tumor volume, the invasive tumor volume (% invasive volume) is significantly greater for GBM14$^{AKD}$ cells implanted into *APLN*$^{WT}$ ($n = 7$), GBM14$^{NSC}$ cells implanted into *APLN*$^{KO}$ ($n = 4$), and GBM14$^{AKD}$ cells implanted into *APLN*$^{KO}$ mice ($n = 4$) as compared with GBM14$^{NSC}$ cells implanted into *APLN*$^{WT}$ mice ($n = 7$). The distance of single invading cells to the tumor center is significantly greater in the *APLN*$^{KO}$ mouse xenografts. **B,** *p53*$^{KO}$PDGFB GBM were grown in immunocompetent *APLN*$^{WT}$ or *APLN*$^{KO}$ mice. Although the overall tumor volume is unchanged in *APLN*$^{KO}$ mice ($n = 8$) compared with *APLN*$^{WT}$ mice ($n = 7$), the invasiveness, as assessed by percent invasive volume and distance of migration, is substantially increased in *APLN*$^{KO}$ mice. Scale size is indicated in individual micrographs; statistical significance (*t* test or one-way ANOVA plus *post hoc* test) is indicated. *, $P < 0.05$; **, $P < 0.005$; ***, $P < 0.0005$.

tumor mass (H&E staining; Fig. 4A; arrowheads indicate compact GFP volume). In addition, individual GFP-positive cells (arrows) were observed to invade the brain. When intratumoral apelin levels were gradually reduced by implanting GBM14$^{AKD}$ cells into *APLN*$^{WT}$ mice, by inoculation of GBM14$^{NSC}$ into *APLN*$^{KO}$ animals or GBM14$^{AKD}$ cells into *APLN*$^{KO}$ mice, the overall tumor volume gradually decreased (as compared with controls), but the invasive volume of GBM cells increased significantly (Fig. 4A; Supplementary Fig. S4A).

We confirmed that the change of *in vivo* tumor volume was not a result of altered GBM cell proliferation (Supplementary Fig. S4B). Consistently, orthotopic implantation of NCH644$^{NSC}$ GSCs generated tumors with few regions of accelerated invasiveness (Supplementary Fig. S4C, arrows), but implantation of NCH644$^{AKD}$ cells resulted in a much more pronounced invasive pattern (Supplementary Fig. S4C, arrows).

Similar observations were made using an immunocompetent model of proneural GBM, in which we implanted *p53*$^{KO}$PDGFB GSCs into apelin-deficient hosts. Again, the resulting tumors were much more invasive than GBM grown in *APLN*$^{WT}$ hosts (Fig. 4B). In *p53*$^{KO}$PDGFB GBM, the distance of tumor cell migration away from the dense tumor mass increased from 1.1 in *APLN*$^{WT}$ to 2.6 mm in *APLN*$^{KO}$ mice. In addition, the invasive ratio increased by 1.6 times (Supplementary Fig. S4D) and the percentage of invasive versus overall volume increased from 59% to 72% (Fig. 4B). Using *cdkn2a*$^{KO}$EGFRvIII GBM as a model of the classical subtype, we found that the compact and overall volumes were decreased by 53% in *APLN*$^{KO}$ mice compared with *APLN*$^{WT}$ mice, but tumor invasiveness significantly increased as well (Supplementary Fig. S4E).

In another approach to investigate apelin-modulated GBM cell invasion, we implanted human primary GBM cells into murine orthotopic brain slice cultures. Here apelin knockdown increased the invasiveness of proneural NCH644 as well as classical GBM5av cells (Supplementary Fig. S4F and S4G).

In summary, we found that apelin derived from the host and tumor cells is an essential mediator of neoangiogenesis in GBM and that apelin also contributes to suppressing GBM cell invasion. This was demonstrated by an inverse correlation between apelin expression levels with GBM invasiveness in our *in vitro*, *ex vivo*, and *in vivo* models and by the direct anti-invasive effect of APLNR stimulation in our collagen-based invasion as well as migration assays.

### Apelin-F13A inhibits GBM angiogenesis and invasion

To study the potential of APLNR as a therapeutic target for GBM, we tested the *in vivo* application of apelin-F13A (37). Apelin-F13A with the C-terminal phenylalanine mutated to alanine can antagonize the APLNR *in vivo* (38), but was also found to act as an agonist on different functional assays, such as adenyl cyclase inhibition or APLNR internalization (39, 40). First, we established that APLNR is abundantly expressed in scattered, infiltrative GBM cells in our models (Supplementary Figs. S3C and S3D and S5A and S5B). Then we explored the therapeutic properties of apelin-F13A *in vivo*. We found that the vascular density of murine proneural-like GBM was reduced from a VLD of 1,069 mm/mm$^3$ in control mice to 629 mm/mm$^3$ in apelin-F13A–treated mice (Fig. 5A). The overall tumor volume was decreased by 56% from 104 mm$^3$ in control mice to 46 mm$^3$ in apelin-F13A–treated mice. While the compact tumor volume did not change significantly, the invasive tumor volume decreased by 53% from 72 mm$^3$ in control mice treated with artificial cerebrospinal fluid (aCSF) to 34 mm$^3$ in apelin-F13A–treated mice (Fig. 5A). We then repeated this experiment using proneural GBM14 GSCs. We observed a reduction in VLD for these human-derived GBM, from 1,333 mm/mm$^3$ in control mice to 749 mm/mm$^3$ in apelin-F13A–treated mice (Fig. 5B). In addition, overall tumor volume decreased by 68% from 69 mm$^3$ in control mice to 22 mm$^3$ in apelin-F13A–treated mice. As in the *p53*$^{KO}$PDGFB model, the compact tumor volume did not change significantly in the human GBM model, but the invasive tumor volume decreased by 59% from 31 mm$^3$ in control mice to 13 mm$^3$ in apelin-F13A–treated mice (Fig. 5B).

To test the binding specificity of the apelin peptides as well as the functional response of the GBM APLNR, we performed two *in vitro* internalization assays (15, 40–43); because internalization rates of GPCRs give valuable insight in signaling activity by native (nonrecombinant) GPCR (44). We found that the addition of apelin-13 and apelin-F13A caused the internalization of the APLNR to cytoplasmic and perinuclear regions (Supplementary Fig. S5C). Most interestingly, we detected a difference in the APLNR redistribution in response to the two peptides. While apelin-13 led to a massive decrease of APLNR localization in the nucleus, apelin-F13A caused exactly the opposite outcome (Supplementary Fig. S5C). In a second internalization assay, we administered GFP-linked apelin peptides to GBM14 cells. We found that both, apelin-13 and apelin-F13A, were internalized by the cells, while a scrambled peptide was not (Supplementary Fig. S5D). In addition, we confirmed the specificity of peptide uptake by performing a dose escalation with unlabeled peptide showing that uptake of both GFP-labeled peptides was specifically blocked by corresponding unlabeled peptides (Supplementary Fig. S5E).

These findings imply that the synthetic APLNR ligand apelin-F13A efficiently suppressed angiogenesis and invasiveness in two models of GBM (Fig. 6A). Apelin-F13A can bind and activate the APLNR, functions as a competitive agonist for other APLNR ligands, and has only partial APLNR-activating properties (19). Our receptor internalization assay revealed that apelin-13 or apelin-F13A induce distinct patterns of intracellular APLNR localization, which can point-out differences in signaling cues initiated by these two peptides. This may explain why only apelin-F13A (but not apelin-13) was able to block the proangiogenic effects of intratumoral apelin while both ligands suppressed tumor invasion (Supplementary Fig. S5F).

### Cotargeting VEGFR2 and APLNR synergistically improved survival of murine models of GBM

One of the major adverse effects of bevacizumab for the treatment of GBM is an increase in tumor cell invasiveness or upregulation of alternative angiogenic factors (10). Hence, we asked whether blocking the proangiogenic and -invasive properties of APLNR could overcome the pathologic side effects of established antiangiogenic regimen like anti-VEGFR2 therapy, and hence improve overall survival. Orthotopically implanted *p53*$^{KO}$PDGFB GBM were allowed to expand for one week in mice. These mice were then treated intracerebrally with apelin-F13A, anti-VEGFR2 antibody, apelin-F13A, and anti-VEGFR2 antibody, or with vehicle (aCSF) alone as a control (Fig. 6B). The median survival of aCSF-treated mice was 52 days. Administration of anti-VEGFR2 increased survival by 28% compared with control mice, with a median survival of 67 days. Administration of apelin-F13A alone achieved a similar increase in survival (63 days; 19%

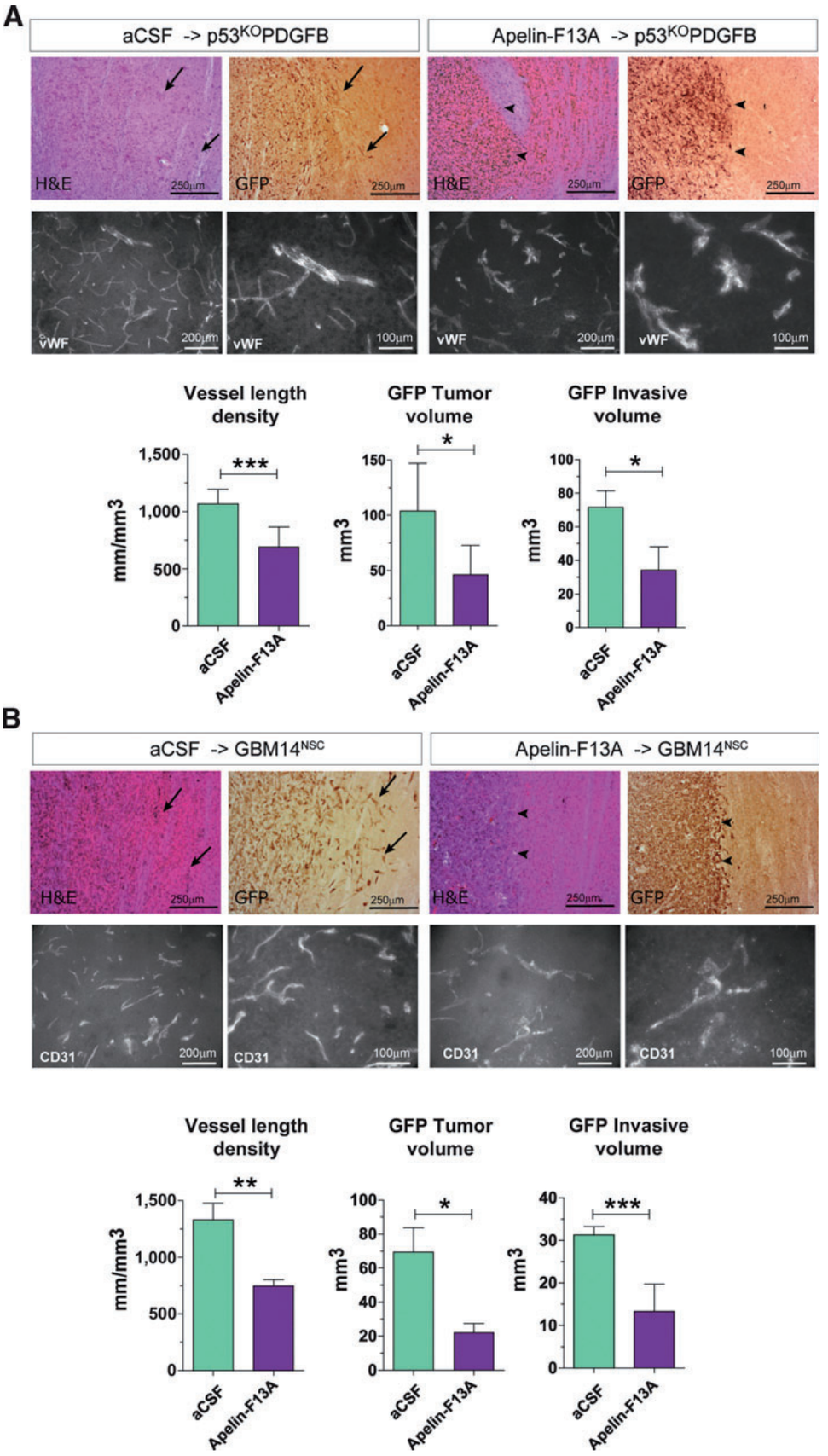


**Figure 5.**

The APLNR ligand apelin-F13A inhibits GBM angiogenesis and invasion. **A** and **B,** murine *p53*$^{KO}$PDGFB (**A**) or human GBM14 (**B**) GSCs were implanted and once GBM were established, aCSF or apelin-F13A was administered intracerebrally. Both, mouse- and patient-derived GBM showed a significant reduction in VLD and VL, as well as for invasive and overall tumor volume. Arrows, single invasive tumor cells in GFP- or H&E-stained sections; arrowheads, compact tumor border. aCSF or apelin-F13A were infused into 8 and 6 mice with murine GBM and 6 and 5 mice with human GBM, respectively. Scale size is indicated in individual micrographs; statistical significance (*t* test) is indicated. *, $P < 0.05$; **, $P < 0.005$; ***, $P < 0.0005$.

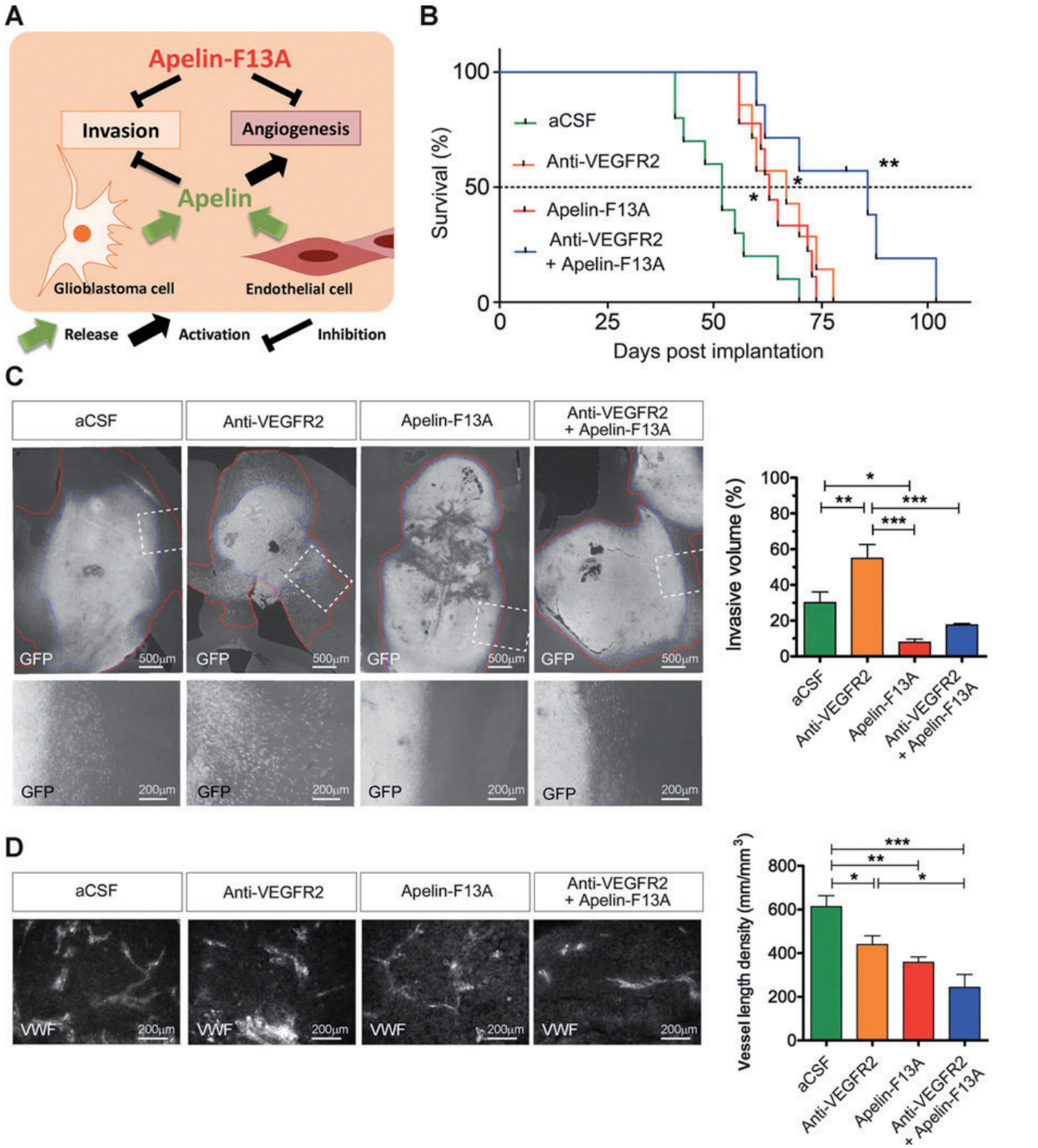


**Figure 6.**

Cotargeting of VEGFR2 and APLNR synergistically improves survival of mice bearing GBM. **A,** Model for apelin/APLNR signaling in GBM. Apelin is released by GBM and/or endothelial cells, activates APLNR on tumor cells (which inhibits invasion) and on endothelia (activating/sustaining angiogenesis); administration of apelin-F13A attenuates both angiogenesis and invasion. **B,** Intracerebral infusion of apelin-F13A and/or anti-VEGFR2 antibody significantly increased survival compared with the infusion of aCSF in mice bearing *p53*$^{KO}$PDGFB GBM. Cotreatment with apelin-F13A and anti-VEGFR2 increased survival by additional 28% ($P < 0.05$) compared with anti-VEGFR2 single treatment. Ten, 7, 9, and 6 mice were treated with aCSF, anti-VEGFR2, apelin-F13A, and anti-VEGFR2 plus apelin-F13A, respectively. **C,** GBM invasiveness was analyzed in GFP-stained sections. In the composite images, the compact border (blue line) and the invasive tumor border (red line) are indicated. In the magnified images, massive invasion of single cells is visible in anti-VEGFR2–treated tumors. While the invasive GBM volume increased in anti-VEGFR2–treated tumors compared with control tumors, the invasive GBM volume was decreased in apelin-F13A-treated and anti-VEGFR2 and apelin-F13A cotreated mice. Data are shown for 4 and 5 tumors for treated versus control group. **D,** VEGFR2 and apelin-F13 treatment significantly decreased VLD to 440 and 357 mm/mm$^3$, respectively, versus 613 mm/mm$^3$ in control mice. Coadministration of anti-VEGFR2 and apelin-F13 decreased VLD to 243 mm/mm$^3$, which was significantly lower than that in anti-VEGFR2–treated tumors. Four tumors were analyzed per group. Scale size is indicated in individual micrographs; statistical significance (one-way ANOVA plus *post hoc* test) is indicated. *, $P < 0.05$; **, $P < 0.005$; ***, $P < 0.0005$.

increase) compared with control mice. Notably, coadministration of anti-VEGFR2 and apelin-F13A had synergistic effects, with a 65% increase in the survival rate (86 days). Median survival of the cotreated mice was significantly improved compared with administration of anti-VEGFR2 ($P = 0.0385$) or apelin-F13A ($P = 0.0327$) alone. Immunohistologic analysis of tumors with comparable overall tumor volume showed that administration of anti-VEGFR2 alone had a proinvasive effect with a 77% increase in the invasive volume relative to control mice (Fig. 6C). Interestingly, the anti-invasive effect of apelin-F13A reduced the invasive volume by 74 % significantly compared with control mice and combined treatment by 66% compared with anti-VEGFR2 treatment alone. Anti-VEGFR2 decreased VLD to 72% and apelin-F13A decreased VLD to 58% relative to control mice (Fig. 6D), while coadministration of apelin-F13A and anti-VEGFR2 decreased the VLD to 40% compared with controls.

In summary, we observed that cotargeting of the APLNR and VEGFR2 signaling pathways exerted synergistic antiangiogenic effects and strongly reduced the proinvasive side effects of established antiangiogenic strategies. We suggest that inhibition of VEGFR2 may be beneficial for the treatment of patients with the proneural subtype of GBM, if apelin-F13A is coadministered to modulate APLNR activation.

## Discussion

In this study, we revealed a central role of the apelin/APLNR signaling pathway in antiangiogenic treatment of GBM and in countering resistance to bevacizumab. We showed that apelin is required for tumor angiogenesis and we uncovered a previously unknown function of the apelin/APLNR signaling pathway in GBM cell invasion (Fig. 6A). Furthermore, we investigated for the first time the pathologic roles of host- or tumor cell–derived apelin separately, and examined their specific effects on GBM expansion, invasion, and angiogenesis. Our data indicate that the apelin/APLNR signaling pathway has dichotomous roles in angiogenesis and invasion in GBM, and we established that stimulation of APLNR using apelin-F13A is a promising strategy to treat distinct subtypes of GBM. A clinical perspective for the coapplication of apelin-F13A together with VEGFA/VEGFR2 inhibitors is also suggested because coadministration of apelin-F13A and DC101 synergistically blunted GBM vascularization and diminished the proinvasive side-effects associated with VEGFA/VEGFR2 inhibition. In addition, the reduced vascularization might be accompanied with vascular normalization that could be supportive for combined chemotherapy (18).

In previous studies, the pathologic function of apelin was largely associated with tumor vascularization (45–47) and consequently we observed that tumor cell- and host-derived apelin has additive effects on tumor angiogenesis. We found that apelin expression levels were positively correlated with vascular density in murine and human GBM models of the proneural GBM subtype as well as in classical GBM. The vascular upregulation of apelin was further confirmed by colocalization of apelin peptide in tumor vessels by immunofluorescence (Supplementary Fig. S6). We focused on the proneural and classical subtypes of GBM because TCGA data suggested that the apelin/APLNR signaling pathway mediates vascularization in these two subtypes, but not in the mesenchymal subtype of GBM.

In this study, we used GSC cultures that were previously extensively characterized for their stem-like capacity (22, 48). A recent publication proposed a critical role of the apelin/APLNR signaling pathway in GSC maintenance (49). However, in our GSC models, we did not find any alterations in cell viability, proliferation, or sphere formation capability following attenuation of apelin expression or APLNR blockade.

Knockdown of *APLN* in GBM cells or knockout of *APLN* in the host both enhanced tumor cell invasion, and implantation of $APLN^{KD}$ cells into $APLN^{KO}$ mice further accelerated the dissemination of GBM cells. This was particularly apparent in GBM cells with elevated APLNR expression levels. Application of apelin-F13A blunted GBM invasion and neoangiogenesis. These findings support the view that autocrine and paracrine apelin signaling has proangiogenic effects on vascular cells and blunts invasion of GBM cells (Fig. 6A). This observation is clinically relevant because bevacizumab lowers intratumoral apelin levels, which may explain why bevacizumab-treated patients often suffer from increased GBM cell invasion (10). We propose that bevacizumab directly (via blockade of VEGFA activity) and indirectly (by lowering apelin expression) exerts powerful antiangiogenic effects. However, we have shown that a reduction in apelin disinhibits GBM cell invasion, which may result in treatment resistance. Our data suggest that the synthetic APLNR ligand apelin-F13A can support antiangiogenic therapies by blocking vascularization (synergistically with VEGFA/VEGFR2 inhibitors) and preventing invasion. In this study, we exploited the pharmacologic properties of apelin-F13A, which acts as a partial agonist for APLNR (19, 50) and as a competitive agonist for natural apelin isoforms, like apelin-13 (37). We hypothesize that apelin-F13A cannot sufficiently activate APLNR expressed on the endothelium to induce vascular sprouting but sufficiently stimulates APLNR on GBM cells to blunt invasion and prolong survival. This can be explained by a lower receptor binding capacity (39) and alternative activation of intracellular signaling pathways (51) by apelin-F13A as compared with natural APLNR ligands. Although we could not formally show direct binding of apelin-F13A on tumor endothelial cells *in vivo*, most recent findings of Zhao and colleagues (52) are in full support of our results by demonstrating apelin-F13A binding to APLNR in a structural *in silico* model and showing antiangiogenic effects of apelin-F13A on APLNR-expressing endothelia in peripheral tumors. We acknowledge that the experimental therapeutic agent apelin-F13A may have further effects on the tumor microenvironment (like, for example, on intratumoural immune cell populations), which could support the antiangiogenic and anti-invasive traits reported here. However, when we quantified tumor-associated myeloid cells in experimental GBM treated with vehicle or apelin-F13A we did not observe a difference in myeloid cell numbers.

Clinical trials of GBM therapies in the last two decades have highlighted the need to identify predictive markers to improve the clinical outcomes of new compounds (2, 53). One approach for patient stratification according to molecular and pathologic criteria involves clustering of GBM into genetic subtypes (12), which may be particularly relevant to antiangiogenic treatments using bevacizumab (14) and apelin-F13A (as in this study) because both agents have beneficial effects on the proneural subtype of GBM. In addition, the high expression of APLNR in GBM may qualify as a marker for an increased propensity of GBM cells to invade during bevacizumab treatment, a process that can be blocked by apelin-F13A.

In conclusion, the results of this study introduce a new strategy to reduce therapeutic resistance during antiangiogenic therapy and identify GBM subtypes that may show better therapeutic responses by cotargeting the apelin/APLNR and VEGFA/VEGFR2 signaling pathways.

## Disclosure of Potential Conflicts of Interest

A.L. Vescovi is a CEO at Stemgen SpA, is a CEO and CSO at Hyperstem SA, and has ownership interest (including stock, patents, etc.) in Hyperstem SA. No potential conflicts of interest were disclosed by the other authors.

## Authors' Contributions

**Conception and design:** G. Mastrella, V.M. Stoecklein, M. Synowitz, R. Glass, R.E. Kälin

**Development of methodology:** G. Mastrella, M. Synowitz, E. Wagner, R. Bjerkvig, R.E. Kälin

**Acquisition of data (provided animals, acquired and managed patients, provided facilities, etc.):** G. Mastrella, M. Hou, M. Li, V.M. Stoecklein, N. Zdouc, M.N.M. Volmar, H. Miletic, C.C. Herold-Mende, K. Eisenhut, P.N. Harter, E. Wagner, M. Mittelbronn, R. Bjerkvig, D. Hambardzumyan, U. Schüller, J. Radke, R. Glass, R.E. Kälin

**Analysis and interpretation of data (e.g., statistical analysis, biostatistics, computational analysis):** G. Mastrella, M. Hou, M. Li, V.M. Stoecklein, N. Zdouc, S. Reinhard, M. Synowitz, A.L. Vescovi, P.N. Harter, M. Mittelbronn, R. Bjerkvig, J. Radke, R. Glass, R.E. Kälin

**Writing, review, and/or revision of the manuscript:** G. Mastrella, M. Li, V.M. Stoecklein, M.N.M. Volmar, S. Reinhard, C.C. Herold-Mende, G. Gargiulo, M. Synowitz, P.N. Harter, E. Wagner, M. Mittelbronn, D. Hambardzumyan, U. Schüller, J.-C. Tonn, J. Radke, R. Glass, R.E. Kälin

**Administrative, technical, or material support (i.e., reporting or organizing data, constructing databases):** M. Li, S. Reinhard, S. Kleber, G. Gargiulo, J.M. Penninger, M. Mittelbronn, U. Schüller, R. Glass, R.E. Kälin

**Study supervision:** R. Glass, R.E. Kälin

**Other (established and provided HGBM cancer stem cell line):** A.L. Vescovi

## Acknowledgments

R. Glass and R.E. Kälin gratefully acknowledge funding by the DFG (GL691/2; SFB824), the "Wilhelm Sander-Stiftung," the "Anni-Hofmann Stiftung," the "Verein zur Förderung von Wissenschaft und Forschung an der Medizinischen Fakultät der LMU München" (WiFoMed), the Curt Bohnewandt Fonds, the "Friedrich-Baur-Stiftung," and the "Familie Mehdorn Stiftung." M. Li was supported by a China Scholarship Council (CSC) graduate scholarship. J. Radke is a participant in the BIH-Charité Clinical Scientist Program funded by the Charité-Universitätsmedizin Berlin and the Berlin Institute of Health. U. Schüller is supported by the "Fördergemeinschaft Kinderkrebs-Zentrum Hamburg". M. Mittelbronn would like to thank the Luxembourg National Research Fond (FNR) for the support (FNR PEARL P16/BM/11192868 grant). We are thankful to Frank L. Heppner, Stefanie Lange, Eva Sušnik, Eskil Eskilsson, Per Øystein Sakariassen, as well as Steffen Dietzel and Andreas Thomae (Core Facility Bioimaging, Biomedical Center, LMU München), Günter Höglinger, Sigrid Schwarz, and Nicholas D. Smith (http://www.scientific-writing.net/).

The costs of publication of this article were defrayed in part by the payment of page charges. This article must therefore be hereby marked *advertisement* in accordance with 18 U.S.C. Section 1734 solely to indicate this fact.

Received March 22, 2018; revised October 19, 2018; accepted January 29, 2019; published first February 4, 2019.

## References

1. Louis DN, Perry A, Reifenberger G, von Deimling A, Figarella-Branger D, Cavenee WK, et al. The 2016 world health organization classification of tumors of the central nervous system: a summary. Acta Neuropathol 2016; 131:803–20.
2. Stupp R, Mason WP, van den Bent MJ, Weller M, Fisher B, Taphoorn MJ, et al. Radiotherapy plus concomitant and adjuvant temozolomide for glioblastoma. N Engl J Med 2005;352:987–96.
3. Weller M, van den Bent M, Tonn JC, Stupp R, Preusser M, Cohen-Jonathan-Moyal E, et al. European Association for Neuro-Oncology (EANO) guideline on the diagnosis and treatment of adult astrocytic and oligodendroglial gliomas. Lancet Oncol 2017;18:e315–e29.
4. Brennan CW, Verhaak RG, McKenna A, Campos B, Noushmehr H, Salama SR, et al. The somatic genomic landscape of glioblastoma. Cell 2013;155: 462–77.
5. Chen J, McKay RM, Parada LF. Malignant glioma: lessons from genomics, mouse models, and stem cells. Cell 2012;149:36–47.
6. Westphal M, Lamszus K. The neurobiology of gliomas: from cell biology to the development of therapeutic approaches. Nat Rev Neurosci 2011;12: 495–508.
7. Jain RK, di Tomaso E, Duda DG, Loeffler JS, Sorensen AG, Batchelor TT. Angiogenesis in brain tumours. Nat Rev Neurosci 2007;8:610–22.
8. Chinot OL, Wick W, Mason W, Henriksson R, Saran F, Nishikawa R, et al. Bevacizumab plus radiotherapy-temozolomide for newly diagnosed glioblastoma. N Engl J Med 2014;370:709–22.
9. Gilbert MR, Dignam JJ, Armstrong TS, Wefel JS, Blumenthal DT, Vogelbaum MA, et al. A randomized trial of bevacizumab for newly diagnosed glioblastoma. N Engl J Med 2014;370:699–708.
10. Lu KV, Bergers G. Mechanisms of evasive resistance to anti-VEGF therapy in glioblastoma. CNS Oncol 2013;2:49–65.
11. Aldape K, Zadeh G, Mansouri S, Reifenberger G, von Deimling A. Glioblastoma: pathology, molecular mechanisms and markers. Acta Neuropathol 2015;129:829–48.
12. Verhaak RG, Hoadley KA, Purdom E, Wang V, Qi Y, Wilkerson MD, et al. Integrated genomic analysis identifies clinically relevant subtypes of glioblastoma characterized by abnormalities in PDGFRA, IDH1, EGFR, and NF1. Cancer Cell 2010;17:98–110.
13. Wang Q, Hu B, Hu X, Kim H, Squatrito M, Scarpace L, et al. Tumor evolution of glioma-intrinsic gene expression subtypes associates with immunological changes in the microenvironment. Cancer Cell 2017;32: 42–56.
14. Sandmann T, Bourgon R, Garcia J, Li C, Cloughesy T, Chinot OL, et al. Patients with proneural glioblastoma may derive overall survival benefit from the addition of bevacizumab to first-line radiotherapy and temozolomide: retrospective analysis of the AVAglio Trial. J Clin Oncol 2015;33: 2735–44.
15. Kälin RE, Kretz MP, Meyer AM, Kispert A, Heppner FL, Brändli AW. Paracrine and autocrine mechanisms of apelin signaling govern embryonic and tumor angiogenesis. Dev Biol 2007;305:599–614.
16. Plate KH, Breier G, Weich HA, Risau W. Vascular endothelial growth factor is a potential tumour angiogenesis factor in human gliomas in vivo. Nature 1992;359:845–8.
17. Kälin S, Kälin RE. Apelin and cancer. In: Reizes O, Berger NA, editors. Adipocitokines, energy balance, and cancer. Basel, Switzerland: Springer International Publishing; 2017. p 137–66.
18. Zhang L, Takara K, Yamakawa D, Kidoya H, Takakura N. Apelin as a marker for monitoring the tumor vessel normalization window during antiangiogenic therapy. Cancer Sci 2016;107:36–44.
19. O'Carroll AM, Lolait SJ, Harris LE, Pope GR. The apelin receptor APJ: journey from an orphan to a multifaceted regulator of homeostasis. J Endocrinol 2013;219:R13–35.
20. Campos B, Wan F, Farhadi M, Ernst A, Zeppernick F, Tagscherer KE, et al. Differentiation therapy exerts antitumor effects on stem-like glioma cells. Clin Cancer Res 2010;16:2715–28.
21. Drachsler M, Kleber S, Mateos A, Volk K, Mohr N, Chen S, et al. CD95 maintains stem cell-like and non-classical EMT programs in primary human glioblastoma cells. Cell Death Dis 2016;7:e2209.
22. Binda E, Visioli A, Giani F, Trivieri N, Palumbo O, Restelli S, et al. Wnt5a Drives an invasive phenotype in human glioblastoma stem-like cells. Cancer Res 2017;77:996–1007.
23. UKCCCR guidelines for the welfare of animals in experimental neoplasia. Cancer Metastasis Rev 1989;8:82–8.

24. Kuba K, Zhang L, Imai Y, Arab S, Chen M, Maekawa Y, et al. Impaired heart contractility in Apelin gene-deficient mice associated with aging and pressure overload. Circ Res 2007;101:e32–42.
25. Shinkai Y, Rathbun G, Lam KP, Oltz EM, Stewart V, Mendelsohn M, et al. RAG-2-deficient mice lack mature lymphocytes owing to inability to initiate V(D)J rearrangement. Cell 1992;68:855–67.
26. Grathwohl SA, Kälin RE, Bolmont T, Prokop S, Winkelmann G, Kaeser SA, et al. Formation and maintenance of Alzheimer's disease beta-amyloid plaques in the absence of microglia. Nat Neurosci 2009;12:1361–3.
27. Bowman RL, Wang Q, Carro A, Verhaak RG, Squatrito M. GlioVis data portal for visualization and analysis of brain tumor expression datasets. Neuro Oncol 2017;19:139–41.
28. Eskilsson E, Rosland GV, Talasila KM, Knappskog S, Keunen O, Sottoriva A, et al. EGFRvIII mutations can emerge as late and heterogenous events in glioblastoma development and promote angiogenesis through Src activation. Neuro Oncol 2016;18:1644–55.
29. Hambardzumyan D, Amankulor NM, Helmy KY, Becher OJ, Holland EC. Modeling adult gliomas using RCAS/t-va technology. Transl Oncol 2009;2:89–95.
30. Pitter KL, Tamagno I, Alikhanyan K, Hosni-Ahmed A, Pattwell SS, Donnola S, et al. Corticosteroids compromise survival in glioblastoma. Brain 2016;139:1458–71.
31. Sonabend AM, Yun J, Lei L, Leung R, Soderquist C, Crisman C, et al. Murine cell line model of proneural glioma for evaluation of anti-tumor therapies. J Neurooncol 2013;112:375–82.
32. Jones TS, Holland EC. Animal models for glioma drug discovery. Expert Opin Drug Discov 2011;6:1271–83.
33. Sakariassen PO, Prestegarden L, Wang J, Skaftnesmo KO, Mahesparan R, Molthoff C, et al. Angiogenesis-independent tumor growth mediated by stem-like cancer cells. Proc Natl Acad Sci U S A 2006;103:16466–71.
34. Keunen O, Johansson M, Oudin A, Sanzey M, Rahim SA, Fack F, et al. Anti-VEGF treatment reduces blood supply and increases tumor cell invasion in glioblastoma. Proc Natl Acad Sci U S A 2011;108:3749–54.
35. Talasila KM, Soentgerath A, Euskirchen P, Rosland GV, Wang J, Huszthy PC, et al. EGFR wild-type amplification and activation promote invasion and development of glioblastoma independent of angiogenesis. Acta Neuropathol 2013;125:683–98.
36. Podergajs N, Brekka N, Radlwimmer B, Herold-Mende C, Talasila KM, Tiemann K, et al. Expansive growth of two glioblastoma stem-like cell lines is mediated by bFGF and not by EGF. Radiol Oncol 2013;47:330–7.
37. Lee DK, George SR, O'Dowd BF. Unravelling the roles of the apelin system: prospective therapeutic applications in heart failure and obesity. Trends Pharmacol Sci 2006;27:190–4.
38. Lee DK, Saldivia VR, Nguyen T, Cheng R, George SR, O'Dowd BF. Modification of the terminal residue of apelin-13 antagonizes its hypotensive action. Endocrinology 2005;146:231–6.
39. Medhurst AD, Jennings CA, Robbins MJ, Davis RP, Ellis C, Winborn KY, et al. Pharmacological and immunohistochemical characterization of the APJ receptor and its endogenous ligand apelin. J Neurochem 2003;84:1162–72.
40. Fan X, Zhou N, Zhang X, Mukhtar M, Lu Z, Fang J, et al. Structural and functional study of the apelin-13 peptide, an endogenous ligand of the HIV-1 coreceptor, APJ. Biochemistry 2003;42:10163–8.
41. Pope GR, Tilve S, McArdle CA, Lolait SJ, O'Carroll AM. Agonist-induced internalization and desensitization of the apelin receptor. Mol Cell Endocrinol 2016;437:108–19.
42. Reaux A, De Mota N, Skultetyova I, Lenkei Z, El Messari S, Gallatz K, et al. Physiological role of a novel neuropeptide, apelin, and its receptor in the rat brain. J Neurochem 2001;77:1085–96.
43. Zou MX, Liu HY, Haraguchi Y, Soda Y, Tatemoto K, Hoshino H. Apelin peptides block the entry of human immunodeficiency virus (HIV). FEBS Lett 2000;473:15–8.
44. Calebiro D, Godbole A. Internalization of G-protein-coupled receptors: Implication in receptor function, physiology and diseases. Best Pract Res Clin Endocrinol Metab 2018;32:83–91.
45. Berta J, Hoda MA, Laszlo V, Rozsas A, Garay T, Torok S, et al. Apelin promotes lymphangiogenesis and lymph node metastasis. Oncotarget 2014;5:4426–37.
46. Berta J, Kenessey I, Dobos J, Tovari J, Klepetko W, Jan Ankersmit H, et al. Apelin expression in human non-small cell lung cancer: role in angiogenesis and prognosis. J Thorac Oncol 2010;5:1120–9.
47. Sorli SC, Le Gonidec S, Knibiehler B, Audigier Y. Apelin is a potent activator of tumour neoangiogenesis. Oncogene 2007;26:7692–9.
48. Podergajs N, Motaln H, Rajcevic U, Verbovsek U, Korsic M, Obad N, et al. Transmembrane protein CD9 is glioblastoma biomarker, relevant for maintenance of glioblastoma stem cells. Oncotarget 2016;7:593–609.
49. Harford-Wright E, Andre-Gregoire G, Jacobs KA, Treps L, Le Gonidec S, Leclair HM, et al. Pharmacological targeting of apelin impairs glioblastoma growth. Brain 2017;140:2939–54.
50. Pitkin SL, Maguire JJ, Kuc RE, Davenport AP. Modulation of the apelin/APJ system in heart failure and atherosclerosis in man. Br J Pharmacol 2010;160:1785–95.
51. De Mota N, Lenkei Z, Llorens-Cortes C. Cloning, pharmacological characterization and brain distribution of the rat apelin receptor. Neuroendocrinology 2000;72:400–7.
52. Zhao H, Tian X, He L, Li Y, Pu W, Liu Q, et al. Apj(+) vessels drive tumor growth and represent a tractable therapeutic target. Cell Rep 2018;25:1241–54.
53. Haynes HR, Camelo-Piragua S, Kurian KM. Prognostic and predictive biomarkers in adult and pediatric gliomas: toward personalized treatment. Front Oncol 2014;4:47.

CellPress
OPEN ACCESS

Cell Systems

Article

# TAMEP are brain tumor parenchymal cells controlling neoplastic angiogenesis and progression

Roland E. Kälin,[1,2,13] Linzhi Cai,[1,2,13,14] Yuping Li,[1,2] Dongxu Zhao,[1,2] Huabin Zhang,[1,2] Jiying Cheng,[1,2] Wenlong Zhang,[2,3] Yingxi Wu,[1,2] Katharina Eisenhut,[1,2] Philipp Janssen,[4] Lukas Schmitt,[4] Wolfgang Enard,[4] Friederike Michels,[5] Charlotte Flüh,[5] Mengzhuo Hou,[1,2] Sabrina V. Kirchleitner,[6] Sebastian Siller,[6] Matthias Schiemann,[7] Immanuel Andrä,[7] Eloi Montanez,[2,8] Claudio Giachino,[9] Verdon Taylor,[9] Michael Synowitz,[5] Jörg-Christian Tonn,[6,10] Louisa von Baumgarten,[2,3,6] Christian Schulz,[2,11,12] Ines Hellmann,[4] and Rainer Glass[1,2,10,15,*]

[1]Neurosurgical Research, University Hospital, LMU Munich, 81377 Munich, Germany
[2]Walter-Brendel-Centre of Experimental Medicine, University Hospital, LMU Munich, 81377 Munich, Germany
[3]Department of Neurology, University Hospital, LMU Munich, 81377 Munich, Germany
[4]Anthropology and Human Genomics, Department Biology II, LMU Munich, 82152 Planegg-Martinsried, Germany
[5]Department of Neurosurgery, University Hospital Center Schleswig Holstein, 24105 Kiel, Germany
[6]Department of Neurosurgery, University Hospital, LMU Munich, 81377 Munich, Germany
[7]Institute for Medical Microbiology, Immunology and Hygiene, Technische Universität München, 81675 München, Germany
[8]Department of Physiological Sciences, Faculty of Medicine and Health Sciences, University of Barcelona and Bellvitge Biomedical Research Institute (IDIBELL), 08907 Hospitalet de Llobregat, Spain
[9]Department of Biomedicine, University of Basel, 4058 Basel, Switzerland
[10]German Cancer Research Center (DKFZ), German Cancer Consortium (DKTK), Partner Site Munich, 69120 Heidelberg, Germany
[11]Medizinische Klinik und Poliklinik I, University Hospital, LMU Munich, 81377 Munich, Germany
[12]German Centre for Cardiovascular Research (DZHK), Partner Site Munich Heart Alliance, 80333 Munich, Germany
[13]These authors contributed equally
[14]Present address: Department of Neurosurgery, Renmin Hospital of Wuhan University, Wuhan 430060, China
[15]Lead contact
*Correspondence: rainer.glass@med.uni-muenchen.de
https://doi.org/10.1016/j.cels.2021.01.002

## SUMMARY

Aggressive brain tumors like glioblastoma depend on support by their local environment and subsets of tumor parenchymal cells may promote specific phases of disease progression. We investigated the glioblastoma microenvironment with transgenic lineage-tracing models, intravital imaging, single-cell transcriptomics, immunofluorescence analysis as well as histopathology and characterized a previously unacknowledged population of tumor-associated cells with a myeloid-like expression profile (TAMEP) that transiently appeared during glioblastoma growth. TAMEP of mice and humans were identified with specific markers. Notably, TAMEP did not derive from microglia or peripheral monocytes but were generated by a fraction of CNS-resident, SOX2-positive progenitors. Abrogation of this progenitor cell population, by conditional *Sox*2-knockout, drastically reduced glioblastoma vascularization and size. Hence, TAMEP emerge as a tumor parenchymal component with a strong impact on glioblastoma progression.

## INTRODUCTION

The microenvironment of primary, malignant brain tumors (glioblastoma; GBM) can strongly support neoplastic progression (Aldape et al., 2019). The GBM parenchyma consists of a complex mix of brain resident as well as immigrating cells (Aldape et al., 2019; Glass and Synowitz, 2014; Hambardzumyan et al., 2016) including subsets of stem and progenitor cells (Audia et al., 2017; Stock et al., 2012). A range of pathologically relevant effects mediated by mesenchymal stem cells (MSCs), neural precursor cells (NPCs), or oligodendrocyte progenitor cells (OPCs) have been reported (Audia et al., 2017; Huang et al., 2014; Stock et al., 2012). MSCs have tumor-supporting or anti-neoplastic functions potentially owing to their origins in the bone marrow or in local perivascular positions (Audia et al., 2017; Behnan et al., 2014; Ho et al., 2013). NPCs curtail GBM progression by the release of bioactive lipids (Stock et al., 2012), but the number of NPCs declines with age, and therefore, NPC-induced GBM suppression is restricted to the young brain and lost at postnatal day 90 (P90) in mice (Walzlein et al., 2008). OPCs can contribute to perivascular cells in GBM and thereby support neovascularization (Huang et al., 2014). However, it is

 © 2021 The Authors. Published by Elsevier Inc.
This is an open access article under the CC BY-NC-ND license (http://creativecommons.org/licenses/by-nc-nd/4.0/).

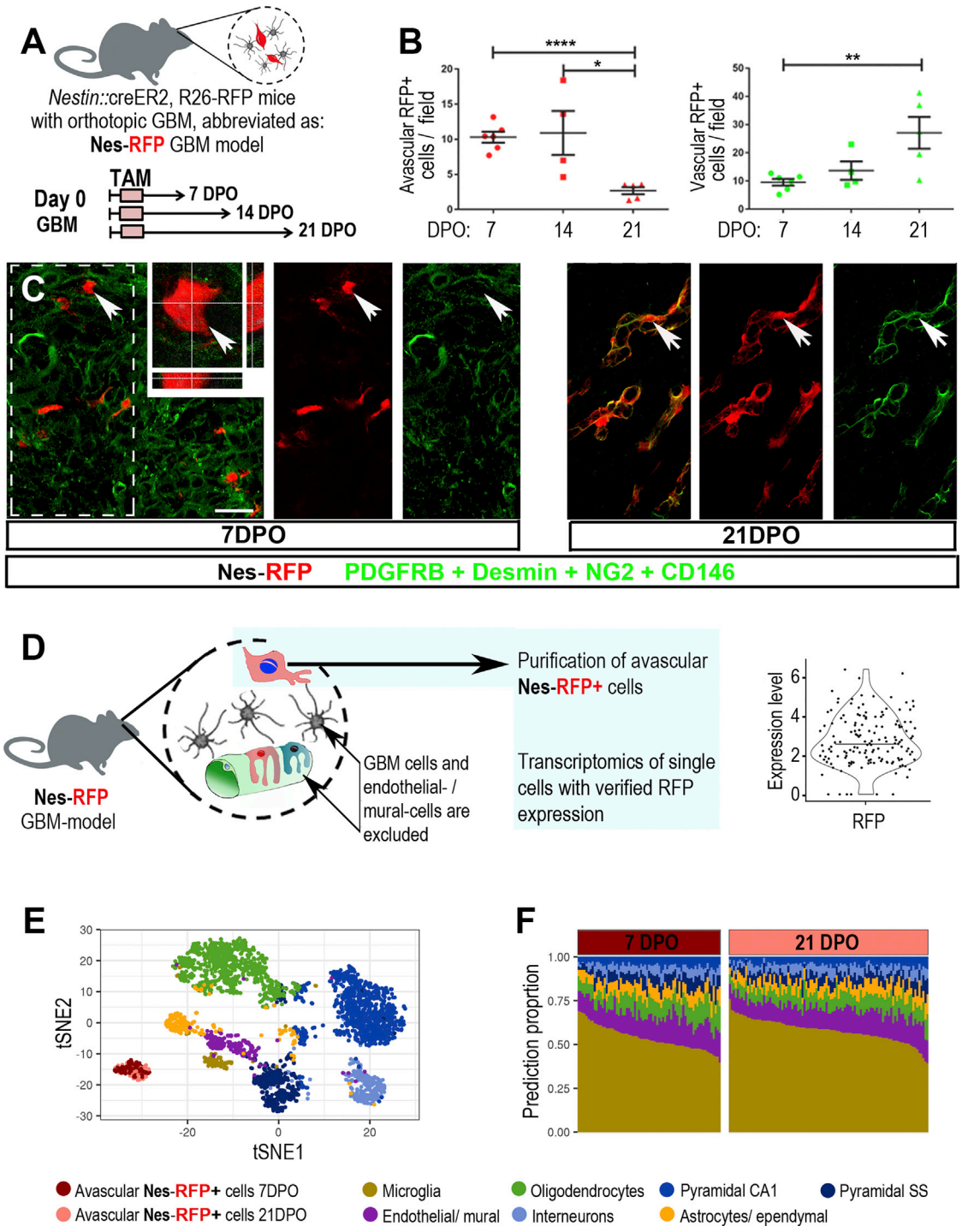


**Figure 1. A model for tracing tumor-associated cells with a myeloid-like expression profile (TAMEP)**

(A) Nes-RFP mice bearing orthotopic glioma were inspected at 7, 14, or 21 DPO.

(B) Quantity of RFP+ cells in an avascular (left) and a vessel-associated (right) position (each dot indicates data from one mouse: n = 6 at 7DPO, n = 4 at 14DPO, and n = 5 at 21 DPO).

(C) Immunofluorescence for pericyte markers (in unison shown in green); at 7DPO pericyte marker-negative RFP+ cells predominate, arrow corresponds to single-channel micrographs (dashed line) and orthogonal view; at 21 DPO RFP+, cells are pericyte marker positive.

(D) Purified cells from orthotopic glioma showed strong RFP expression; in $\log_2$(CPM).

(E) A t-SNE plot of classified mouse brain cells combined with our scRNA-seq data.

*(legend continued on next page)*

currently unclear if other (e.g., tissue resident) pools of stem and progenitor cells contribute to GBM progression.

Vascular cells as well as tumor-associated myeloid cells constitute the major components of the GBM parenchyma (Aldape et al., 2019; Audia et al., 2017). Myeloid cells, which consist of microglia and peripheral macrophages, accelerate GBM cell-invasion (Glass and Synowitz, 2014; Hambardzumyan et al., 2016) and the rich vascular network of GBM has important tumor-trophic functions (Aldape et al., 2019; Audia et al., 2017). Microglia are ontogenetically distinct from bone-marrow-derived immune cells, but otherwise share the cellular plasticity, innate immune functions, and sets of markers with peripheral macrophages (Hammond et al., 2018; Prinz et al., 2017). Under physiological conditions, the bone marrow contributes only to ventricular (choroid plexus) macrophages but not to other pools of CNS phagocytes (Goldmann et al., 2016), while large numbers of peripheral immune cells can accumulate in the brain during neuropathology (Glass and Synowitz, 2014; Hambardzumyan et al., 2016; Hammond et al., 2018; Prinz et al., 2017).

While the role of tumor-associated myeloid cells on GBM progression is well documented, we have only partial knowledge of the pathological impact of GBM-parenchymal progenitor cells. Therefore, we investigated the GBM microenvironment using a transgenic lineage-tracing model indicating progenitor cells of the brain and their progeny (Giachino and Taylor, 2009). Detailed inspection of this cell subset revealed a previously unacknowledged population of GBM-associated cells with a myeloid expression profile. This newly identified set of myeloid-like cells derives from local progenitors without any contribution from the bone marrow. Hence, this cell subset is clearly distinct from microglia or monocyte-derived macrophages. We show that this population supports tumor growth in murine models of GBM by inducing angiogenesis.

## RESULTS

### Tracing a subpopulation of myeloid-like cells in GBM

GBM-associated progenitor cells may modulate the course of disease progression, but data on the intratumoral fate of progenitor-derived cell types are sparse. Mouse strains for tamoxifen-induced cre-recombinase expression under the control of various nestin gene-promoters (*Nestin*::creER2) allow tracing of CNS-resident progenitors (and their progeny), for e.g., NPC, OPC, and partly also of pericytes (Sun et al., 2014), which share characteristics with MSC (Crisan et al., 2008; Sun et al., 2014). All these cell types are part of the GBM microenvironment (Audia et al., 2017; Huang et al., 2014; Stock et al., 2012). Animal models containing genetically modified gene-promoter elements for the intermediate filament Nestin allow transgene expression preponderantly in stem and progenitor cells (Giachino and Taylor, 2009). Nestin promoter controlled expression of cre recombinase fused with a mutant estrogen receptor (creER2) permits tamoxifen-induced (timed) transgene expression (Giachino and Taylor, 2009). In combination with cre-mediated excision of a loxP-flanked (floxed) stop codon driving the expression of a fluorescent reporter (tdTomato; RFP), this provides a system for inheritable cell labeling (Madisen et al., 2010). Initially, we compared two *Nestin*::creER2 mouse strains (Giachino and Taylor, 2009; Lagace et al., 2007) and chose the model (abbreviated as Nes-RFP mice) with superior sensitivity and specificity as an experimental model (Figures S1A–S1C). Nes-RFP mice traced larger numbers of intratumoral cells (Figure S1D) that were negative for the astrocyte-marker glial fibrillary acidic protein (GFAP) (Figure S1E) and were non-leaky (Figure S1F; see Tables S1 and S2 for details on all models). NPC-migration to GBM is restricted to the young brain (before postnatal day 90; P90) and we excluded effects of tumor-associated NPCs by using mice of P100 or older for all experiments (Stock et al., 2012; Walzlein et al., 2008). Thereby, we obtained a technically sound model for tracing of tumor parenchymal cells from a Nestin-positive source without contribution by astrocytes or NPCs.

Experiments were performed according to the experimental schedule in Figure 1A and inspection over a time course showed a number of traced (RFP+) avascular cells, whose numbers declined during tumor progression (from 7 to 21 days post-operatively; DPO), whereas a population of vascular RFP+ cells increased (Figure 1B). Immunofluorescence for platelet-derived growth factor-B (PDGFRB), Desmin, neural/glial antigen-2 (NG2), and CD146 (Armulik et al., 2011) identified vessel-associated RFP+ cells as pericytes (Figures 1C and S1G–S1N), whereas avascular cells were not labeled for pericyte markers (Figure 1C). Intravital imaging of traced cells during glioma expansion over a time course of 3 weeks and longer showed that both sets of cells remained in their respective localization (Figure S2), thereby excluding the possibility that avascular RFP+ cells may acquire a pericyte identity throughout tumor growth or that pericytes detach from vessels. Of note, this also shows that traced cells in our study are different from OPCs, which exert a pathological role in GBM by contributing perivascular cells form an avascular source (Huang et al., 2014).

In order to uncover the identity of the non-vascular RFP+ cells, we purified these by flow cytometry from experimental gliomas at 7 and 21 DPO and analyzed them by single-cell transcriptomics (scRNA-seq; Figures 1D–1F). Note that due to the tight association with blood vessels, vascular RFP+ cells were excluded by our cell-isolation protocol (Bondjers et al., 2006). Cells were processed using SCRB-seq, a sensitive 3′-tagged RNA-seq protocol (Parekh et al., 2018; Ziegenhain et al., 2017), and we obtained high-quality single-cell expression profiles with 6,000 to 50,000 transcripts for 155 out of 180 processed cells with confirmed RFP expression (Figure 1D). Integrating our RFP+ avascular cells with the expression profiles of over 3,000 neuronal and non-neuronal cells from the mouse brain (Zeisel et al., 2015) within a t-distributed stochastic neighbor embedding (t-SNE) plot showed that they form a homogeneous cell fraction (Figure 1E) and a classification algorithm suggested a similarity with microglia (Figure 1F). In summary, this indicates that our Nes-RFP

(F) A random-forest analysis indicated a high statistical proximity of traced avascular cells with microglia at 7 and 21 DPO. All immunofluorescence data were retrieved with $n \geq 4$ mice per group and scRNA-seq analysis was performed with n = 6 animals. Scale bar is 50 μm; data (in B) are presented as mean ± SD; statistical significance was determined by one-way ANOVA with post hoc test and is indicated as follows: *$p < 0.05$, **$p < 0.01$, ****$p < 0.0001$. See also Figures S1 and S2.

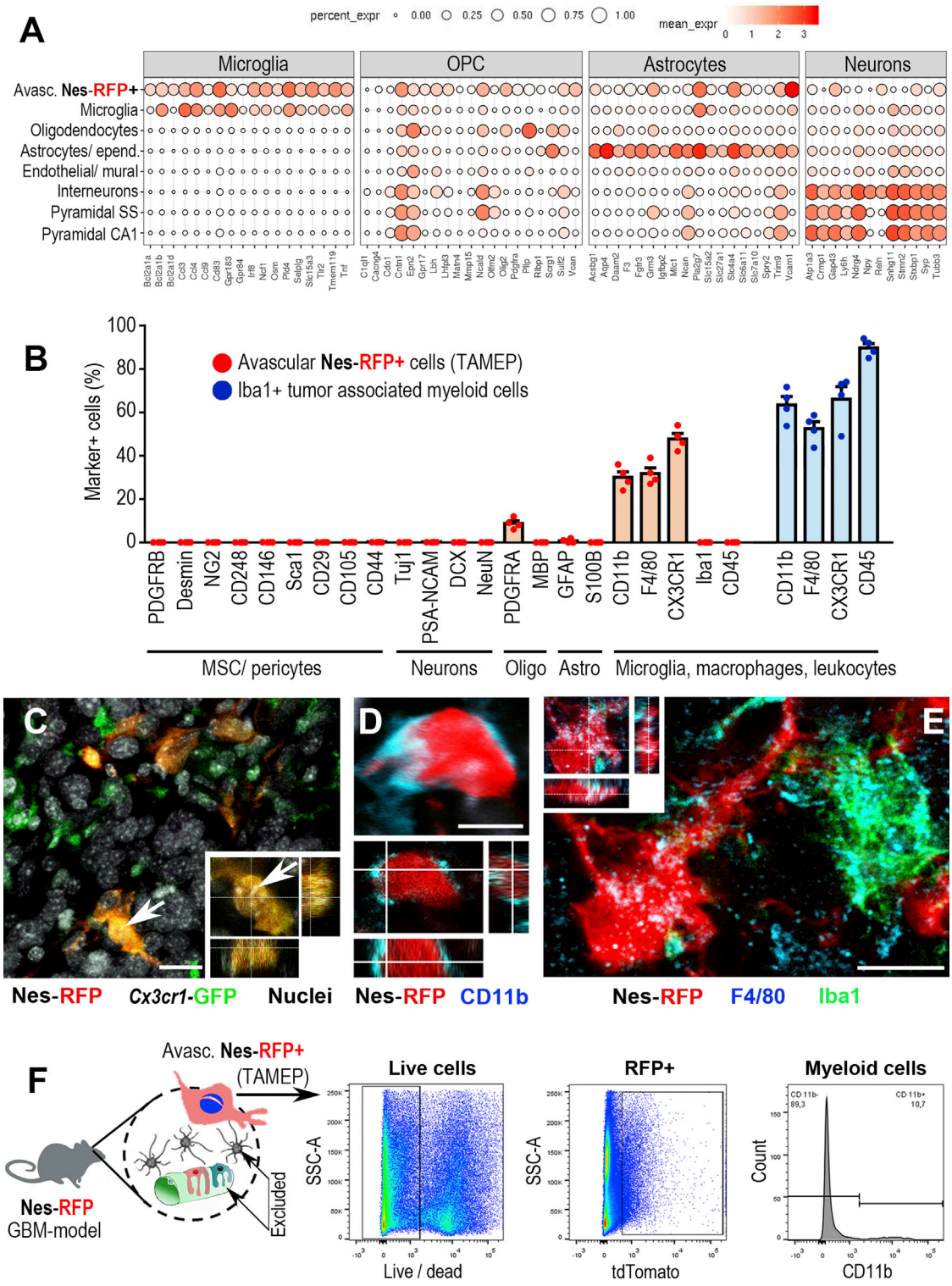


**Figure 2. Traced myeloid-like cells express phagocyte markers but differ from microglia or macrophages**

(A) ScRNA-seq data indicate that avascular RFP+ cells (Avasc. RFP+; TAMEP) express microglia or some OPC markers.

(B) Immunofluorescence markers in avascular RFP+ cells (at 14 DPO; as compared with Iba1+ myeloid cells; each dot indicates data from one mouse; n = 4 animals in all groups).

(C) Nes-RFP, *Cx3cr1*-GFP glioma models corroborate myeloid differentiation of RFP+ avascular cells at 7 DPO (a single cell is shown in orthogonal view; arrow).

(D) Three-dimensional and orthogonal view of a traced avascular cell (within a glioma; Nes-RFP strain) expressing CD11b at 7 DPO.

*(legend continued on next page)*

strain traced a transient population of intratumoral cells, which stably remained in a non-vascular position and acquired a microglia-like transcription profile.

## Characterization of TAMEP

Single-cell gene expression levels for traced avascular cells (Figure 2A) were compared with established gene expression profiles for microglia, OPCs, astrocytes, or neurons and confirmed that traced avascular cells have high similarity with microglia (plus a minor overlap with OPC; Figure 2A). In addition, we quantified immuno-positivity for a range of cell-lineage-identifying molecules (Armulik et al., 2010; Hammond et al., 2018; Jones and Schäfer, 2015; Kovacs, 2017; Prinz et al., 2017) in traced avascular cells (Figure 2B) and found that these were different from pericytes, MSC, mature/immature neurons or astrocytes (Astro). PDGFRA (an OPC marker) was expressed in a subset of RFP+ avascular cells, whereas myelin basic protein (MBP; for mature oligodendrocytes; Oligo) was absent; several key-markers for microglia (CD11b, F4/80, and CX3CR1) were abundant, but other canonical markers for myeloid cells like Iba1 and CD45 were not found (whereas Iba1+ tumor-associated myeloid cells abundantly expressed CD11b, F4/80, CX3CR1, and CD45; Figure 2B). Additional evidence, that traced avascular cells have a myeloid appearance (Figure 2C), was obtained after crossbreeding Nes-RFP mice with the *Cx3cr1*-GFP strain, which reliably identifies macrophages (Jung et al., 2000; Mizutani et al., 2012). Coherently, we detected immuno-positivity (Figures 2D and 2E) for myeloid (CD11b) and macrophage (F4/80) markers (Van Hove et al., 2019) in traced RFP+ cells. Flow cytometry analysis of traced avascular cells from orthotopic gliomas at 14 DPO fully substantiated that viable, traced avascular cells can express myeloid markers on the protein level (Figures 2F and S3). Altogether, scRNA-seq of traced, avascular RFP+ cells revealed a GBM-parenchymal, atypical myeloid component (hereafter referred to as tumor-associated cells with a myeloid-like expression profile; TAMEP). Immunofluorescence, reporter mouse strains, and FACS confirmed that TAMEP resemble myeloid cells.

## TAMEP derive from Sox2-dependent progenitors

So far our study characterized TAMEP as a transient, myeloid-like subset of cells, which are largely confined to earlier/intermediate phases of glioma growth. Modification of the tamoxifen-schedule revealed that TAMEP could be traced from different time points (1 DPO or 7 DPO) of gliomagenesis, while injection of tamoxifen into tumor-free animals followed by a chase period and implantation of tumors thereafter did not yield traced cells (Figure 3A). This suggests that our model specifically traced TAMEP in a disease context and that this cell population is not present in the healthy brain. Labeling with thymidine analogs showed that TAMEP are proliferative and can repetitively enter the cell cycle (Figure 3B). We reasoned that this may imply that TAMEP originates from a progenitor through activation by a pathological stimulus, followed by rapid expansion. Therefore, we investigated the expression of stem and progenitor cell markers in traced intratumoral cells of Nes-RFP mice (Figures 3C and 3D). Indeed, we detected an expression of the stem cell transcription factor SOX2 (Sarkar and Hochedlinger, 2013) in avascular RFP+ cells (Figure 3C) but never in vascular RFP+ cells (Figure 3D). Next, we asked if SOX2 has a particular biological role in avascular RFP+ cells and induced a conditional *Sox2*-knockout (Shaham et al., 2009) using our Nes-RFP mouse strain (*Nestin*::creER2, R26-RFP, *Sox2*$^{fl/fl}$; as compared with Nes-RFP controls) after tumor inoculation (Figure 3E). Remarkably, we observed that *Sox2*-loss diminished the number of RFP+ avascular cells in gliomas. In particular, we found that traced avascular cell numbers were very strongly reduced in *Nestin*::creER2, R26-RFP, Sox2$^{fl/fl}$ mice at 14 DPO (in average 2.07 cells per counting frame in knockouts as compared with 10.9 cells per frame in wild-type controls). At 7 DPO, a tendency for a reduction in avascular RFP+ cell numbers was already seen and at 21 DPO the amount of RFP+ non-vascular cells had also declined in controls (consistent with the transient nature of this avascular cell subset). We found that SOX2 was expressed in 42% of avascular RFP+ cells (Figure 3E, pie diagram). Thus, it is apparent that *Sox2*-loss in *Nestin*::creER2, R26-RFP, Sox2$^{fl/fl}$ animals affected a much larger population of traced cells than only the fraction of cells initially characterized as SOX2 positive. In particular, SOX2+ TAMEP were necessary for generating the entire population of traced avascular, myeloid-like cells. As SOX2+ TAMEP were the source for all TAMEP they are hereafter referred to as TAMEP progenitors.

Interestingly, we also noted that in addition to homozygous Sox2-knockouts (see above), even loss of a single Sox2-allele (*Nestin*::creER2, R26-RFP, Sox2$^{fl/WT}$) profoundly reduced TAMEP-numbers at 14DPO (Figure 3F) showing that TAMEP are haploinsufficient for *Sox2*. *Sox2*-haploinsufficiency is well described for some cell subsets, e.g., cells of the cochlea (Atkinson et al., 2018), while NPC or OPC remain fully functional with a single Sox2 allele (Mich et al., 2014; Zhao et al., 2015). Using mouse models (Arnold et al., 2011; Riccardi et al., 2016), tracing cells with a single (*Sox2*::creER2, R26-RFP) or with two functional copies (*Sox2*::IRES-creER2, R26-RFP) of Sox2, we find that TAMEP were traced exclusively with the *Sox2*::IRES-creER2, R26-RFP model (Figure 3F). Crossbreeding of *Sox2*::-IRES-creER2, R26-RFP mice with *Cx3cr1*-GFP strain (Jung et al., 2000) corroborated that traced cells in this model had a myeloid appearance (Figure 3G); of note, the *Sox2*::IRES-creER2, R26-RFP model did not immunolabel for PDGFRB, which confirmed that pericytes did not derive from TAMEP. Overall, we traced TAMEP from two independent mouse models and found that TAMEP are haploinsufficient for SOX2, distinguishing TAMEP from astrocytes, OPC, or NPC, which show no *Sox2*-gene dosage effects.

## TAMEP do not derive from peripheral or CNS macrophages

We investigated if TAMEP (and/or their progenitors) may be derived from the hematopoietic system. To do this, we

(E) Confocal maximum projection for Iba1 and F4/80 at 7 DPO (Nes-RFP model); note that traced cells express F4/80 but not Iba1 (orthogonal view).
(F) Intratumoral avascular RFP+ cells (Nes-RFP model) were analyzed by FACS; immune-positivity for CD11b was detected (representative data of 9 independent FACS experiments).
Data (in B) are presented as mean ± SD. Scale bars are 15 μm. See also Figure S3.

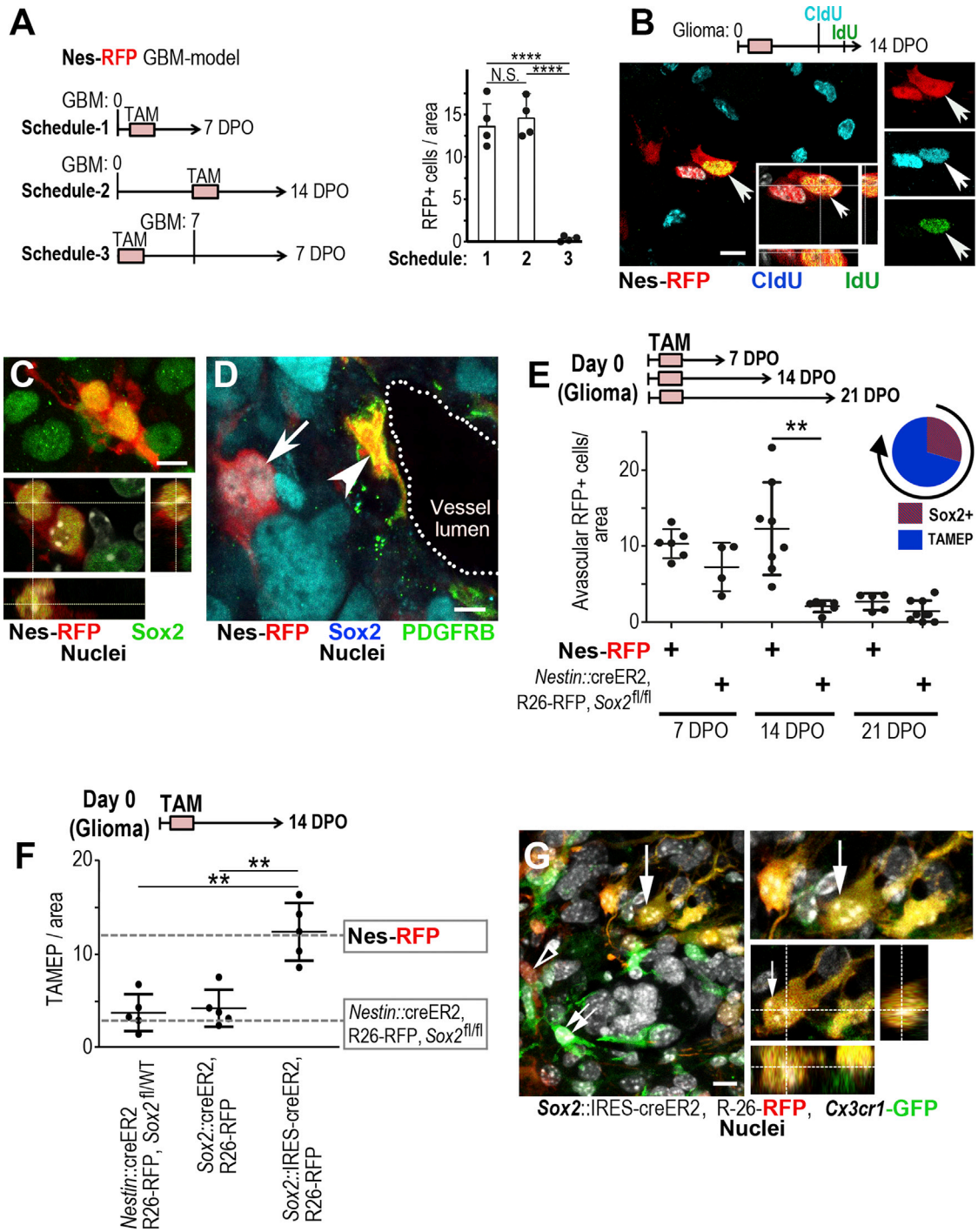


**Figure 3. TAMEP are generated by a SOX2-dependent progenitor**

(A) Different experimental schedules in Nes-RFP mice (each group: n = 4 animals); avascular RFP+ cells were only traced from tumor-bearing brains.

(B) CldU/IdU uptake inspected by immunofluorescence (arrow indicates one identical cell) at 14DPO (see schedule; n = 8 Nes-RFP mice).

(C and D) (C) Robust SOX2 expression in a set of avascular traced cells (maximum projection; orthogonal view) in the Nes-RFP glioma model was (D) restricted to the avascular cell population (arrow); absent from traced (PDGFRB+) perivascular cells (arrowhead).

(E) Quantification of avascular RFP+ cells in GBM of Nes-RFP mice or conditional *Sox2*-knockouts: *Sox2*-knockout strongly reduced avascular traced cells at 14 DPO; pie diagram: SOX2 is expressed in 42% of avascular RFP+ cells and SOX2-loss abrogates the vast majority of TAMEP; hence, Sox2+ TAMEP progenitors are necessary for the generation of TAMEP (arrow); each dot indicates data from one mouse; with n = 4 to n = 8 animals per experimental group.

*(legend continued on next page)*

generated bone-marrow chimeric models, in which lethally irradiated Nes-RFP mice received bone marrow from the *Spi1*-GFP strain (Back et al., 2005), abbreviated as chimera-1. The *Spi*1-gene encodes the transcription factor PU.1, which is essential for establishing the myeloid lineage and some other lymphocytes (Back et al., 2005). Also, we transplanted bone marrow from Nes-RFP animals into wild-type mice (chimera-2). After established bone-marrow reconstitution, mice were orthotopically inoculated with glioma, and cell-tracing was initiated by tamoxifen-application (scheme in Figure 4A). Non-irradiated Nes-RFP mice were used as controls. As expected, in chimera-1, we observed a massive accumulation of bone-marrow-derived *Spi1*-GFP+ cells in GBM, and brain-endogenous Nes-RFP+ cells remained at control levels (Figures 4A and 4B). However, no intracranial accumulation of bone-marrow transplanted Nes-RFP+ cells was observed in chimera-2 (Figures 4A and 4B). Intratumoral traced cells of the Nes-RFP strain never expressed the pan-leukocyte marker CD45 (Figure 4C) or the monocyte-marker CCR2 (Figure 4D), as investigated with Nes-RFP, CCR2-GFP transgenic mice (Bowman et al., 2016; Chen et al., 2017). The *Flt3*-cre mouse line containing a GFP-reporter for lineage tracing from bone-marrow stem cells (Benz et al., 2008) was used as a glioma model and revealed that SOX2 was absent from bone-marrow-derived cells (Figure 4E). Finally, we also tested a microglia-origin of TAMEP by using the *Cx3cr1*::creER, R26-RFP model, which accurately identifies microglia (and other CNS-resident macrophages) after adequate tamoxifen pulse/chase schedules (Huang et al., 2018; Wieghofer et al., 2015). This showed that cells of the microglia lineage never expressed Sox2 (Figure 4F), thereby excluding that TAMEP progenitors (and subsequently TAMEP) stem from brain macrophages. All in all, we used a range of models identifying blood-borne macrophages or microglia as well as other CNS-resident phagocytes and consistently observed that TAMEP do not relate to established sets of myeloid cells (Figure 4G).

## Identification of TAMEP in human GBM

Hitherto, we relied on transgenic mouse models with orthotopic implantation of glioma cells to identify TAMEP. In order to extend our study to different models and human brain tumor biopsies, we sought to establish scRNA-seq profiles as well as immunohistochemical procedures to locate TAMEP in human material. We have shown that TAMEP and their progenitors express myeloid markers (without belonging to the myeloid lineage) and require SOX2 (in order to maintain their own lineage). Our previous experiments demonstrated that SOX2 is absent from blood-borne myeloid cells or tissue macrophages (Figures 4E–4G), which is in full agreement with other reports (Liu et al., 2018; Rosager et al., 2017; Sarkar et al., 2014). However, TAMEP expressing the myeloid marker CX3CR1 derive from SOX2-positive progenitors (Figure 3G). Therefore, we investigated if SOX2 and CX3CR1 coexpressing TAMEP would be observed in our scRNA-seq data from lineage-traced intratumoral cells. This was indeed the case, we detected RFP+, CX3CR1/SOX2-coexpressing TAMEP (Figures 5A and S4A), which have similarity with microglia (Figure S4B). Immunofluorescence inspection corroborated that Nes-RFP, *Cx3cr1*-GFP+ transgenic mice express SOX2 (Figure 5B).

Combinatorial detection of (nuclear) transcription factors represents a very reliable way for cell identification, and hence, we asked if some TAMEP also express the (essential) myeloid transcription factor *Spi1*/PU.1 (Back et al., 2005). Therefore, we first investigated if PU.1 was expressed in GBM-parenchymal cells traced with the *Sox2*::IRES-creER2, R26-RFP model and confirmed PU.1 in *Sox2*-traced cells (Figure 5C). Second, we determined if Nes-RFP, *Spi1*-GFP mice (reporting PU.1-expression as GFP-signal) would express SOX2, which was also the case (Figure 5D). We found that SOX2 immuno-positivity in myeloid-reporter strains (*Cx3cr1*-GFP or *Spi1*-GFP) was exclusively observed in cells coexpressing RFP (from the Nes-RFP strain). Hence, SOX2-expression in myeloid marker positive cells in our models was restricted to TAMEP and combinatorial immuno-detection of SOX2 and PU.1 or CX3CR1 represents a useful strategy to identify TAMEP in human material since SOX2/PU.1 coexpression is otherwise only seen in some forms of leukemia (Tosic et al., 2018).

These defining features for TAMEP from transgenic mouse models (data from immunofluorescence analysis and from scRNA-seq data identifying TAMEP) were now applied to human GBM-derived datasets. We analyzed scRNA-seq datasets from CD45+ GBM-associated cells (Sankowski et al., 2019) and from samples without enrichment for specific cell types (Wang et al., 2019). Coherent with our previous finding that TAMEP are CD45 negative (Figure 4C), we did not find any SOX2+/SPI1+ double-positive cells in CD45+ GBM-derived cells, while we detected SOX2+/SPI1+ double-positive cells in three out of five GBM samples obtained without CD45-targeting purification (Figure S4C). Regional abundance (or scarcity) of TAMEP (subsequently observed by immunofluorescence, as described below) may explain why two biopsies did not contain SOX2+/SPI1+ cells. Detailed transcriptome information was then obtained from the dataset with the best coverage (SF11644 in Figure S4C). We observed that cells with a myeloid expression profile from this sample were segregated into 4 clusters (Figure 5E) and that SOX2+/SPI1+ cells were significantly enriched in cluster 2 ($chi^2$-test: OR = 16.96, $p < 10^{-16}$). A machine-learning approach (Malta et al., 2018) named one-class logistic regression (OCLR) allowed to score patient-derived expression profiles for their overall similarity with mouse TAMEP scRNA-seq data. This indicated that cells in cluster 2 have a higher TAMEP index than other clusters. In agreement with our TAMEP profile, cluster 2 was enriched for cells that express the OPC marker PDGFRA and for CX3CR1. It cannot be formally excluded that multiplets contribute to expression profiles of datasets from microfluidics

(F) Ablation of one *Sox2*-allele was sufficient to reduce TAMEP-numbers (comparable to *Sox2*-knockouts; lower dashed line); the *Sox2*::creER2 strain (with one functional *Sox2*-allele) did not trace TAMEP; the *Sox2*::IRES-creER2 strain (containing two functional Sox2 alleles) traced TAMEP (comparable to Nes-RFP controls; upper dashed line; n = 5 mice per experimental group).

(G) *Sox2*::IRES-creER2, R26-RFP, *Cx3cr1*-GFP glioma models were used to trace TAMEP (arrow); single-positive cells (GFP+; double-arrow) or RFP+ (bi-color arrowhead) are also shown. Each value (in E and F) represents one mouse, data (in A, E, and F) are presented as mean ± SD; statistical significance (in A, E, and F) was tested by one-way ANOVA with post hoc test and is indicated: (N.S., non-significant; **$p < 0.01$; ****$p < 0.001$); scale bars are 5 μm.

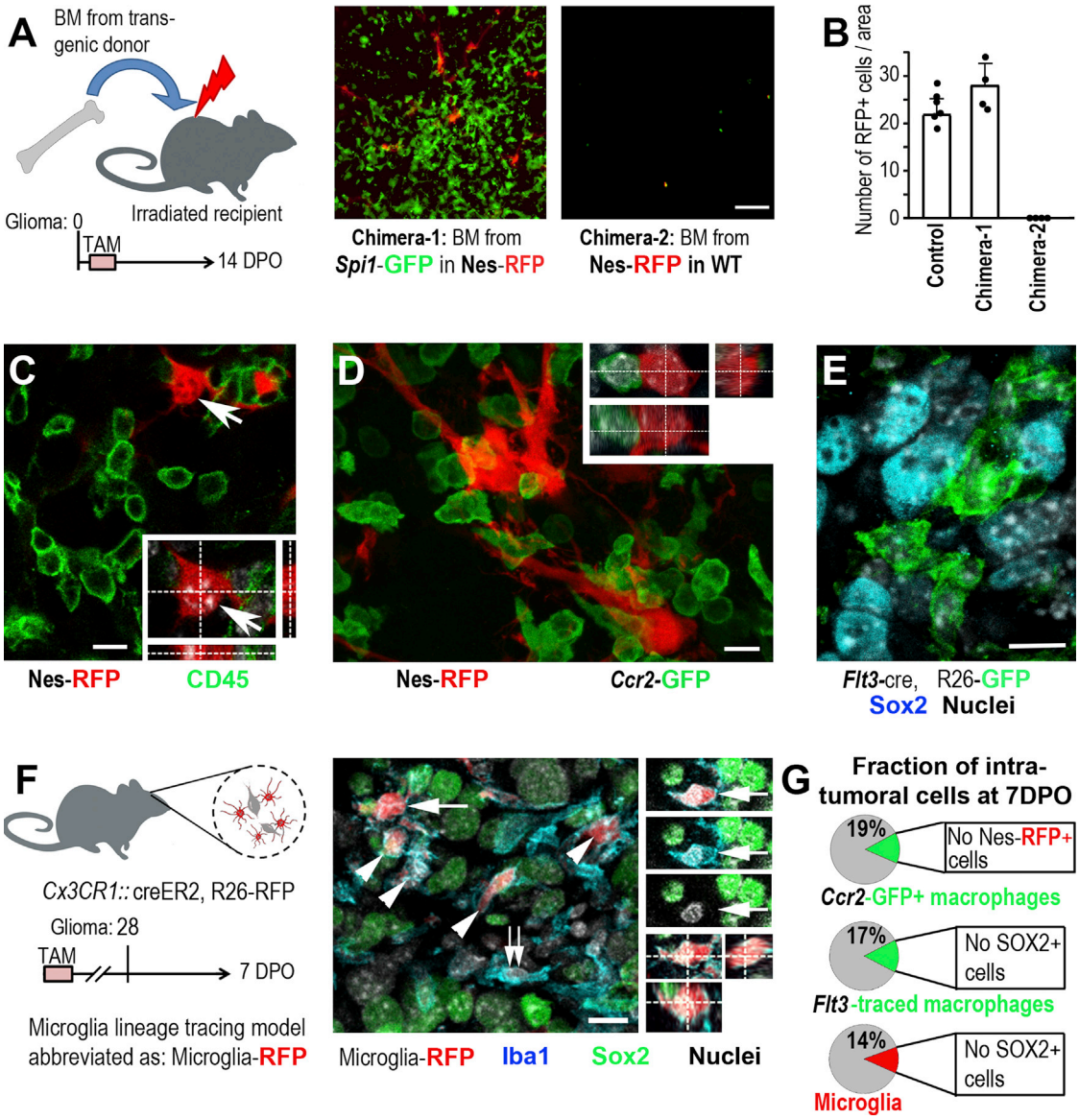


**Figure 4. TAMEP and their progenitors do not derive from the myeloid lineage**

(A) Lineage tracing in bone marrow (BM) chimeric models at 14DPO, chimera-1: Nes-RFP mice received BM from *Spi1*-GFP mice. Chimera-2: wild-type mice obtained BM from Nes-RFP mice.

(B) BM-transfer was successful (GFP+ cells in glioma of chimera-1, n = 4 mice); BM-derived RFP+ cells had no tropism to GBM (chimera-2; n = 4 mice); controls (without BM-exchange; n = 6 mice).

(C) RFP+ avascular cells do not express CD45.

(D) The Nes-RFP, *Ccr2*-GFP glioma-bearing mice contained no GFP+/RFP+ cells.

(E) *Flt3*-cre traced cells (GFP+) in gliomas never express SOX2.

(F) A pulse-chase paradigm in a *Cx3cr1*::creER, R26-RFP model excluded SOX2-expression from traced glioma-associated microglia (RFP+ cells; arrow); staining for Iba1 in microglia (arrowheads) and macrophages (double-arrow).

(G) Nes-RFP+ or Sox2+ cells never overlapped with macrophages (*Ccr2*-GFP+), did not derive from BM stem cells (*Flt3*-traced) and did not origin from microglia. Data (in B) are presented as mean ± SD; statistical significance was tested by one-way ANOVA with post hoc test and is indicated: *p < 0.05, ****p < 0.0001); scale bars are 50 μm in (A), 10 μm in (C), (D) and (E).

(human GBM). However, expression profiles for mouse TAMEP (clearly excluding multiplets by flow cytometry) served to identify human TAMEP with high reliability. Altogether, this underscores the validity of our approach for TAMEP detection in samples from human GBM.

The bioinformatics identification of TAMEP in mouse and human GBM was substantiated by immunofluorescence inspection of TAMEP in GBM models and human GBM specimen. First, we used a genetic GBM mouse model (Figures S5A and S5B) and explored immunofluorescence for SOX2 and PU.1. We

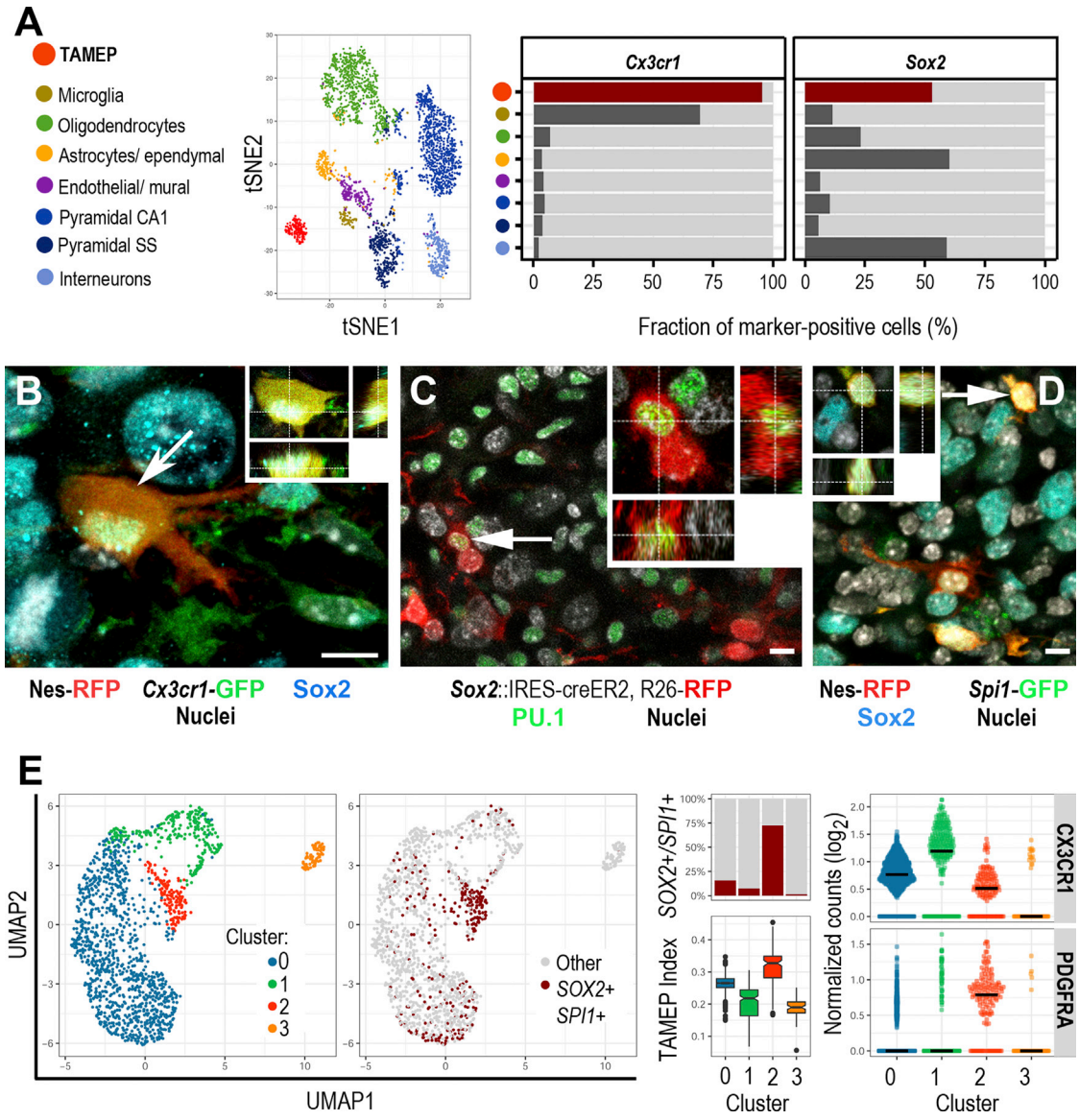


**Figure 5. TAMEP are observed in murine and human GBM**

(A) Nes-RFP cells were purified from experimental gliomas and scRNA-seq data (TAMEP), compared with established single-cell expression profiles of identified brain cells after unsupervised clustering and presented as tSNE-plot; expression levels for Cx3cr1 and Sox2 were quantified in all cell populations.

(B) SOX2 and GFP colabel exclusively in avascular RFP+ cells in glioma-bearing Nes-RFP, *Cx3cr1*-GFP models.

(C) Immunofluorescence for PU.1 in tumor-associated RFP+ cells from the *Sox2*::IRES-creER2, R26-RFP model (arrow).

(D) Sox2-immunolabeling is restricted to traced avascular cells in Nes-RFP, *Spi1*-GFP transgenic mice.

(E) scRNAseq data from 3/5 human GBM-datasets indicated abundance of TAMEP. One dataset was inspected in detail for tumor-associated myeloid cells and a UMAP-plot indicated 4 different myeloid clusters; *SOX2+/SPI1+* cells are enriched in cluster 2. A large TAMEP-defining gene set was obtained from mouse transgenic models and the same set of genes identified TAMEP in cluster-2 of human GBM by a OCLR model (TAMEP index). Expression pattern for *CX3CR1* and *PDGFRA* recapitulate the expectations for TAMEP in human GBM. Scale bars represent 5 μm ( B-D). See also Figure S4.

found Sox2 single-positive nuclei (Figure 6A) indicating glioma cells, PU.1 single-positive nuclei (representing tumor-associated myeloid cells), and areas with many SOX2/PU.1 double-positive nuclei indicating a loco-regional abundance of TAMEP. TAMEP were reliably detected in GBM but were absent from mouse models for stroke or neuro-inflammation (Figures S5D–S5K) as quantified in Figure 6B. SOX2/PU.1 coexpressing cells were locally abundant (with regional heterogeneity) in a range of human CNS neoplasms comprising GBM and additional othotopic models (Figures 6C–6E and S6A–S6D), whereas SOX2/PU.1 double-positive cells were absent from tumor-free human brain (Table S3). Altogether, we were able to consistently identify cells expressing the combinatorial TAMEP markers SOX2+/SPI1+ or PDGFRA/CX3CR1 in multiple human GBMs and identified a

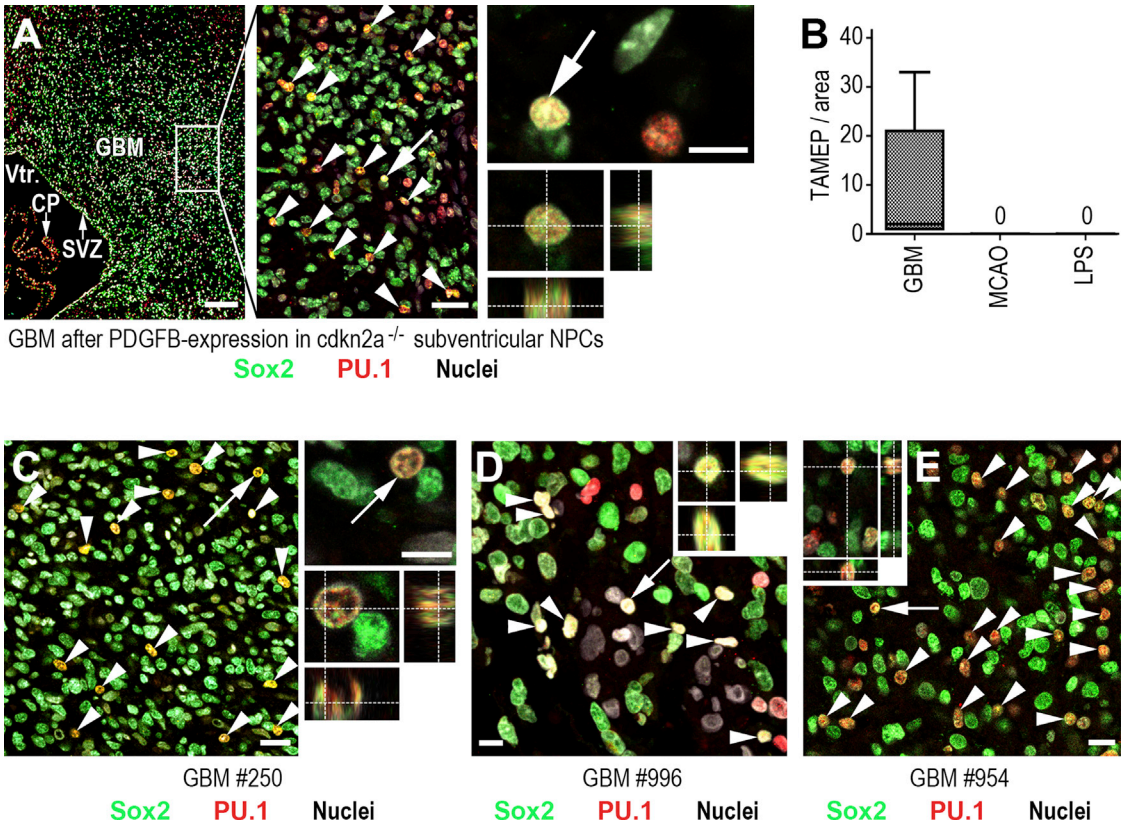


**Figure 6. Confirmation of TAMEP in human and mouse transgenic GBM**

(A) Regional abundance of TAMEP (SOX2+/PU.1+; arrowheads) in a genetic glioma model (arrow; magnified).

(B) Quantification of TAMEP after middle cerebral artery occlusion (MCAO), LPS (i.c.) or in GBM (n = 4 mice per group in all cases; box and whisker plot).

(C–D) TAMEP (arrowheads) in biopsies from human GBM; magnified in orthogonal view (arrows). Scale bars are 200 μm (A), 30 μm (in magnified part of A), 10 μm (insert in A), and 30 μm (C–E). See also Figures S5 and S6.

population of cells in one human GBM whose transcriptional profile showed a high TAMEP-score. These data suggest that TAMEP are present in human GBMs.

## TAMEP shape GBM angiogenesis

Next, we asked if TAMEP and their progenitors have a particular pathological role in GBM. In *Nestin*::creER2, R26-RFP, *Sox2*$^{fl/fl}$ mice (Sox2-KO; Figures 7A–7C and S7A–S7G), we observed morphological changes in tumor vessels (as compared with *Sox2* wild-type controls; WT) and therefore quantified the extent of GBM vascularization in Nes-RFP or *Sox*-deficient mice over a time course (Figure 7A). At earlier time points (7 and 14 DPO; Figure S7H), we noted a reduction in vessel branch-points after conditional *Sox2*-loss, in comparison with controls, and this effect persisted into advanced glioma stages (Figure 7B). Intratumoral vascularization was strongly reduced at 21DPO in *Nestin*::creER2, R26-RFP, *Sox2*$^{fl/fl}$ mice (and in *Nestin*::creER2, R26-RFP, *Sox2*$^{fl/WT}$ models; Figure S7A), as compared with *Sox2*-WT mice. Furthermore, we included an additional control and ablated the entire population of traced cells by conditional expression of diphtheria toxin-A (*Nestin*::creER2, R26-RFP, R26-iDTA; abbreviated as iDTA in Figure 7B), which did not mediate any additive effects with respect to the extent of tumor vascularization in comparison with conditional *Sox2*-KO models. However, conditional *Sox2*-loss affected vessel-morphology generating vessels with a very large lumen and little complexity (this was rare in controls; Figures 7C and S7B–S7G). The vascular cavities in gliomas from the *Sox2*-knockout model lacked full pericyte coverage (Figure 7C). We investigated a potential reciprocal connection between TAMEP and tumor vessels by determining if anti-angiogeneis can reduce TAMEP density, but this was not the case (Figure S7I). Overall, this revealed that TAMEP (and their progenitors) have a strong impact on GBM vascularization and can persistently modulate the intratumoral vascular network.

## TAMEP affect GBM expansion

GBM growth is supported by tumor vascularization (Jain et al., 2007) and reduced tumor vessel density (as seen after TAMEP-reduction) should impact on GBM expansion (Mastrella et al., 2019; von Baumgarten et al., 2011). In order to investigate this point, we used our established mouse models that produce diminished TAMEP cell numbers (*nestin*::creER2, R26-RFP, *Sox2*$^{fl/fl}$ or *nestin*::creER2, R26-RFP, *Sox2*$^{fl/WT}$), ablating TAMEP plus intratumoral pericytes (*nestin*::creER2, R26-RFP, R26-iDTA) or controls (Nes-RFP; leaving TAMEP intact). After implanting GBM and stimulation with tamoxifen (Figure 7D), we determined GBM volumes (Figures 7E and 7F) by histological inspection of

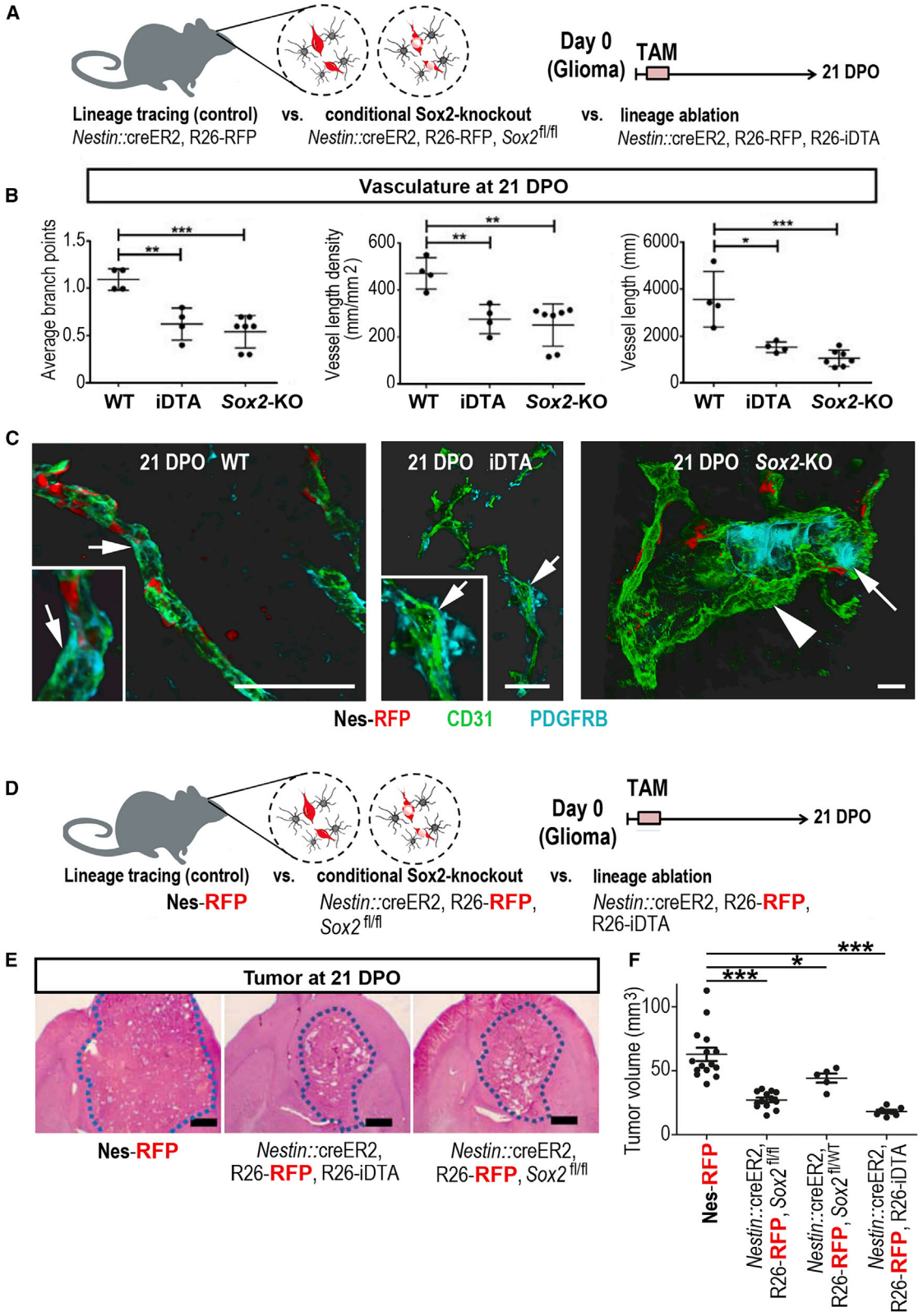


*(legend on next page)*

brain serial sections. In agreement with the role of TAMEP in GBM vascularization, we found that numbers of TAMEP (or TAMEP plus pericytes) largely reduced GBM volumes (Figure 7F). This effect was TAMEP-specific as heterozygosity for *Sox2* already modulated tumor expansion and as *Sox2*-conditional knockout in endothelia, pericytes or microglia of GBM-models did not reduce the tumor-size (Figure S7J). In summary, our work introduces TAMEP as a GBM-parenchymal component with high pathological impact.

## DISCUSSION

We described a progenitor cell type of the brain tumor microenvironment, termed TAMEP-progenitor, which has a profound role in neoplastic angiogenesis in the brain. These progenitors were initially characterized by expression of the stem-cell-related transcription factor SOX2 (Sarkar and Hochedlinger, 2013) and by an active transgenic *Nestin* gene-promoter serving as a marker for immature cells (Bernal and Arranz, 2018). TAMEP progenitors were specifically ablated by conditional *Sox2*-knockout, preventing the intratumoral accumulation of TAMEP. Also, we discovered that TAMEP progenitors are sensitive to alterations in *Sox2* gene-dosage, which served as a criterion for additional TAMEP tracing models corroborating our findings from Nes-RFP mice. Our scRNA-seq data indicated an aberrant, myeloid-like expression profile in TAMEP. This was subsequently validated in different models by transgenic reporters and immunofluorescence markers, e.g., PU.1, CD11b, F4/80, or CX3CR1 (Back et al., 2005; Glass and Synowitz, 2014). However, despite this myeloid appearance, we could clearly show that TAMEP are not myeloid cells: we excluded that TAMEP (or their progenitors) derive from hematopoietic niches in the bone marrow (using mouse-chimera, *CCR2*-reporters, or *Flt3*-based tracing), and we ruled out that TAMEP derive from microglia using the Cx3cr1-creER2 model (Benz et al., 2008; Chen et al., 2017; Wieghofer et al., 2015). A non-myeloid origin for TAMEP is also supported by the notion that these cells are generated from a (*Sox2*-dependent) progenitor, which excludes a microglial source (Huang et al., 2018). All in all, this supports the view that tumor-associated myeloid cells are highly heterogeneous (Audia et al., 2017; Glass and Synowitz, 2014; Hambardzumyan et al., 2016) and even bear non-myeloid subsets disguised as a myeloid component.

TAMEP progenitors are different from established, GBM-associated stem and progenitor cell types, such as MSC, OPC, or NPC, as observed by intravital imaging, immunofluorescence studies in different transgenic lineage-tracing models, or pathological outcome in lineage-ablation experiments. The most prominent sources for MSC include the vascular mural compartment (Crisan et al., 2008) or the bone marrow (Frenette et al., 2013), but these were experimentally excluded for TAMEP. In addition, MSC markers (Jones and Schäfer, 2015) were absent from TAMEP. OPCs (which are not vessel associated) contribute to GBM expansion by generating mural cells of the intratumoral vasculature (Huang et al., 2014), but such a contribution was again ruled out by intravital imaging. NPC have a strong GBM tropism only in the young brain but not in the age range of mice used in our study (Stock et al., 2012; Walzlein et al., 2008). Furthermore, NPCs exert anti-tumor effects in young mice (Stock et al., 2012), whereas TAMEP support glioma expansion. Sox2-based tracing of TAMEP requires models (Riccardi et al., 2016) that are different from lineage-tracing models for NPC or OPC (Mich et al., 2014; Zhao et al., 2015), as progenitors for TAMEP are Sox2-haploinsufficient (whereas NPC/OPC are not). These features clearly distinguish TAMEP progenitors from other known progenitors within the GBM parenchyma.

We show that a small and distinct population of cells with a myeloid expression profile has a specific impact on brain neoangiogenesis. A role for myeloid cells in GBM angiogenesis was previously observed (Brandenburg et al., 2016; Mathivet et al., 2017). Reducing the numbers of monocyte-derived macrophages was exploited to improve chemotherapy but had no direct tumor-suppressing effect (Mathivet et al., 2017). In contrast, CNS-specific ablation of CD11b-positive cells resulted in an overall reduction in intratumoral vessels and glioma size (Brandenburg et al., 2016). Hence, dissecting the set of CD11b-positive cells is interesting in order to establish strategies for direct anti-tumor effects. In this work, we explored one GBM-associated subpopulation of CD11b-positive cells (TAMEP) with striking angiogenic capacity. Altogether, the transient set of TAMEP is required for a dense and functional vascularization of GBM, thus offering a new and promising therapeutic target in neurooncology.

## STAR★METHODS

Detailed methods are provided in the online version of this paper and include the following:

- KEY RESOURCES TABLE
- RESOURCE AVAILABILITY
  - Lead contact

**Figure 7. TAMEP and their progenitors control glioma expansion**

(A) Intratumoral vascularization was quantified in controls, *Sox2* conditional knockouts (*Sox2*-KO), or in a lineage-ablation model (iDTA) at 21 DPO.

(B) Parameters for vascular morphology like intratumoral vascular branching and vascular complexity are strongly modulated in *Sox2*-KO (n = 7 mice) with no additional effects in the iDTA model (n = 4) as compared with controls (n = 4).

(C) 3D-reconstruced intratumoral vessels with immunofluorescence for endothelia (CD31) and pericytes (PDGFRB); arrows correspond to magnified areas in WT (control) and iDTA models; specific ablation of TAMEP (*Sox2*-KO) generates enlarged vascular cavities with patchy association of pericytes (arrow) and pericyte-free areas (arrowhead).

(D) Orthotopic GBM were induced in Nes-RFP mice (controls), *Sox2* conditional knockouts, or in a lineage-ablation model, tamoxifen was applied and tumor size was quantified in all models at 21 DPO.

(E) Representative micrographs for GBM histopathology in three experimental models at 21 DPO; the cell-dense tumor mass is outlined.

(F) Quantification of GBM size in controls (Nes-RFP, n = 15), homozygous (n = 5) or heterozygous (n = 13) *Sox2*-ablation in Nes-RFP and iDTA strains (n = 6). Data (in B and F) are presented as mean ± SD; statistical significance according to one-way ANOVA with post hoc test is indicated: $^{**}p < 0.01$, $^{****}p < 0.0001$. Each dot (in the diagrams) represents the average statistical value obtained from one mouse. Scale bars are 100 μm (C) or 1mm (E). See also Figure S7.

## SUPPLEMENTAL INFORMATION

Supplemental Information can be found online at https://doi.org/10.1016/j.cels.2021.01.002.

## ACKNOWLEDGMENTS

R.G. and R.E.K. gratefully acknowledge funding by the "Anni-Hofmann Stiftung," the DFG (GL691/2; SFB824), and the "Wilhelm Sander Stiftung." L.C., Y.L., W.Z., X.W., and D.Z. were supported by the "China Scholarship Council" (CSC) graduate scholarships and K.E. by the LMU FöFoLe program. C.G. was funded by "the Swiss Cancer League" (KLS-4518-08-2018). E.M. was supported by DFG (MO2562/1-2) and L.v.B. by the "Else Kröner Fresenius Stiftung (A265)" and the "Bayerische Gleichstellungsförderung." C.S. was supported by the DFG (SFB914) and the DZHK and BMBF. W.E., I.H., and P.J. were supported by LMUexcellent SFB1243. Furthermore, we are grateful to the Core Facility Bioimaging at the Biomedical Center and the animal facilities at the University Clinics Munich. PU.1kiGFP mice were provided by Dr. Philippe Kastner (IGBMC - CNRS UMR 7104), *Ve-cadherin*-creER2 mice by Ralf Adams (MPI Mol. Biomedicine), and Sox2-IRES-creER2 mice by the Novartis Institutes of BioMedical Research. We thank Christoph Ziegenhain for scRNA-seq library generation, Magali Soumillon and Tarjei Mikkelsen for the SCRB-seq protocol, Stefan Krebs and Helmut Blum from the LAFUGA platform (LMU) for sequencing, and Aaron Diaz (UCSF) for sharing scRNA-seq data.

## AUTHOR CONTRIBUTIONS

R.E.K., M.Synowitz, L.v.B., C.S., W.E., E.M., and R.G. designed experiments; R.E.K., L.C., Y.L., D.Z., H.Z., J.C., W.Z., Y.W., K.E., L.S., P.J., I.H., F.M., C.F., M.H., S.V.K., S.S., M.S., I.A., E.M., L.v.B., C.S., W.E., and R.G. conducted experiments and analyzed data. P.J. analyzed human scRNA-seq datasets. R.E.K., Y.L., Y.W., K.E., J.C.T., M. Schiemann, I.A., C.G., V.T., M. Synowitz, E.M., and R.G. obtained and characterized experimental models, generated the mouse model or provided scientific support. R.G. wrote the manuscript. All authors discussed the results and revised the manuscript text.

## DECLARATION OF INTERESTS

The authors declare no competing interests.

Received: September 26, 2019
Revised: April 7, 2020
Accepted: January 4, 2021
Published: February 15, 2021

## REFERENCES

Aldape, K., Brindle, K.M., Chesler, L., Chopra, R., Gajjar, A., Gilbert, M.R., Gottardo, N., Gutmann, D.H., Hargrave, D., Holland, E.C., et al. (2019). Challenges to curing primary brain tumours. Nat. Rev. Clin. Oncol. *16*, 509–520.

Aran, D., Looney, A.P., Liu, L., Wu, E., Fong, V., Hsu, A., Chak, S., Naikawadi, R.P., Wolters, P.J., Abate, A.R., et al. (2019). Reference-based analysis of lung single-cell sequencing reveals a transitional profibrotic macrophage. Nat. Immunol. *20*, 163–172.

Armulik, A., Genové, G., and Betsholtz, C. (2011). Pericytes: developmental, physiological, and pathological perspectives, problems, and promises. Dev. Cell *21*, 193–215.

Armulik, A., Genové, G., Mäe, M., Nisancioglu, M.H., Wallgard, E., Niaudet, C., He, L., Norlin, J., Lindblom, P., Strittmatter, K., et al. (2010). Pericytes regulate the blood-brain barrier. Nature *468*, 557–561.

Arnold, K., Sarkar, A., Yram, M.A., Polo, J.M., Bronson, R., Sengupta, S., Seandel, M., Geijsen, N., and Hochedlinger, K. (2011). Sox2(+) adult stem and progenitor cells are important for tissue regeneration and survival of mice. Cell Stem Cell *9*, 317–329.

Atkinson, P.J., Dong, Y., Gu, S., Liu, W., Najarro, E.H., Udagawa, T., and Cheng, A.G. (2018). Sox2 haploinsufficiency primes regeneration and Wnt responsiveness in the mouse cochlea. J. Clin. Invest. *128*, 1641–1656.

Audia, A., Conroy, S., Glass, R., and Bhat, K.P.L. (2017). The impact of the tumor microenvironment on the properties of glioma stem-like cells. Front. Oncol. *7*, 143.

Back, J., Allman, D., Chan, S., and Kastner, P. (2005). Visualizing PU.1 activity during hematopoiesis. Exp. Hematol. *33*, 395–402.

Behnan, J., Isakson, P., Joel, M., Cilio, C., Langmoen, I.A., Vik-Mo, E.O., and Badn, W. (2014). Recruited brain tumor-derived mesenchymal stem cells contribute to brain tumor progression. Stem Cells *32*, 1110–1123.

Benz, C., Martins, V.C., Radtke, F., and Bleul, C.C. (2008). The stream of precursors that colonizes the thymus proceeds selectively through the early T lineage precursor stage of T cell development. J. Exp. Med. *205*, 1187–1199.

Bernal, A., and Arranz, L. (2018). Nestin-expressing progenitor cells: function, identity and therapeutic implications. Cell. Mol. Life Sci. *75*, 2177–2195.

Binda, E., Visioli, A., Giani, F., Trivieri, N., Palumbo, O., Restelli, S., Dezi, F., Mazza, T., Fusilli, C., Legnani, F., et al. (2017). Wnt5a drives an invasive phenotype in human glioblastoma stem-like cells. Cancer Res. *77*, 996–1007.

Bondjers, C., He, L., Takemoto, M., Norlin, J., Asker, N., Hellström, M., Lindahl, P., and Betsholtz, C. (2006). Microarray analysis of blood microvessels from PDGF-B and PDGF-Rbeta mutant mice identifies novel markers for brain pericytes. FASEB J. *20*, 1703–1705.

Bowman, R.L., Klemm, F., Akkari, L., Pyonteck, S.M., Sevenich, L., Quail, D.F., Dhara, S., Simpson, K., Gardner, E.E., Iacobuzio-Donahue, C.A., et al. (2016). Macrophage ontogeny underlies differences in tumor-specific education in brain malignancies. Cell Rep. *17*, 2445–2459.

Brandenburg, S., Müller, A., Turkowski, K., Radev, Y.T., Rot, S., Schmidt, C., Bungert, A.D., Acker, G., Schorr, A., Hippe, A., et al. (2016). Resident microglia rather than peripheral macrophages promote vascularization in brain tumors and are source of alternative pro-angiogenic factors. Acta Neuropathol. *131*, 365–378.

Breiman, L. (2001). Random forests. Mach. Learn. *45*, 5–32.

Campos, B., Wan, F., Farhadi, M., Ernst, A., Zeppernick, F., Tagscherer, K.E., Ahmadi, R., Lohr, J., Dictus, C., Gdynia, G., et al. (2010). Differentiation therapy

exerts antitumor effects on stem-like glioma cells. Clin. Cancer Res. *16*, 2715–2728.

Chen, Z., Feng, X., Herting, C.J., Garcia, V.A., Nie, K., Pong, W.W., Rasmussen, R., Dwivedi, B., Seby, S., Wolf, S.A., et al. (2017). Cellular and molecular identity of tumor-associated macrophages in glioblastoma. Cancer Res. *77*, 2266–2278.

Crisan, M., Yap, S., Casteilla, L., Chen, C.W., Corselli, M., Park, T.S., Andriolo, G., Sun, B., Zheng, B., Zhang, L., et al. (2008). A perivascular origin for mesenchymal stem cells in multiple human organs. Cell Stem Cell *3*, 301–313.

Drachsler, M., Kleber, S., Mateos, A., Volk, K., Mohr, N., Chen, S., Cirovic, B., Tüttenberg, J., Gieffers, C., Sykora, J., et al. (2016). CD95 maintains stem cell-like and non-classical EMT programs in primary human glioblastoma cells. Cell Death Dis. *7*, e2209.

Frenette, P.S., Pinho, S., Lucas, D., and Scheiermann, C. (2013). Mesenchymal stem cell: keystone of the hematopoietic stem cell niche and a stepping-stone for regenerative medicine. Annu. Rev. Immunol. *31*, 285–316.

Giachino, C., and Taylor, V. (2009). Lineage analysis of quiescent regenerative stem cells in the adult brain by genetic labelling reveals spatially restricted neurogenic niches in the olfactory bulb. Eur. J. Neurosci. *30*, 9–24.

Glass, R., and Synowitz, M. (2014). CNS macrophages and peripheral myeloid cells in brain tumours. Acta Neuropathol. *128*, 347–362.

Goldmann, T., Wieghofer, P., Jordão, M.J., Prutek, F., Hagemeyer, N., Frenzel, K., Amann, L., Staszewski, O., Kierdorf, K., Krueger, M., et al. (2016). Origin, fate and dynamics of macrophages at central nervous system interfaces. Nat. Immunol. *17*, 797–805.

Goodpaster, T., and Randolph-Habecker, J. (2014). A flexible mouse-on-mouse immunohistochemical staining technique adaptable to biotin-free reagents, immunofluorescence, and multiple antibody staining. J. Histochem. Cytochem. *62*, 197–204.

Grathwohl, S.A., Kälin, R.E., Bolmont, T., Prokop, S., Winkelmann, G., Kaeser, S.A., Odenthal, J., Radde, R., Eldh, T., Gandy, S., et al. (2009). Formation and maintenance of Alzheimer's disease beta-amyloid plaques in the absence of microglia. Nat. Neurosci. *12*, 1361–1363.

Haghverdi, L., Lun, A.T.L., Morgan, M.D., and Marioni, J.C. (2018). Batch effects in single-cell RNA-sequencing data are corrected by matching mutual nearest neighbors. Nat. Biotechnol. *36*, 421–427.

Hambardzumyan, D., Gutmann, D.H., and Kettenmann, H. (2016). The role of microglia and macrophages in glioma maintenance and progression. Nat. Neurosci. *19*, 20–27.

Hammond, T.R., Robinton, D., and Stevens, B. (2018). Microglia and the brain: complementary partners in development and disease. Annu. Rev. Cell Dev. Biol. *34*, 523–544.

Ho, I.A., Toh, H.C., Ng, W.H., Teo, Y.L., Guo, C.M., Hui, K.M., and Lam, P.Y. (2013). Human bone marrow-derived mesenchymal stem cells suppress human glioma growth through inhibition of angiogenesis. Stem Cells *31*, 146–155.

Huang, Y., Hoffman, C., Rajappa, P., Kim, J.H., Hu, W., Huse, J., Tang, Z., Li, X., Weksler, B., Bromberg, J., et al. (2014). Oligodendrocyte progenitor cells promote neovascularization in glioma by disrupting the blood-brain barrier. Cancer Res. *74*, 1011–1021.

Huang, Y., Xu, Z., Xiong, S., Sun, F., Qin, G., Hu, G., Wang, J., Zhao, L., Liang, Y.-X., Wu, T., et al. (2018). Repopulated microglia are solely derived from the proliferation of residual microglia after acute depletion. Nat. Neurosci. *21*, 530–540.

Jain, R.K., di Tomaso, E., Duda, D.G., Loeffler, J.S., Sorensen, A.G., and Batchelor, T.T. (2007). Angiogenesis in brain tumours. Nat. Rev. Neurosci. *8*, 610–622.

Jones, E., and Schäfer, R. (2015). Where is the common ground between bone marrow mesenchymal stem/stromal cells from different donors and species? Stem Cell Res. Ther. *6*, 143.

Jung, S., Aliberti, J., Graemmel, P., Sunshine, M.J., Kreutzberg, G.W., Sher, A., and Littman, D.R. (2000). Analysis of fractalkine receptor CX(3)CR1 function by targeted deletion and green fluorescent protein reporter gene insertion. Mol. Cell. Biol. *20*, 4106–4114.

Kovacs, G.G. (2017). Cellular reactions of the central nervous system. Handb. Clin. Neurol. *145*, 13–23.

Krithje, J.H. (2015). T-distributed stochastic neighbor embedding using Barnes-hut implementation. J. Mach. Learn. Res. *9*, 2579–2605.

Lagace, D.C., Whitman, M.C., Noonan, M.A., Ables, J.L., DeCarolis, N.A., Arguello, A.A., Donovan, M.H., Fischer, S.J., Farnbauch, L.A., Beech, R.D., et al. (2007). Dynamic contribution of nestin-expressing stem cells to adult neurogenesis. J. Neurosci. *27*, 12623–12629.

Law, C.W., Chen, Y., Shi, W., and Smyth, G.K. (2014). voom: precision weights unlock linear model analysis tools for RNA-seq read counts. Genome Biol. *15*, R29.

Liu, Z., Kuang, W., Zhou, Q., and Zhang, Y. (2018). TGF-beta1 secreted by M2 phenotype macrophages enhances the stemness and migration of glioma cells via the SMAD2/3 signalling pathway. Int. J. Mol. Med. *42*, 3395–3403.

Llorens-Martín, M., and Trejo, J.L. (2011). Multiple birthdating analyses in adult neurogenesis: a line-up of the usual suspects. Front. Neurosci. *5*, 76.

Lun, A.T., McCarthy, D.J., and Marioni, J.C. (2016). A step-by-step workflow for low-level analysis of single-cell RNA-seq data with bioconductor. F1000Res. *5*, 2122.

Madisen, L., Zwingman, T.A., Sunkin, S.M., Oh, S.W., Zariwala, H.A., Gu, H., Ng, L.L., Palmiter, R.D., Hawrylycz, M.J., Jones, A.R., et al. (2010). A robust and high-throughput Cre reporting and characterization system for the whole mouse brain. Nat. Neurosci. *13*, 133–140.

Malta, T.M., Sokolov, A., Gentles, A.J., Burzykowski, T., Poisson, L., Weinstein, J.N., Kamińska, B., Huelsken, J., Omberg, L., Gevaert, O., et al. (2018). Machine learning identifies stemness features associated with oncogenic dedifferentiation. Cell *173*, 338–354.e15.

Mastrella, G., Hou, M., Li, M., Stoecklein, V.M., Zdouc, N., Volmar, M.N.M., Miletic, H., Reinhard, S., Herold-Mende, C.C., Kleber, S., et al. (2019). Targeting APLN/APLNR improves antiangiogenic efficiency and blunts proinvasive side effects of VEGFA/VEGFR2 blockade in glioblastoma. Cancer Res. *79*, 2298–2313.

Mathivet, T., Bouleti, C., Van Woensel, M., Stanchi, F., Verschuere, T., Phng, L.K., Dejaegher, J., Balcer, M., Matsumoto, K., Georgieva, P.B., et al. (2017). Dynamic stroma reorganization drives blood vessel dysmorphia during glioma growth. EMBO Mol. Med. *9*, 1629–1645.

Mich, J.K., Signer, R.A., Nakada, D., Pineda, A., Burgess, R.J., Vue, T.Y., Johnson, J.E., and Morrison, S.J. (2014). Prospective identification of functionally distinct stem cells and neurosphere-initiating cells in adult mouse forebrain. eLife *3*, e02669.

Mizutani, M., Pino, P.A., Saederup, N., Charo, I.F., Ransohoff, R.M., and Cardona, A.E. (2012). The fractalkine receptor but not CCR2 is present on microglia from embryonic development throughout adulthood. J. Immunol. *188*, 29–36.

Nutt, S.L., Metcalf, D., D'Amico, A., Polli, M., and Wu, L. (2005). Dynamic regulation of PU.1 expression in multipotent hematopoietic progenitors. J. Exp. Med. *201*, 221–231.

Parekh, S., Ziegenhain, C., Vieth, B., Enard, W., and Hellmann, I. (2018). zUMIs - a fast and flexible pipeline to process RNA sequencing data with UMIs. GigaScience *7*, giy059.

Prinz, M., Erny, D., and Hagemeyer, N. (2017). Ontogeny and homeostasis of CNS myeloid cells. Nat. Immunol. *18*, 385–392.

Riccardi, S., Bergling, S., Sigoillot, F., Beibel, M., Werner, A., Leighton-Davies, J., Knehr, J., Bouwmeester, T., Parker, C.N., Roma, G., and Kinzel, B. (2016). MiR-210 promotes sensory hair cell formation in the organ of corti. BMC Genomics *17*, 309.

Rosager, A.M., Sørensen, M.D., Dahlrot, R.H., Boldt, H.B., Hansen, S., Lathia, J.D., and Kristensen, B.W. (2017). Expression and prognostic value of JAM-A in gliomas. J. Neuro-Oncol. *135*, 107–117.

Sankowski, R., Böttcher, C., Masuda, T., Geirsdottir, L., Sagar, Sindram, E., Seredenina, T., Muhs, A., Scheiwe, C., Shah, M.J., et al. (2019). Mapping microglia states in the human brain through the integration of high-dimensional techniques. Nat. Neurosci. *22*, 2098–2110.

Sarkar, A., and Hochedlinger, K. (2013). The sox family of transcription factors: versatile regulators of stem and progenitor cell fate. Cell Stem Cell *12*, 15–30.

Sarkar, S., Döring, A., Zemp, F.J., Silva, C., Lun, X., Wang, X., Kelly, J., Hader, W., Hamilton, M., Mercier, P., et al. (2014). Therapeutic activation of macrophages and microglia to suppress brain tumor-initiating cells. Nat. Neurosci. *17*, 46–55.

Serrano, M., Lee, H., Chin, L., Cordon-Cardo, C., Beach, D., and DePinho, R.A. (1996). Role of the INK4a locus in tumor suppression and cell mortality. Cell *85*, 27–37.

Shaham, O., Smith, A.N., Robinson, M.L., Taketo, M.M., Lang, R.A., and Ashery-Padan, R. (2009). Pax6 is essential for lens fiber cell differentiation. Development *136*, 2567–2578.

Sörensen, I., Adams, R.H., and Gossler, A. (2009). DLL1-mediated Notch activation regulates endothelial identity in mouse fetal arteries. Blood *113*, 5680–5688.

Soumillon, M., Cacchiarelli, D., Semrau, S., van Oudenaarden, A., and Mikkelsen, T.S. (2014). Characterization of directed differentiation by high-throughput single-cell RNA-seq. biorxiv. https://doi.org/10.1101/003236.

Stock, K., Kumar, J., Synowitz, M., Petrosino, S., Imperatore, R., Smith, E.S.J., Wend, P., Purfürst, B., Nuber, U.A., Gurok, U., et al. (2012). Neural precursor cells induce cell death of high-grade astrocytomas through stimulation of TRPV1. Nat. Med. *18*, 1232–1238.

Stuart, T., Butler, A., Hoffman, P., Hafemeister, C., Papalexi, E., Mauck, W.M., 3rd, Hao, Y., Stoeckius, M., Smibert, P., and Satija, R. (2019). Comprehensive integration of single-cell data. Cell *177*, 1888–1902.e21.

Sun, M.Y., Yetman, M.J., Lee, T.C., Chen, Y., and Jankowsky, J.L. (2014). Specificity and efficiency of reporter expression in adult neural progenitors vary substantially among nestin-CreER(T2) lines. J. Comp. Neurol. *522*, 1191–1208.

Tosic, N., Petrovic, I., Grujicic, N.K., Davidovic, S., Virijevic, M., Vukovic, N.S., Pavlovic, S., and Stevanovic, M. (2018). Prognostic significance of SOX2, SOX3, SOX11, SOX14 and SOX18 gene expression in adult de novo acute myeloid leukemia. Leuk. Res. *67*, 32–38.

Van Hove, H., Martens, L., Scheyltjens, I., De Vlaminck, K., Pombo Antunes, A.R., De Prijck, S., Vandamme, N., De Schepper, S., Van Isterdael, G., Scott, C.L., et al. (2019). A single-cell atlas of mouse brain macrophages reveals unique transcriptional identities shaped by ontogeny and tissue environment. Nat. Neurosci. *22*, 1021–1035.

von Baumgarten, L., Brucker, D., Tirniceru, A., Kienast, Y., Grau, S., Burgold, S., Herms, J., and Winkler, F. (2011). Bevacizumab has differential and dose-dependent effects on glioma blood vessels and tumor cells. Clin. Cancer Res. *17*, 6192–6205.

Walzlein, J.H., Synowitz, M., Engels, B., Markovic, D.S., Gabrusiewicz, K., Nikolaev, E., Yoshikawa, K., Kaminska, B., Kempermann, G., Uckert, W., et al. (2008). The antitumorigenic response of neural precursors depends on subventricular proliferation and age. Stem Cells *26*, 2945–2954.

Wang, L., Babikir, H., Müller, S., Yagnik, G., Shamardani, K., Catalan, F., Kohanbash, G., Alvarado, B., Di Lullo, E., Kriegstein, A., et al. (2019). The phenotypes of proliferating glioblastoma cells reside on a single axis of variation. Cancer Discov. *9*, 1708–1719.

Wieghofer, P., Knobeloch, K.P., and Prinz, M. (2015). Genetic targeting of microglia. Glia *63*, 1–22.

Yu, G., and He, Q.Y. (2016). ReactomePA: an R/Bioconductor package for reactome pathway analysis and visualization. Mol. Biosyst. *12*, 477–479.

Zeisel, A., Muñoz-Manchado, A.B., Codeluppi, S., Lönnerberg, P., La Manno, G., Juréus, A., Marques, S., Munguba, H., He, L., Betsholtz, C., et al. (2015). Brain structure. Cell types in the mouse cortex and hippocampus revealed by single-cell RNA-seq. Science *347*, 1138–1142.

Zhang, Y., Chen, K., Sloan, S.A., Bennett, M.L., Scholze, A.R., O'Keeffe, S., Phatnani, H.P., Guarnieri, P., Caneda, C., Ruderisch, N., et al. (2014). An RNA-sequencing transcriptome and splicing database of glia, neurons, and vascular cells of the cerebral cortex. J. Neurosci. *34*, 11929–11947.

Zhao, C., Ma, D., Zawadzka, M., Fancy, S.P., Elis-Williams, L., Bouvier, G., Stockley, J.H., de Castro, G.M., Wang, B., Jacobs, S., et al. (2015). Sox2 sustains recruitment of oligodendrocyte progenitor cells following CNS demyelination and primes them for differentiation during remyelination. J. Neurosci. *35*, 11482–11499.

Ziegenhain, C., Vieth, B., Parekh, S., Reinius, B., Guillaumet-Adkins, A., Smets, M., Leonhardt, H., Heyn, H., Hellmann, I., and Enard, W. (2017). Comparative analysis of single-cell RNA sequencing methods. Mol. Cell *65*, 631–643.e4.